iTi Conference on Turbulence XI

July 27 – 30, 2025 | Bertinoro, Italy

Book of Abstracts

OSLO METROPOLITAN UNIVERSITY
STORBYUNIVERSITETET

ALMA MATER STUDIORUM
UNIVERSITÀ DI BOLOGNA

UNIVERSITÄT BAYREUTH

TECHNISCHE UNIVERSITÄT DARMSTADT

iTi CONFERENCE ON TURBULENCE XI

July 27 - 30, 2025 | Bertinoro, Italy

Editors:

Ramis Örlü
Dept. Mechanical, Electrical and
Chemical Engineering
OsloMet – Oslo Metropoltian University
Oslo, Norway

Alessandro Talamelli
Department of Industrial Engineering
Università di Bologna
Forlì, Italy

Michael Wilczek
Theoretical Physics I
University of Bayreuth
Bayreuth, Germany

Martin Oberlack
Department of Mechanical Enginering
TU Darmstadt
Darmstadt, Germany

Workshop Editors:

Gabriele Bellani
Department of Industrial Engineering
CIRI Aerospace
University of Bologna
Forlí, Italy

Giacchino Cafiero
Department of Mechnical and
Aerospace Engineering
Politecnico di Torino
Turin, Italy

iTi Workshop on
Structure and control of wall-bounded turbulent flows

July 27, 2025 | Bertinoro, Italy

Time	Sunday (27th of July)
08.30	Registration and Introductory remarks
	Session 1 – Chair: Marios Kotsonis
9:00	***Keynote:*** *Smooth surface modifications for passive laminar flow control: recent results and future steps.* **M. Kotsonis** *page 3*
10:00	*Direct numerical simulation of streamwise traveling wave induced turbulent pipe flow relaminarization*. **C. Bauer**, C. Wagner *page 4*
10:20	*Towards optimal plasma actuator arrays for friction drag reduction.* **E. Fracchia**, L. Antal, G. Cafiero, D. Gatti and J. Serpieri *page 6*
10:40	*Space-time wall-pressure–velocity correlations spanning across a turbulent boundary layer and large streamwise offsets.* **R. Deshpande**, A. Hassanein, W. J. Baars *page 8*
11:00	*On the optimal parameters of spanwise forcing for turbulent drag reduction.* **F. Gattere**, A. Chiarini, M. Castelletti, M. Quadrio *page 10*
	Coffee break (11:20 -11:50)

	Sunday (27th of July)
	Session 2 – Chair: Clara Marika Velte
11:50	*Real-time particle image velocimetry using event-based imaging*. **C. Willert**, L. Franceschelli *page 12*
12:10	*Design and characterization of the transient response of oscillating plasma actuators for turbulent skin-friction control.* **L. Magnani**, G. Neretti, J. Serpieri, A. Popoli, A. Cristofolini, A. Talamelli, G. Bellani *page 14*
12:30	*Turbulent drag reduction using metamaterial surfaces*. **N. Fu,** J. Morrison, M. Santer *page 16*
12:50	*Wall-bounded turbulence manipulation using miniature Helmholtz resonators*. **A. H. Hassanein**, D. Modesti, W. J. Baars *page 18*
	Lunch (13:10 – 14:30)
	Session 3 – Chair: Peter Schmid
14:30	***Keynote:*** *Data-driven flow control.* **P. Schmid** *page 20*
15:30	*From robotics to fluid dynamics: opportunities and pitfalls of Reinforcement Learning in flow control.* **O. Semeraro**, L. Mathelin *page 21*
15:50	*Gradient-enriched machine learning control of wingtip vortices via online S-PIV and synthetic jets*. **G. Salomone**, A. Scala, G. Paolillo, T. Astarita, G. Cardone, C.S. Greco Page 22
16:10	*Towards a bio-inspired flow estimation in wall-bounded turbulence*. **A. Ianiro** *page 24*
16.30	*Deep reinforcement learning for turbulent control: drag reduction and heat transfer management.* Z. Zhou, **X. Zhu** *page 25*
	Coffee break (16:50-17:20)
	Session 4 – Chair: Woutjin Baars
17:20	*Intra-phase recovery in a turbulent boundary layer subjected to spatial square-wave spanwise forcing.* **M. Knoop,** R. Deshpande, B. van Oudheusden *page 26*
17:40	*Boundary layer development derived from Galilean symmetry.* **C. M. Velte,** P. Buchhave *page 28*
18:00	*Reconstructed modal velocity fields in wall turbulence*. **M. Guala,** R. Ehsani, A. Ghosh, M. Heisel, I. Jacobi *page 30*
18:20	*On the manipulation of coherent structures in turbulent flows using Fourier-based wall modifications.* **Y. Dincoglu**, S. Verma, A. Hemmati *page 32*
18:40	**Concluding remarks and final discussion: Chair G. Bellani and G. Cafiero**

iTi CONFERENCE ON TURBULENCE XI

July 28 - 30, 2025 | Bertinoro, Italy

time	Sunday (27th of July)
19:00	Welcome buffet - Registration

Time	Monday (28th of July)
08.30	Registration and Introductory remarks
	Session 1 – Roughness I – Chair: Elias Balaras
9:00	***Keynote:*** *Urban Aerodynamics and Turbulent Dispersion.* **C. Vanderweel** *page 37*
9:30	*Turbulent Boundary Layers over Multiscale Urban Arrays.* **C. Southgate-Ash,** S. Grimmond, A. Robins, M. Placidi *page 39*
9:50	*Energetic aspects of the Reynolds analogy in rough-wall turbulent forced convection.* F. Secchi, D. Gatti, U. Piomelli, **B. Frohnapfel** *page 41*
10:10	*The influence of wall-normal oscillating roughness on a turbulent boundary-layer.* **A. Ramani,** T. P. Illukkumbura, B. Ganapathisubramani, J. P. Monty, N. Hutchins *page 43*
10:30	*Influence of oncoming boundary layer on flow over a protruding forward-facing step.* **R. J. Martinuzzi,** E. Larose *page 45*
	Coffee break (10:50 -11:20)

Time	Monday (28th of July)
	Session 2 – Turbulence Theory I – Chair: Martin Oberlack
11:20	*Wavenumber-to-wavenumber energy exchange by triadic Fourier-mode interactions in wall turbulence*. **T. Kawata,** T. Tsukahara *page 47*
11:40	*On velocity spectra in turbulent wall-bounded flows.* **S. Pirozzoli** *page 49*
12:00	*The Reynolds shear stress phase distribution and its relationship to spectral energy density in wall bounded flows*. **S. Zimmerman,** J. Philip, J. Klewicki *page 50*
12:20	*Homogeneous shear turbulence: kinetic energy growth rate as a nonlinear eigenvalue problem*. **J. Albert,** T. Gebler, M. Oberlack *page 52*
12.40	*Two-point enstrophy budget and energy cascade in turbulence*. **A. Cimarelli,** C.B. da Silva, G. Boga *page 53*
	Lunch (13:00 – 14:00)
	Session 3 – Wall Turbulence I – Chair: Ramis Örlü
14:00	**Keynote:** *Turbulent drag reduction by streamwise traveling waves of wall deformation.* **K. Fukagata** *page 55*
14:30	*Restricted Nonlinear Investigation of Developing Boundary Layers over Accelerating Walls.* **A. Risha,** B. A. Minnick, D. F. Gayme *page 56*
14:50	*Towards a composite mean velocity profile for adverse pressure gradient turbulent boundary layers*. **A. Zarei,** M. Lozier, R. Deshpande, I. Marusic *page 58*
15:10	*Constructing wall turbulence using attached hairpin vortices*. Y. Ge, W. Shen, Z. Han, **Y. Zhao,** Y. Yang *page 60*
15.30	*High Spatial Resolution PIV Study of Self-Similar Adverse Pressure Gradient Turbulent Boundary Layer on the Verge of Separation.* **Z. Chen,** B. Sun, A. Heidarian, C. Atkinson, J. Soria *page 62*
15:50 – 16:50	**Coffee break and Poster presentation (session 1)**

time	Monday (28th of July)
	Session 4 – Roughness II – Chair: Christina Vanderweel
16:50	*Characterisation of rough-wall drag in compressible turbulent boundary layers.* **D. D. Wangsawijaya,** R. Baidya, S. Scharnowski, B. Ganapathisubramani, C. J. Kähler *page 64*
17:10	*Relaxation of staggered roughness generated turbulence in a low Re number channel flow*. **S. Tardu,** B. Arrondeau *page 66*
17:30	*A rough recovery*. **M. Formichetti,** A. Kwong, S. Symon, B. Ganapathisubramani *page 68*
17:50	*Influence of windward and effective slope on the structure of turbulent channel flow over ratchet-type roughness.* **O. Zhdanov,** A. Busse *page 70*
18:10	*DNS of turbulent boundary layers over dense soft filaments*. N. Beratlis, A. Camminatiello, K. Squires, **E. Balaras** *page 72*
18:30	**Possible Visit to CICLoPE**

time	Tuesday (29th of July)
	Session 5 – Turbulence Theory II – Chair: Martin Oberlack
8:30	**Keynote:** *Breakup of small aggregates in turbulent flows.* **A. Lanotte** *page 74*
9:00	*A Universal Relation Between Intermittency and Dissipation in Turbulence.* **F. Schmitt,** J. Peinke, M. Obligado *page 75*
9:20	*Spontaneous generation of helicity in anisotropic turbulence near the two-dimensional limit.* **S. Sukoriansky,** E. Barami *page 77*
9:40	*Near and far field development of the turbulent round jet derived from Galilean symmetry*. P. Buchhave, **C. M. Velte** *page 79*
10:00	*Amplitude Modulation in Restricted Nonlinear Turbulence.* **B. Viggiano,** B. Minnick, D. F. Gayme *page 81*
	Coffee break (10:20 -10:50)
	Session 6 – Wake Turbulence – Chair: Bettina Frohnapfel
10:50	*Turbulent/turbulent entrainment in a planar wake*. **O. R. H. Buxton,** J. Chen *page 83*
11:10	*Coherent structures in the turbulent near-wake of a flapping wing*. **Y. Goodwin,** G. Rigas, J. F. Morrison *page 85*
11:30	*Turbulent wake resonance via oscillation of a solid plate.* **G. Xiangyu,** K. Steiros *page 87*
11:50	*A CFD Flow Control Study Using Plasma Actuation on the Leading Edge of a Bluff Body*. **G. Minelli,** R. Magal, G. Bellani *page 89*
	Lunch (12:10-13:10)

	Session 7 – Turbulence theory III – Chair: Michael Wilczek
13:10	**Keynote:** *Turbulence: statistical approach versus coherent structures.* **J. Peinke** *page 91*
13:40	*Entrainment and small-scale features in merging turbulent regions*. **F. A. Branco,** C. B. da Silva page 92
14.00	*Multiscale circulation in wall-parallel planes of turbulent channel flows.* **P.-Y. Duan,** X. Chen, K. R. Sreenivasan *page 94*
14:20	*Noise-expansion cascade – a fundamental property of turbulence*. **S. Liao,** S. Qin *Page 95*
14:40	*Extending Kolmogorov Theory to Polymeric Turbulence*. **A. Chiarini,** R. K. Singh, M. E. Rosti *page 96*
15:00 – 16:00	**Coffee break and Poster presentation (session 2)**
	Session 8 – Simulation Techniques – Chair: Martin Obligado
16:00	*Resolvent-Based Models for Wall-Modelled Large-Eddy Simulations*. Z. Hantsis, M. Chan, N. Hoang, B. J. McKeon, **U. Piomelli** *page 98*
16:20	*Investigation of the physical role of backward scatter in minimal channel flow*. **K. Inagaki** *page 100*
16:40	*Efficient Compressible Turbulent Flow Simulations: Entropy Projection and Correction for an ILES in a Discontinuous Galerkin solver*. A. Crivellini, L. Alberti, **E. Carnevali,** A. Colombo *page 102*
17:00	*Merging Filtering, Modeling and Discretization to Simulate Large Eddies in Burgers' Turbulence*. **R. Verstappen** *page 104*
17:50	**Conference dinner: Bagno Holiday, Milano Marittima (BUS)**

time	Wednesday (30th of July)
	Session 9 – Convection & Complex flows – Chair: Sergio Pirozzoli
8:30 8:50 9:10 9:30 9:50	*Very low Ekman number turbulent rotating convection.* **E. Knobloch,** A. van Kan, B. Miquel, K. Julien, G. Vasil *page 106* *Heat transfer fluctuations measurements with a heated thin foil*. **A. Cuéllar,** E. Amico, J. Serpieri, G. Cafiero, W. J. Baars, S. Discetti, A. Ianiro *page 108* *Validation of helicity turbulence model and its application to stellar convection.* **N. Yokoi** *page 110* *Richtmyer-Meshkov induced turbulent mixing in a shock tube*. **J. Griffond,** O. Soulard, Y. Bury, S. Jamme *page 112* *Learning to Backtrace Turbulent Scalar Fields.* **M. Carbone,** L. Piro, R. Heinonen, L. Biferale, M. Cencini *page 114*
	Coffee break (10:10-10:30)
	Session 10 – Wall turbulence II – Chair: Hassan Nagib
10:30 10:50 11:10 11:30	*On the flow statistics and dynamics of axial rotating turbulent pipe flows: A DNS study*. **L. Yang,** J. Yao *page 116* *Momentum and heat transfer in turbulent channels with drag-increasing riblets*. S. Cipelli, N. Rapp, B. Frohnapfel, **D. Gatti** *page 117* *Identity variation of turbulent spots in pipe flow associated with multigenerational splits, reconnect and re-splits*. **X. Wu,** P. Moin, R. J. Adrian *page 119* *Direct Numerical simulations of Taylor-Couette flows with extreme small radius inner rotating cylinders*. **P. Orlandi,** S. Pirozzoli *page 121*
	Coffee break (11:50-12:10)

	Session 11 – Wall turbulence III – Chair: Alessandro Talamelli
12:10	*Experimental and numerical investigations of laminarization via preconditioning in turbulent pipe flows*. **S. Nozarian,** M. J. Rincón, P. Forooghi, M. Reclari, M. Abkar *page 123*
12:30	*High Reynolds number trends of centerline mean velocity and normal stress in pipe flow*. **H. Nagib,** L. Lazzarini, G. Bellani, A. Talamelli *page 125*
12:50	*On the inertial sublayer of the mean velocity profile in turbulent wall-flows*. **J. Klewicki,** J. Philip *page 127*
13.10	*High-order moment scaling of near-wall turbulence for arbitrary velocities: Extending the symmetry approach.* **M. Oberlack,** S. Hoyas, S. Görtz *page 129*
13:30	**Concluding remarks**
	Lunch (13:40-14:40)

Posters

iTi Conference on Turbulence XI

July 27- 30, 2025 | Bertinoro, Italy

WORKSHOP

Smooth surface modifications for passive laminar flow control: recent results and future steps

Marios Kotsonis[1]

[1] Delft University of Technology, The Netherlands

Abstract:
Boundary layer instabilities are of paramount importance for the dynamics of transitional flows, themselves dominating drag production and efficiency of many relevant systems such as aircraft wings. However, in most real-life cases, aerodynamic surfaces are not smooth or geometrically perfect. Surface non-uniformities are inevitable due to debris, damages, and manufacturing features such as joints, panels, rivets etc. These geometrical features have a profound effect on boundary layer instabilities and transition. These effects are reviewed in this talk, based on recent experimental and numerical studies of our team. Expectedly, in most cases the effect of these features is detrimental, thus leading to anticipation of transition. However, we have discovered limited cases where surface modifications can actually lead to a delay of transition. These cases have revealed a wealth of fundamental interaction mechanisms, which can pave the way to passive flow control methods. Some next steps and ideas in moving forward will be shared.

Direct numerical simulation of streamwise traveling wave induced turbulent pipe flow relaminarization

C. Bauer [1], and C. Wagner [1,2]

[1] Institute of Aerodynamics and Flow Technology
German Aerospace Center, Göttingen, Germany
[2] Institute of Thermodynamics and Fluid Mechanics
Technische Universität Ilmenau, Germany

key-words: turbulent pipe flow, streamwise traveling wave

Abstract:
For technically relevant flows with high Reynolds numbers, more than 90% of the energy required to pump fluids through pipes is dissipated by turbulence near the wall. However, Koganezawa et al. [1] showed for the low friction Reynolds number of $\mathrm{Re}_\tau = u_\tau R/\nu = 110$—where u_τ is the friction velocity, ν is the kinematic viscosity and R is the pipe radius—that for certain wave parameters, streamwise traveling waves of wall blowing/suction can lead to relaminarization, thereby significantly reducing drag. However, as reported in the recent review paper by Fukagata et al. [2], higher Reynolds number data are required for engineering applications. Therefore, we have adapted our fourth-order finite volume solver [3] to perform direct numerical simulations of turbulent pipe flow with streamwise traveling wave boundary conditions of the wall-normal velocity of friction Reynolds numbers up to $\mathrm{Re}_\tau = 720$. For each Reynolds number the optimal set of the blowing/suction parameters is determined in terms of the drag reduction rate $R_D = (C_{f0} - C_f)/C_{f0}$, where $C_f(C_{f0})$ is the skin friction drag of the (un)controlled flow. In addition to the drag reduction rate R_D, the net energy saving S is a crucial metric for evaluating the efficiency of the control method. The net energy saving is defined as $S = (W_{p0} - (W_p + W_a))/W_{p0}$, where $W_p(W_{p0})$ is the driving power of the (un)controlled flow and W_a is the actuation power of the control. Figure 1 shows the net energy saving map at $\mathrm{Re}_\tau = 180$ and a wavelength of $\lambda^+ = 360$ wall units. As illustrated in Figure 1, downstream traveling waves with $\lambda^+ = 360$, $c = U_{c,lam}$, and $a = 0.07U_{c,lam}$ induce relaminarization and a maximum of net energy saving of approximately 80%. Here, $U_{c,lam} = 1/2\mathrm{Re}_\tau u_\tau$ is the centerline velocity of the corresponding laminar flow. In addition, standing waves ($c = 0$) with low amplitudes ($a \leq 0.15U_{c,lam}$) and slow upstream traveling waves ($c = 0.1U_{c,lam}$) lead to positive net energy savings. In the following, we are performing a parametric study by varying Re_τ, as well as the traveling wave amplitude a, length λ, and velocity c. At the conference we will present the Reynolds number scaling of the blowing/suction parameters that lead to relaminarization, minimum drag, and maximum net energy saving, and elucidate the underlying mechanisms. Figure 2 presents the Reynolds number scaling of the turbulent kinetic energy decay rate of flow cases with relaminarization.

References

[1] S. Koganezawa, A. Mitsuishi, T. Shimura, K. Iwamoto, and A. Murata. *Int. J. Heat Fluid Flow*, **77**, 388-401,2019.

[2] K. Fukagata, K. Iwamoto, and Y. Hasegawa. *Annu. Rev. Fluid Mech.*, **56**, 69-90, 2024.

[3] C. Bauer, D. Feldmann, and C. Wagner. *Phys. Fluids*, **29**, 125105, 2017.

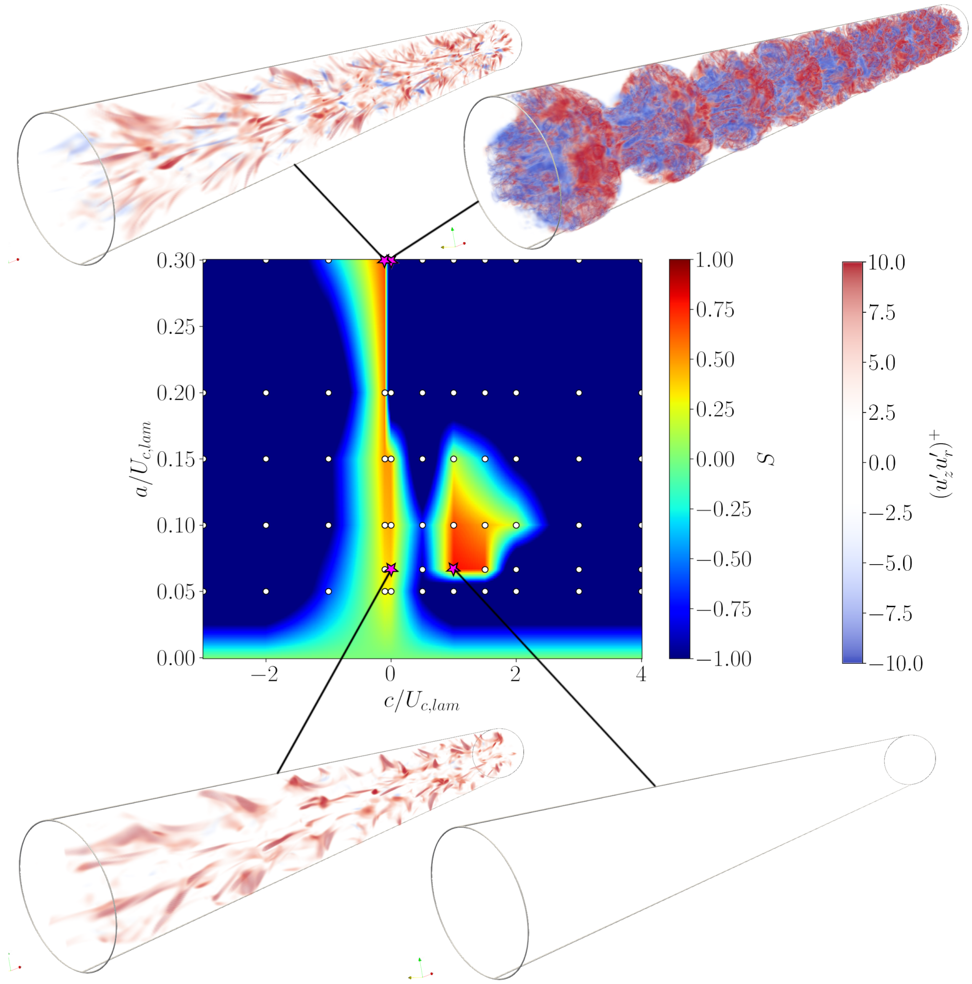

Figure 1: Net energy savings S for $\mathrm{Re}_\tau = 180$ and $\lambda^+ = 360$ as a function of wave amplitude a and velocity c normalized with $U_{c,lam}$. For selected cases, the volume rendering of the instantaneous Reynolds shear stress $u_z'u_r' = u_z u_r - \langle u_z\rangle_\varphi \langle u_r\rangle_\varphi$ normalized in wall units at time $t = 7.5u_\tau/D$ after the start of the control is shown.

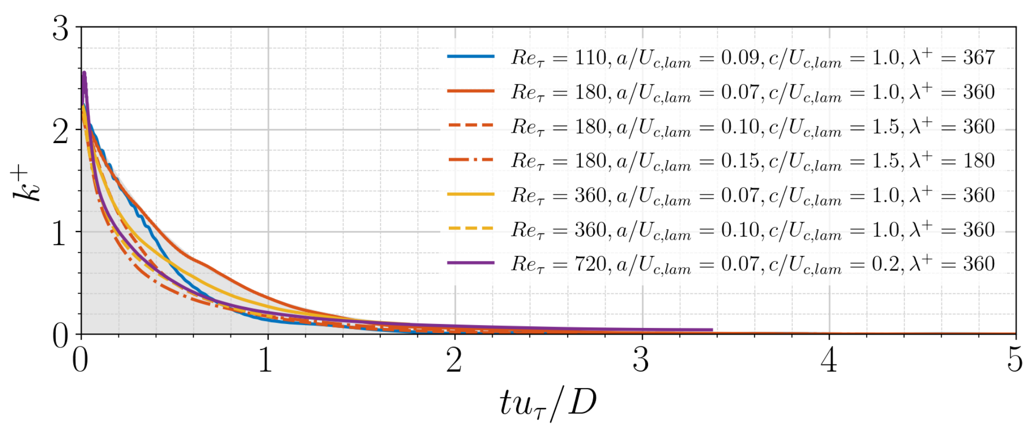

Figure 2: Turbulent kinetic energy decay for streamwise traveling wave-induced relaminarization at different Re_τ, a, c, and λ. $k^+ = 1/2(\langle u_z'u_z'\rangle^+_{r\varphi z} + \langle u_\varphi'u_\varphi'\rangle^+_{r\varphi z} + \langle u_r'u_r'\rangle^+_{r\varphi z})$. The shaded area indicates the exponential decay function $k^+ = 2.2\exp(tu_\tau/D/0.55)$.

Towards optimal plasma actuator arrays for friction drag reduction

E. Fracchia [1], L. Antal [1], G. Cafiero [1], D. Gatti [2], and J. Serpieri [1]

[1] Department of Mechanical and Aerospace Engineering, Politecnico di Torino, Turin, Italy
[2] Institute for Fluid Mechanics, Karlsruhe Institute of Technology, Karlsruhe, Germany

key-words: Friction drag reduction, Plasma actuators, Optimization

Different research efforts have shown how the wall shear stress, and the related friction drag, can be lowered by oscillating the walls along the spanwise direction. Nevertheless, the cumbersome realization of those wall motions bounds this approach to laboratory efforts [5]. Arrays of plasma actuators can be lain out to realize this forcing approach [4]. These devices allow to inject wall motions at the wall and are characterized by high frequency response, reduced weight and size, low power consumption and lack of moving parts. Nonetheless, plasma-induced spanwise-oscillating flow motions differ from the desired oscillating-wall flow. In fact, first, the induced velocity peaks somewhere above the wall for the PAs fields and at the wall for Stokes' second problem flows. Second, the PAs-induced jets require a supply of mass from the surrounding fluid. This causes a downwash motion that can enhance the local skin friction. This parasitic effect can overcome the possible reduction of turbulence-induced downwash motions (i.e. sweeps) and thus cause an overall undesired increase of skin friction. Thereof, the scope of the current work is to investigate a rather broad range of PAs' control parameters to retrieve those configurations that minimize the mentioned parasitic effect and identify optimal PAs for friction drag reduction.

PAs are electrical devices and, as such, have a wide operating range, meaning that the applied voltage, modulation frequency, duty cycle, and actuator geometry are mostly independent and greatly influence the resulting body force fields and the related induced velocity fields and can make the difference between drag reduction and increase, as discussed in [2]. Given this wide range of possible actuation parameters, and their non-linear effects, when designing PA arrays for friction drag reduction, it might prove crucial to optimize the actuation parameter space with numerical investigations. To do so, in the current study, a channel flow DNS code adapted from the engine by Luchini & Quadrio [1], was exploited. The code was modified to allow for the inclusion of time-varying PAs-induced body force fields in the spanwise momentum equation. The body force model introduced in [3] was selected. In fact, this model computes the body force fields based on the physical and operational properties of the modeled PA, thus obtaining crucial information for future experimental endeavors. Forcing and geometric parameters are investigated by running an optimization routine aimed at reducing the velocity gradient at the wall, as shown in figure 1.

At first laminar flows will be investigated and so the skin friction coefficient will be estimated solely from the wall velocity gradient, neglecting the turbulence transport effects. In other words, the optimization feedback variable is proportional to the time- and spanwise- averaged streamwise velocity gradient at the wall. Figure 2 shows that there is an optimal duty cycle (DC) value and that this changes depending on the modulation frequency. Different single-parameter optimization will be explored and eventually also a multiparametric optimization will be performed. Finally, the optimal forcing configurations will be tested in a fully-developed turbulent flow to assess the effect of the performed actuation on the overall skin friction drag.

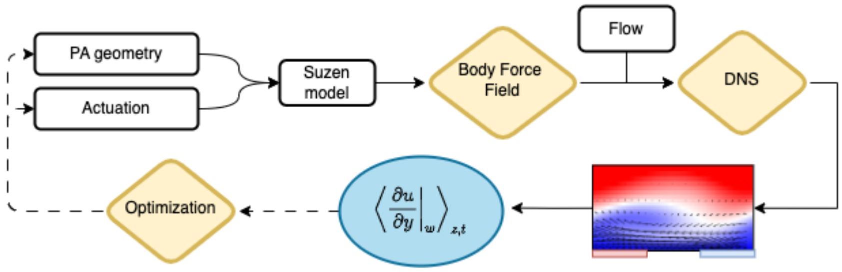

Figure 1: Logic scheme of the performed optimization. The yellow diamonds represent the computation blocks. In the blue circle, the optimization feedback is shown. The contour plot is a velocity field, with the two exposed electrodes shown with the light blue and red shades.

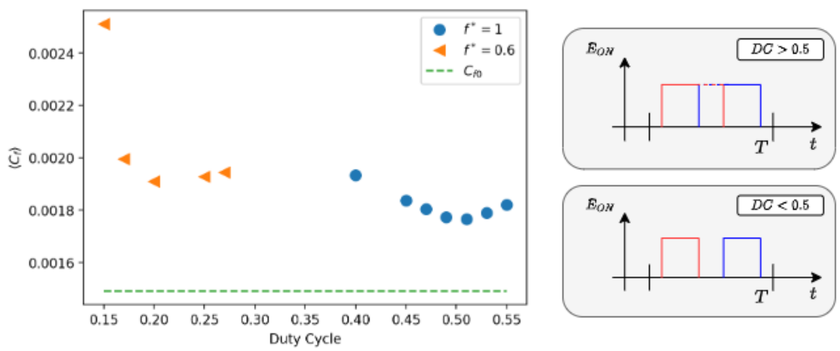

Figure 2: (Left) Laminar-flow wall skin friction coefficient, averaged over a period and along the crosswise direction; the dashed line represents the friction coefficient without actuation. (Right) Schematic of the voltage modulation signals color-coded as the electrodes in the contour plot of figure 1.

References

[1] Luchini, P., Quadrio, M. (2006), A low-cost parallel implementation of direct numerical simulation of wall turbulence. *J. Comput. Phys., 211(2), 551–571.*

[2] Mahfoze, O., Laizet, S. (2017), Skin-friction drag reduction in a channel flow with streamwise-aligned plasma actuators. *Int. J. Heat Fluid Flow, 66, 83–94.*

[3] Suzen, Y., Huang, G., Jacob, J., Ashpis, D. (2005), Numerical simulations of plasma based flow control applications *35th AIAA Fluid Dynamics Conference and Exhibit (p. 4633)*

[4] Jukes, T. N., Choi, K.-S., Johnson, G. A., Scott, S. J., Francisco, S. (2006), Turbulent Drag Reduction by Surface Plasma through Spanwise Flow Oscillation. *3rd AIAA Flow Control Conference. 2006.*

[5] Ricco, P., Skote, M., Leschziner, M. A. (2021), A review of turbulent skin-friction drag reduction by near-wall transverse forcing. *Prog. Aerosp. Sci. 123*

Space-time wall-pressure–velocity correlations spanning across a turbulent boundary layer and large streamwise offsets

Rahul Deshpande[1], Abdelrahman Hassanein[2] and Woutijn J. Baars[2]

[1] Department of Mechanical Engineering, University of Melbourne, Parkville, VIC 3010, Australia
[2] Faculty of Aerospace Engineering, Delft University of Technology, 2629 HS Delft, The Netherlands

Key-words: Turbulent boundary layers, Boundary layer structure, wall pressure

Abstract:
The fluctuating wall pressure (p_w) field beneath a turbulent boundary layer (TBL) is primarily responsible for structural excitation and associated radiated noise for submarines and aircraft. Structural resonances generally occur in the low wavenumber regime of the p_w-spectrum, known as the *sub-convective* regime, while the most energetic amount of turbulence energy resides at higher convective wavenumbers (k_x) and their associated frequencies (f), popularly known as the *convective* regime. Both these regimes have previously been analyzed through the k_x-f spectrum of p_w [1], with their respective energy distributions increasing proportionally with the boundary layer friction Reynolds number (Re_τ) owing to energization of the inertial motions [2]. However, many past studies investigating the k_x-f spectrum of p_w have either been limited to low Re_τ, or in the case of higher Re_τ experiments, have not simultaneously measured velocities across the TBL. These limitations have hindered our understanding of the coupling between turbulence velocity fluctuations and the space-time wall-pressure field.

In the present study, we experimentally investigate the Re_τ-variation of the k_x-f wall-pressure spectra across $1000 \lesssim Re_\tau \lesssim 5000$, acquired simultaneously with the streamwise velocity fluctuations in the grazing TBL flow. An array of flush-mounted microphones (figure 1a) were mounted inside the Delft University Boundary Layer Facility (DUBLF). The linear array comprised 63 microphones with an equidistant spacing in the streamwise direction. This array spanned 5 times the boundary layer thickness (δ), making it sufficiently large to capture p_w-footprints of the long energetic inertial motions (figure 1b). Each microphone was exposed to the flow through a unique 5-pin hole arrangement, designed with the intention to spatially under-resolve the p_w-signal, and thereby avoid aliasing of the very large k_x in the k_x-f spectrum [1]. A conventional hotwire sensor, measuring time-resolved streamwise velocity fluctuations (u) synchronously with p_w, was positioned above the most downstream microphone and traversed vertically across 30 logarithmically-spaced points in the boundary layer. Bulk parameters estimated from the velocity profile confirm that the pressure array has no influence on the near-wall flow.

Figure 2(a) shows the k_x-f spectrum computed from the wall-pressure field shown in figure 1(b), for a canonical TBL at $Re_\tau \sim 1500$. One can observe that the most energetic pressure fluctuations convect at $f^+/k_x^+ \sim 15$ (indicated by the grey dashed line) and correspond to the *convective regime*. The associated 1-D k_x and f-spectra are obtained by integrating the spectrum in figure 2(a), and are shown in figures 2(b,c), respectively. These unique measurements would be used to test popular scaling arguments [3] for the *sub-convective* and *convective* regimes of the k_x-f spectra. Their physical significance would be explained through p_w-u correlations [3], reconstructed across $0 \leq x \leq 5\delta$ and $y \lesssim \delta$.

References

[1] Butt, H., Damani, S., Devenport, W.J. and Lowe, T., (2024) Identification of Sources of Sub-Convective Wall Pressure Fluctuations Using Space-Time Pressure-Velocity Correlations, *In 30th AIAA/CEAS Aeroacoustics Conference p. 3166.*

[2] Baars, W.J., Dacome, G. and Lee, M., (2024) Reynolds-number scaling of wall-pressure–velocity correlations in wall-bounded turbulence, *Journal of Fluid Mechanics, 981, A15*

[3] Willmarth, W.W. and Wooldridge, C.E. (1962), Measurements of the fluctuating pressure at the wall beneath a thick turbulent boundary layer, *Journal of Fluid Mechanics 14(2): 187-210*

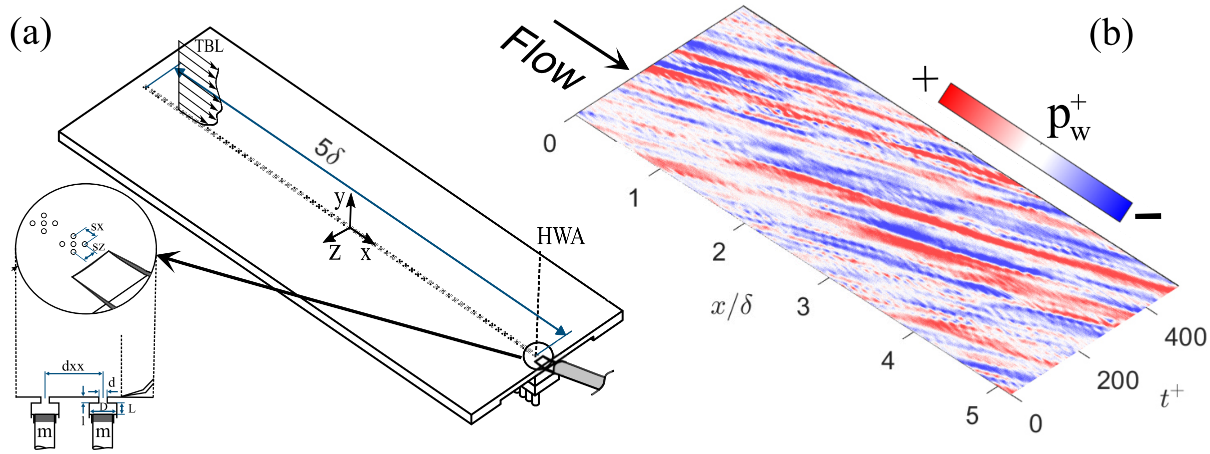

Figure 1: (a) Schematic of the experimental setup comprising 63 wall-mounted microphones (m) with an equidistant spacing, spanning 5δ in x. Each microphone is mounted inside a sub-surface cavity, and is exposed to the flow via an arrangement of 5 pinholes. A single-wire hotwire is positioned vertically above the most downstream microphone. (b) Space-time plot of p_w^+ acquired with the microphone array.

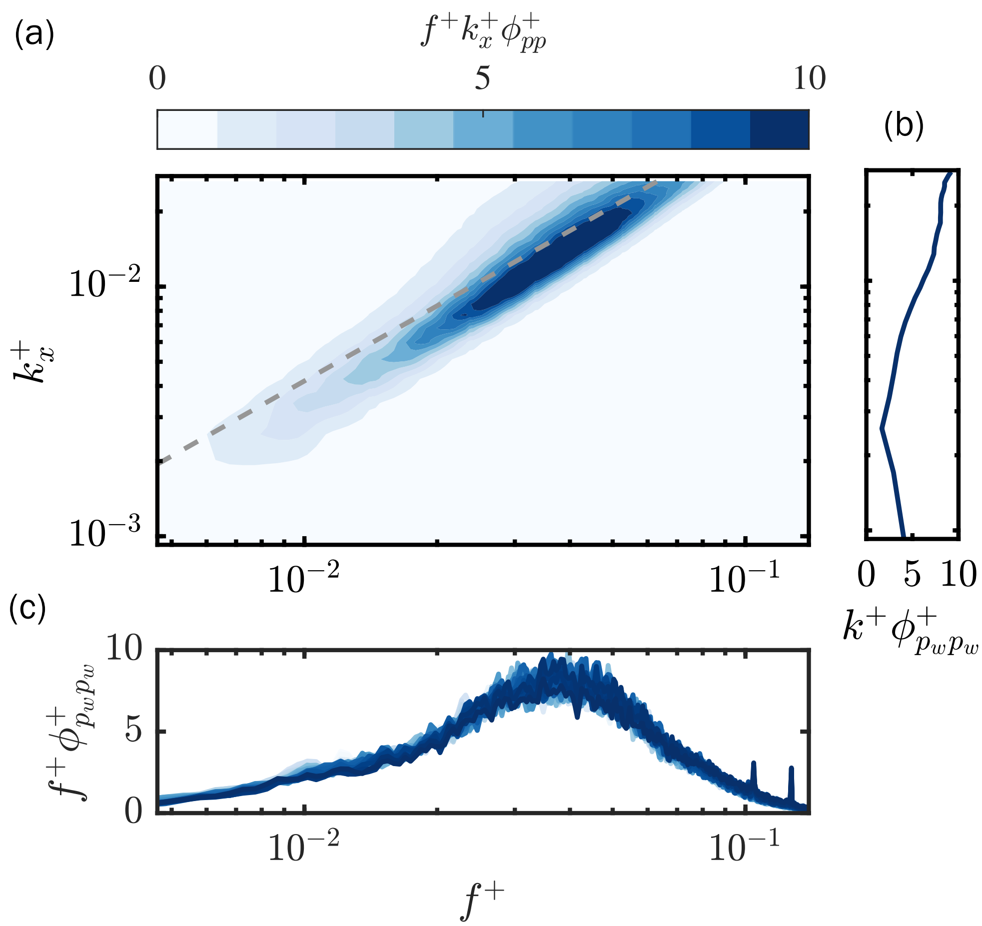

Figure 2: (a) Premultiplied viscous-scaled f-k_x spectrum of p_w for $Re_\tau \sim 1500$. The grey dashed line indicates the convection velocity of the most energetic pressure fluctuations ($15u_\tau$). (b,c) premultiplied 1-D p_w-spectrum as a function of (b) k_x and (c) f obtained by integrating f-k_x spectrum in (a).

ON THE OPTIMAL PARAMETERS OF SPANWISE FORCING FOR TURBULENT DRAG REDUCTION

F. Gattere [1], A. Chiarini [1], M. Castelletti [1] and M. Quadrio [1]

[1] Department of Aerospace Science and Technologies, Politecnico di Milano, 20156 Milan, Italy

key-words: Drag reduction, Simulation

Abstract:
Efforts to reduce turbulent skin-friction drag are important for both environmental and economic reasons. Various methods have been proposed over the years; among these, techniques that use active predetermined wall-based actuation are particularly noteworthy for their simplicity and effectiveness. The most simple active forcing that leads to a reduction of turbulent skin friction drag is the spanwise wall oscillation [1]. The wall periodically oscillates in the spanwise direction as a function of time:

$$w(t) = A \sin\left(\frac{2\pi}{T}t\right),$$

and generates a spanwise cross-flow that is periodic after space- and phase-averaging and coincides (with small deviations for large T) with the analytical laminar solution of the second Stokes problem, referred to as the Stokes layer (SL):

$$w_{SL}(y,t) = Ae^{-\frac{y}{\delta}} \sin\left(\frac{2\pi}{T}t - \frac{y}{\delta}\right).$$

It depends on three parameters: the amplitude A, the period of the oscillation T and the thickness of the spanwise velocity profile δ. The latter two quantities are not independent, i.e. $\delta \equiv \sqrt{\nu T/\pi}$ and evidences suggest that the maximum drag reduction is obtained for $T^+ \approx 100$ and $\delta^+ \approx 6$, although there is no consensus on their physical interpretation. Hereinafter the + superscript identifies quantities made dimensionless with the viscous quantities of the uncontrolled case.

In this work we overcome the conventional oscillating wall and remove the $\delta - T$ constraint. We perform a DNS study at $Re_\tau = 400$ directly enforcing a mean spanwise velocity profile at each time step to a turbulent channel flow, varying δ and T independently. The new drag reduction map is shown in figure 1. We conclude that the values $T^+ \approx 100$ and $\delta^+ \approx 6$ do not possess a special meaning and they are the optimum when we are constrained by the control actuator to lie on the black line of figure 1; instead designing a control which allows to decouple T and δ provides higher drag reduction performance and we find the optimal parameters for drag reduction to be $T^+ = 30$ and $\delta^+ = 14$.

We also measure positive net benefit, i.e. the control is still beneficial after accounting also for the power required to imposed the spanwise velocity profile; see figure 2. This result paves the way for the implementation of alternative actuators. The control law does not need to be the result of the choice of the actuator as in the case of the wall oscillation, but more conveniently the actuator can be designed to induce the desired control law to the flow field.

References

[1] Jung W.J., Mangiavacchi N. and Akhavan R. (1992), Suppression of turbulence in wall-bounded flows by high-frequency spanwise oscillations, *Phys. Fluids A, vol. 4(8), pp. 1605–1607*

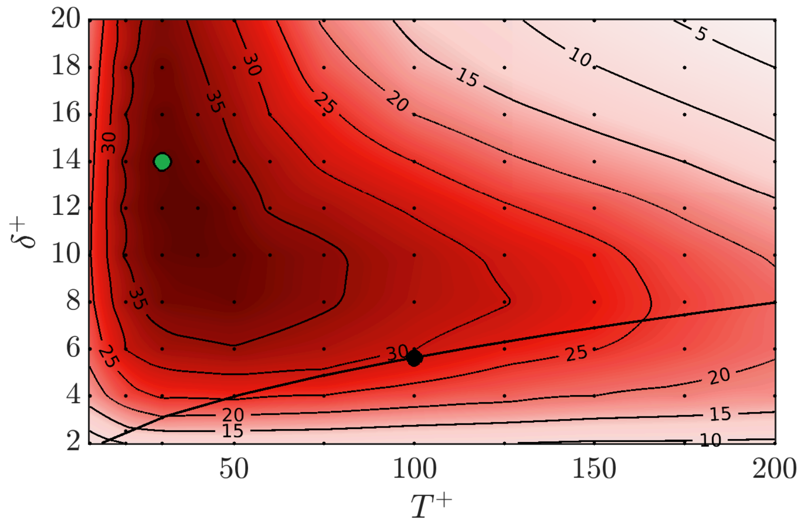

Figure 1: *Drag reduction ($\mathcal{R} = 100 \times (C_{f,0} - C_f)/C_{f,0}$) map in the ($T$, δ) two-dimensional space of parameters, with C_f and $C_{f,0}$ the skin-friction coefficients of the uncontrolled and controlled cases, respectively. The black thick line indicates the $T - \delta$ constraint. The green dot identifies the point of maximum drag reduction, whereas the black dot indicates the maximum along the line where the $T - \delta$ constraint holds. The small black dots indentify the sets of parameters of each simulation.*

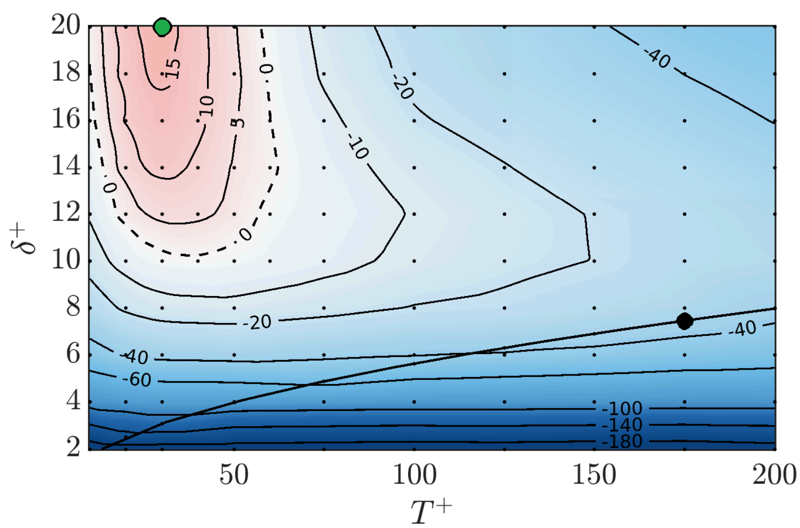

Figure 2: *Net power saving ($P_{net} = \mathcal{R} - 100 \times P_c/P_0$) map in the ($T$, δ) two-dimensional space of parameters, with $\mathcal{R}$ the drag reduction and P_c/P_0 the power to enforce the spanwise velocity profile expressed as a fraction of the pumping power to move the flow. The black thick line indicates the $T - \delta$ constraint. The green dot identifies the point of maximum net power saving, whereas the black dot indicates the maximum along the line where the $T - \delta$ constraint holds. The small black dots indentify the sets of parameters of each simulation.*

Real-time particle image velocimetry using event-based imaging

C. Willert [1] and L. Franceschelli [2]

[1] DLR Institute of Propulsion Technology, German Aerospace Center, Köln, Germany
[2] Department of Aerospace Engineering, Universidad Carlos III de Madrid, Leganés, Madrid, Spain

key-words: on-line processing, experiment, turbulence measurement, flow control

Abstract:
In the context of active flow control the continuously increasing speed of both imaging and computing hardware are enabling real-time particle image velocimetry (RT-PIV) processing scenarios such as outlined in Fig. 1a ([4, 2]). The basic idea is to extract flow relevant information from real-time processed PIV data to determine flow-controlling parameters with minimal inference time (latency). The proposed contribution describes the implementation of a PIV system based event-based vision (EBV) camera technology and is capable of processing incoming imagery at high frame rates approaching 1 kHz. Unlike conventional cameras, EBV cameras only detect and report intensity changes in the observed scene, providing an asynchronous data stream of contrast change events. With its reduced data rate and potentially rapid data processing capability, EBV is a strong candidate for this purpose [1]. To date, the real-time capability of EBV has not been fully exploited with the exception of the 3d particle tracking velocimetry (PTV) implementations by [3] that reconstructed the (time-averaged) 3d flow field in real-time. However, their setup can only simultaneously track a small number of particles of O(50-100). The present work aims at acquiring and processing imagery containing O(1000) particles necessitating approaches differing from conventional PTV.

While notluc making direct use of the asynchronous nature of the data provided by the EBV camera, the generation of pseudo-frames from the event stream was found to be considerably more efficient than trying to continuously extract (and track) clusters over time. The pseudo-frames can then be processed using conventional PIV algorithms, which are easily parallelized in comparison to PTV schemes. Compared to RT-PIV implementations using framing cameras, the latency of real-time EBIV (RT-EBIV) is reduced by at least one framing interval: the second pseudo-frame is immediately available at the end of the time-slicing period (see Fig. 1b).

Initial implementations of RT-EBIV operate by accumulating pseudo-image pairs at a defined framing intervals followed by a single-pass PIV algorithm with subsequent validation to provide velocity field data. A bench-top validation on a rotating disc and a turbulent water flow in a small tank is shown in Fig. 2 and demonstrated a velocity field processing speed of several hundred Hz. For higher pseudo-image rates the incoming data stream must be down-sampled, which however, does not affect the overall latency. The proposed contribution will compare the performance with a RT-PIV implementation based on a streaming CMOS camera and showcases an application to a turbulent boundary layer using the profile-PIV technique.

References

[1] Franceschelli, L., Willert, C. E., Raiola, M., and Discetti, S. An assessment of event-based imaging velocimetry for efficient estimation of low-dimensional coordinates in turbulent flows. *Experimental Thermal and Fluid Science* (2025).

[2] McCormick, F., Gibeau, B., and Ghaemi, S. Reactive control of velocity fluctuations using an active deformable surface and real-time PIV. *Journal of Fluid Mechanics 985* (2024), A9.

[3] Rusch, A., and Rösgen, T. TrackAER: real-time event-based quantitative flow visualization. *Experiments in Fluids 64* (2023), 136.

[4] Willert, C., Munson, M., and Gharib, M. Real-time particle image velocimetry for closed-loop flow control applications. In *15th International Symposium on Applications of Laser Techniques to Fluid Mechanics, Lisbon, 5-8 July 2010.* (2010).

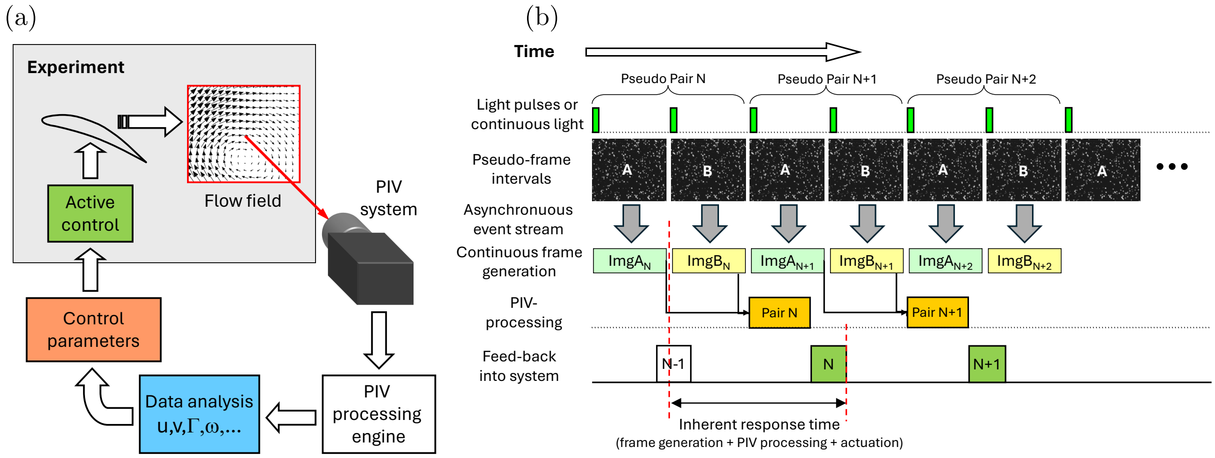

Figure 1: (a): possible implementation of active flow-control based on real-time flow field data (from [4]); (b): data stream for pseudo-frame-based, real-time event-based imaging velocimetry (EBIV). Contrary to framing cameras the pseudo-frames are available immediately after the end of framing period, thereby reducing system latency.

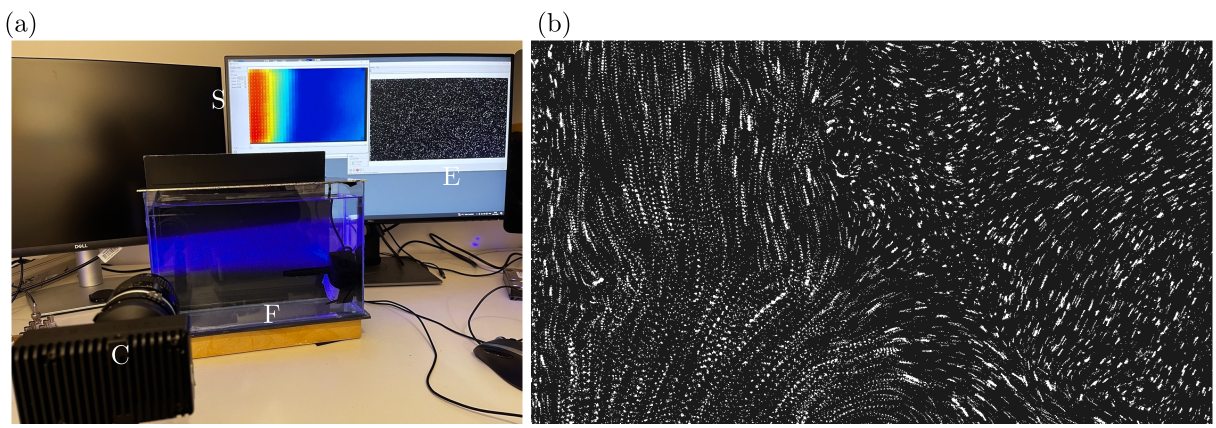

Figure 2: (a): benchtop demonstration of the implemented RT-EBIV configuration on a turbulent water flow (F) using a Prophesee EVK2 camera (C) and a low-cost pulse-modulated blue laser. Computer screen displays raw event imagery (E) and continuously updated flow statistics (S). (b): pseudo-frame obtained of the water flow at a laser pulsing frequency of 800 Hz capturing 8 pulses (10 ms).

Design and characterization of the transient response of oscillating plasma actuators for turbulent skin-friction control

L. Magnani [1], G. Neretti [3], J. Serpieri [4], A. Popoli [3], A. Cristofolini [3], A. Talamelli [1,2] and G. Bellani [1,2]

[1] Dipartimento di Ingegneria Industriale, University of Bologna, Italy

[2] Centro Interdipartimentale di Ricerca Industriale aerospaziale, University of Bologna, Forlì, Italy

[3] Electric Electronic and Information Engineering Department, University of Bologna, Italy

[4] Department of Mechanical and Aerospace Engineering, Politecnico di Torino, Turin, Italy

key-words: WORKSHOP, Plasma actuators, Active flow control, Drag reduction

Abstract:

Reducing the aerodynamic drag of next-generation aircraft is a key objective in sustainable development plans at national, European, and international levels. To reduce friction drag, which accounts for approximately 50% of the total drag during cruise, smart surfaces are being developed and tested. Reducing the friction drag of large airliners requires controlling turbulent fluctuations, in particular with the near-wall cycle [1]. Several studies have demonstrated that oscillating a wall in a specific direction can lead to a significant reduction in friction drag [2]. Recent numerical studies showed a gain in drag-reduction performance by tuning the actuation time-scales on the very-large scale motions [3, 4], highlighting the need of developing flow-control strategies in high-Reynolds number flow conditions. Another technological challenge is to approximate the Stokes layer induced by wall-oscillations with actuators that do not require any moving surface. To this end, plasma actuators with Dielectric Barrier Discharge (DBD) have been developed and have shown promising performance [5, 6].

To test and optimize their performance in realistic flow conditions, the geometry, actuation timing and electrical actuation parameters must be tuned based on the temporal and spatial scales of high-Reynolds number turbulent flows. The Long Pipe facility of the Centre for International Cooperation in Long Pipe Experiments (CICLoPE) [7] provides an ideal environment for such studies: with a diameter of 0.9 m and a length of 111.5 m, it allows precise measurements of near-wall flow fluctuations, providing a reliable baseline for evaluating smart surfaces. To achieve an oscillating wall-parallel flow, several pairs of actuators must be alternately turned on and off at frequencies that scale with the Reynolds number, therefore the transient response of the actuators, rather than the steady state, must be carefully characterized.

In this work, we present a full characterization of the transient response of plasma actuators specifically designed to operate in the high-Reynolds number regime of the Long Pipe facility (Re_τ>10000). Experiments were conducted using the Schlieren technique, which visualizes flow density variations induced by the actuators. Images, acquired with a high-speed camera up to 50,000 fps(Fig. 1), are processed to track the propagation of the density and temperature variation front over time(Fig. 2). Results are presented for several actuation parameters, including modulation frequency (5-80 ms), input voltage (3.5-5 kV), and carrier frequency (20-40 kHz). Based on these results, we discuss potential and limitations of this approach deployed on a large-scale, high-Reynolds number application. Results are also compared in light of a newly-developed mathematical model for plasma generation and its interaction with the surrounding flow.

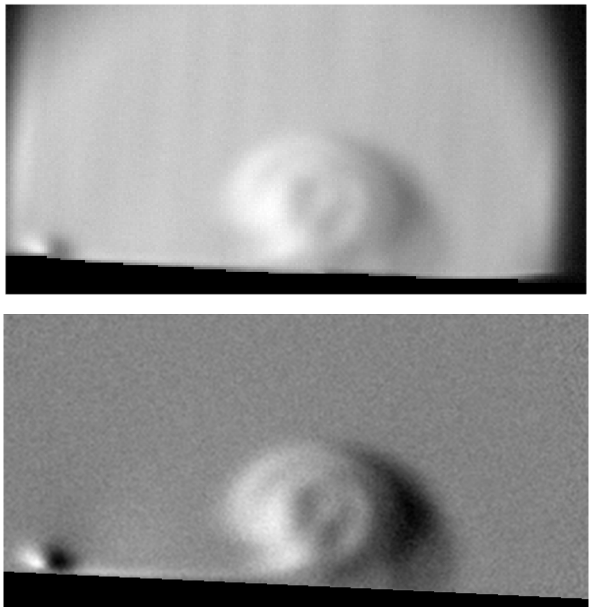

Figure 1: *Raw (above) and background subtracted (below) Schlieren images.*

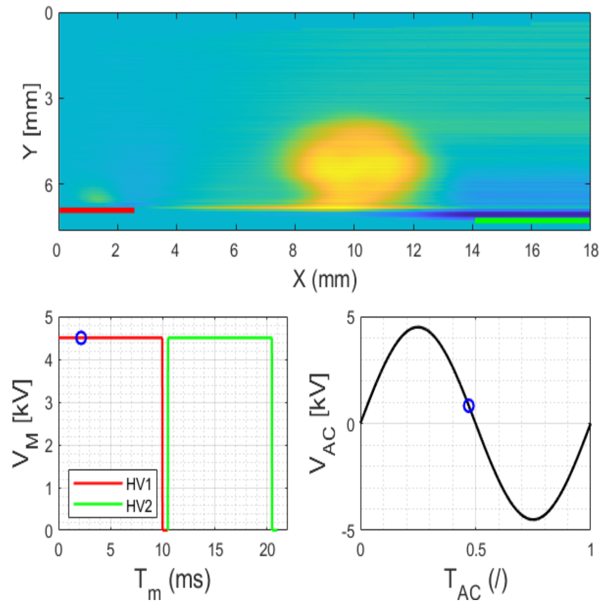

Figure 2: *Temperature field after luminosity integration.*

References

[1] P. Ricco, M. Skote, M.A. Leschziner, (2021), A review of turbulent skin-friction drag reduction by near-wall transverse forcing, *Progress in Aerospace Sciences, vol. 123*

[2] M.Quadrio, (2011), Drag reduction in turbulent boundary layers by in-plane wall motion, *Philosophical transactions, Math, physical and engineering sciences, vol. 369, pp. 1428–42*

[3] D. Chandran, A. Zampiron, A. Rouhi, et al. (2023), Turbulent drag reduction by spanwise wall forcing. Part 2. High-Reynolds-number experiments, *J. of Fluid Mechanics, vol.968*

[4] R. Deshpande, A.G. Kidanemariam, I. Marusic, (2024), Pressure drag reduction via imposition of spanwise wall oscillations on a rough wall, *J. of Fluid Mechanics, vol. 979*

[5] R. Erfani, H. Zare-Behtash, C. Hale, K. Kontis, (2015), Development of DBD plasma actuators: The double encapsulated electrode, *Acta Astronautica, vol. 109, pp. 132-143*

[6] G. Neretti, A. Cristofolini, C. A. Borghi, A. Gurioli, R. Pertile, (2012), Experimental results in dbd plasma actuators for air flow control, *IEEE, Transactions on Plasma Science, vol. 40, pp. 1678-1687*

[7] A. Talamelli, F. Persiani, J. Fransson, P.H. Alfredsson, A. Johansson, N. Hassan, J.D. Rueedi, K. Sreenivasan, P. Monkewitz (2009), CICLoPE - A response to the need for high Reynolds number experiments, *Fluid Dynamics Research, vol.41*

Turbulent drag reduction using metamaterial surfaces

Ningyuan Fu [1], Jonathan Morrison [1] and Matthew Santer [1]

[1] Department of Aeronautics, Imperial College London, London, UK

key-words: Metamaterials, Drag reduction

Abstract:
The idea of reducing the turbulent skin friction drag with the use of streamwise travelling surface waves

$$W = W_0 \sin(\kappa_x x - \omega t) \tag{1}$$

where W is the wall velocity, $\kappa_x = \frac{2\pi}{\lambda}$ is the streamwise wave number and $\omega = 2\pi f$ is the angular velocity, has been proved by various studies both numerically [1]and experimentally [2]. However, at a high Reynolds number ($Re_\tau \sim O(10^5)$) closer to flight conditions, few experimental work has been done in evaluating the feasibility and efficiency of the moving wall technique in drag reduction. An accurate and reliable mechanism to generate surface waves is a key challenge when designing such experiments. Here, a novel way of generating surface waves via a metamaterial surface is proposed. High frequency (on the order of kHz) and low amplitude actuation can be achieved by manipulating the elastic wave propagating through the surface.

In order to manipulate the wave in the surface, it is essential to understand how it propagates through the medium. Therefore, the elastic wave equation was solved in the frequency domain

$$-\omega^2 \frac{\partial^2 \hat{\mathbf{u}}}{\partial t^2} + i\omega\gamma \frac{\partial \hat{\mathbf{u}}}{\partial t} = c_L^2 \nabla(\nabla \cdot \hat{\mathbf{u}}) - c_S^2 \nabla \times \nabla \times \hat{\mathbf{u}} \tag{2}$$

where $\hat{\mathbf{u}}$ is the displacement vector in the frequency domain, γ is the attenuation parameter, c_L and c_S are the longitudinal and transverse wave speed in the material, respectively. The advantage of a frequency domain solution is mainly because of the huge savings in time and computing resources compared with the time domain solver. Now the steady-state waveform can be computed in just one step, without the need to calculate numerous time steps as in a time domain solver. This equation is solved using FEM for every design iteration.

The use of topology optimization with solid isotropic material with penalization (SIMP) has been very successful in solving such inverse design problems, where the microscopic material distribution is solved for to achieve some desired macroscopic properties. The element-wise density variable ρ_e (normally, 0 for void and 1 if material is present in that element) becomes the main variable in this optimization problem. Both the Helmholtz filter and projection functions were utilised to encourage a binary design [4], since those intermediate densities are not practically useful.

It is worth noting that $\rho_e = 0$ doesn't represent void here in this study. A good reason for this is that the void in a surface would lead to aerodynamic problems in wind tunnel tests and real-life applications. The structure itself would perturb the boundary layers even without the surface waves. Two materials are present in this metamaterial surface. The wave speeds c_L and c_S are different in these two materials and some interesting phenomena, such as wave scattering can be observed. A simple yet illustrative example of this is shown in Figure 2, where a circular inclusion with a different material was added to the centre of the rectangular domain. This is one of the fundamental working principles behind acoustic metamaterials and shows the possibility of using a metamaterial surface to generate the desired waveform for the purpose of drag reduction in the future. By carefully choosing the types of materials and their distribution in the design domain, various waveform can be achieved, which could be used in future wind tunnel tests.

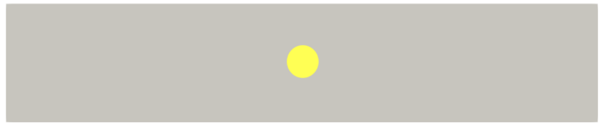

Figure 1: Location of the circular inclusion in the domain

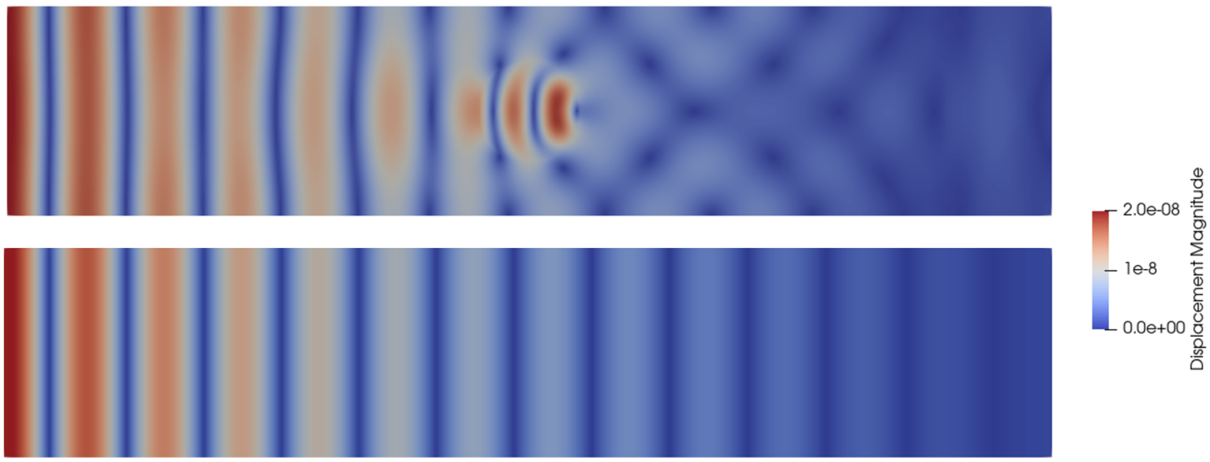

Figure 2: Top: Wave being scattered when encountering the circular inclusion; Bottom: Reference case with a homogeneous domain

References

[1] Quadrio, M., Ricco, P. Viotti, C. , (2009): Sreamwise-travelling waves of spanwise wall velocity for turbulent drag reduction, *Journal of Fluid Mechanics*

[2] Chandran, D., Zampiron, A., Rouhi, A., Fu, M. K., Wine, D., Holloway, B., Smits, A. J. Marusic, I. (2023), Turbulent drag reduction by spanwise wall forcing. part 2. high-reynolds-number experiments, *Journal of Fluid Mechanics*

[3] Thillaithevan, D., Murphy, R., Hewson, R. Santer, M., (2024): Inverse design of periodic microstructures with targeted nonlinear mechanical behaviour, *Structural and Multidisciplinary Optimization, 67(4),55*

[4] Author1 A., Author2 B., Author3 C. and Author4 D., (Year): *Title*, Publisher

[5] Author1 A., Author2 B., Author3 C. and Author4 D., (Year): Title, *Proceedings*, City, pp. ...-...

Wall-bounded turbulence manipulation using miniature Helmholtz resonators

A.H. Hassanein[1], D. Modesti[2], and W.J. Baars[1]

[1] Faculty of Aerospace Engineering, Delft University of Technology, 2629 HS Delft, The Netherlands
[2] Gran Sasso Science Institute, Viale Francesco Crispi 7, 67100 L'Aquila, Italy

key-words: Helmholtz resonator, Channel flow, DNS, PIV

Helmholtz resonators have shown promise as wall-embedded modifications for manipulating near-wall turbulence. They thereby have the potential to control the wall-shear stress (WSS). Flynn et al. [1990] and Flynn and Panton [1990] demonstrated how the natural frequency of a macro-Helmholtz resonator (MHR), which has an orifice diameter similar to the boundary layer thickness ($d \sim \delta$), can be tuned to interact with turbulence near the wall, leading to an increase in streamwise and wall-normal velocity fluctuations downstream of the resonator. Recent work by Dacome et al. [2024] focused on the effects of a miniature Helmholtz resonator (mHR), whose orifice diameter scales as $d \sim \nu/u_\tau$, on different temporal scales of near-wall velocity fluctuations. They found that near the resonator's natural frequency, the energy of the streamwise velocity fluctuations is amplified downstream of the resonator. This amplification is accompanied by a reduction in the larger-scale energy of streamwise velocity fluctuations. Hassanein et al. [2024] further investigated the flow-interaction mechanism of a mHR. By assessing the mechanism on a per-scale basis—with the aid of the local, spectral impedance condition present at the resonator's orifice—an explanation was provided for the attenuation and intensification of turbulence scales. They also examined the effects of the resonator on WSS and found that the resonator decreases WSS within close proximity downstream of it.

Despite the valuable insights provided by Hassanein et al. [2024] into the downstream effects of a mHR on WSS, there remains a need to understand and quantify the resonator's effects over a larger area and to assess the added pressure drag acting on the resonator's orifice. Additionally, there is currently no insight into the behavior of a mHR as a meta-unit in an array configuration; insight into this is valuable for scaling up the number of resonators to achieve flow control surfaces.

To address these gaps, a high-fidelity direct numerical simulation (DNS) of turbulent open-channel flow was performed, over a single resonator, replicating the flow conditions of the experiments conducted by Hassanein et al. [2024]. This is supplemented with a time-resolved particle image velocimetry (TR-PIV) experimental study involving two mHRs in a tandem configuration, with variable spacing between the orifices.

Here, we present the spatial fields of the streamwise Reynolds stress obtained from DNS, highlighting the integral effect of the resonator on the streamwise velocity fluctuations $\overline{u'u'}$ (Fig. 1a). The effect of the resonator on the streamwise velocity fluctuations is more apparent in Fig. 1b, where the percentage difference in the streamwise Reynolds stress with respect to a smooth-wall case is shown. Above and slightly downstream of the resonator, $\overline{u'u'}$ is amplified by more than 20%, followed by an attenuation of $\overline{u'u'}$ that reaches 6%.

Similarly, we present the spatial fields of the streamwise Reynolds stress obtained from the TR-PIV measurements around the two resonators separated in the streamwise direction (Fig. 2a), along with the percentage difference in the streamwise Reynolds stress compared to a smooth-wall case (Fig.2b). A similar trend in energy manipulation is observed when the two resonators are placed in tandem, in comparison to a single resonator.

The full conference contribution will comprehensively address the effects of a single resonator on drag and provide key insights into the behavior of two resonators in a tandem configuration.

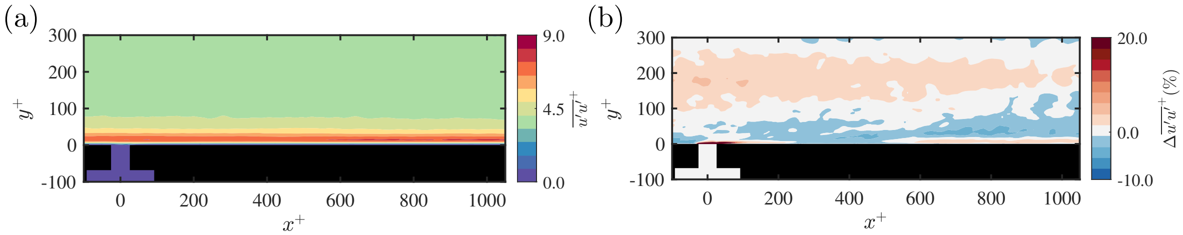

Figure 1: Contours of (a) the streamwise Reynolds stress around the resonator and (b) the percentage difference in the streamwise Reynolds stress relative to the smooth-wall case, obtained using DNS.

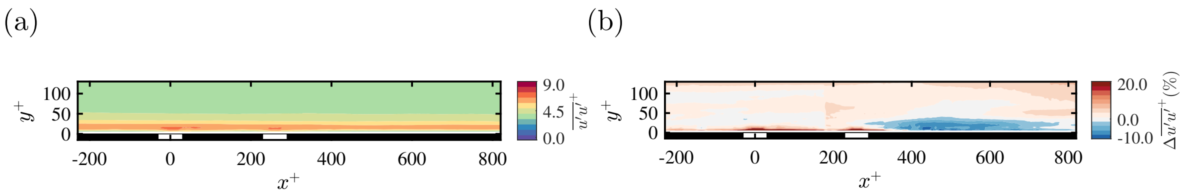

Figure 2: Contours of (a) the streamwise Reynolds stress around the two resonators and (b) the percentage difference in the streamwise Reynolds stress relative to the smooth-wall case, obtained using TR-PIV.

References

G. Dacome, R. Siebols, and W. J. Baars. Small-scale Helmholtz resonators with grazing turbulent boundary layer flow. *J. Turbul.*, 2024.

K. P. Flynn and R. L. Panton. The interaction of Helmholtz resonators in a row when excited by a turbulent boundary layer. *J. Acoust. Soc. Am.*, 87(4):1482–1488, 1990.

K. P. Flynn, R. L. Panton, and D. G. Bogard. Effect of Helmholtz resonators on boundary-layer turbulence. *AIAA J.*, 28(11):1857–1858, 1990.

A. Hassanein, D. Modesti, F. Scarano, and W.J. Baars. Interaction of an inner-scaled Helmholtz resonator with boundary-layer turbulence. *Phys. Rev. Fluids*, 9:114610, 2024.

Data-driven flow control

P. Schmid[1]

[1]King Abdullah University of Science and Technology, Saudi Arabia

Data-based control of fluid systems aims at manipulating flows whose dynamics and receptivity to external forcing are known from measurements only. This type of control is particularly attractive for physical systems whose governing equations are elusive or too complex for a model-based approach. Data-based control critically relies on system identification, a discipline that recovers amodel equation of a physical system from input-output data streams. In this talk, we will touch on rudimentary but fundamentalconcepts of control setup, system identification, and optimal control design. Identification based on impulse responses, subspace projections, and dynamic observers will be treated, together with model-predictive control algorithms. Applications to generic flow configurations will demonstrate the efficacy and usefulness of these techniques under realistic conditions.

From robotics to fluid dynamics: opportunities and pitfalls of Reinforcement Learning in flow control

Onofrio Semeraro and Lionel Mathelin

Laboratoire interdisciplinaire des sciences du numérique (LISN), CNRS, U. Paris-Saclay, Orsay, France

key-words: Fundamentals, Flow control

Abstract:
Reinforcement Learning (RL) has emerged as a powerful tool for controlling complex dynamical systems [2], delivering remarkable results across a diverse range of application domains, from robotics to fluid dynamics, including flow control. Notably, in the context of flow control, key applications include navigation problems [5] and the optimization of external flows for drag/perturbation minimization [3, 6]. These applications are not surprising: although often presented as one of the three main paradigms in machine learning – alongside supervised and unsupervised learning – due to its interdisciplinary nature, RL can be analyzed from multiple viewpoints, including optimal control [4, 1]. Specifically, certain RL algorithms can be interpreted as fully data-driven counterparts to discrete-time optimal control strategies based on the Bellman equation [1], where the policy (i.e., the control action) is learned through interactions with the environment, with the objective of maximizing or minimizing a reward or value function, with or without physical priors.

Crucially, reconciling RL with traditional control theory also highlights its potential limitations. Issues such as lack of observability, controllability, time delays, and system uncertainties cannot be bypassed through off-the-shelf applications of these tools. Additionally, when applied to high-dimensional environments, RL's exploration-driven approach often leads to sample inefficiency, convergence to suboptimal local minima, and challenges in ensuring safety in critical applications. In this talk, we will discuss some of these challenges and briefly introduce potential solutions, such as optimistic-order methods, credit-assignment strategies, and model predictive control approaches hybridized with RL.

This contribution draws upon the research of past and present students and collaborators, including Michele Alessandro Bucci, Rémy Hosseinkhan-Boucher, Luigi Marra, and Amine Saibi.

References

[1] Bertsekas D., (2019): *Reinforcement learning and optimal control*, Athena Scientific

[2] Bucci M. A., Semeraro O., Allauzen A., Wisniewski G., Cordier L. and Mathelin, L., (2019), Control of chaotic systems by deep reinforcement learning, *Proc. R. Soc. A, vol. 475-2231, pp. 20190351*

[3] Rabault J., Kuchta M., Jensen A., Réglade U. and Cerard N., (2019), Artificial neural networks trained through deep reinforcement learning discover control strategies for active flow control, *J. Fluid Mech., vol. 865, pp. 281–302*

[4] Sutton R. S. and Barto A. G., (2018): *Reinforcement learning: An introduction*, A Bradford Book

[5] Vergassola M., Villermaux E. and Shraiman B. I., (2007), 'Infotaxis' as a strategy for searching without gradients, *Nature, vol. 445-7126, pp. 406–409*

[6] Vignon C., Rabault J. and Vinuesa R., (2023), Recent advances in applying deep reinforcement learning for flow control: Perspectives and future directions, *PoF, vol. 35-3*

Gradient-enriched machine learning control of wingtip vortices via online S-PIV and synthetic jets

Gabriele Salomone [1], A. Scala [1], G. Paolillo [1], T. Astarita [1], G. Cardone [1] and C.S. Greco [1]

[1] Department of Industrial Engineering (DII), University of Naples "Federico II", Naples, Italy

key-words: Active Flow Control, Artificial Intelligence, Stereo-Particle Image Velocimetry

Abstract:

This work presents an innovative approach for driving active flow control of wingtip vortices on a finite wing via synthetic jets. The gradient-enriched Machine Learning Control (gMLC) algorithm[1] is chosen as optimization tool to drive the control strategy toward an optimal voltage signal provided to the actuator. The experiments are conducted in a subsonic open-circuit wind tunnel with a rectangular test chamber 300 $\times$ 400 mm, operated at a mean free-stream velocity of 12 m/s. The test article is a rectangular finite-span wing mounting a NACA 0015 airfoil, a chord of $c = 0.05$ m and wingspan $b = 0.10$ m, mounted at a negative angle of attack of -5 °. Control signals are created by a signal generator, amplified and fed to a loudspeaker that is incorporated into the hollow sting of the test article. A fast multipass process [2, 3] is employed to acquire and process Stereo-Particle Image Velocimetry (S-PIV) measurements to quantify the effectiveness of the control strategies. S-PIV image pairs are acquired in a plane downstream of the wing ($z/c = 5$) within a square image field of $0.3c \times 0.3c$, centered on the right wingtip vortex (Figure 1).The generic control law can be expressed as $b(t) = K(\mathbf{h}(t))$, where $\mathbf{h}(t)$ represents a set of harmonic functions built from a reference actuation frequency f_a, chosen equal to the Crow instability frequency. The aim of the optimization process is to find the control law K^* minimizing the cost function $J = \langle\bar{\zeta_c^*}\rangle/\langle\bar{\zeta_u^*}\rangle$, being $\langle\bar{\zeta_c^*}\rangle$ and $\langle\bar{\zeta_u^*}\rangle$ spatial averages of the dimensionless vorticity of the mean flow in the controlled case and in the baseline condition, respectively. Different optimization runs are conducted by evaluating waveshapes of the input voltage signal showing an increasing level of complexity in the recombination of the functions in $\mathbf{h}(t)$. The gMLC-optimized controllers achieves a mean vorticity reduction of up to 71 % of the baseline condition. The effectiveness of optimal control laws is proven through time averaged maps of streamwise vorticity (Figure 2) and through the effect on vortices' unsteady behavior in phase-averaged measurements, where it can be seen that the gMLC-optimized controller is able to mitigate the outward displacement of the vortex during its periodic motion (Figure 3).

References

[1] Maceda G. et al., (2021), Stabilization of the fluidic pinball with gradient-enriched machine learning control, *Journal of Fluid Mechanics, vol. 917,A42*

[2] Astarita T., (2007), Analysis of weighting windows for image deformation methods in PIV, *Experiments in Fluids, vol. 43 , pp. 859-872*

[3] Astarita T., (2008), Analysis of velocity interpolation schemes for image deformation methods in PIV, *Experiments in Fluids, vol. 45 , pp. 257-266*

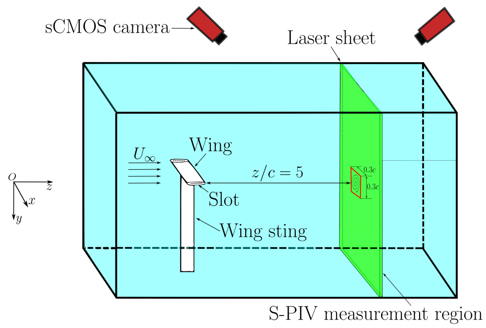

Figure 1: *S-PIV measurements setup: the red-contoured square zone represents the vortex core region corresponding to the image field.*

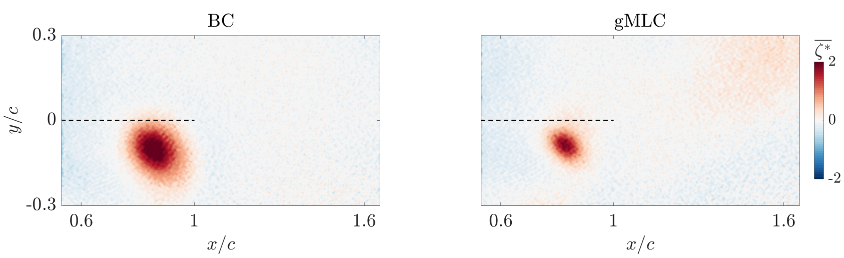

Figure 2: *Dimensionless time-averaged vorticity fields maps* $\langle\bar{\zeta}^*\rangle$ *for the baseline condition and gMLC-based most performing control case.*

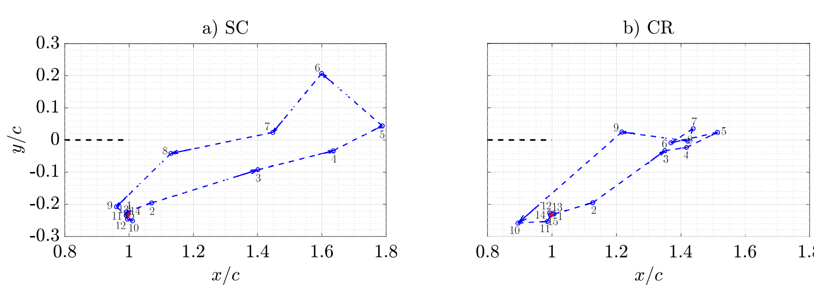

Figure 3: *Phase-averaged evolution of the vortex position at* $z/c = 5$ *for (a) a sinusoidal control (SC) law and (b) a gMLC-optimized control. The black dotted line represents the wing trailing edge projection, while the numbers represents the increasing phase. The time-averaged position is marked with a red dot.*

Towards a bio-inspired flow estimation in wall-bounded turbulence

Andrea Ianiro [1]

[1] Department of Aerospace Engineering, Universidad Carlos III de Madrid, Leganés, Spain

key-words: Flow control, flow sensing, reduced-order modelling

Abstract:

The non-linearities and the large range of scales challenge our ability to model and control turbulent flows. However, the ubiquitous nature of turbulence motivates unabated research efforts. The closed-loop control of unsteady turbulent flows requires the ability to sense the flow state. This presentation will introduce the research roadmap toward developing bio-inspired sensors for turbulent flows.

In the last years, both linear [1] and non-linear [2] flow estimation tools were developed. The talk will highlight as the state of the art techniques require an intractable number of sensors, making the data acquisition and analysis unfeasible in a practical scenario [3]. Data rate of practical applications is further challenged by the Nyquist criterion leading to a requirement of high-repetition-rate sampling.

Our recent findings show that many complex flows can be represented on low-dimensional manifolds [4]. The availability of a reduced set of coordinates for state representation is a key enabler for the choice of a sparse set of sensors in space [5]. The observation of natural fliers, moreover, suggests that classical Nyquist sampling might be overcome. I will discuss how insects estimate the flow surrounding them with a few event-based sensors embedded in their wings [6]. Algorithms for event-based signal processing avoid aliasing without the need for high-frequency periodic sampling, reducing the amount of data needed to estimate complex temporal series [7]. This could enable flow estimation with easy-to-handle and cheap-to-compute data. Coupling manifold learning and event-based sensors we could develop sensors for turbulent flows with easy-to-handle data rates.

References

[1] Encinar, M. and Jiménez, J., (2019), Logarithmic-layer turbulence: a view from the wall, *Phys. Rev. Fluids, vol. 4, n. 114603.*

[2] Cuéllar, A., Güemes, A., Ianiro, A., Flores, O., Vinuesa, R. and Discetti, S., (2024), Three-dimensional generative adversarial networks for turbulent flow estimation from wall measurements, *J. Fluid Mech., vol. 991, n. A1.*

[3] Cuéllar, A., Ianiro, A. and Discetti, S., (2024), Some effects of limited wall-sensor availability on flow estimation with 3D-GANs, *Theor. Comp. Fluid Dyn., vol. 38, pp. 729–745.*

[4] Farzamnik, E., Ianiro, A., Discetti, S., Deng, N., Oberleithner, K., Noack, B. R. and Guerrero, V., (2023), Some effects of limited wall-sensor availability on flow estimation with 3D-GANs, *J. Fluid Mech., vol. 955, n. A34.*

[5] Whitney, H., (1944), The self-intersections of a smooth n-manifold in 2n-space, *Ann. Math., vol. 45, pp. 220-246.*

[6] Aiello, B. R., Stanchak, K. E., Weber, A. I., Deora, T., Sponberg, S. and Brunton, B. W., (2021), Spatial distribution of campaniform sensilla mechanosensors on wings: form, function, and phylogeny, *Curr. Opin. Insect Sci., vol. 48, pp. 8-17.*

[7] Lazar, A. A and Tóth, L. T., (2004), Perfect recovery and sensitivity analysis of time encoded bandlimited signals, *IEEE T. Circuits I, vol. 51, pp. 2060–2073.*

Deep reinforcement learning for turbulent control: drag reduction and heat transfer management

Zisong Zhou[1] and Xiaojue Zhu[1]

[1] Max Planck Institute for Solar System Research, Göttingen, Germany

key-words: Turbulent control, deep reinforcement learning

Abstract:

Turbulent flows, ubiquitous in engineering systems from aircraft to energy devices, pose critical challenges in drag management and thermal efficiency. Traditional control strategies, which often rely on empirically designed functions, struggle to cope with the multiscale complexity and nonlinear dynamics of turbulence, particularly in extreme scenarios such as wall-bounded turbulence at high Reynolds numbers (Re_τ) and turbulent convection at high Rayleigh numbers (Ra). These limitations highlight the need for adopting deep reinforcement learning (DRL), which provides an adaptive, data-driven control approach to address the intricate nonlinear relationships in turbulent flows.

We implement a unified DRL framework using the Twin Delayed Deep Deterministic Policy Gradient (TD3) algorithm coupled with direct numerical simulations (using the AFiD code), as shown in figure 1. For drag reduction in channel flows with Re_τ up to 1000, wall actuation via blowing and suction is optimized using the streamwise velocity fluctuations in the near-wall region. In turbulent Rayleigh-Bénard convection with Ra up to 5×10^8, temperature fluctuations at the wall are dynamically adjusted based on boundary layer thermal signals. Both systems employ an Actor-Critic architecture where the policy network continuously interacts with flow simulations to maximize predefined rewards (drag reduction rate or Nusselt number).

The DRL controller achieves 27.7% drag reduction at $Re_\tau = 1000$ [1], significantly surpassing the performance of traditional opposition control methods. Simultaneously, it enhances heat transfer by 38.5% in convection systems through spatiotemporally optimized thermal boundary modulation, achieving more than 1.5 times the performance of empirical sine-form temperature distribution methods. These results demonstrate DRL's unique capability to decode multiscale turbulence interactions and establish control principles in wall-bounded turbulence and turbulent convection.

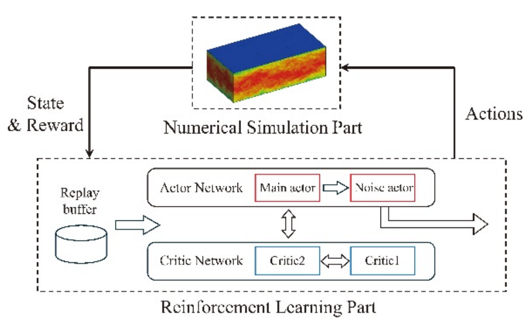

Figure 1: *Flow chart of reinforcement-learning-driven turbulent control*

References

[1] Zhou, Z., Zhang, M., & Zhu, X. (2025). Reinforcement-learning-based control of turbulent channel flows at high Reynolds numbers. *arXiv preprint arXiv:2501.01573*.

Intra-phase recovery in a turbulent boundary layer subjected to spatial square-wave spanwise forcing

Max W. Knoop[1], Rahul Deshpande[2], Bas W. van Oudheusden[1]

[1] Faculty of Aerospace Engineering, Delft University of Technology, 2629 HS Delft, The Netherlands
[2]Department of Mechanical Engineering, The University of Melbourne, Parkville, VIC 3010, Australia

key-words: Turbulent boundary layer, Wall-based forcing, Working mechanism, Experiment

Abstract:
We experimentally investigate the response of a turbulent boundary layer (TBL) to a spatially imposed wall-forcing in the spanwise direction, which is a well-established method to achieve turbulent friction drag reduction [1]. The study implements a square-wave (SqW) type discretization of the traditionally studied steady spanwise wall velocity: $W_w(x) = A\sin(2\pi x/\lambda_x)$[2], where A and λ_x represent forcing amplitude and wavelength, respectively. The experimental setup comprises an array of 48 streamwise-spaced belts (fig. 1 a,b) [3] that can be activated to run in alternating spanwise directions. This setup allows to investigate the influence of wavelength on the streamwise evolution of a TBL at $\lambda_x^+ = 471$ (sub-optimal; green), 942 (near-optimal; blue), and 1884 (post-optimal conditions; red), while fixing the amplitude, $A^+ = 12$, at friction Reynolds number, $Re_\tau = 960$ (based on the inflow TBL thickness $\delta_0 = 70\,\mathrm{mm}$), by using particle image velocimetry (PIV; fig. 1 c).

At the initial imposition of forcing ($x/\delta_0 \leq 0.5$), fig. 2 (FOV1) a markedly similar attenuation pattern of the turbulent stresses across all wavelength regimes is observed, with $-\overline{uv}^+$ decreasing by approximately 80% within $x/\delta_0 \lesssim 0.1$, while $\overline{uu}^+$ exhibits a more gradual response. Subsequently, the (sub-)optimal regimes display a (nearly-)streamwise homogeneous response. Interestingly, however, in the post-optimal case, of which FOV1 captures one complete wavelength (i.e., $\lambda_x \sim 2\delta_0$), the turbulence reflects a significant recovery over the half-phase, most notable in the Reynolds shear stress. Following this intra-phase recovery, the turbulence is 're-attenuated' near $x/\delta_0 \approx 1$, where the wall-forcing direction reverses. This modification can plausibly be linked to the phase-wise 'rate-of-change' of the Stokes strain, $\partial^2\overline{W}/\partial x\partial y$ (*i.e.*, Stokes strain rate; SSR). Agostini *et al.* [4] found the SSR to interact, and effectively attenuate the near-wall self-sustaining cycle through a strong vortex tilting/stretching mechanism, while the turbulent dynamics were found to recover under a near-zero SSR. Assuming a laminar Stokes layer solution [2, 3], the SqW is characterized by localized regions of high SSR (hence, turbulence attenuation), while there is only minimal spatial variation of $\partial\overline{W}/\partial y$ over the rest of the half-phase where W_w is constant (i.e., turbulence recovery). Supporting this hypothesis, the post-optimal case under fully established forcing conditions (FOV2) in fig. 3(d) exhibits significant intra-phase variations in the streamwise stress, which is highlighted by subtracting its phase-averaged value $\langle\overline{uu}\rangle_x^+$. We observe a notable attenuation following each forcing reversal ($x/\delta_0 \approx 9.75,\ 10.75$) while the stress recovers to a maximum preceding these regions. A similar trend is also reflected by the wall-normal location of the streamwise stress peak (black '+'-marked lines). Ongoing analysis aims on further elucidating these intra-phase recovery phenomena through the budgets of turbulent production and transport, which will be presented at the conference.

References

[1] P. Ricco, M. Skote, and M. A. Leschziner, "A review of turbulent skin-friction drag reduction by near-wall transverse forcing," *Prog. Aerosp. Sci.*, vol. 123, p. 100713, 2021.

[2] C. Viotti, M. Quadrio, and P. Luchini, "Streamwise oscillation of spanwise velocity at the wall of a channel for turbulent drag reduction," *Phys. Fluids*, vol. 21, 2009.

[3] M. W. Knoop, F. H. Hartog, F. F. J. Schrijer, O. W. G. van Campenhout, M. van Nesselrooij, and B. W. van Oudheusden, "Experimental assessment of square-wave spatial spanwise forcing of a turbulent boundary layer," *Exp. Fluids*, vol. 65, no. 5, p. 65, 2024.

[4] L. Agostini, E. Touber, and M. Leschziner, "The turbulence vorticity as a window to the physics of friction-drag reduction by oscillatory wall motion," *Int. J. Heat Fluid Flow*, vol. 51, pp. 3–15, 2015.

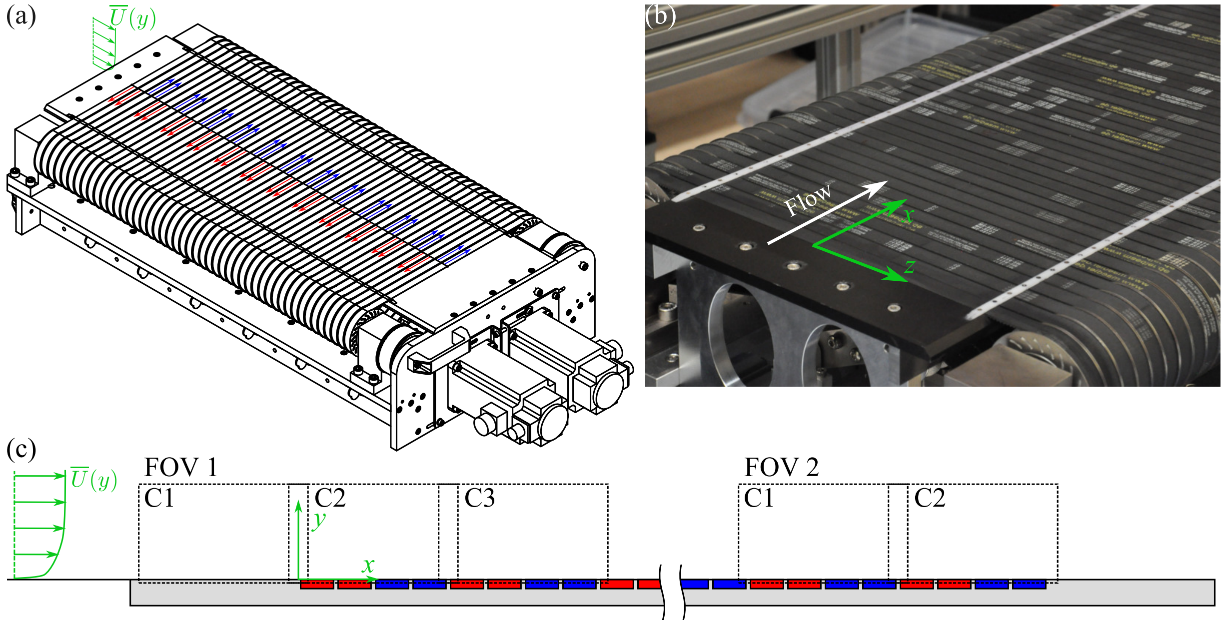

Figure 1: (a) Schematics of the experimental apparatus, of which (b) shows a photographic. (c) Schematic of the multi-camera PIV (2D-2C) experiment, conducted at the initiation of forcing (FOV1) and in the fully-established region downstream (FOV2). Coloured arrows and belts indicate their respective positive (red) and negative (blue) W_w for the specific case of $\lambda_x^+ = 942$.

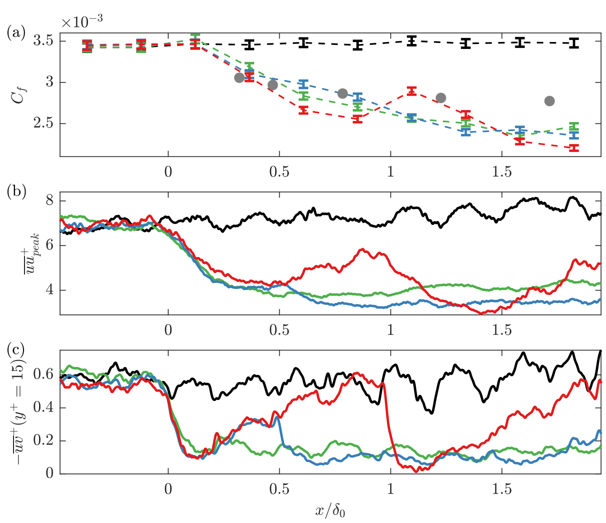

Figure 2: Streamwise evolution at the onset of actuation (FOV1), of (a) C_f, (b) the peak magnitude of $\overline{uu}^+$, and (c) $-\overline{uv}^+$ at $y^+ = 15$. Wall-forcing at $A^+ = 12$, for respectively, $\lambda_x^+ = 471$ (green; sub-optimum), $\lambda_x^+ = 942$ (blue; near-optimum), $\lambda_x^+ = 1884$ (red; post-optimum), and the non-actuated reference (black).

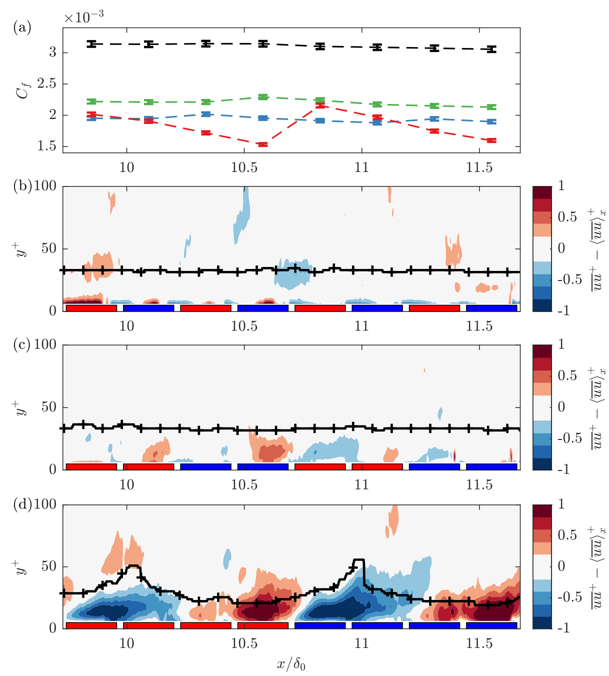

Figure 3: Streamwise evolution under established forcing (FOV2) of (a) C_f, and (b-d) $x-y$ contours of phase-wise variation of $\overline{uu}^+ - \langle\overline{uu}\rangle_x^+$, for the three respective wavelength regimes, black '+'-marked line denoted the wall-normal height of the near-wall peak. Coloured patches indicate the belts' position and their respective positive (red) and negative (blue) W_w.

Boundary layer development derived from Galilean symmetry

Clara M. Velte[1] and Preben Buchhave[2]

[1] Dept. Civil and Mechanical Engineering, Technical University of Denmark, Kgs. Lyngby, Denmark
[2] Intarsia Optics, Birkerød 3460, Denmark

key-words: Galilean symmetry, ZPG boundary layer, Pipe flow boundary layer, Evolving turbulence, Non-equilibrium turbulence

Abstract: In previous work, we have derived analytically and numerically simulated the statistical development of the round turbulent jet, from the jet exit and across the self-similar region [1]. These inferences were based solely on the fundamental assumption of the existence of the Galilean Symmetry Group and a constant density Newtonian fluid. Hence, we are not implementing the equations governing fluid flow, but instead basic symmetries that translate directly to the relevant conservation laws through Emmy Noether's theorem [2].

The only inputs required using this methodology are the initial flow statistics (e.g. the initial mean velocity profile), which will vary between different flow generators, and the kinematic turbulent (eddy) viscosity, which specifies how the turbulent diffusion affects the development of the flow.

In the present work, these concepts of methodology have been extended to pipe flow boundary layers and flat plate zero pressure gradient (ZPG) boundary layers. The pipe flow boundary layer solution is achieved simply by keeping the cylindrical coordinate system formulation of the round jet and extending a cylindrical no-slip surface from the initial profile and downstream. The ZPG boundary layer is formulated using the same methodology, in a Cartesian coordinate system with no-slip along the flat wall.

The recursive program yields directly the relevant differential equation, simply from physical reasoning, from which we will also derive an analytical solution to the mean velocity profile in each case. The relevant differential equations describe, as for the round jet, the diffusion of momentum, similarly to the heat conduction equation describing the diffusion of heat. A control volume analysis of each respective flow describes the momentum diffusion due to internal shear forces. Our equations cover both the developing turbulent flow as well as the flow in the self-similar regions and the agreement with experimental data is excellent.

Figure 1 shows the laminar ZPG boundary layer (Blasius) simulated for three different developing times / lengths using our recursive numerical solver. The profiles are similarity scaled and overlap perfectly. The fact that the Blasius profile is achieved validates the numerical method based on laminar flow.

Figure 2 shows measurement data for a turbulent ZPG boundary layer for a wall friction-based Reynolds number Re_τ=6.000 (blue squares) along with results from our numerical simulations (black line). The simulations have been fitted to the measurement data by adapting the turbulent (eddy) viscosity. The simulations can thus be used as a tool to solve for the turbulent (eddy) viscosity from measured profiles, and thereby the turbulent momentum diffusion, as a function of the wall-normal coordinate. This information may be valuable for turbulent boundary layer modeling applications. Figure 3 shows the simulated development of the turbulent pipe flow boundary layer profile, from an initial 100th order Super Gauss profile. These results will be compared to the measurement results of [4].

The resulting simulations and analytical solutions for both turbulent boundary layer cases will be analyzed in detail, in particular with respect to the details of the near wall velocity profiles. This numerical tool will also be used to predict the statistics of the turbulent velocity fluctuations.

References

[1] Buchhave, P. and Velte, C. M., (2022), A similarity scaling model for the axisymmetric turbulent jet based on first principles, Physics of Fluids, vol. 34, no. 9, http://dx.doi.org/10.1063/5.0102809
[2] Noether, E., (1918), Invariante Variationsprobleme, Nachrichten von der Gesellschaft der Wissenschaften zu Göttingen, Mathematisch-Physikalische Klasse 1918: 235-257.
[3] Samie, M., Marusic, I., Hutchins, N., Fu, M. K., Fan, Y., Hultmark, M. and Smits, A. J. (2018). Fully resolved measurements of turbulent boundary layer flows up to. Journal of Fluid Mechanics, 851, 391-415.
[4] Hultmark, M., Vallikivi, M., Bailey, S. C. C. and Smits, A. J. (2012). Turbulent pipe flow at extreme Reynolds numbers. Physical review letters, 108(9), 094501.

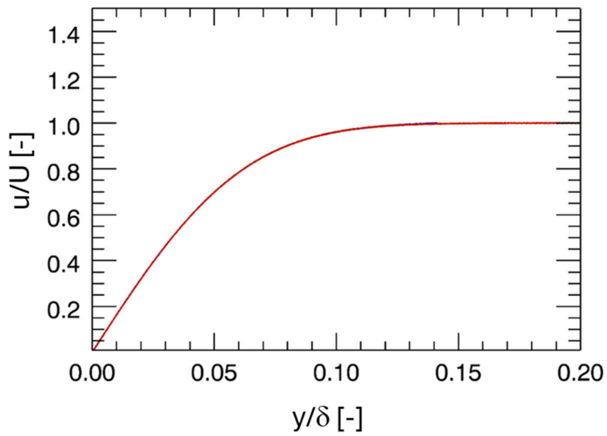

Figure 1: Simulated Blasius boundary layer solution for Re_τ=6.000. Three perfectly overlapping similarity scaled velocity profiles are displayed for three respective time steps: Green 75.000, Blue 150.000, Red 300.000. The discrete time step $\Delta t = 10^{-5}$ s. The boundary layer thickness is scaled by $\delta \sim (\nu t)^{1/2}$ or $(\nu x/U)^{1/2}$, as in the Blasius boundary layer solution or Stoke's first problem.

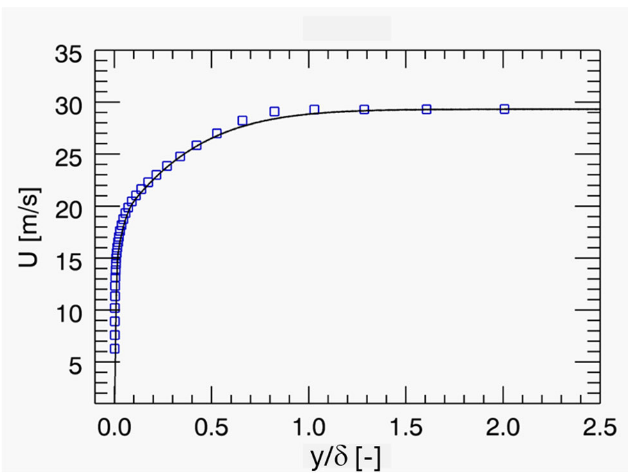

Figure 2: Turbulent ZPG boundary layer velocity profile for Re_τ = 6.000. Blue squares: Measured average velocity profile [3]. Black line: Numerical solution yielding the turbulent momentum diffusion (eddy viscosity) as a function of wall-normal distance.

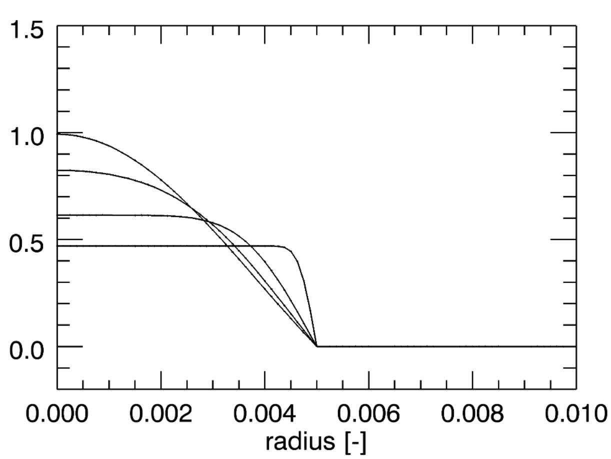

Figure 3: Turbulent pipe flow computed for a 10 mm diameter straight pipe with air. Initial profile: 100th order Super Gauss, Developing profiles after 10, 100, 300, 1000 time steps, Δt=10^{-5} s.

Reconstructed modal velocity fields in wall turbulence

Michele Guala[1,2], Roozbeh. Ehsani[1,2], Agnivo Ghosh[1,3], Michael Heisel[4] and Ian Jacobi[5]

[1] St. Anthony Falls Laboratory, University of Minnesota, Minneapolis, MN, USA
[2] Department of Civil, Environmental, and Geo- Engineering, University of Minnesota, Minneapolis, MN, USA
[3] Department of Mechanical Engineering, University of Minnesota, Minneapolis, MN, USA
[4] School of Civil Engineering, University of Sidney, Sydney, AUS
[5] Faculty of Aerospace Engineering, Technion Israel Institute of Technology, Haifa, IL
key-words: Wall turbulence, Experiments, Stochastic modeling

Abstract:
In the last few years we have developed a modeling framework to generate instantaneous streamwise velocity profiles able to reproduce adequately the statistical properties of experimental datasets acquired in rough wall, canonical, turbulent boundary layers (Ehsani et al., 2024a).
The experiments were performed in the SAFL wind tunnel (Heisel et al., 2020) and in the atmospheric surface layer within the EOLOS Wind research facility in Rosemount, MN, USA (Iungo et al. 2024).
Instantaneous profiles are constructed from a sequence of velocity steps that represent the dynamic contribution of Uniform Momentum Zones (UMZ) and internal shear layers to the structure and variability of wall turbulence (see Meinhart et al, 1995 De Silva, 2006, Heisel 2020).
The probabilistic distributions of UMZ attributes, including the modal velocity u_m, the elevation z_m and the thickness h_m , were extracted from spatially resolved measurements obtained by Particle Image Velocimetry (PIV). An inverse transform sampling technique is used to invert the height-dependent cumulative distribution functions and generate a rich ensemble of (differently correlated) UMZ attributes starting from the wall and extending throughout the logarithmic region, as illustrated in Fig 1. The validation of this low dimensional model was based on the velocity jump between UMZs, which was not imposed in the generation process and was observed to correctly scale with the shear velocity u_*.

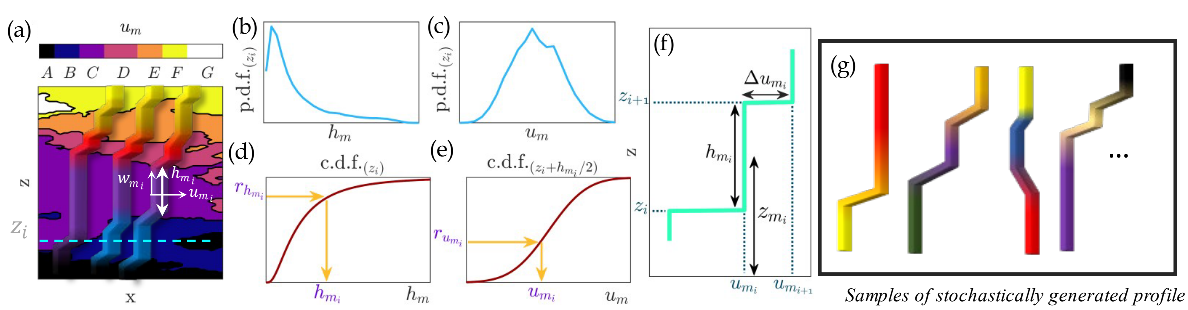

Figure 1*: a) PIV field and UMZ detection; z_i -dependent distribution of UMZ heigh h_m (b) and modal velocity u_m (c), leading to the associated cumulative density functions, (d), (e) , respectively, which can be inverted using random numbers [0-1] to generate each step height h_{mi} and UMZ velocity u_{mi}. Consecutive steps contribute to form the instantaneous velocity profile, which can be generated efficiently in large numbers (f)*

The extension from instantaneous velocity profiles to a two-dimensional modal velocity field is described in Ehsani et al. (2024b). Independent, stochastically generated, profiles were connected to

each other using different algorithms capturing: the similarity of the profiles, the alignment of the internal shear layers, or the coherence in the modal velocities. An example of reconstructed modal velocity field is plotted in fig 2 (comparing measured vs generated streamwise velocity contours).
In addition to UMZs and shear layers, the third reconstructed feature, currently under investigation, the properties of vortex cores, including their intensity, size, and location. Those were identified in the PIV dataset and statistically characterized by Heisel et al. (2021). They have been preliminarily inserted in the shear layers separating UMZs, including the one just above the surface. The metrics employed to validate our hierarchy of models include the mean and r.m.s. flow statistics as well as the streamwise velocity power spectrum. The modal velocity reconstruction has been tested on both smooth and rough walls, over a wide range of Reynolds numbers. The overall goal is to provide and validate a modeling framework for the generation of a synthetic near wall regions, extending into the logarithmic layer, reproducing the variability and stochasticity of wall turbulence, and able to interface with large scale domain flow simulations.

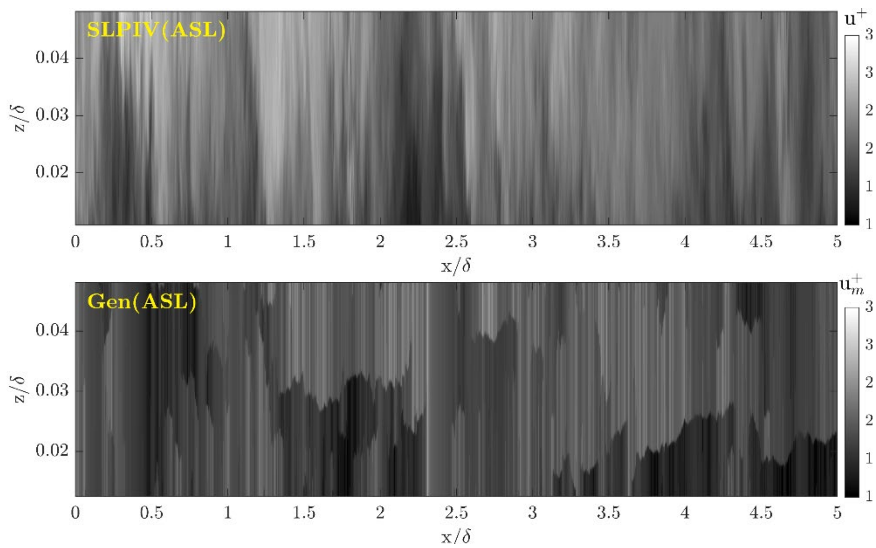

Figure 2: *(a) Time resolved PIV measurements in the Atmospheric Surface Layer (ASL) reprojected in space; (b) reconstructed modal velocity field starting from the same first initial step-like profile*

References

De Silva CM, Hutchins N, Marusic I (2016) Uniform momentum zones in turbulent boundary layers Journal of Fluid Mechanics 786, 309-331

Ehsani R, M Heisel, M Puccioni, J Hong, V Iungo, V Voller, M Guala (2024a) Stochastic modal velocity field in rough-wall turbulence. Journal of Fluid Mechanics 999, A56

Ehsani R, M Heisel, J Li, V Voller, J Hong, M Guala (2024b) Stochastic modelling of the instantaneous velocity profile in rough-wall turbulent boundary layers. Journal of Fluid Mechanics 979, A12

Heisel M, CM De Silva, N Hutchins, I Marusic, M Guala (2021) Prograde vortices, internal shear layers and the Taylor microscale in high-Reynolds-number turbulent boundary layers Journal of Fluid Mechanics 920, A52

Heisel M, CM De Silva, N Hutchins, I Marusic, M Guala (2020) On the mixing length eddies and logarithmic mean velocity profile in wall turbulence. Journal of Fluid Mechanics 887, R1

Iungo GV, M Guala, J Hong, N Bristow, M Puccioni, P Hartford, R Ehsani et al. (2024) Grand-Scale Atmospheric Imaging Apparatus (GAIA) and Wind Lidar Multiscale Measurements in the Atmospheric Surface Layer. Bulletin of the American Meteorological Society 105 (1), E121-E143

Meinhart, CD, Adrian, RJ (1995) On the existence of uniform momentum zones in a turbulent boundary layer. Phys. Fluids 7 (4), 694–696

On the manipulation of coherent structures in turbulent flows using Fourier-based wall modifications

Yaren Dincoglu [1], Suyash Verma [2] and Arman Hemmati [3]

[1] Mechanical Engineering, University of Alberta, Edmonton, Canada

key-words: Turbulent Flow Control, CFD

Abstract:

Turbulent pipe flow can be described by coherent structures that can extract, dissipate, or hold energy [1]. These structures respond to perturbations induced by changes in geometry or surface conditions, leading to lasting effects in turbulent flow behavior. For example, Antonia & Luxton (1971) demonstrated that the turbulence structure in the inner layer was strongly influenced by the roughness of the pipe, while Smits et al. (1979) identified that a non-monotonic response could be induced by a short region of concave curvature. More recent studies [4,5] have identified unique azimuthal structures in turbulent pipe flow that contain turbulence kinetic energy (TKE) and drive turbulence production. Van Buren & Hellstrom (2017) highlighted these interactions by modifying the cross-sectional shape of the pipe to selectively excite or suppress azimuthal energy modes. A distinct peak of energy was observed in the targeted mode, with a significant decrease in TKE in all non-targeted azimuthal modes, suggesting a potential method for manipulating coherent structures to effectively control turbulent pipe flow. An understanding of the effects of geometric variations in wall modifications is essential for advancing a potential turbulent flow control strategy.

This study expands on existing research by investigating the mechanisms responsible for the manipulation of near-wall turbulence and energy distribution using targeted Fourier-based wall modifications. The influence of the thickness and length of the wall modification on flow response and recovery is assessed. The varying geometries are shown in Figure 1. Wall modifications are implemented as pipe-inserts and are numerically assessed using Large Eddy Simulation (LES). Preliminary LES results for a pipe-insert of length 4D and thickness 0.1D (where D represents the pipe diameter) reveal coherent structures with high rotation near the wall that persist up to $x/D = 5$, presented in Figure 2. Initial steady-state modeling further demonstrates a non-monotonic TKE response across various geometries, where both increased length and thickness lead to higher stream-wise TKE peaks. Increasing the pipe-insert thickness intensifies the near-wall momentum exchange (primarily governed by the Reynolds shear stress), thereby inducing turbulent convection in the perturbed flow and inducing a sharper TKE peak that delays recovery. Furthermore, an increase in pipe-insert length maintains the induced Reynolds stress gradients caused by the insert's sinusoidal shape for a longer distance, allowing persistence of targeted coherent structures near the wall of the pipe. Future POD (Proper Orthogonal Decomposition) analysis will characterize the dynamics of induced coherent structures and provide new insights into turbulence control strategies.

References

[1] Jimenez J. (2018), Coherent structures in wall-bounded turbulence, *Journal of Fluid Mechanics, vol. 842, pp. P1*

[2] Antonia R., Luxton R., (1971), The response of a turbulent boundary layer to a step change in surface roughness Part 1. Smooth to rough, *Journal of Fluid Mechanics, vol. 48, pp 721-761*

[3] Smits A.J., Young T.B., Bradshaw P., (1979), The effect of short regions of high surface curvature on turbulent boundary layers, *Journal of Fluid Mechanics, vol. 94, pp 209-242*

[4] Hellstrom L.H.O., Smits A.J., (2014), The energetic motions in turbulent pipe flow, *Physics of Fluids, vol. 26*

[5] Baltzer, J.R., Adrian R.J., Wu X., (2013), Structural organization of large and very large scales in turbulent pipe flow simulation, *Journal of Fluid Mechanics, vol. 720, pp 236-279*

[6] Van Buren T., Hellstrom L.H.O., Marusic L., Smits A.J., (2017), Turbulent pipe flow response to wall changes targeting specific azimuthal modes, *Proceedings of TSFP10*, Chicago, USA.

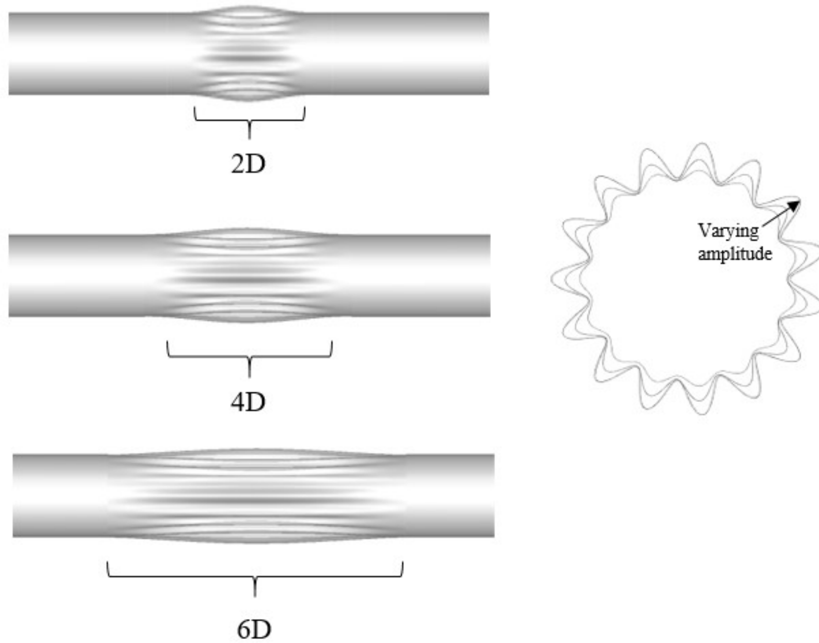

Figure 1: *Fourier pipe-insert geometry*

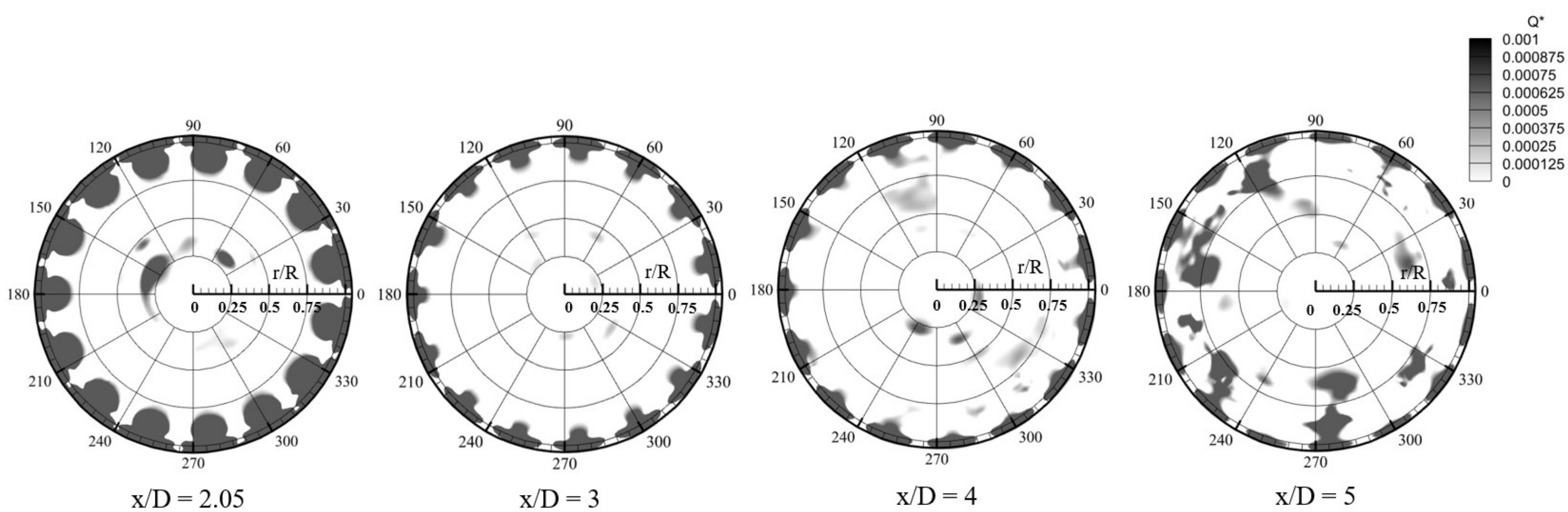

Figure 2: *2D Q-Criterion contour plots at several span-wise locations*

ORAL PRESENTATION

Urban Aerodynamics and Turbulent Dispersion.

Christina Vanderwel[1]

[1] Department of Aeronautical and Astronautical Engineering, University of Southampton, Southampton, UK

key-words: wind engineering, turbulent dispersion, building aerodynamics, turbulent boundary layers

Abstract:
The accurate understanding of urban aerodynamics at pedestrian-relevant scales and how air pollution dispersion is influenced by heterogeneous urban terrain is important for air quality forecasting and to inform urban planning and policy.

In the University of Southampton Recirculating Water Tunnel, we are able to perform high-fidelity experiments using scaled building and city models with a passive dye as a surrogate for air pollution. Simultaneous Particle Image Velocimetry (PIV) and Planar Laser-Induced Fluorescence (PLIF) capture full two-dimensional quantitative images of the velocity and concentration at the fine scales near the pollution sources and at the city scale. Case studies include smooth turbulent boundary layers [1], isolated buildings [2], and full neighbourhood-scale models [3] to directly measure the advective and turbulent transport mechanisms important to these flows.

The results highlight the role of tall buildings and local geometry on the turbulent diffusion processes and reveal the limitations of current turbulent dispersion models in the context of simplified, urban, and indoor applications.

Funding by the UKRI Future Leaders Fellowship (MR/S015566/1 and MR/Y020014/1) is gratefully acknowledged.

References

[1] Lim, HD & Vanderwel, Christina (2023) Turbulent dispersion of a passive scalar in a smooth-wall turbulent boundary layer. *Journal of Fluid Mechanics*. 969:A26.

[2] Biswas, Subhajit &Vanderwel, Christina (2024) Flow through a hollow cube in a turbulent boundary layer: towards understanding indoor pollutant dispersion. *Flow*. 4:E19.

[3] Rich, Tomos (2025) Experimentally modelling urban air pollution and measuring turbulent dispersion. *University of Southampton, Doctoral Thesis*

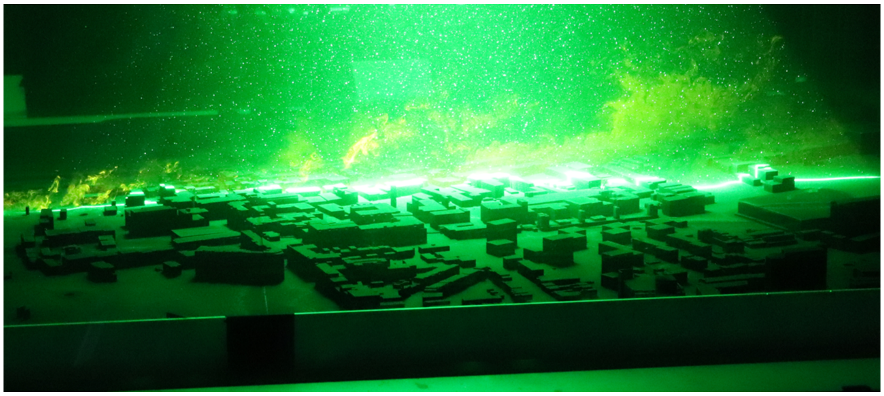

Figure 1: *Photo of the PIV/PLIF experiment to measure turbulent dispersion over a 1:1000 scale city model in the recirculating water flume using fluorescent dye.*

Turbulent Boundary Layers over Multiscale Urban Arrays

Cameron Southgate-Ash[1], Sue Grimmond[2], Alan Robins[1] and Marco Placidi[1]

[1] University of Surrey, School of Engineering, Environmental Flow Research Centre (EnFlo), Guildford, GU2 7XH, United Kingdom
[2] University of Reading, Department of Meteorology, Brian Hoskins Building, University of Reading, Whiteknights campus, RG6 7BE, United Kingdom

Key-words: Urban Arrays - Multiscale Roughness - Turbulent Boundary Layer - Wind Tunnel Experiments - Rough Walls - Fractal Buildings

Abstract

Wind tunnel experiments were conducted on multiscale building model arrays immersed in a deep turbulent boundary layer. Reference cuboid models of aspect ratios 1 and 3 were used (Standard and Tall respectively), each with two fractal iterations which systemically added smaller length scales, totalling in six building models and, in turn, six roughness arrays of varying length scales. Through these iterations, the frontal and plan solidities, λ_f and λ_p respectively, are kept the same (and so are the average height and width of the buildings) to isolate the effects of the additional length scales on the flow structure and the aerodynamic parameters. Three-dimensional Laser Doppler Anemometry measurements were taken to measure the mean velocity profiles along with a pressure tapped model in each array, see Figure 1, allowing for a direct calculation of the friction velocity, u_τ, and an estimation of the virtual origin, d, using Jackson's (1981)[1] interpretation. Vertical velocity profiles we were taken above the canopy at various downstream locations as well as up to 18 in-canopy profiles within a repeating unit for each building model to allow for the velocity profiles to be spatially averaged (Figure 2). Preliminary results suggest that d increases slightly with the addition of smaller length scales. The pressure also gives a good approximation for the virtual origin when compared to its evaluation from costumary log law fitting procedures. The roughness length, z_0, shows a significant increase with each iteration for the Tall models, which is in contradiction to many morphometric methods that would suggest it should remain unchanged given the fixed frontal and plan solidities. For the Standard models, z_0, increases from iteration 0 to 1 and then decreases for iteration 2. This is in line with the trend seen for the drag of these models in isolation (Southgate-Ash, 2024[2]). The friction velocity calculated from pressure is found to be within 10% of that estimated from the Reynolds shear stress (Reynolds & Castro 2008[3]). The talk will discuss the effect of additional length scales on flow similarity as well as the extent of the roughness and inertial sublayers.

References

[1] Jackson, P. S. 1981 On the displacement height in the logarithmic velocity profile. Journal of Fluid Mechanics 111, 15–25.
[2] Southgate-Ash, C. 2024 Wake Characteristics of Multiscale Buildings in a Turbulent Boundary Layer. In preprint
[3] Reynolds, R T & Castro, I P 2008 Measurements in an urban-type boundary layer. Experiments in Fluids 45, 141–156.

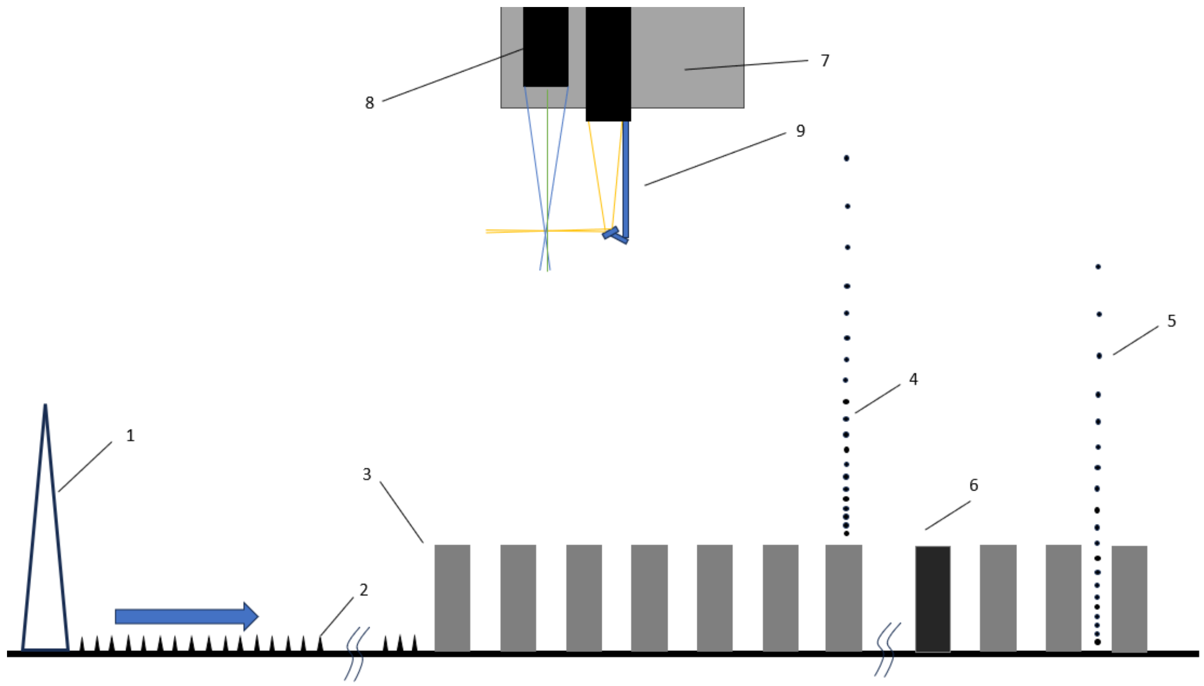

Figure 1: *Wind tunnel set up showing [1] Irwin spires, [2] floor roughness, [3] building models, [4] above canopy vertical profile measurement points, [5] in canopy vertical profile measurement points, [6] pressure tapped building model, [7] LDA shroud, [8] LDA probs and [9] LDA mirror.*

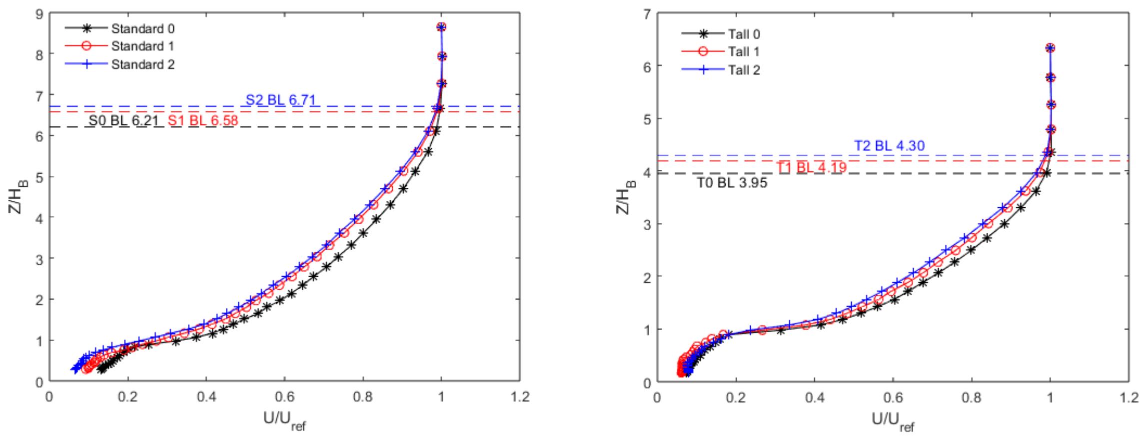

Figure 2: *Mean streamwise velocity profiles of Standard (left) and Tall (right) arrays. Dashed line represents the boundary layer height.*

Energetic aspects of the Reynolds analogy in rough-wall turbulent forced convection

F. Secchi[1], D. Gatti[1], U. Piomelli[2] and B. Frohnapfel[1]

[1] Institute of Fluid Mechanics, Karlsruhe Institute of Technology, Karlsruhe, Germany
[2] Department of Mechanical and Materials Engineering, Queen's University, Kingston, Canada

key-words: Turbulent convection, Turbulence simulation

Abstract:
The Reynolds analogy relates momentum and scalar transfer between a flow and a solid surface. In practical applications, the analogy breaks down due to pressure-driven momentum exchange, which does not equally affect scalar transfer. In turbulent flows over rough walls, the dissimilarity grows with the roughness Reynolds number, $k^+ = k/\delta_\nu$ (k represents the peak-to-trough height of the random roughness topography, and δ_ν is the viscous length scale). While the phenomenological reason behind this disparity is understood, no consensus exists on a scalar transfer law as a function of k^+ [1].

We present an alternative framework for assessing the Reynolds analogy and apply it to rough-wall channel flow, replicating two direct numerical simulation (DNS) cases presented in [2, 3, 4]. The DNSs are performed using the solver `Nek5000` and a body-fitted mesh to resolve the random roughness topography. Two roughness regimes are explored: $k^+ = 15$ and $k^+ = 90$. In both cases, a unit Prandtl number is considered. The approach seeks similarity between the kinetic energy $\mathcal{K} = u_i u_i/2$ and the half-squared magnitude of the scalar field, $\Gamma = \vartheta^2/2$ (u_i indicates the ith velocity component, ϑ is the scalar field, and summation is implied over repeated indices). For statistically stationary flow, the similarity reflects into structurally similar equations for the mean mechanical energy $\overline{\mathcal{B}} = \overline{\mathcal{K}} + (\overline{p}/\rho)$ and $\overline{\Gamma}$ (with p and ρ being, respectively, the pressure and fluid density; an overline denotes time averaging). Integration of these equations in the channel volume leads to an equivalence between the mean bulk velocity and scalar to the volume averages of the respective mean dissipation rates, $\nu\overline{\omega_i\omega_i}$ and $\alpha\overline{\vartheta_{,i}\,\vartheta_{,i}}$ (ω_i is the ith vorticity component, and partial differentiation is denoted with a comma subscript). This equivalence enables the assessment of mean-flow dissipation contributions, $\mathcal{E}^m$ and $\mathcal{E}^m_\theta$, and turbulent-flow dissipation contributions, $\mathcal{E}^t$ and $\mathcal{E}^t_\theta$, to the mean bulk velocity and scalar, as shown in figure 1. The assessment of the time-averaged dispersive dissipation fields, reported in figure 2, identifies *attached, exposed regions* (AER) and *well-mixed regions* (WMR) to contribute differently to the mean momentum and scalar transfer. Conditional averaging of the mean dissipation rates in these regions show that, at high k^+, AER dominate the mean momentum and scalar transfer, in particular enhancing the former in comparison to the latter. This result is reported in figure 3.

References

[1] Z. Hantsis and U. Piomelli. Numerical simulations of scalar transport on rough surfaces. *Fluids*, 9(7), 2024.

[2] M. Thakkar. *Investigation of turbulent flow over irregular rough surfaces using direct numerical simulations.* PhD thesis, University of Southampton, October 2017.

[3] J. W. R. Peeters and N. D. Sandham. Turbulent heat transfer in channels with irregular roughness. *Int. J. Heat Mass Transf.*, 138:454–467, 2019.

[4] F. Secchi, D. Gatti, U. Piomelli, and B. Frohnapfel. A framework for assessing the Reynolds analogy in turbulent forced convection. *J. Fluid Mech. (Accepted)*, 2025.

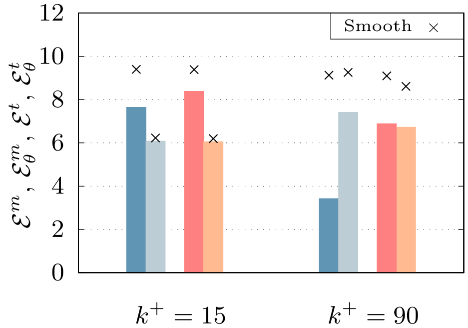

Figure 1: *Mean and turbulent flow contributions to the mean bulk velocity and scalar.* ▬, $\mathcal{E}^m$*;* ▬, $\mathcal{E}^t$*;* ▬, $\mathcal{E}_\theta^m$*;* ▬, $\mathcal{E}_\theta^t$*. The figure is adapted from [4].*

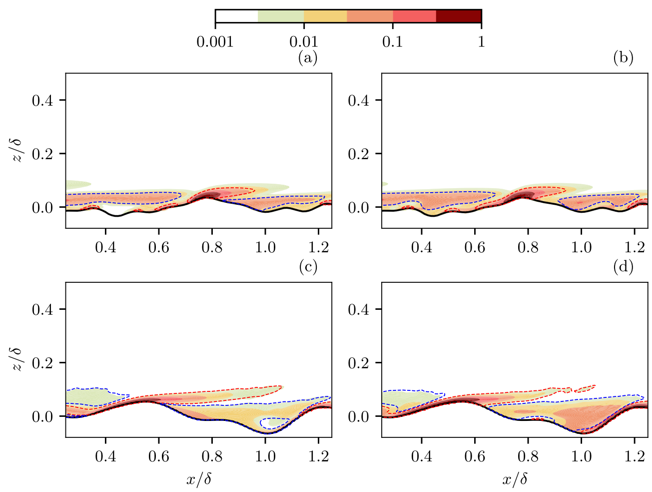

Figure 2: *Time-averaged dispersive dissipation rates.* $k^+ = 15$ *(a, b), and* $k^+ = 90$ *(c, d) cases(a, c)* $\overline{\omega_i''^+\omega_i''^+}$*; (b, d)* $\overline{\theta_{,i}''^+\theta_{,i}''^+}$*. Red-dashed lines denote AER; blue-dashed lines indicate WMR. A double prime is used to denote dispersive fluctuations with respect to the time and space average. A + superscript indicates viscous-scaled quantities. The figure is adapted from [4].*

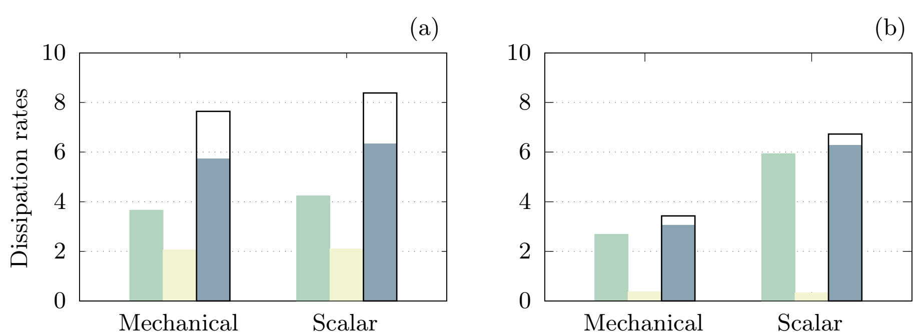

Figure 3: *AER and WMR contributions to the mean dissipation rates. (a),* $k^+ = 15$*; (b),* $k^+ = 90$*.* ▬*, AER;* ▬*, WMR;* ▬*, sum of AER and WMR contributions; a black solid outline indicates* $\mathcal{E}^m$ *and* $\mathcal{E}_\theta^m$*. The figure is adapted from [4].*

The influence of wall-normal oscillating roughness on a turbulent boundary-layer

A. Ramani [1], T.P. Illukkumbura[1], B. Ganapathisubramani[2], J.P. Monty[1], N. Hutchins[1],

[1] Department of Mechanical Engineering, University of Melbourne, Parkville, Victoria, Australia
[2] Department of Aeronautics and Astronautics, Univeristy of Southampton, UK

key-words: Turbulent Boundary Layers, Flow-control

Abstract:

One strategy for the manipulation of turbulent structures is wall-normal deformation (1). To explore this strategy, an experimental device for wall-normal forcing in the form of oscillating roughness elements is developed. The setup produces strips of hemispherical bumps by inflating a rubber membrane through a perforated metal plate using compressed air. Dynamic forcing is achieved via in-line solenoid valves - enabling oscillating and travelling wave roughness. Schematics of the construction of the device are shown in Fig. 1a,b. As a first step, experiments aimed at characterising device capabilities have been carried out in a boundary-layer wind-tunnel at zero pressure-gradient conditions. Flow statistics are acquired using hot-wire anemometry at five streamwise locations on the device as shown in Fig. 1c. The static smooth flow (i.e. when the device is off, left in Fig 1b) has $Re_\tau \approx 1000$ while the static rough flow (right in Fig 1b) has $Re_\tau \approx 1400$ with the Hama roughness-function, $\Delta U^+ \approx 4$. Subsequently, the roughness is oscillated between these two states (Fig. 1d) at a dimensionless time-scale, $T\delta/U_\infty \approx 100$ or $T^+ \approx 5100$ (corresponding to a physical frequency of 2Hz). Contours of the pre-multiplied energy spectra of the active case (dashed lines) are shown superimposed over those of the static smooth and rough cases (solid, filled) in Fig. 2(a,b) respectively. The additional energy from the perturbation appears in a spectral band outside the energetic scales of the flow (exact time-scale marked by the horizontal dotted-line). However, for the active case, the energy associated with the near-wall cycle (centred at $T^+ \approx 100$) seems to extend further away from the wall than the smooth case, though not as far as the static rough case. Fig. 3a-c shows the phase-averaged mean velocity profiles of the active case, taken at the most downstream location. At $\phi = \pi/2$ and $\phi = 3\pi/2$, the phase averaged profile is seen to match the mean profiles of the static smooth and rough cases respectively (Fig. 3a) and remains matching until the surface condition is changed - i.e. the flow achieves a quasi-equilibrium with the wall. However, shortly after the wall condition changes, the velocity profile begins to transition from these states of quasi-equilibrium. At $\phi = 0.1\pi$ (Fig. 3b), which is soon after the surface transitions to smooth, most of the mean-profile continues to remain at the rough limit, except near the wall where the profile has commenced transitioning towards the smooth state. The opposite is seen just after the surface transitions to rough ($\phi = 1.2\pi$, Fig. 3c). In both Fig. 3b and c, the height of the developing internal layer at that instant in phase (defined as the height at which the phase averaged profile deviates from the static curve corresponding to the previous wall state) is marked by the filled circle. This height is tracked through all phase positions and at all measurement locations and is shown in Fig. 3d. While the height to which the internal layer grows is limited by the streamwise fetch from the leading edge of the device, the rate (dz/dt) at which it grows is seen to be nearly matched at all locations - approximately $0.4U_\tau$ (of the static smooth state). This implies that for a periodic wall-normal forcing to affect the log-region ($z^+ > 100$), a periodicity of $T^+ > z^+/0.4 = 250$ is required. Hence, wall-normal forcing at slower time-scales will necessarily be drag increasing due to the quasi-equilibrium with the rough state. Consequently, measurements are planned in a turbulent water-tunnel, where oscillations at time-scales of $15 \lessapprox T^+ \lessapprox 150$ can be achieved. At these oscillation speeds, only the buffer layer (6 - 60 wall units) is expected to be affected by the dynamic wall state due to the growing internal layer. This will permit the non-equilibrium regime to be explored. The findings of this next campaign will also be presented at the meeting.

References

[1] Gibeau B. and Ghaemi S., (2023) Manipulation of a turbulent boundary layer using active surface deformations, *J. Fluid Mech., vol. 966, pp. A6*

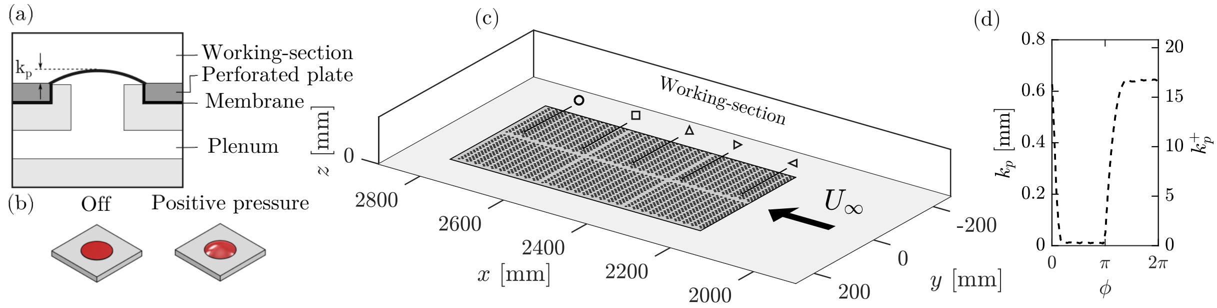

Figure 1: *(a) Construction of the active surface roughness device; (b) the two static states of a single roughness element; (c) layout of the device in the wind-tunnel working section with the flow direction indicated by the arrow. Measurement locations and their corresponding labels are indicated by the dots; (d) profile of the roughness element height, k_p, plotted against the phase of the oscillation. The viscous scaling on the right is based on the U_τ of the static smooth flow.*

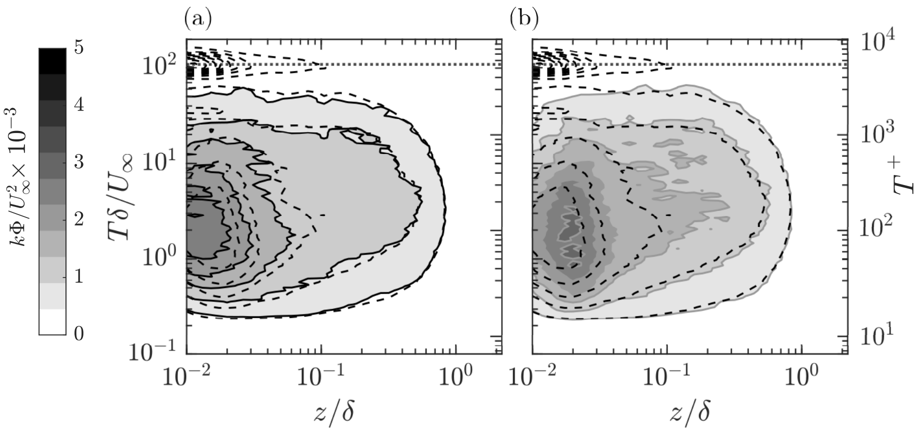

Figure 2: *Pre-multiplied energy spectrograms of the streamwise velocity fluctuations for the (a) static smooth (unperturbed, black lines) and (b) static rough cases (grey lines). In both panels, the dashed lines show the dynamic case; the horizontal dotted line marks the exact time-scale of the oscillations.*

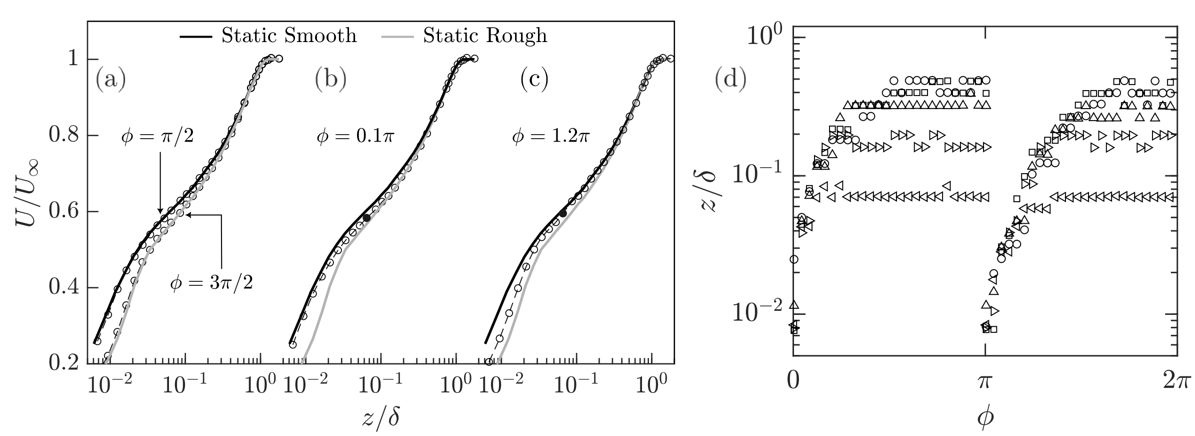

Figure 3: (a–c) Phase-averaged mean velocity profiles of the active case at select phases (dashed lines, open circles) shown over the static smooth (solid black) and rough limits (solid gray) from the most downstream measurement. The filled circles in (b,c) indicate the height to which the internal layer has developed at that phase.; (d) Internal layer height tracked in phase at all measurement locations (marked in Fig. 1c).

Influence of oncoming boundary layer on flow over a protruding forward-facing step

R. J. Martinuzzi, and E. Larose

Dept. Mech. & Manuf. Eng., Schulich School of Engineering, University of Calgary, Calgary, Canada

key-words: Forward-facing step, Boundary layer separation, Low-frequency dynamics, Scale interaction, Experimental, Direct Numerical Simulation.

Abstract:
The influence of the oncoming flow on the dynamics over a forward-facing step (FFS) of height H is investigated using particle image velocimetry (PIV) and direct numerical simulation (DNS) for thin laminar and turbulent boundary layers of thickness $\delta/H \approx 0.5$ for Reynolds number, based on the uniform freestream velocity and H, $1000 < Re_H < 11{,}000$. It is shown that very weak perturbations can trigger three-dimensional (3D) instabilities, which can excite low-frequency coherent motions linked to the generation of large-scales impacting the mean and turbulent structure over the step.

The flow over the FFS is a diagnostic configuration to study fundamental instability and separation mechanisms. The FFS is a simple 2D geometry with complex dynamics and intrinsic 3D instabilities arising from step-induced upstream adverse pressure gradients (APG) and downstream favorable pressure gradients (FPG). The FFS is thus a heuristic flow for testing turbulence models [1,2]. The FFS is relevant to applications such as damage mitigation for low-rise buildings or noise generation [1-3].

FFS flows are characterized by two separation regions: one at the foot of the step due to the APG-induced BL separation and another immediately downstream of the sharp, salient edge. FFS flows are classified using the oncoming BL state, δ/H and Re_H. Most earlier studies have focused on FFS immersed in the inner layer of TBL $\delta/H \geq\sim 4$. For these immersed steps, the spectral characteristics and scales of the inner layer are impressed on both separation regions [2,3].

For $0.3 < \delta/H < 2$, the time and spatial scales of the oncoming flow and those intrinsic to the step are similar and can interact. Figure 1 illustrates the influence of the BL state and Re_H for $\delta/H \sim 0.5$. In the figure, mean streamlines superpose contours of the Reynolds shear stress $-\overline{uv}$. For $Re_H = 1700$, the large upstream recirculation is 2D. The shear layer laminar-turbulent transition occurs far downstream. At $Re_H = 4800$, an incipient boundary layer separation occurs upstream of the step. This region is a source of low-frequency excitation (Fig. 2) triggering a 3D instability of the upstream recirculation. This instability results in large scale structures (Fig. 3) transported over the salient edge amplifying $-\overline{uv}$, causing a shorter attachment length. For the TBL at $Re_H = 8100$, the boundary layer scales are smaller (Fig. 3) with spectral energy at higher frequencies (Fig. 2). The perturbations still trigger the 3D intrinsic instability, but the amplification of motion is less than at 4800 (Fig. 1, 2) resulting in a weaker salient edge perturbation, lower turbulence levels and longer reattachment length. It will be shown that dynamics and dominant scales can be captured using a low-dimensional model.

References:
[1] Awasthi, M., Devenport, W.J., Clegg, S.A.L., Forest, B.., (2014) *Pressure fluctuations produced by forward steps immersed in a turbulent boundary layer*. J. Fluid Mech. 756, 384–421.
[2] Fang, X., Tachie, M.F., 20(2020) *Spatio-temporal dynamics of flow separation induced by a forward-facing step submerged in a thick turbulent boundary layer.* J. Fluid Mech. 892, A40.
[3] Pearson, D.S., Goulart, P.J., Ganapathisubramani, B., (2013) *Turbulent separation upstream of a forward-facing step*. J. Fluid Mech. 724, 284–3042.

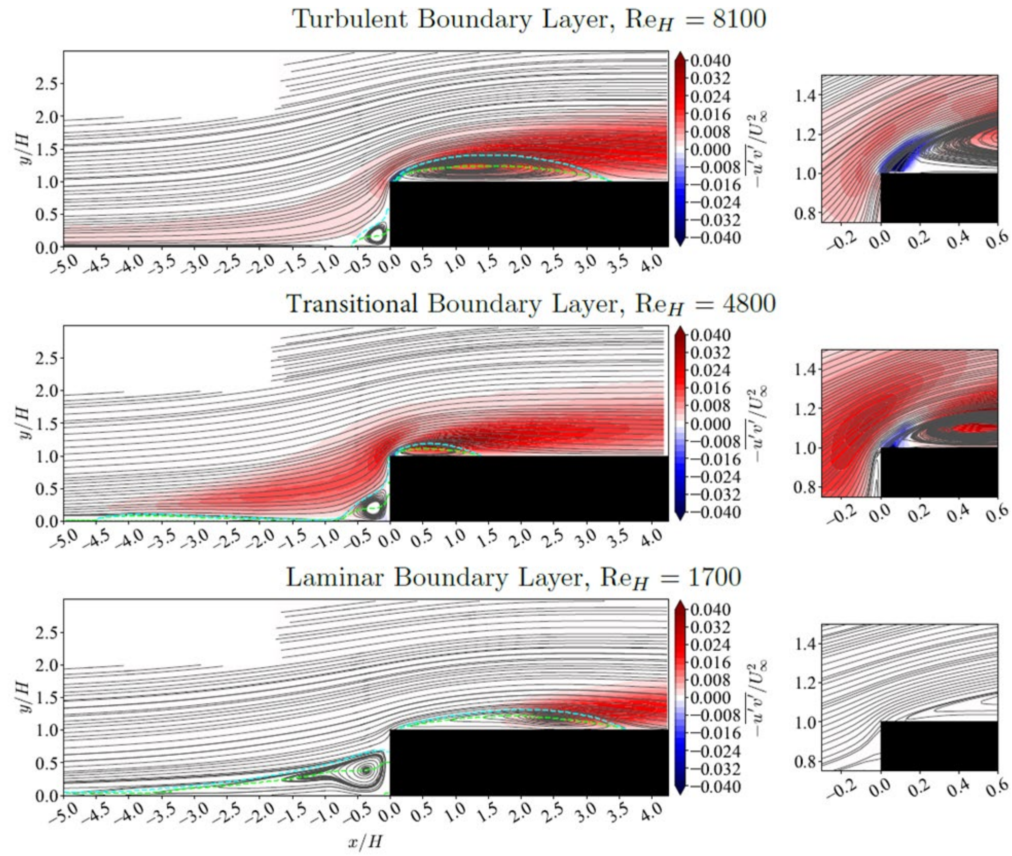

Figure 1: *Mean streamlines overlaid with contours of the Reynolds shear stress* $-\overline{uv}$ *for* $\delta/H \sim 0.5$ *and* Re_H *= 1700, 4800 and 8100. Right column is an expanded view about the salient edge. The green coloured lines indicate that dividing streamline (i.e. recirculation region).*

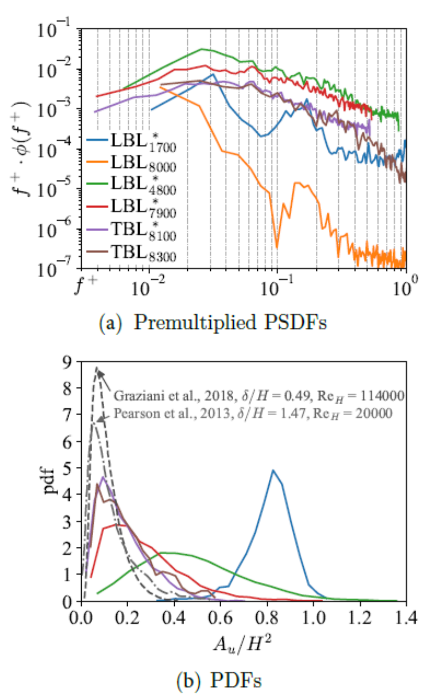

Figure 2: *Dynamics of upstream recirculation region:*

(a) Premultiplied power spectral density function

(b) Probability density function.

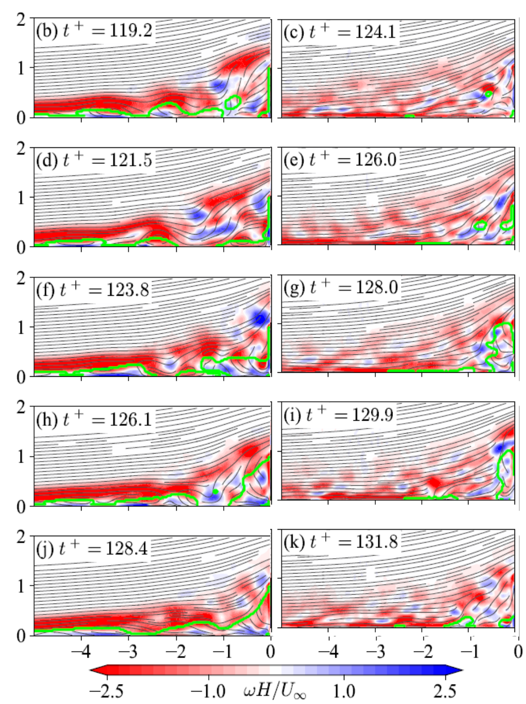

Figure 3: *Instantaneous vorticity field for* $Re_H = 4800$ *(left) and* $Re_H = 8100$ *(right)*

Wavenumber-to-wavenumber energy exchange by triadic Fourier-mode interactions in wall turbulence

T. Kawata[1] and T. Tsukahara[2]

[1] Department of Mechanical Engineering, Shibaura Institute of Technology, Tokyo, Japan
[2] Department of Mechanical and Aerospace Engineering, Tokyo University of Science, Chiba, Japan

key-words: direct numerical simulation, plane Couette turbulence

Abstract:
Wall turbulence exhibits a complex energy transfer process, including both forward and inverse energy cascades, due to the characteristic dynamics of coherent structures. Since the interscale energy transfer terms in the energy transport equations are expressed as triple correlation quantities, detailed analysis by decomposing them into triadic Fourier-mode interactions may provide significant insights to better understand the mechanism of the interscale energy transfers. In wall turbulence, however, nonlinear interactions between different scales result in both interscale and spatial energy transports, and it is not straightforward to separate these two types of transport effects. In the present study, we derive a direct expression for the interscale energy transfers by Fourier-mode triadic interactions and investigate the energy exchange between different wavenumbers by analysing DNS dataset of wall turbulence.

Our analysis is based on the DNS dataset of a turbulent plane Couette flow at the friction Reynolds number $Re_\tau = 126$ obtained in our previous study[1], the configuration of which is given in Fig. 1(a). Figure 1(b) presents the obtained distribution of the interscale energy flux $Tr_{uu}(k_x)$, the flux of streamwise turbulent energy through streamwise wavenumber k_x from lower to higher wavenumber side. As shown in Fig. 1(b), Tr_{uu} is basically positive for the entire y-k_x range investigated, indicating that the energy is transferred from smaller to larger wavenumbers (i.e., from larger to smaller scales). The most significant energy flux is found in the near-wall region at the wavenumber around $k_x h/2\pi = 0.62$, which approximately corresponds to the streamwise wavelength $\lambda_x^+ \approx 400$ (here, $^+$ indicates the scaling by the viscous units). Now, the interscale energy flux of the Reynolds stress is expressed by the Fourier modes as

$$Tr_{ij}(k_x) = -\left(\frac{2\pi}{L_x}\right)^2 \sum_{\substack{\alpha,\ \beta>k_x \\ |\beta-\alpha|\le k_x}}^{\alpha} \sum^{\beta} \mathcal{B}_{ij}^{(-)}(\alpha,\beta) + \left(\frac{2\pi}{L_x}\right)^2 \sum_{\substack{\alpha,\ \beta\le k_x \\ \alpha+\beta>k_x}}^{\alpha} \sum^{\beta} \mathcal{B}_{ij}^{(+)}(\alpha,\beta),$$

$$\text{where} \quad \mathcal{B}_{ij}^{(+)}(\alpha,\beta) = \frac{4\pi}{L_x}\Re\left(\overline{\widetilde{u_i}(\alpha)\widetilde{u_k}(\beta)\widetilde{\partial_k u_j}^*(\alpha+\beta)} + \overline{\widetilde{u_j}(\alpha)\widetilde{u_k}(\beta)\widetilde{\partial_k u_i}^*(\alpha+\beta)}\right),$$

$$\mathcal{B}_{ij}^{(-)}(\alpha,\beta) = \frac{4\pi}{L_x}\Re\left(\overline{\widetilde{u_i}(\alpha)\widetilde{u_k}^*(\beta)\widetilde{\partial_k u_j}(\beta-\alpha)} + \overline{\widetilde{u_j}(\alpha)\widetilde{u_k}^*(\beta)\widetilde{\partial_k u_i}(\beta-\alpha)}\right).$$

Here, $\widetilde{u_i}$ and $\widetilde{\partial_j u_i}$ are the Fourier mode coefficient of fluctuating velocity u_i and velocity gradient $\partial u_i/\partial x_j$, respectively, the overline represents the operation of averaging in time and in the spanwise (z-) direction, the asterisk and $\Re$ denote the conjugate and the real part of complex quantities. The above expression shows that Tr_{ij} is obtained by integrating $-\mathcal{B}_{ij}^{(-)}$ and $\mathcal{B}_{ij}^{(+)}$ over Region I and Region II given in Fig. 2(a), respectively. Figure 2(b) presents the distribution of $-\mathcal{B}_{uu}^{(-)}$ and $\mathcal{B}_{uu}^{(+)}$ corresponding to the maximum of Tr_{uu}, revealing significant contributions from $-\mathcal{B}_{uu}^{(-)}(\alpha,\beta)$ in Region I with $\alpha \approx \beta$. These contributions represent direct energy exchanges between extremely long wavelengths (corresponding to $k_x \approx 0$) and relatively short wavelengths in the range $\lambda_x^+ < 400$.

In the presentation at the iTi conference, we will investigate not only forward cascade of streamwise turbulent energy but also the inverse cascade of spanwise turbulent energy in detail by decomposing them into the wavenumber-to-wavenumber energy exchanges by triadic Fourier-mode interactions.

References

[1] Kawata T. and Tsukahara T., (2021), Scale interactions in turbulent plane Couette flows in minimal domains, *J. Fluid Mech., vol. 911, A55*

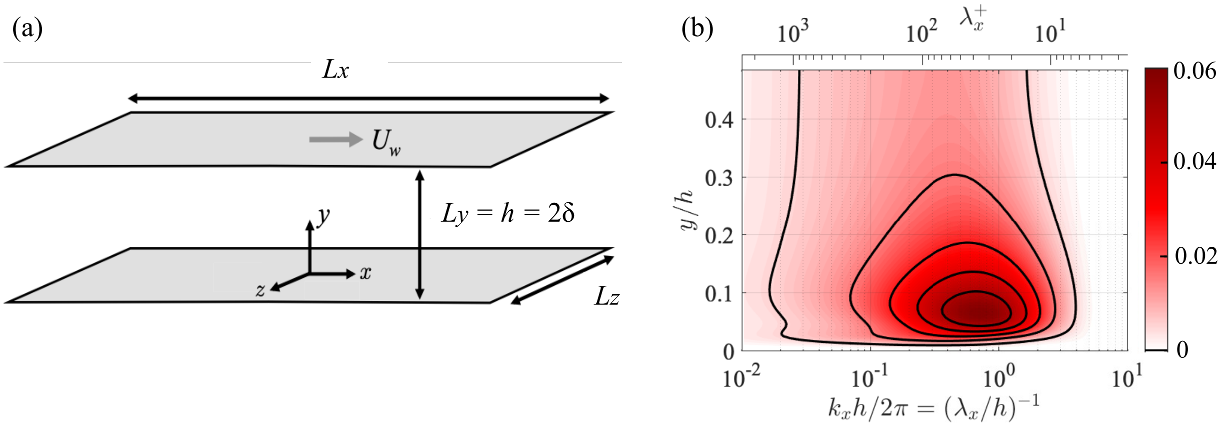

Figure 1: DNS dataset of a turbulent plane Couette flow obtained in our previous study[1]: (a) configuration of DNS, where the domain sizes in each direction is $(L_x, L_y, L_z) = (96.0h, h, 12.8h)$, the number of computational grid is $(N_x, N_y, Nz) = (2048, 96, 512)$, and the obtained friction Reynolds number is $Re_\tau = u_\tau\delta/\nu = 126$ (u_τ is the friction velocity and nu is the fluid kinematic viscosity); (b) wavenumber-space (k_x-y) diagram for distribution of interscale flux of streamwise turbulent energy Tr_{uu} scaled by u_τ^4/ν.

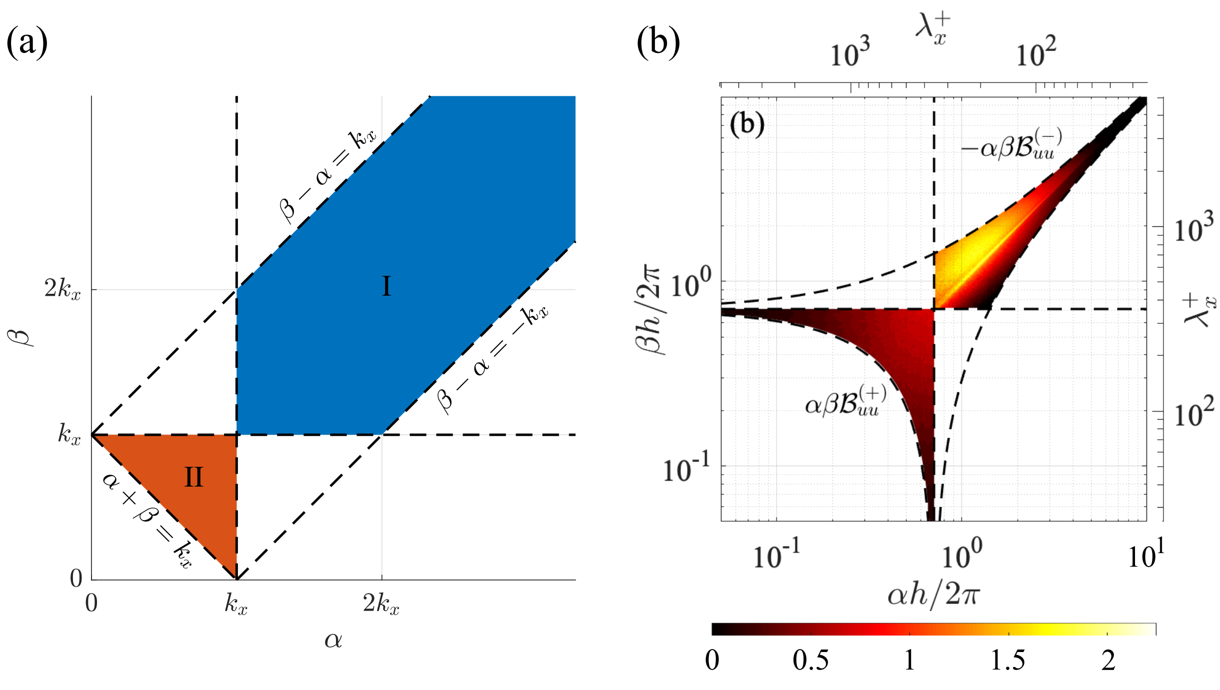

Figure 2: Triadic interactions constituting interscale energy flux Tr_{ij}: (a) schematics of Rigion I and Region II for interscale energy flux Tr_{ij} at wavenumber k_x; (b) distributions of premultiplied bispectra $-\alpha\mathcal{B}_{uu}^{(-)}$ and $\alpha\mathcal{B}_{uu}^{(+)}$ normalised by u_τ^4/ν in Region I and Region II, respectively, which correspond to interscale energy flux Tr_{uu} at wavenumber $k_x h/2\pi = 0.62$ (corresponding to $\lambda_x^+ \approx 400$) and wall-normal position $y^+ = 16$. In the panel (b), the black dashed lines indicate the same as in the panel (a), the boundaries of Region I and II.

On velocity spectra in turbulent wall-bounded flows

Sergio Pirozzoli [1]

[1] Dipartimento di Ingegneria Meccanica e Aerospaziale, Sapienza Università di Roma, Via Eudossiana 18, 00184 Roma, Italy

Key-words: Wall turbulence, velocuty spectra

Abstract:
We derive scaling laws for the spectral density and variance of the streamwise velocity in turbulent wall-bounded flows by analyzing DNS data from pipe flow up to $Re_\tau \approx 12,000$. Examination of the spanwise spectra in the near-wall viscous region reveals the presence of an overlap layer characterized by an anomalous spectral scaling of the form $E_u^+ \sim (k^+)^{-1+\alpha}$, with $\alpha \approx 0.18$, deviating from the classical scaling with $\alpha = 0$ proposed by Perry *et al.* (1986). The wall-normal dependence is fully consistent with the Townsend-Bradshaw model (Bradshaw, 1967; Townsend, 1976), in which wall-attached eddies influence the near-wall region through turbulent Stokes layers. These findings generalize the results of Pirozzoli (2024), enabling a complete characterization of spectral density distributions in the near-wall region and providing a basis for extrapolating the behavior of streamwise velocity variance in the infinite Reynolds number limit. One important consequence is that the near-wall peak of the streamwise velocity variance should be bounded at infinite Reynolds number. By isolating the contribution of the wall-attached eddies to velocity variance, we conclude that this component should increase with Reynolds number and wall distance, reaching a maximum near the root of the logarithmic layer. Extrapolating the observed trends strongly suggests the emergence of a distinct outer-layer peak in this region at high enough Reynolds number. Finally, analysis of the contribution from δ-sized eddies indicates that they dominate the outer wall layer, where velocity variance is found to decrease linearly with the outer-scaled wall distance to leading order, with higher-order corrections inversely proportional to wall distance.

References

Bradshaw, P. 1967 'Inactive' motion and pressure fluctuations in turbulent boundary layers. *J. Fluid Mech.* **30**, 241–258.

Perry, A.E., Henbest, S. & Chong, M.S. 1986 A theoretical and experimental study of wall turbulence. *J. Fluid Mech.* **165**, 163–199.

Pirozzoli, S. 2024 On the streamwise velocity variance in the near-wall region of turbulent flows. *J. Fluid Mech.* **989**, A5.

Townsend, A.A. 1976 *The Structure of Turbulent Shear Flow*. 2nd edn. Cambridge University Press.

The Reynolds shear stress phase distribution and its relationship to spectral energy density in wall bounded flows

Spencer J. Zimmerman [1], J. Philip [2] and J. Klewicki [2]

[1] Department of Mechanical Engineering, Stony Brook University, Stony Brook, NY 11794, USA
[2] Department of Mechanical Engineering, University of Melbourne, Melbourne, VIC 3010, Australia

key-words: Boundary layers, Pipe flow

Abstract:
Contributions to the Reynolds shear stress (RSS) in turbulent boundary layers and pipe flows are examined via Fourier and wavelet decompositions. This analysis is performed on the experimental datasets of [1] collected at friction Reynolds numbers up to 10^4 in the Centre for International Cooperation in Long Pipe Experiments (CICLoPE) at the University of Bologna, the Melbourne Wind Tunnel (MWT) at the University of Melbourne, and the Flow Physics Facility (FPF) at the University of New Hampshire.

Regions of high cospectral energy density are identified and demarcated relative to noteworthy features of the streamwise and wall-normal velocity component autospectra. This relationship is then examined more closely via the RSS coherence spectrum (figure 1) and, most notably, the distribution of relative phase between the two velocity components (figure 2). The tendency of modes of matched aspect ratio (i.e. wall distance x_2 versus streamwise wavelength λ_1) to have matched relative phase in both a mean and instantaneous sense is explored. This relationship is illustrated in figure 2 below, which (in essence) shows the mean phase lag between the streamwise velocity and the (negative) wall-normal velocity as a function of wall-distance and streamwise wavelength. It is shown that the isocontours of relative phase in figure 2 are parallel to lines of constant aspect ratio over certain subdomains of each flow. This implies a self-similar organization of the streamwise and wall-normal velocity modes in a mean sense that will be discussed in the context of the attached eddy hypothesis [2] and the findings of e.g. [3] and [4]. This mean phase lag relationship is further probed via wavelet decomposition to examine the probability that any given phase lag will occur for each wavelength/wall-distance pair.

References

[1] Zimmerman S., Philip, J., Monty J., Talamelli, A., *et al.*, (2019), A comparative study of the velocity and vorticity structure in pipes and boundary layers at friction Reynolds numbers up to 10^4, *Journal of Fluid Mechanics, vol. 869, pp. 182-213.*

[2] Townsend, A. A., (1976): *The structure of turbulent shear flow*, Cambridge University Press.

[3] Baars, W. J., Hutchins, N. and Marusic, I. (2017), Self-similarity of wall-attached turbulence in boundary layers, *Journal of Fluid Mechanics, vol. 823, p. R2.*

[4] Baidya, R., Baars, W. J., Zimmerman, S., Samie, M., *et al.*, (2019), Simultaneous skin friction and velocity measurements in high Reynolds number pipe and boundary layer flows, *Journal of Fluid Mechanics, vol. 871, pp. 377-400.*

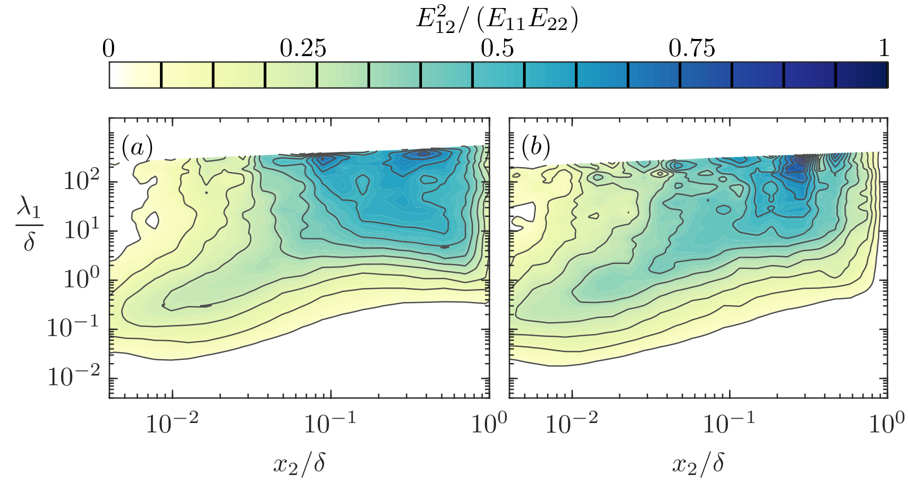

Figure 1: Magnitude-squared coherence spectrum between the streamwise u_1 and wall-normal u_2 velocity components for (a) a turbulent boundary layer at $Re_\tau = 6300$ and (b) a turbulent pipe flow at $Re_\tau = 7700$.

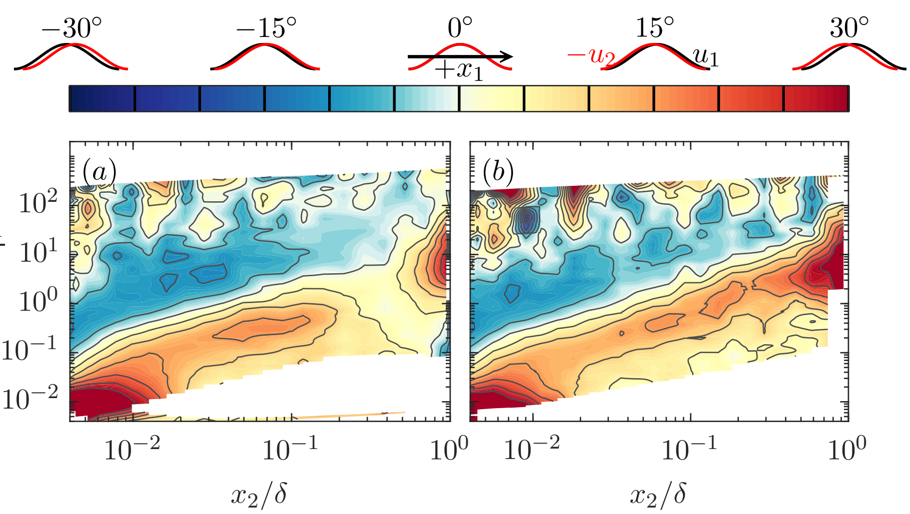

Figure 2: Angle between real and imaginary components of the RSS cospectrum, or 'relative phase spectrum' between the streamwise u_1 and negative wall-normal $-u_2$ velocity components for (a) a turbulent boundary layer at $Re_\tau = 6300$ and (b) a turbulent pipe flow at $Re_\tau = 7700$. Regions with low coherence (cf. figure 1) obscured for clarity.

Homogeneous shear turbulence: kinetic energy growth rate as a nonlinear eigenvalue problem

J. Albert [1], T. Gebler [1] and M. Oberlack [1,2]

[1] Chair of Fluid Dynamics, Technische Universität Darmstadt, Germany
[2] Graduate School of Computational Engineering, Technische Universität Darmstadt, Germany

key-words: turbulent scaling laws, nonlinear eigenvalue problems, homogeneous shear turbulence, symmetry methods

The temporal growth of fluctuations in homogeneous shear turbulence and its generalization is investigated. We therefore introduce a novel symmetry-based approach and derive a nonlinear eigenvalue problem (NEVP) that describes the growth of perturbations, where the growth rate is the sought eigenvalue.

Tavoularis (1985) [1] may have been the first to recognize that turbulent kinetic energy in linear shear flows in the final phase exhibits exponential growth, i.e. $\mathcal{K}(t) \propto \exp(2\lambda t)$. The ratio of λ and the constant shear rate A is known to be a constant for flows at high Reynolds numbers. $\lambda/A \sim 0.2$ seems to be an upper bound in both experimental and numerical investigations [2].

We employ the incompressible Euler equations to model the phenomena as we intend to investigate scales way above the Taylor length scale. Furthermore, we apply the Reynolds decomposition $\boldsymbol{u} = \bar{\boldsymbol{u}} + \boldsymbol{u}'$ and assume the mean velocity to be $\bar{\boldsymbol{u}} = \boldsymbol{A} \cdot \boldsymbol{x}$, where, $\boldsymbol{A}$ is the constant velocity gradient tensor. Besides the above-mentioned classical homogeneous shear flow, i.e. $A = A_{12}$, the latter generalization also includes, rotation, strain, and combinations thereoff.

In order to formulate the NEVP for λ we consider two classical symmetry groups of the Euler equations, i.e. the scaling in space: $x_i^* = e^{a_{Sx}} x_i$, and the translation in time: $t^* = t + a_t$. Employing group-theoretical methods, we obtain a reduced set of symmetry-invariant variables denoted by a tilde:

$$x_i = \tilde{x}_i e^{\lambda t} \quad , \quad u_i' = \tilde{u}_i'(\tilde{\boldsymbol{x}}) e^{\lambda t} \quad , \quad p' = \tilde{p}'(\tilde{\boldsymbol{x}}) e^{2\lambda t}, \tag{1}$$

where the eigenvalue turns out to be a function of the group parameters, i.e. $\lambda := \frac{a_{Sx}}{a_t}$.

The above result of Tavoularis is obviously consistent with (1), i.e., more generally for the Reynolds stress we find $\overline{u_i' u_j'} \propto \exp(2\lambda t)$. Employing (1) into the Euler equations for a rotating frame (with the rotation vector Ω_i and centrifugal forces absorbed in the pressure term) leads to the aforementioned NEVP

$$-\lambda \tilde{x}_k \frac{\partial \tilde{u}_i'}{\partial \tilde{x}_k} + \lambda \tilde{u}_i' + \tilde{u}_j' \frac{\partial \tilde{u}_i'}{\partial \tilde{x}_j} + A_{jk} \tilde{x}_k \frac{\partial \tilde{u}_i'}{\partial \tilde{x}_j} + \tilde{u}_j' A_{ij} + \frac{\partial \tilde{p}'}{\partial \tilde{x}_i} + 2\epsilon_{ijk} \Omega_j \tilde{u}_k' = 0, \tag{2}$$

where the following homogeneous boundary conditions (BC) apply $\tilde{\boldsymbol{u}}' = 0$, $\tilde{p}' = 0$ for $|\boldsymbol{x}| \to \infty$. Integrating the energy integral of the fluctuations from (2) using u_i', and using the latter BC, then all boundary integrals drop out and an expression for the eigenvalue λ is determined

$$\lambda = -\frac{2}{5} \frac{\int_\Omega \tilde{u}_i' A_{ij} \tilde{u}_j' d\tilde{x}^3}{\int_\Omega \tilde{u}_i' \tilde{u}_i' d\tilde{x}^3}. \tag{3}$$

We show that the eigenvalue is bounded from above and below using the spectral norm of the mean flow velocity gradient tensor: $|\lambda| \leq \frac{2}{5} \|\boldsymbol{A}\|_2$. Similarly, we show that for linear shear we have $|\lambda| \leq \frac{1}{5}|A|$, i.e. we have an upper limit for the growth of turbulent kinetic energy of $\mathcal{K}(t) \propto \exp(2\lambda t) \leq \exp(2/5At)$.

The formula (3) does not replace the eigenvalue problem (2), since, for example, system rotation has a fundamental influence on the eigenvalue λ via Coriolis forces. However, in (3) all Coriolis forces cancel out. For this reason, the complete NEVP (2) will be solved. Keeping the nonlinear term, this will be done numerically, while for a linearized version we intend to derive analytical solutions.

References

[1] Tavoularis S., (1985), Asymptotic laws for transversely homogeneous turbulent shear flows, *Physics of Fluids, vol. 28, no. 3, pp. 999-1001.*

[2] Briard A., Gomez T., Mons V. and Sagaut P., (2016), Decay and growth laws in homogeneous shear turbulence, *Journal of Turbulence, vol. 17, pp. 699-726.*

Two-point enstrophy budget and energy cascade in turbulence

A. Cimarelli [1], C.B. da Silva [2] and G. Boga [1]

[1] DIEF, University of Modena and Reggio Emilia, 41125 Modena, Italy
[2] IDMEC/IST, Technical University of Lisbon, 1049-001 Lisboa, Portugal

key-words: Cascade in turbulence, enstrophy

Abstract:
According to Kolmogorov's four-fifths law, the prominent feature of high Reynolds number flows is the energy transfer from large to small scales which is described by a single scalar quantity, the average dissipation rate. Kolmogorov's groundbreaking intuition was reducing the complex problem of turbulence to its essential features, by assuming homogeneity and isotropy. However, actual turbulent flows have a much richer physics, involving, beyond energy transfer and dissipation, anisotropic turbulent production and inhomogeneous spatial fluxes. The multi-scale feature of these energy injection/release phenomena gives rise to a split cascade where energy flows simultaneously both to small and large scales. The split in forward and reverse cascade is particularly relevant in wall turbulence where it challenges turbulence closures and theories. To shed light on these energy cascade processes it is relevant to adopt a statistical tool able to distinguish physical processes occurring among different scales. In this respect, the generalized Kolmogorov equation [1] has already shown to provide relevant information about cascade, see [2] and references therein. It consists in the evolution equation of the second-order moment of the two-point velocity increments. However, such equation alone is not able to provide also information about the phenomena dominating cascade in turbulence. In the present work, we provide insights about such physical phenomena by combining the results of the Kolmogorov equation with those from the evolution equation for the second-order moment of the two-point vorticity increment. DNS data of both homogeneous isotropic turbulence and turbulent boundary layer are analysed and the main results will be reported at the conference talk. An example of the two-point velocity and enstrophy budgets are reported in figure 1 for the case of homogeneous isotropic turbulence.

References

[1] Hill R.J., (2002), Exact second-order structure-function relationships, *Journal of Fluid Mechanics, vol. 468, pp. 317-326*

[2] Cimarelli A., Boga G., Pavan A., Costa P. and Stalio E., (2024), Spatially evolving cascades in wall turbulence with and without interface, *Journal of Fluid Mechanics, vol. 987, A4*

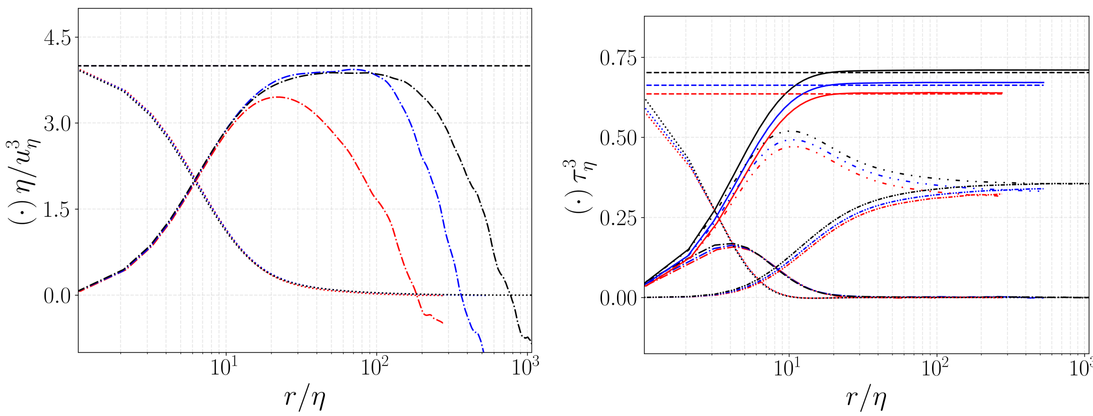

Figure 1: *Budgets of second-order structure function of velocity* $\langle \delta q^2 \rangle$ *(left) and enstrophy* $\langle \delta \xi^2 \rangle$ *(right) in homogeneous isotropic turbulence at* $Re_\lambda \approx 140$ *(red lines),* $Re_\lambda \approx 240$ *(blue lines) and* $Re_\lambda \approx 400$ *(black lines). Left plot: dissipation (dashed lines), diffusive transport (dotted lines) and inertial transport (dash-dotted lines). Right plot: enstrophy destruction (dashed lines), diffusive transport (dotted lines), inertial transport (dash-dotted lines) and vortex stretching (solid lines). All the curves are made dimensionless by using Kolmogorov scales.*

Turbulent drag reduction by streamwise traveling waves of wall deformation

Koji Fukagata[1]

[1] Department of Mechanical Engineering, Keio University, Yokohama, Japan

key-words: Flow Control, Drag Reduction

Abstract:
Friction drag in turbulent flow over a solid wall is much larger than that of the laminar flow at the same Reynolds number. Since the larger friction drag means that more energy is wasted as heat through dissipation, its reduction is of crucial importance for improving the energy efficiency of industrial products and mitigating environmental burden. Therefore, flow control methods for friction drag reduction have been extensively investigated for a long time. In this talk, we review some promising studies on turbulent drag reduction including our early attempts on feedback control for turbulent friction drag reduction [1] and our recent attempts on predetermined control using streamwise traveling waves (Fig. 1) [2] and uniform blowing [3]. If time allows, we will also briefly introduce our ongoing attempts for flow control design based on machine learning [4].

References

[1] Kasagi N., Suzuki Y., Fukagata K. (2009), Microelectromechanical system-based feedback control of turbulence for skin friction reduction, *Annual Review of Fluid Mechanics, vol. 41, pp. 231-251.*

[2] Fukagata K., Iwamoto K., Hasegawa Y. (2024), Turbulent drag reduction by streamwise traveling waves of wall-normal forcing, *Annual Review of Fluid Mechanics, vol. 56, pp. 69*-90.

[3] Miura S., Ohashi M., Fukagata K., Tokugawa N, (2022), Drag reduction by uniform blowing on the pressure surface of an airfoil, *AIAA Journal, vol. 60, pp. 2241-2250.*

[4] Ishize T., Omichi H., Fukagata K. (2024), Flow control by a hybrid use of machine learning and control theory, *International Journal of Numerical Methods in Heat & Fluid Flow, vol. 34, pp. 3253-3277.*

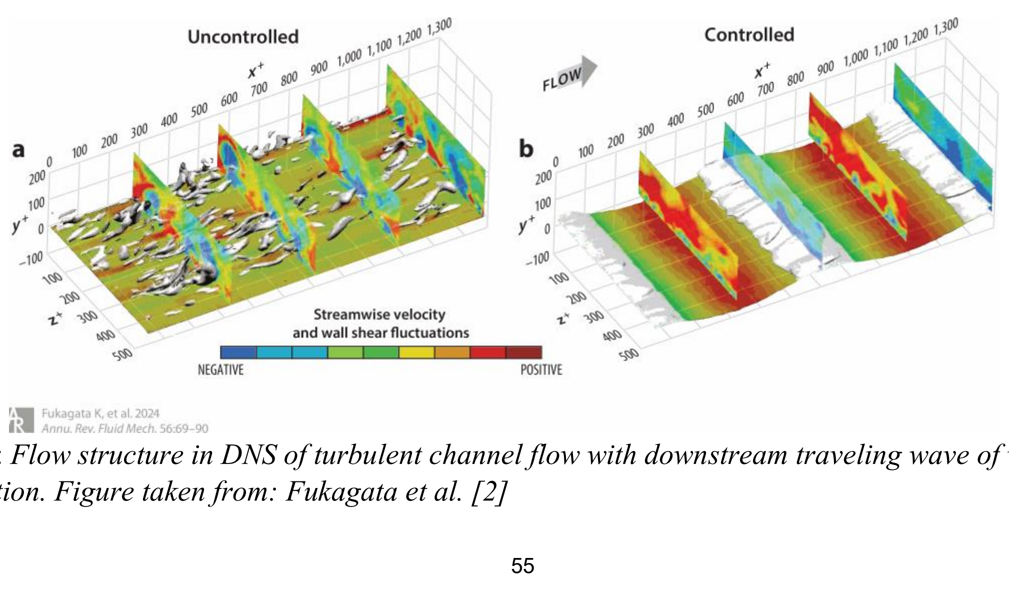

Figure 1: *Flow structure in DNS of turbulent channel flow with downstream traveling wave of wall deformation. Figure taken from: Fukagata et al. [2]*

Restricted Nonlinear Investigation of Developing Boundary Layers over Accelerating Walls

Alexandra C. Risha [1], Benjamin A. Minnick [2] and Dennice F. Gayme [1]

[1] Mechanical Engineering, Johns Hopkins University, Baltimore, USA
[2] Maneuvering and Control, Naval Surface Warfare Center Carderock Division, West Bethesda, USA

key-words: developing boundary layer, adverse/favorable pressure gradient, reduced-order model

Abstract:

Turbulent boundary layers (TBLs) exposed to pressure gradients are prevalent in many engineering applications. Recent works aimed at better understanding these flows have focused on coherent structures, in particular, examining how pressure gradients influence large-scale features, and subsequently, the low-order statistics [1, 2]. Amplitude modulation of the small-scales has also been shown to intensify in TBLs subject to adverse pressure gradients [2]. Additionally, rolling motions responsible for re-organizing the flow and redistributing momentum are altered with increasing pressure gradient intensity.

The significance of coherent structures in TBLs has inspired the development of structure-based analysis tools and reduced-order models. The restricted nonlinear (RNL) model is one such model, where the flow is decomposed into a large-scale streamwise-averaged mean interacting with a limited number of small-scale streamwise-varying perturbations. RNL simulations of temporally-developing TBLs over a moving wall were recently shown to reproduce first- and second-order statistics [3]. The similarity between the statistical behavior of temporally-developing TBLs and spatially-developing TBLs [4] suggest the promise of the RNL framework for studying TBLs exposed to pressure gradients in a similar manner.

This work employs the RNL large eddy simulation (LES) framework to study favorable (FPG) and adverse (APG) pressure gradients in spatially developing TBLs through acceleration and deceleration of a moving bottom wall. The governing equations are solved using a modification of the lesgo.me.jhu.edu code. The bottom wall initially moves at a constant velocity, $u_{w,0}$, then after a prescribed time, $t_{x,loc}$, is accelerated according to a power-law relationship and a varying acceleration parameter, m (see Figure 1). Random noise is applied near the wall up to a distance δ_0 to initialize the flow. Figure 2 highlights the ability of the model to capture critical structural features in accelerating, non-accelerating, and decelerating wall TBLs. Figure 2(a) shows the time history of the streamwise mean velocity at a spanwise location, where the BL thickness is shown to grow differently for each case. Figure 2(b) reports the time-resolved instantaneous velocity fluctuations for all cases, illustrating how the streamwise mean time-scale shortens for the accelerating wall and elongates for the decelerating wall, similar to [2].

Figure 3(a) presents ensemble-averaged mean velocity profiles, consisting of 100 samples, at $t^* = tu_{w,0}/\delta_0 = 480$. The varying accelerations influence the statistics, particularly in the log-layer and wake regions. Figure 3(b) shows the root mean square of velocity and the Reynolds stresses which demonstrate trends consistent with direct numerical simulation (DNS) results from the literature[1, 2]. The model's ability to predict these trends indicates that the temporal development of truncated streamwise scales may provide similar alterations to flow as the full range of scales in a spatially developing TBL. Future work will include more detailed interrogation of the scale interactions that are naturally decomposed in the RNL modeling framework.

References

[1] Harun Z., Monty J., Mathis R., and Marusic I., (2013): Pressure gradient effects on the large-scale structure of turbulent boundary layers, *J. Fluid Mech., vol. 715, pp. 477-498*

[2] Lee J. H., (2017): Large-scale motions in turbulent boundary layers subjected to adverse pressure gradients, *J. Fluid Mech., vol. 810, pp. 323-361*

[3] Minnick B. and Gayme D., (2024): Restricted nonlinear boundary layers over a moving wall, *Proc. of the 13th Int'l Symposium on Turbulence and Shear Flow Phenomenon*, Montreal, pp. 216-221

[4] Kozul M., Chung D., and Monty J.P., (2016): Direct numerical simulation of the incompressible temporally developing turbulent boundary layer, *J. Fluid Mech., vol. 796, pp. 437-472*

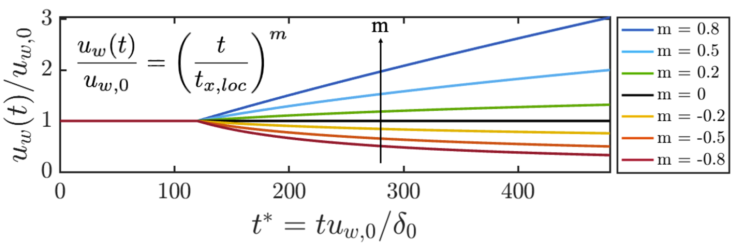

Figure 1: *Wall velocity boundary condition profile for given accelerations (m).*

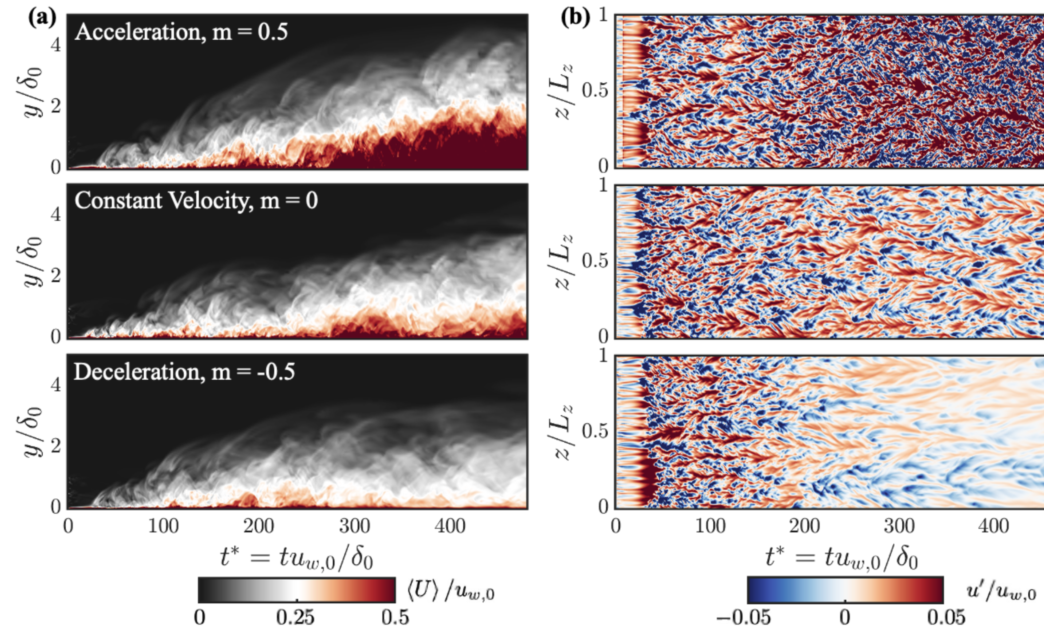

Figure 2: *(a) Time history of streamwise mean velocity at a same spanwise (z) location, (b) instantaneous velocity fluctuations at a wall-normal (y) location, near the wall ($y/\delta_0 = 0.004$).*

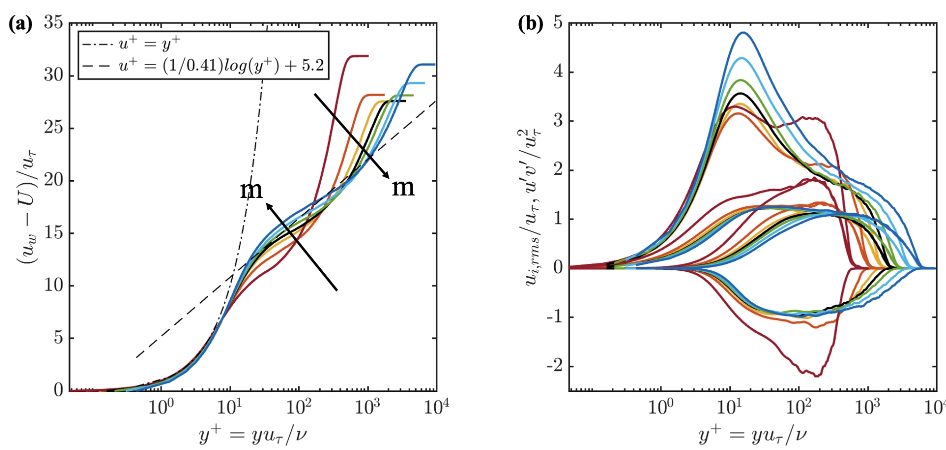

Figure 3: *(a) Mean velocity profiles and (b) second-order statistics of 200 ensemble-averaged samples at $t^* = 480$ with varying friction Reynolds numbers, Re_τ. Color legend corresponds to Figure 1.*

Towards a composite mean velocity profile for adverse pressure gradient turbulent boundary layers

Ahmad Zarei, Mitchell Lozier, Rahul Deshpande and Ivan Marusic

Department of Mechanical Engineering, The University of Melbourne, Parkville VIC, Australia

Key-words: turbulent boundary layers, scaling laws

Abstract:
Adverse pressure gradient (APG) turbulent boundary layers (TBLs) are pertinent to various engineering applications, such as aircraft wings and wind turbine blades. Previous studies [2] have shown that the scaling of APG TBL statistics is influenced by the pressure gradient strength (defined by the Clauser pressure gradient parameter, β), the upstream pressure gradient history, and the Reynolds number (Re). However, majority of the past studies investigating the universality of APG TBL scalings have been limited to low Re, or in the case of experiments, have been associated with unique upstream pressure gradient histories. Here, we experimentally investigate, via oil film interferometry (OFI) and hot wire anemometery (HWA), the streamwise development of APG TBLs with minimal upstream pressure gradient history. That is, the upstream history corresponds to the development of a high-Re, zero pressure gradient (ZPG) TBL. A schematic of the experimental setup [2] and profiles of the mean pressure coefficient (C_P) for various pressure gradient configurations, with minimal upstream history, are shown in Fig.1.

Here, we consider mean velocity scaling over a range of APG conditions with the aim of developing a composite mean velocity profile for general APG TBLs. This will be achieved through strategic modification of Nickels composite profile [3]. The functional form of the Nickels fit consists of three distinct components: the sublayer, the overlap region, and the wake region ($U^+ = U^+_{\text{inner}} + U^+_{\text{overlap}} + U^+_{\text{wake}}$). The original profile [3] was developed using a viscous scaled pressure gradient parameter, p_x^+, which approaches zero at high-Re. As a result, the original profile does not accurately reflect deviations from classical mean velocity scaling, which are observed for high-Re APG TBLs [1] as shown in Fig.2-b. Modifications to the original profile are based on analysis of an extensive compilation of experimental datasets with β ranging from 0 to 33 and Re based on friction velocity and TBL thickness from 500 to 13,000. A physical model will also be introduced to explain variation of the different parameters in the modified profile with the pressure gradient strength. Preliminary results in figure 2(a) show that this new model accurately reflects deviations from the classical mean velocity scaling.

References

[1] Pozuelo, R., Li, Q., Schlatter, P., Vinuesa, R, (2021), An adverse-pressure-gradient turbulent boundary layer with nearly constant $\beta \simeq 1.4$ up to $Re_\theta \simeq 8700$, *Journal of Fluid Mechanics.939:A34*

[2] Deshpande, R., Van Den Bogaard, A., Vinuesa, R., Lindić, L., Marusic, I.(2023), Reynolds-number effects on the outer region of adverse-pressure-gradient turbulent boundary layers, *Physical Review Fluids, 8(12), 124604.*

[3] Nickels, T. B. (2004), Inner scaling for wall-bounded flows subject to large pressure gradients, *Journal of Fluid Mechanics, 521, 217-239.*

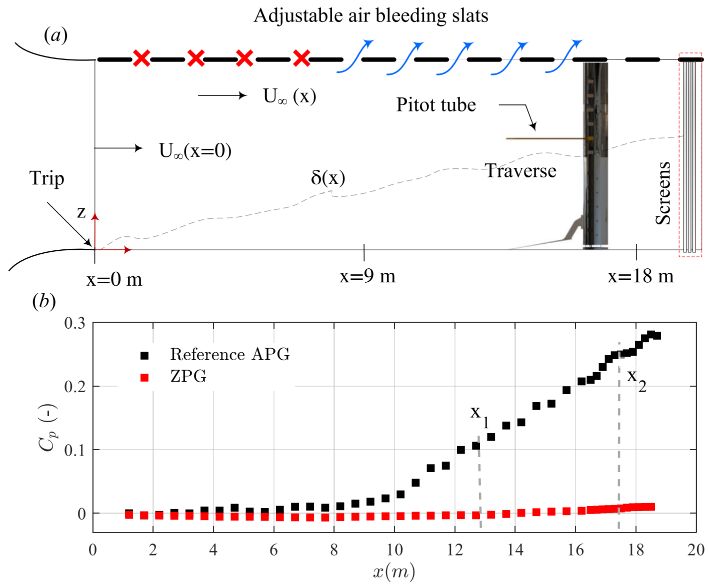

Figure 1: *(a) Schematic of the experimental setup used to develop APG TBLs with minimal upstream pressure gradient histories. (b) Streamwise variation of C_P for various pressure gradient configurations. The dashed lines represent OFI and HWA measurement locations.*

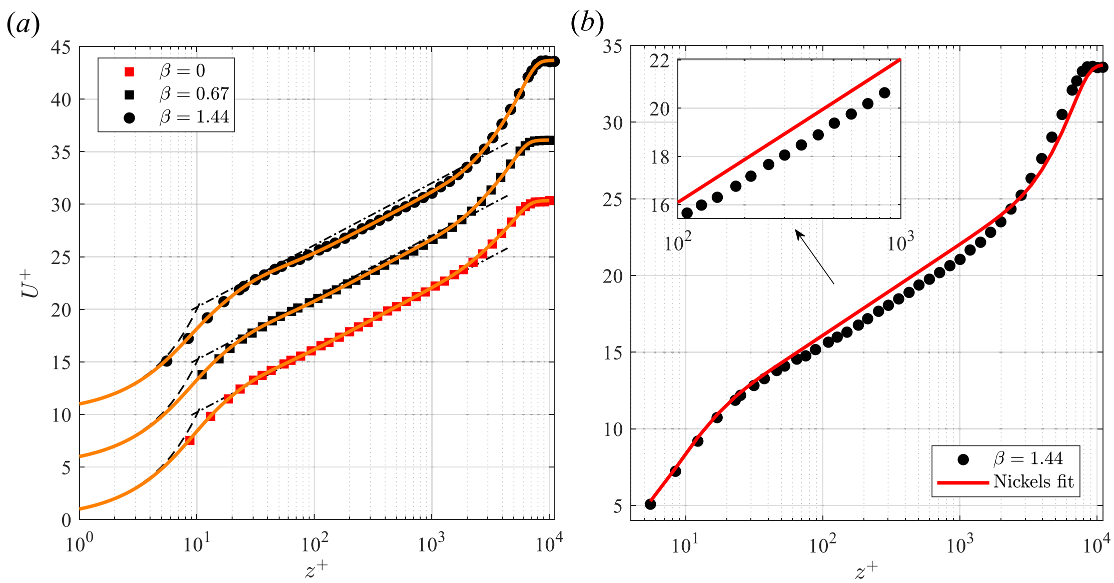

Figure 2: *(a) Experimental mean velocity data and the modified profile fit (solid orange lines) for different pressure gradient cases ($\beta = 0 \,\&\, 0.67$ are at x_1 and $\beta = 1.44$ is at x_2), (b) the same mean velocity data and the corresponding Nickels profile (solid red line). The dash and dash-dot lines show the classical log-law and $U^+ = z^+$. The mean velocity profiles are separated by five vertical units.*

Constructing wall turbulence using attached hairpin vortices

Y. Ge [1], W. Shen [1,2], Z. Han [1], Y. Zhao [1] and Y. Yang [1]

[1] State Key Laboratory for Turbulence and Complex Systems, College of Engineering, Peking University, Beijing 100871, PR China
[2] Max Planck Institute for Solar System Research, 37077 Göttingen, Germany

key-words: wall-bounded flow, vortex dynamics

Abstract:

Wall turbulence is observed to be packed with coherent structures, such as hairpin vortices [1]. The organization of these vortices near the wall can be modeled using the attached eddy hypothesis [2], which effectively describes velocity statistics in the log-law region and energy-containing motions. However, the complex geometry, diverse scales, and internal twisting of vortical structures in wall turbulence present significant challenges for developing physics-based models, and constructing wall turbulence based on realistic coherent structures remains a formidable task.

In this study, we model wall turbulence as an ensemble of complex vortices (Fig. 1a), generating turbulence fields enriched with hierarchically organized hairpin vortex packets (Fig. 1b). Specifically, three dimensional fields consisting of these vortices are numerically constructed using a recently developed method [3]. The geometry and spatial distribution of these vortex packets, including their spanwise meandering, are calibrated to align with physical observations and flow statistics. Our model successfully reproduces key characteristics of wall turbulence, including mean velocity profiles, higher-order velocity fluctuation moments, near-wall streaks, and energy spectra in the log-law region, which are consistent with theoretical and numerical predictions (Fig. 1c).

This framework provides an efficient approach for generating initial or inlet conditions for numerical simulations without relying on external data. It has been tested in cases with Reynolds numbers ranging from $Re_\tau = 10^3$ to 10^4, and generating turbulence fields at $Re_\tau = 10^4$ with $O(10^9)$ grid points requires $O(1)$ CPU hours. Furthermore, this framework provides a testing ground for developing more advanced turbulence models based on vortical structures.

References

[1] Wu X. and Moin P., (2009), Direct numerical simulation of turbulence in a nominally zero-pressure-gradient flat-plate boundary layer, *Journal of Fluid Mechanics, vol. 630, pp. 5–41*

[2] Marusic I. and Monty J., (2019), Attached Eddy Model of Wall Turbulence, *Annual Review of Fluid Mechanics, vol. 51, pp. 49–74*

[3] Shen W., Yao J. and Yang Y., (2024), Designing turbulence with entangled vortices, *Proceedings of the National Academy of Sciences, vol. 121, pp. e2405351121*

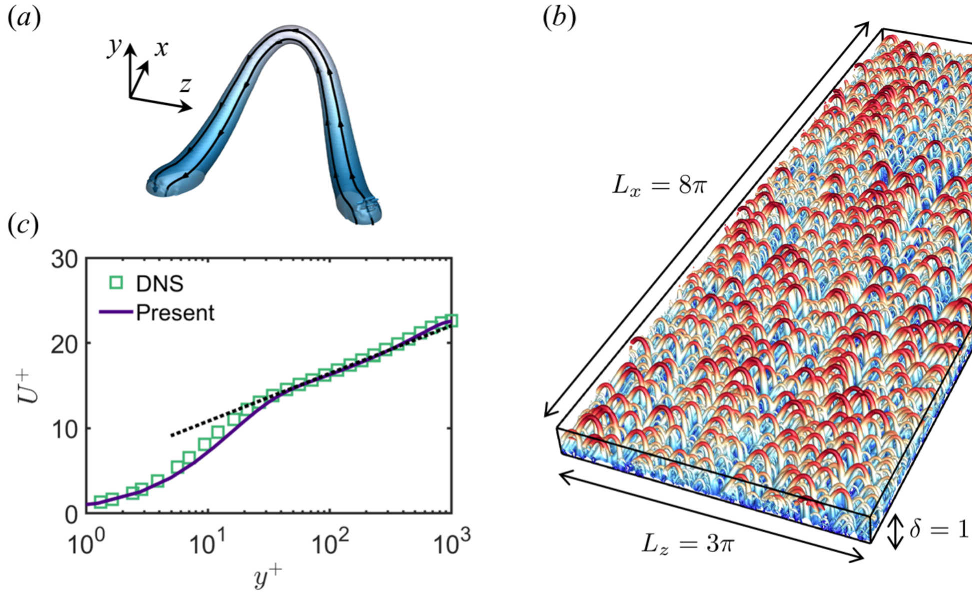

Figure 1: Constructing wall turbulence using hierarchically complex vortices. (a) Single vortex structure with complex geometry and variable thickness, integrating several vortex lines on the vortex surface. (b) Vortex-surface visualization of a synthetic wall turbulence ($Re_\tau = 1,000$), composed of hierarchically vortex packets with spanwise meandering features. The isosurfaces are color-coded by the wall distance. (c) The mean velocity profile of the synthetic turbulent channel flow. The dashed line shows the log-law $U^+ = \kappa^{-1} \ln y^+ + B$, where $\kappa = 0.41$ and $B = 5.2$.

High Spatial Resolution PIV Study of Self-Similar Adverse Pressure Gradient Turbulent Boundary Layer on the Verge of Separation

Z. Chen, B. Sun, A. Heidarian, C. Atkinson and J. Soria

Laboratory for Turbulence Research in Aerospace and Combustion (LTRAC), Department of Mechanical and Aerospace Engineering, Monash University, Melbourne VIC 3800, Australia

key-words: Particle Image Velocimetry, Turbulent Boundary Layer

Abstract:
Adverse pressure gradient turbulent boundary layers (APG-TBLs) are prevalent in natural and engineering flows, often leading flow separation and efficiency losses. Understanding APG-TBL dynamics is crucial for optimising aerodynamic performance and flow control.
This study used high-spatial-resolution particle image velocimetry (HSR-PIV) to investigate a self-similar APG-TBL at the verge of separation in the wind tunnel at the Laboratory for Turbulence Research in Aerospace and Combustion (LTRAC) at Monash University. The 4.5-meter-long test section has an adjustable roof profile, allowing the flow to develop with a low and constant skin friction coefficient $C_f = 4.8 \times 10^{-4}$, enabling an equilibrium turbulent boundary layer flow, which is essential for maintaining self-similarity, shown in figure 1.
A dual-camera system comprising two PCO-Panda sCMOS cameras was employed to achieve high spatial resolution shown in figure 2. The top camera captured a large field of view (FOV) for boundary layer measurements ($0.9\delta \times 0.9\delta$) with a spatial resolution of 28.55µm/pixel. The bottom camera provided a detailed view spanning from the wall to the log-law region ($0.2\delta \times 0.2\delta$), with a spatial resolution of 6.5µm/pixel.
The multi-grid, multi-pass cross-correlation PIV (MCCDPIV) technique[1] was employed for the analysis of the single-exposed image pairs. A third-order polynomial model corrected lens distortion, keeping residual errors below one pixel[2]. At a friction velocity of 0.1m/s, viscous length of 139µm and a boundary layer thickness of around 157mm, the most probable the streamwise velocity at y = 0.03% δ ($y^+ = 0.36$) above the wall measured by probability density function is almost zero, indicating the flow is on the verge of separation, shown in figure 3.

Acknowledgment:
The authors would like to acknowledge the funding of this research by the Australian Research Council through a Discovery Grant, and National Computational Infrastructure (NCI), supported by the Australian Government through computational grants awarded by the National Computational Merit Allocation Scheme (NCMAS) funded by the Australian Government.

References

[1] Soria J., (1996), An investigation of the near wake of a circular cylinder using a video-based digital cross-correlation particle image velocimetry technique, *Exp. Therm. Fluid Sci, vol.12, pp.221-233*

[2] Sun B., (2021), Distortion correction of two-component two-dimensional PIV using a large imaging sensor with application to measurements of a turbulent boundary layer flow at $Re_\tau = 2386$, *Experiments in Fluids, vol.62*

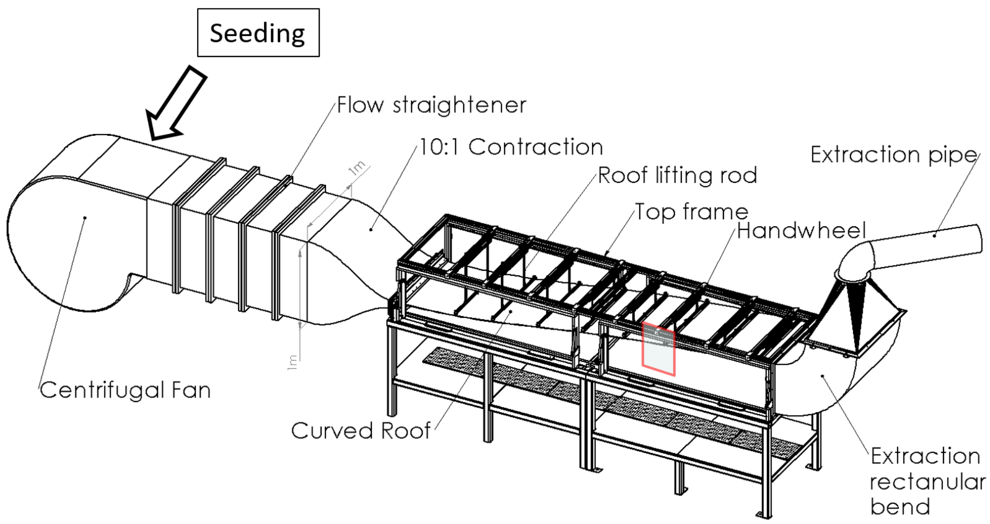

Figure 1: *Schematic of the APG-TBL wind tunnel with normal region of interest (ROI) at the centre plane of the tunnel along streamwise direction(highlighted in red)*

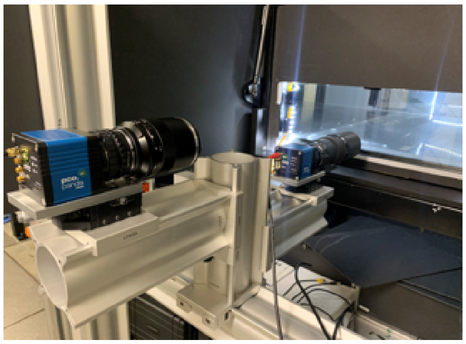

Figure 2: *The dual-camera system*

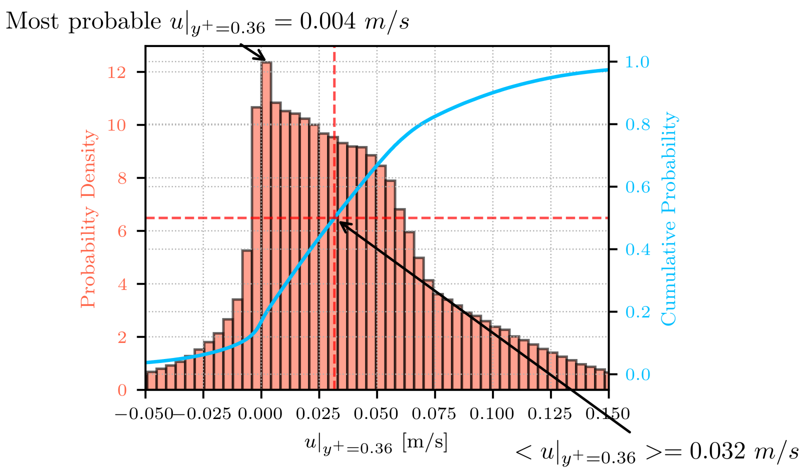

Figure 3: *The PDF of fluctuating streamwise velocity at $y^+ = 0.36$*

Characterisation of rough-wall drag in compressible turbulent boundary layers

D. D. Wangsawijaya[1], R. Baidya[2,3], S. Scharnowski[3], B. Ganapathisubramani[1] & C. J. Kähler[3]

[1] Aeronautical and Astronautical Engineering, University of Southampton, United Kingdom

[2] Mechanical Engineering, University of Melbourne, Australia

[3] Aerospace Engineering, University of the Bundeswehr Munich, Germany

key-words: turbulent boundary layers, compressible flows, experiments, rough walls

Abstract:
Compressible turbulent boundary layers (TBLs) developing over rough walls comprise of phenomena related to high-speed flight vehicles, where the roughness is likely to be induced during operations due to thermal expansion, ablation, dust impact, water and ice droplets. In incompressible flows, drag penalty due to surface roughness is characterised by the log-law deficit corresponding to the Hama roughness function [1]. In this study, we aim to transfer this existing framework for rough wall drag in incompressible flows to the compressible flow regime, subjected to various velocity transformations [2] to account for the compressibility effect.

We investigate the TBLs developing over a $58\delta_1 \times 22\delta_1$ ($x \times y$) flat plate installed inside the trisonic wind tunnel (TWM) at the University of the Bundeswehr Munich (figure 1a), where δ_1 is the reference 99% smooth-wall boundary-layer thickness at a freestream Mach number $M_\infty = 0.3$. Test surfaces comprise of a smooth wall and two rough walls constructed from P60- and P24-grit sandpaper sheets (figure 1b, c), subjected to a range of M_∞ ($0.3 \leq M_\infty \leq 2.9$) and friction Reynolds numbers ($2200 \leq Re_\tau \equiv \delta U_\tau/\nu_w \leq 30300$), where δ is the 99% boundary-layer thickness for each test case at the PIV (particle image velocity) measurement location ($29\delta_1$ from the leading edge, figure 1a), U_τ the friction velocity, and ν_w the air kinematic viscosity at the wall. The rough-wall test matrix is presented in table 1, showing variation of Re_τ while maintaining a constant $M_\infty = 2$.

As direct wall shear stress measurements are not performed in this campaign, figure 2(a) shows the transformed Hama roughness function ΔU_I^+, estimated by fitting the log region of the transformed mean velocity U_I. All cases are within the "fully rough" regime, with an apparent proportional relation between M_∞ and the log-law intercept. Here, the subsonic and transonic test cases follow the log relation $\Delta U_I^+ = 1/\kappa \log(k_s U_\tau/\nu_w) + B - B_{FR}$, where k_s is the equivalent sandgrain roughness [3], while the intercept $B - B_{FR}$ is proportional to M_∞ for the supersonic cases, independent of the velocity transformations (each symbol corresponds to a different transformation in figure 2). A new roughness lengthscale, similar to that of a pervious study [4], $k_* = (\nu_w/\nu_\infty)k_s$ and $k_*^+ \equiv k_s U_\tau/\nu_\infty$ collapses all cases to the log relation (figure 2b), where ν_∞ is the freestream kinematic viscosity. It should be noted that the (ν_w/ν_∞) correction factor is obtained empirically. The derivation of the theoretical correction factor from the roughness function, accounting for the appropriate incompressible flow analogies, will follow.

References

[1] F. R. Hama (1954). Boundary-Layer Characteristics for Smooth and Rough Surfaces, *Trans. SNAME* 62, pp. 333–351.

[2] P. S. Volpiani et al. (2020). Data-driven compressibility transformation for turbulent wall layers, *Phys. Rev. Fluids* 5, 052602(R).

[3] J. Nikuradse (1933). Laws of flow in rough pipes, *NACA Tech. Mem.* 1292.

[4] D. Modesti et al. (2022). Direct numerical simulation of supersonic turbulent flows over rough surfaces, *J. Fluid Mech.* 942, A44.

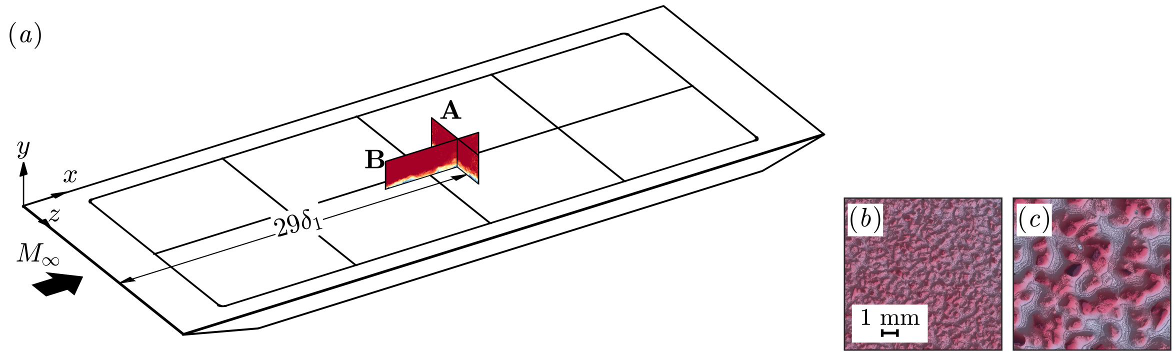

Figure 1: (a) Illustration of PIV setup and the measurement location. **A**: 2D3C cross-stream stereoscopic PIV in y–z plane and **B**: 2D2C PIV in x–y plane. Height contours of (b) P60- and (c) P24-grit sandpaper samples obtained from optical profilometer scans.

Surf.	P60					P24				
M_∞	0.3	0.8	2	2	2.9	0.3	0.8	2	2	2.9
Re_τ	7430	22390	10450	20270	7810	9830	27020	15590	30290	11170
Sym.	●	●	●	●	●	●	●	●	●	●

Table 1: The rough wall test matrix

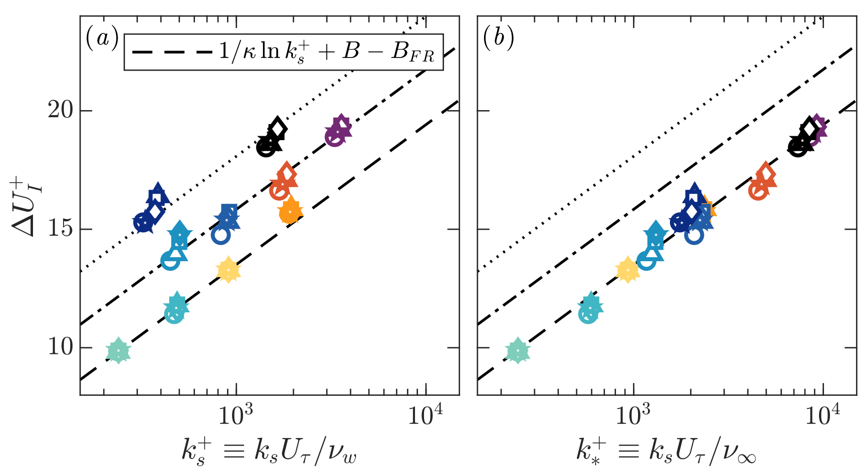

Figure 2: The momentum deficit ΔU_I^+ as a function of (d) k_s^+ and (e) k_*^+. Colours mark the test cases shown in table 1, while symbols mark various velocity transformations. Lines correspond to M_∞: < 1 (- - -, $1/\kappa \log k_s^+ + B - B_{FR}$), 2 (-·-·-), and 2.9 (······).

Relaxation of staggered roughness generated turbulence in a low Re number channel flow

Sedat Tardu, Benjamin Arrondeau

University Grenoble Alpes, Grenoble, France
key-words: Roughness, Direct Numerical Simulations, Relaxation and Decay

Abstract:
Relaxation of the turbulent and fluctuating passive scalar fields generated by a specific staggered roughness distribution [1] in the entrance region of an initially laminar channel flow is studied through direct numerical simulations. Large staggered roughness elements of height $k = 0.27H$ partly recover the entry zone, prior to a smooth channel wherein both the turbulent flow and scalar fields decay, because the Karman number $Re_\tau = \frac{H\bar{u}_\tau}{\nu} \approx 70$ is significantly below the subcritical limit (the Taylor scale-based Reynolds number is typically $5 < Re_\lambda < 20$). Here H is the channel half width, $\bar{u}_\tau$ is the shear velocity and ν stands for the kinematic viscosity. A typical flow configuration is shown in figure 1(left). The quantity $\delta_0^* = \frac{\delta_0}{H}$ local denotes the thickness of the boundary layer in the developing zone, from which the channel is rough downstream. Thus, in the case $\delta_0^* = 0$, the whole entry region is covered by the roughness elements, while for $\delta_0^* = 0{,}7$ there is a relatively large zone upstream which is smooth and stays laminar. Figure 1 (right) shows the quasi-streamwise vortices generated by the by-pass transition mechanism in the rough zone and the turbulence decay in the smooth channel downstream (labeled as the *control* channel (CC) hereafter). We will present different configurations with different δ_0^* , and discuss also the effect of twice smaller roughness elements with $k = 0.135H$. The idea is to not intervene in the CC directly but to passively manage its inlet to improve the flow and scalar transport within, and this at particularly low Reynolds numbers. Besides some attractive fundamental aspects rarely considered in the literature, the main applications are in microfluidics in general with some particular potentiality in the thermal management of ultrahigh intensity lasers [2]. Figure 2 shows the decay of the fluctuating passive scalar intensity $[\theta'\theta']$ and its dissipation $[\varepsilon_{\theta'}]$ at the CC centerline where the turbulence is locally homogeneous and (quasi) isotropic (HIT). It is seen that $[\theta'\theta'] \sim x^\gamma$, with $\gamma \approx -1.3$, in close agreement with the literature [3]. One should have $[\varepsilon_{\theta'}] \sim x^{\gamma-1}$, in decaying HIT, and this is confirmed in figure 2(right). The decay characteristics of the fluctuating velocity field at the centerline are also in close agreement with the HIT features. Figure 3 shows the Nusselt number Nu in the smooth CC, as a function of the bulk Reynolds number and in different δ_0^* configurations. Despite the decay of the turbulent fields, Nu is only slightly smaller than what one would have in the fully developed turbulent regime, and nearly twice larger compared to the laminar Poiseuille flow, over a large streamwise extend up to $x = 40H$. Other detailed results on the development of flow and scalar fields in the CC will be presented during the symposium.

References

[1] N. N. Anika, L. Djenidi, S. Tardu (2020), Roughness effect in an initially laminar channel flow, J. of Fluid Mechanics, 892, A34.
[2] M. Belec, A.Girard, G. Balarac, U. Bieder, F. Millet, N. Luchier (2021), Effect of turbulence on the wavefront of an ultrahigh intensity laser beam, J. Fluids Eng., 143, 031504.
[2] S.K. Lee, S. K., R.A. Antonia (2012), Scaling range of velocity and passive scalar spectra in grid turbulence, Physics of Fluids 24.

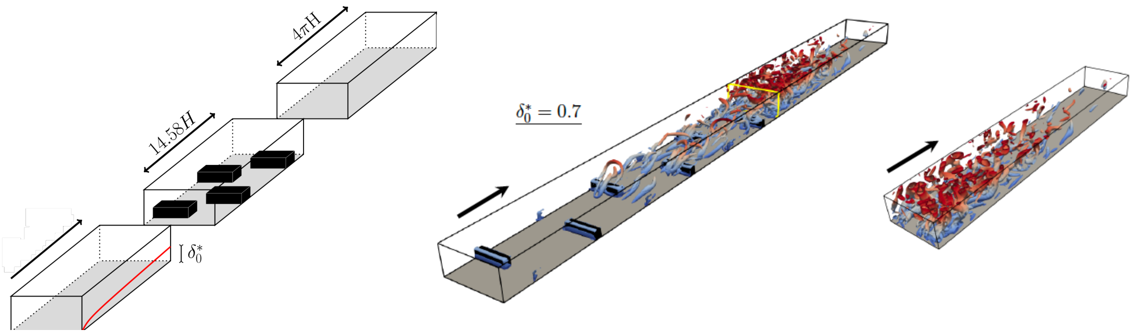

Figure 1: *Typical flow configuration (left)*, right: *quasi-streamwise vortices generated by the by-pass transition in the entry zone for $\delta_0^* = 0{,}7$ prior to the decay in the subsequent smooth control channel downstream of the yellow rectangle (end on the right).*

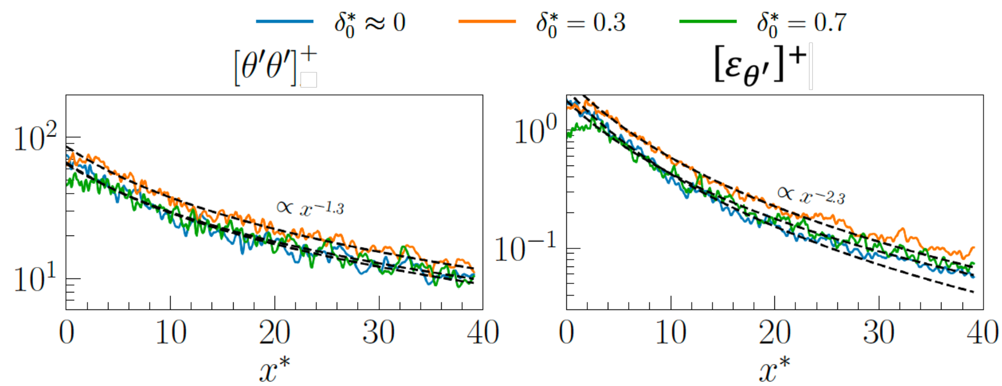

Figure 2: *Decay of the turbulent intensity of the fluctuating scalar field (left) and its dissipation (right) at the centerline of the control channel, as a function of the streamwise distance $x^* = \frac{x}{H}$ from the inlet. The Prandtl number is $Pr = 1$.*

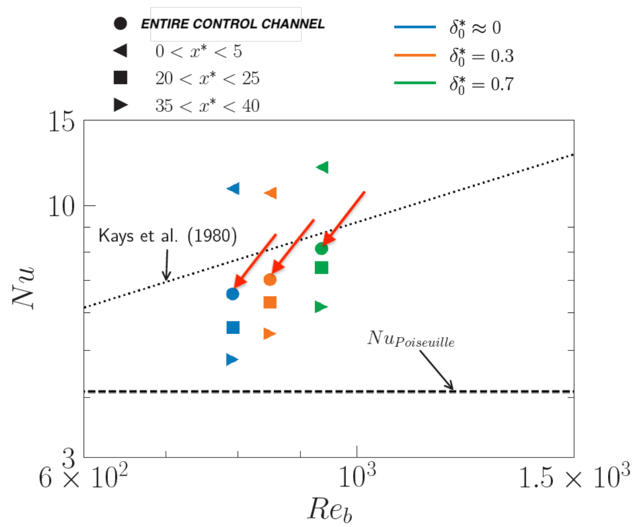

Figure 3: *The Nusselt number $Nu = \frac{2Re_\tau Pr}{\bar{\theta}_b^+}$ as a function of the Reynolds number based on the bulk velocity in the control channel. Here $(\ \ )^+$ refers to the quantities scaled by the shear velocity and the wall temperature. Different symbols correspond to the averaging in different zones beginning by the inlet at $x^* = 0$. The arrows show the Nu averaged over the entire CC. The dashed line is the Kays correlation.*

A rough recovery

Martina Formichetti [1], A. Kwong [1], S. Symon [1] and B. Ganapathisubramani [1]

[1] Department of Flight Mechanics and Aerodynamics, University of Southampton, Southampton, UK

Key-words: Turbulence, Boundary Layers, Roughness

Abstract:

Numerous studies have examined turbulent boundary layers (TBLs) over streamwise homogeneous roughness, leading to a comprehensive understanding of their internal structure, particularly in the fully rough regime [1]. Additionally, investigations into TBL responses to step changes in surface roughness (smooth-to-rough or rough-to-smooth) have provided valuable insight into their behaviour [2, 3]. However, the streamwise roughness length (fetch length) required for the TBL to reach equilibrium—independent of transition effects—remains unclear. Furthermore, the applicability of the equivalent sand-grain roughness height, k_s, for modelling TBLs after a step change has not been explored in detail, potentially overlooking a simple and generic way to describe non-equilibrium conditions.

This study aims to determine the minimum fetch length required for a TBL to fully adjust to a new roughness condition. A drag balance and particle image velocimetry (PIV) were used to measure the TBL response to 0-to-40 ms^{-1} inlet-velocity sweeps for 22 different roughness lengths upstream of the balance (up to $\approx 40\delta$). The roughness consisted of P24 sandpaper strips sequentially added to the test section floor of the University of Southampton Boundary Layer Wind Tunnel (BLWT). A top view of the P24 laser scan is shown in Figure 1. The results indicate that equilibrium recovery occurs at a fetch length of approximately $L \approx 20\delta_2$, where equilibrium was defined as the convergence of C_f with fetch length.

To assess whether roughness geometry influences equilibrium recovery, additional experiments were conducted using three roughness configurations: (1) a LEGO baseboard, (2) a LEGO baseboard with spanwise-aligned LEGO bricks, and (3) a LEGO baseboard with staggered LEGO bricks (Figure 2). Each configuration was tested at increasing fetch lengths until equilibrium was reached. The spanwise ribs and staggered bricks attained equilibrium at approximately $18\delta_2$ and $15\delta_2$, respectively, whereas the baseboard showed no indication of becoming fully rough, leading to testing being halted at $15\delta_2$.

A comparison of C_f recovery with fetch length across different cases is shown in Figure 3, where increasing fetch is represented by darker to lighter colours. These results suggest that both roughness height and arrangement influence the recovery length. Specifically, smaller roughness elements require a longer fetch for the TBL to reach equilibrium. Moreover, the spanwise and staggered configurations, despite having the same statistical height, exhibited distinct recovery behaviours—reaching equilibrium within 3δ of each other and between 5δ and 2δ of the sandpaper case. This highlights the role of roughness organisation, in addition to geometry, in equilibrium development.

Finally, the mean velocity profiles over the P24 sandpaper case are plotted against wall-normal distance normalised by k_s in Figure 4. The profiles illustrate the blending of two logarithmic regions following the step change in roughness and the subsequent equilibrium recovery with increasing fetch length. Here, k_s is calculated for the longest fetch case, where the flow is in equilibrium with the rough wall, following standard rough-wall practices. For shorter fetch cases, the profiles diverge in the log region due to non-equilibrium effects, suggesting that an adaptation of k_s based on fetch length could improve existing models.

References

[1] J. Jiménez, (2004), Turbulent Flows Over Rough Walls, *Ann. Rev. Fluid Mech., vol. 36, pp. 173-196*

[2] W. P. Elliott, (1958), The growth of the atmospheric internal boundary layer, *Eos, Transactions, vol. 39 (6), pp. 1048-1054*

[3] A. A. Townsend, (1965), The response of a turbulent boundary layer to abrupt changes in surface conditions, *J. Fluid Mech., vol. 22 (4), pp. 799-822*

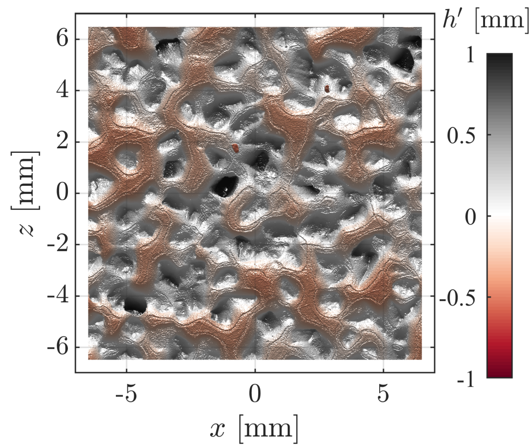

Figure 1: Top view of the laser scan of a sample of P24 sandpaper, where h' is the height variation from the mean height $\bar{h}$

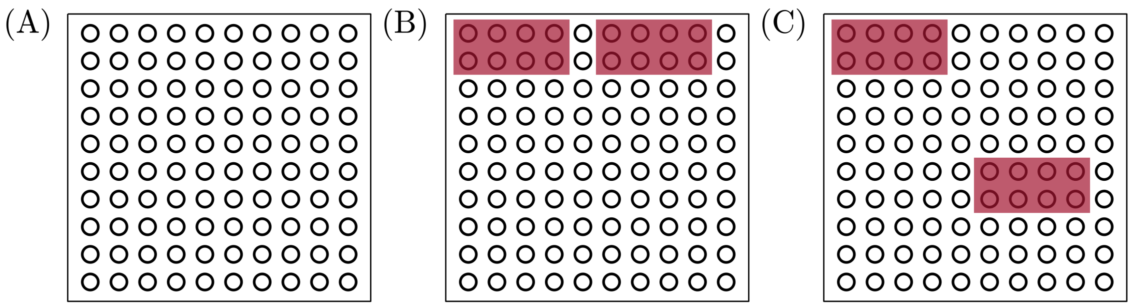

Figure 2: Top view of a sketch of the repeated units of the 3 LEGO roughness configurations: (A) LEGO baseboard, (B) LEGO baseboard and bricks in a quasi spanwise ribs orientation, (C) LEGO baseboard and staggered bricks.

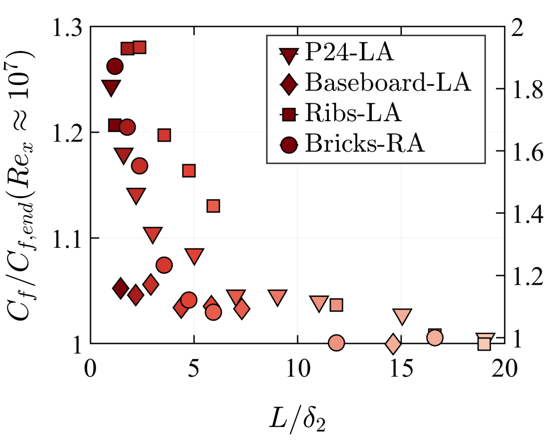

Figure 3: C_f evolution for 4 roughnesses i.e. P24 sandpaper (P24), LEGO baseboard (Baseboard), LEGO baseboard and bricks in quasi spanwise ribs configuration (Ribs), and LEGO baseboard and staggered bricks (Bricks). LA stands for left axis and RA stands for right axis.

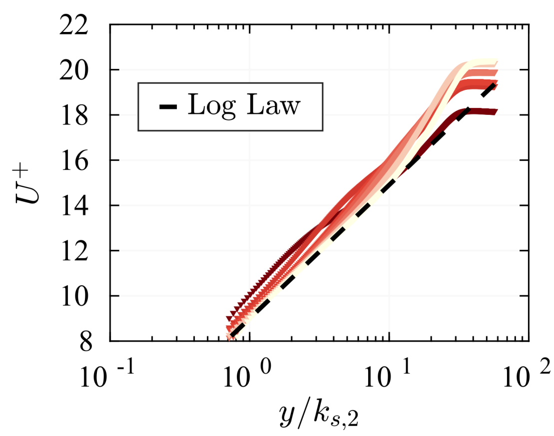

Figure 4: Mean velocity profiles in viscous units for different fetch lengths after a step change in roughness plotted against the wall-normal coordinate normalised by $k_{s,2}$, where $k_{s,2}$ is the equivalent sand-grain roughness height computed for the longest fetch case.

Influence of windward and effective slope on the structure of turbulent channel flow over ratchet-type roughness

Oleksandr Zhdanov [1] and Angela Busse [2]

[1] James Watt School of Engineering, University of Glasgow, Glasgow, UK
[2] Fachgebiet Numerische Fluiddynamik, Technische Universität Berlin, Berlin, Germany

key-words: Direct numerical simulations, Roughness, Turbulence

Abstract:

Ratchet surfaces are a simple two-dimensional form of directional roughness with a slope imbalance between the windward and leeward oriented faces. Examples of ratchet-type surfaces are widely found in nature, e.g., large-scale river dunes, barchan dunes, and sand ripples. Our previous investigations show that these surfaces break the forward-backward statistical symmetry of the flow and that they induce a fluid dynamic roughness effect that strongly depends on both windward (WS) and effective slope (ES) [1, 2]. The aim of the present ongoing study is to systematically investigate changes in the structure of turbulent channel flow over ratchet-type roughness considering both the effect of WS, which affects the upward deflection of the flow, and ES, which at constant ratchet height determines its length.

To this end, a series of direct numerical simulations of turbulent channel flow over ratchet-type surfaces were performed at friction Reynolds number 550. The ratchet-type surfaces are composed of transverse triangular bars with scalene cross-section which fully cover both channel walls (figure 1). In all cases, the ratchet height is fixed at $h/\delta = 0.08$, where δ is the mean channel half-height. Four groups of surfaces with systematically varied ES ($ES = 0.5, 0.333, 0.25$, and 0.167) are considered. For each ES, a range of windward slope angles α ($WS = \tan\alpha$) is considered that covers most of the range of possible angles within the limit of the right-angled triangle. The mean flow statistics can be found in [2]; the present study focusses on the effect of ES and WS on the structure of the near-wall turbulence.

Preliminary results indicate that windward slope has a significant impact on the flow structure close to the roughness. In figure 2 instantaneous streamwise velocity fluctuations (u'^+) in the $x-y$ plane at $z^+ \approx 6$ above ratchet crests are shown for two cases, namely $\alpha = 5°$ and $\alpha = 90°$ at constant $ES = 0.167$ together with the reference smooth-wall data. The presence of ratchets appears to affect the size and spacing of the high-speed flow structures. As part of an ongoing study, this is now being quantified using spectral analysis and correlation statistics. For $\alpha = 90°$ the streaks are disrupted at the locations of the ratchet crests (figure 2b), while no such effect is observed for $\alpha = 90°$. To gain further insight into the flow behaviour above the ratchet crests, a local quadrant analysis of streamwise and wall-normal velocity fluctuations is performed at the streamwise location of the ratchet peaks at $z^+ \approx 6$ above the ratchet crests. The results (figure 3) show that while for the case with $\alpha = 5°$ the probability of events in each quadrant is similar to the smooth wall case, for the case with $\alpha = 90°$ the probability of sweeps and ejections is reduced in favour of inward and outward interactions. In addition, the case with $\alpha = 90°$ has significantly different quadrant contributions to the Reynolds shear stress compared to the case with $\alpha = 5°$ or the smooth wall case. In particular, most of the contributions come from Q1 and Q3, which also results in the change of sign of $\overline{u'w'}^+$ at this location. In the next stage of this ongoing study, global and local flow statistics will be considered, including further analysis of quadrant statistics, Reynolds stress spectra, turbulence anisotropy, and velocity correlations.

References

[1] Busse A. and Zhdanov O., (2022), Direct numerical simulations of turbulent channel flow over ratchet roughness, *Flow, Turbulence and Combustion, vol. 109(4), pp. 1195–1213*

[2] Zhdanov O., Jelly T.O. and Busse A., (2024), The influence of windward and effective slope on turbulent channel flow over ratchet roughness, *Proceedings of the 13th International Symposium on Turbulence and Shear Flow Phenomena (TSFP-13)*, Montreal

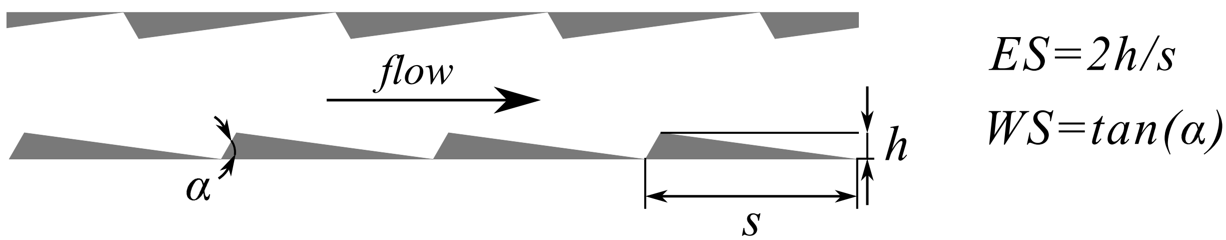

Figure 1: *Schematic of the channel with ratchet-type roughness (not to scale).*

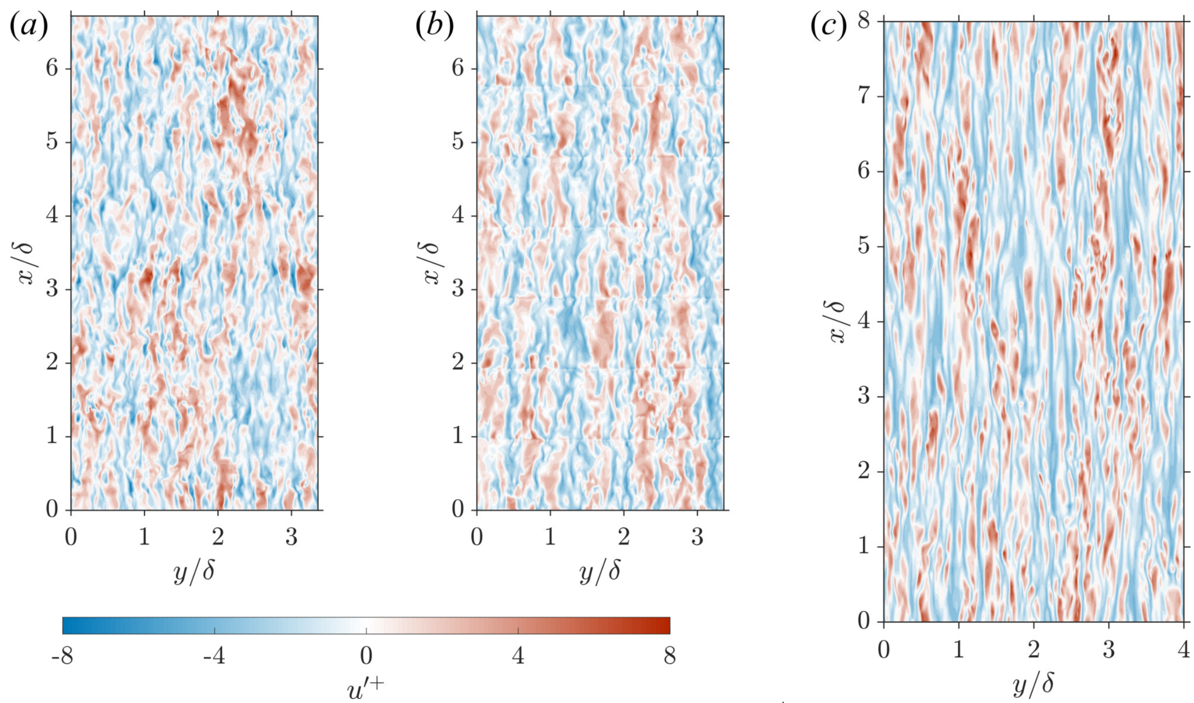

Figure 2: *Instantaneous streamwise velocity fluctuations at $z^+ \approx 6$ above the ratchet crests for ratchet-type surfaces with $ES = 0.167$ (a) $\alpha = 5°$, (b) $\alpha = 90°$, and (c) smooth channel.*

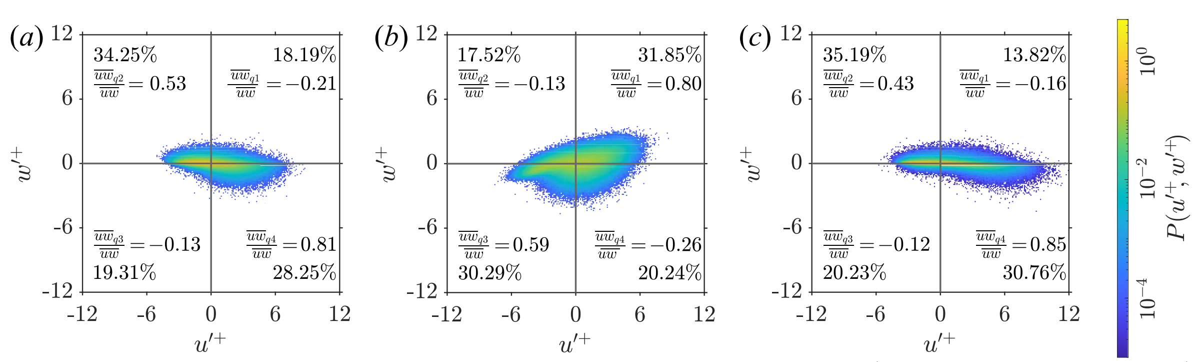

Figure 3: *Joint probability density function of local streamwise (u'^+) and wall-normal (w'^+) velocity fluctuations at $z^+ \approx 6$ above the ratchet crests for ratchet-type surfaces with $ES = 0.167$ (a) $\alpha = 5°$, (b) $\alpha = 90°$, and (c) smooth channel. The numbers in each panel show the probability of events in the corresponding quadrant and contributions of the quadrant to the total shear stress.*

DNS of turbulent boundary layers over dense soft filaments

Nikolaos Beratlis [2], Angelo Camminatiello [1], Kyle Squires [2] and Elias Balaras [1]

[1] Dept. of Mechanical and Aerospace Engineering, George Washington University, Washington DC, USA
[2] School for Engineering of Matter, Transport and Energy, Arizona State University, Tempe, AZ, USA

keywords: DNS, turbulent channel flow, rough walls, flexible fibers

Abstract:
Turbulent boundary layers over dense canopies consisting of flexible filaments have many applications in geophysical and engineering flows. In this work we will focus on canopies that are characteristic of soft-fouling. The latter takes place in the parts of a naval vessel submerged in sea water and exposed to marine organisms which colonize these surfaces. Today it is generally assumed that soft fouling results in minimal reduction in ship performance and therefore if found during a hull inspection is not considered a reason to clean the hull. Recent work however, indicates that biofilms can induce a steep drag penalty. The experiments by Murphy *et al.* [1], for example, on biofilms consisting of very low stiffness streamers grown under shear in a channel flow configuration indicate that the mean velocity profile exhibits a standard log-law region with the expected downward shift found in rough-wall flows. The resulting equivalent sand-grain roughness height, k_s, was significantly larger than the physical height of the biofilm possibly due to the flapping streamers. In this work we will illuminate the underlying mechanics of the increased drag using topography-resolving direct numerical simulations (DNS).

We will consider the case of a fully developed turbulent channel flow, where one of the walls is covered by a flexible canopy consisting of an array of filaments randomly distributed to match the desired open area ratio. The complex fluid-structure interaction problem is governed by the Navier-Stokes equations coupled to an inextensible Kirchhoff rod model that accounts for the dynamic deformations of the filaments. The fluid flow equations are solved on a structured Cartesian grid and the effect of the filaments is introduced via an immersed boundary formulation [2]. A collision model is utilized to account for short-range interactions between filaments and between a filament and the wall. A total of eighteen simulations will be presented with different canopy coverage ratios, slender ratios and Reynolds numbers. The Reynolds number based on the half channel height and the bulk velocity varies from $20000 < Re < 100000$ and the filaments length to diameter ratio $20 < l/d < 80$. The Cauchy number representing the ratio of fluid forces to bending force is always $Ca >> 1$, which means that the filaments are extremely flexible as in most biofilms. The ratio of filament to fluid density $\alpha = \rho_f/\rho \sim 1.05$ approaching the neutrally buoyant state. The solidity parameter defined as $\lambda = n_f ld/(L_x L_z)$, where n_f is the number of filaments, l and d are the filament length and diameter, and L_x and L_z is the extend of the domain, varied from 1.2 and 3.6. A typical computation involves the interaction of $\sim$ 50000 filaments interacting with the near-wall turbulent flow, where each filament is represented by $\sim$ 100 markers. Overall the two distinct layers found in canopy flows are observed. An example is shown in Fig. 1 where the average velocity for various cases is plotted in inner coordinates. The near wall profiles collapse when normalized with the friction velocity at the wall. Further away, the log-law is preserved but with a shift, ΔU^+, as for the case of rough-walls, when the total wall stress at a virtual point within the canopy is used as a reference velocity scale. Fig. 2 shows an instantaneous snapshot of the flow from the simulation at $Re_b = 80,0000$ and $\lambda = 2.6$. Here, we visualize the turbulent structures via the *Q-criterion.* The flexible canopy is also shown for reference and colored by the vertical coordinate (darker green at the bottom and lighter green away from the wall). Spanwise rollers forming at the local canopy tip can be seen. Their extent in the spanwise direction appears to be comparable to the filament length.

References

[1] Murphy, E.A., Barros, J.M., Schultz, M.P., Flack, K.A., Steppe, C.N., Reidenbach, M.A., (2018). Roughness effects of diatomaceous slime fouling on turbulent boundary layer hydrodynamics. *Biofouling*, 34:976–988.

[2] Kaminaris, I.K., Balaras, E., Schultz, M.P., Volino, R.J., (2023). Secondary flows in turbulent boundary layers developing over truncated cone surfaces. *Journal of Fluid Mechanics*, 961:A23.

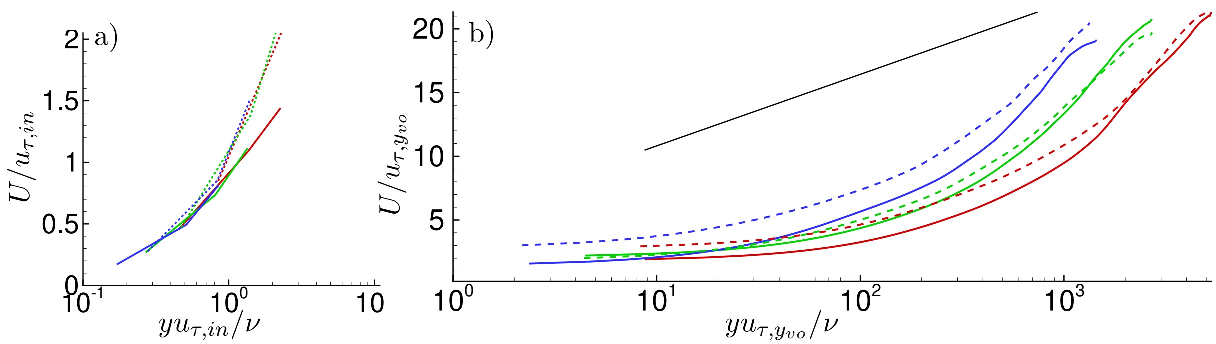

Figure 1: Profiles of the streamwise velocity averaged over time and space and scaled by a) $u_{\tau,in}$ and b) $u_{\tau,y_{vo}}$. Lines represent: — log-law for smooth wall, —; $Re_b = 80000$ and $\lambda = 2.6$, —; $Re_b = 40000$ and $\lambda = 2.6$, —; $Re_b = 20000$ and $\lambda = 2.6$, - -; $Re_b = 80000$ and $\lambda = 1.3$, - -; $Re_b = 40000$ and $\lambda = 1.3$, - -; $Re_b = 20000$ and $\lambda = 1.3$

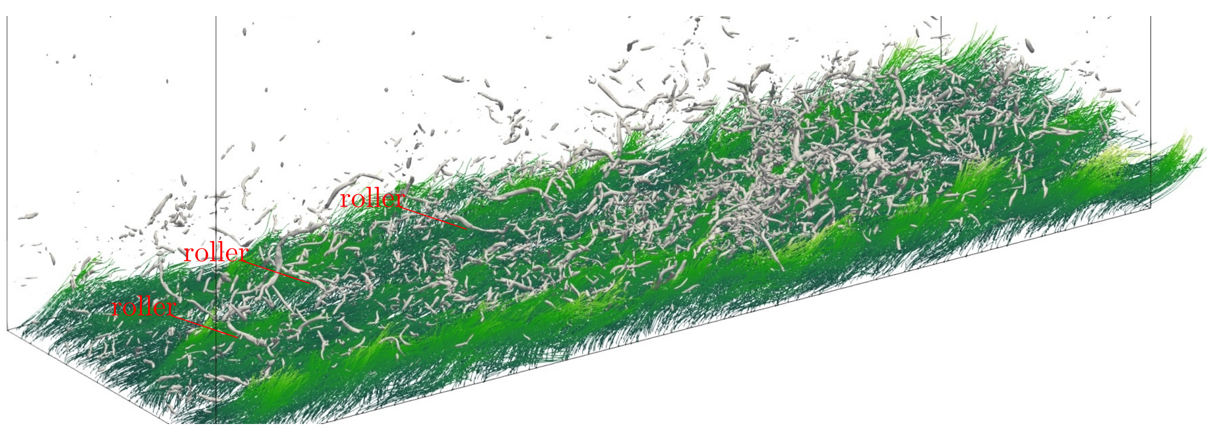

Figure 2: Flow visualization using the Q-criterion of the vortical structures in the flow. The flexible filaments are also shown at the bottom wall and they are colored by their vertical coordinate.

Breakup of small aggregates in turbulent flows

A. Lanotte[1]

[1]CNR NANOTEC, Institute of Nanotechnology, Lecce, Italy

The breakup of solid aggregates in turbulent colloidal suspensions is a physical process relevant for a broad variety of problems, from environmental sciences, to engineering, pharmaceutics and food industry. I will briefly discuss a general modeling approach to estimate the fragmentation rate of small aggregates in three-dimensional turbulent flows, and then focus on a data-driven model that we recently developed. This is based on a neural network - which includes geometrical features of the aggregates-, that can be trained to predict if an aggregate breaks or not, once the turbulent velocity gradient statistics is known.

A Universal Relation Between Intermittency and Dissipation in Turbulence

F. Schmitt [1,2], J. Peinke [2] and M. Obligado [3]

[1] LEGI, Univ. Grenoble-Alpes, Grenoble, France
[2] Physics, Univ. Oldenburg, Oldenburg, Germany
[3] LMFL, Ecole Centrale de Lille, Lille, France

key-words: Fundamental turbulence, hot-wire anemometry, energy dissipation, intermittency

Abstract:

Turbulence is still one of the major unsolved problems in physics [1]. The most common approach is to define equations where factors or exponents are obtained by dimensional arguments and experiments. This is usually applied in the context of Kolmogorov's phenomenologies from 1941 (K41) [2] and 1962 (K62) [3]. The focus is often on the universality of these quantities, considering them, in most cases, within the framework of homogeneous isotropic turbulence (HIT). Among relevant parameters, the key constants describing turbulent flows are, arguably, the dissipation constant C_ε, the intermittency factor μ, the exponent of the power-law of the energy spectral density within the inertial range γ and the Kolmogorov constant C_k. For the energy cascade, C_ε is known to reflect its basic overall properties [4], while μ quantifies the emerging intermittency down the cascade [5]. While for C_ε there has recently been strong evidence that its value is not constant for a given flow within HIT [4], the other three quantities are still accepted to have a universal value for high Reynolds numbers Re in turbulence.
We experimentally explore the relationships between these four parameters for a wider class of turbulent flows using a large dataset (including planar and axisymmetric turbulent wakes, grid-generated turbulence and an axisymmetric jet) covering HIT and inhomogeneous turbulence. In all cases, 1D-hot-wire anemometry was used, which allowed us to resolve all scales of the flow.
We find that μ is inversely proportional to C_ε, providing a new empirical principle, which is independent of the Reynolds number: $\mu\, C_\varepsilon = \alpha =$ const. (see figures 1a) and 1b). This can also be viewed as two Π-parameters. In this sense, our result reads as $\mu\, C_\varepsilon = \Pi_1 \cdot \Pi_2 =$ const. $\neq f(Re)$. Moreover, their relation is transferred to γ and C_k (see figures 1c) and 1d), so that all four quantities present large variations with respect to the expected values for HIT within the K41 phenomenology. Hence, our results potentially define a new law for turbulent flows that seems to be valid for a wide range of boundary conditions.

References

[1] Frisch U. (1995), *Turbulence: the legacy of A. N. Kolmogorov*, Cambridge Univ. Press.

[2] Kolmogorov A. N. (1991), Local structure of turbulence, *Proc. Royal Soc. A, vol. 434*

[3] Kolmogorov A. N. (1962), Refinement of hypotheses on turbulence, *J. Fluid Mech., vol. 13*

[4] Vassilicos J. C. (2015), Dissipation in turbulent flows, *Annu. Rev. Fluid Mech., vol. 47*

[5] Arneodo A. et al. (1996), Structure functions in turbulence, *Europhys. Lett., vol. 34*

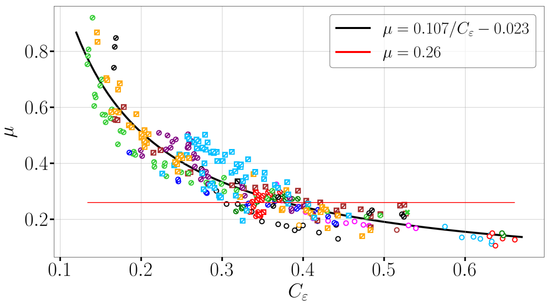

(a)

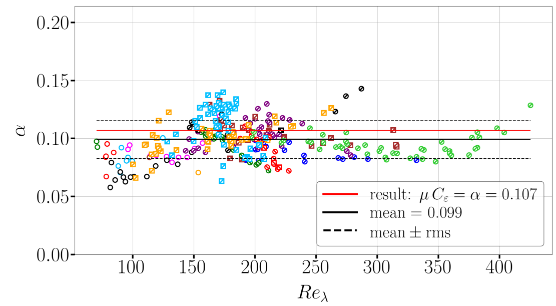

(b)

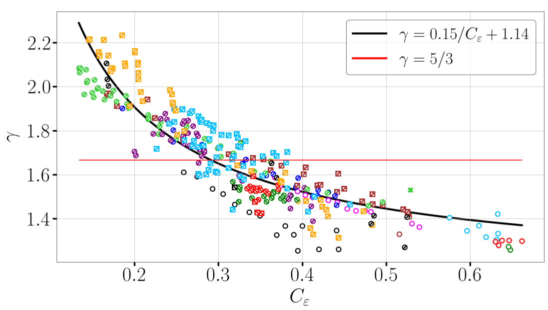

(c)

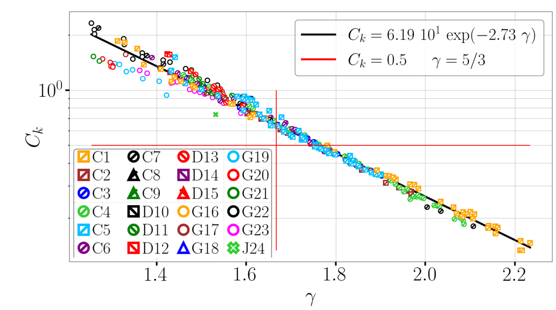

(d)

Figure 1: a) μ as a function of C_ε. The red line indicates a commonly accepted value for μ for homogeneous isotropic turbulence, and the black line corresponds to a least-square fit ($R^2 = 0.86$ with the fitted values of 0.1067 ± 0.0025 and 0.0227 ± 0.0091). b) α versus the Taylor-length based Reynolds number Re_λ. The red line indicates the result for α from the fit from a) while the black solid line represents the actual mean value of the ensemble of α values. Additionally, two black dashed lines indicate the corresponding standard deviations from the mean. c) γ as a function of C_ε and d) C_k versus γ. The red lines indicate both the commonly accepted value for C_k and γ for HIT, while the black lines correspond to a least-square fit for c) and d) with R^2 being 0.8 and 0.98, respectively. In general, the symbols in the legend in d) are identical for all four subfigures. For laminar inflow, squared markers are used. For the regular grid and the active grid, markers are shaped as circles and triangles, respectively. For cylinders as generators, the markers contains a "/" (case names start with "C") while for disks a "\" (case names start with "D") is used. Hollow circular markers means no object and is equivalent to grid turbulence (case names start with "G"). The "x" marker indicates a free jet (case names start with "J").

Spontaneous generation of helicity in anisotropic turbulence near the two-dimensional limit

S. Sukoriansky[1] and E. Barami[2]

[1] Department of Mechanical Engineering, Ben-Gurion University of the Negev, Beer Sheva, Israel
[2] SOREQ, Nuclear Research Center, Yavne, Israel

key-words: Helicity, Anisotropy, Symmetry breaking

Abstract:
Helicity can be spontaneously generated by strong rotation or injected into a flow either by boundary conditions or by adding a helical volume force to the system. W. Agoua et al. [1] have shown how helicity can be spontaneously created by symmetry breaking of an initially nonhelical system. They studied unstably stratified turbulence of electrically conducting fluid in the presence of a uniform density gradient and externally imposed vertical magnetic field. The field generates Lorentz force that acts as Joule dissipation in the direction of the field lines. When a sufficiently strong magnetic field is applied, the turbulence tends to become two-dimensional, three-component (2D3C). The generation of mean helicity takes place due to spontaneous symmetry breaking, when the flow is close to the 2D3C limit.

Can helicity be spontaneously generated in anisotropic, incompressible, homogenous turbulent flow of a constant density fluid? We conducted DNS [2] of a large-scale forced turbulence governed by 3D Navier-Stokes equation with the Lorentz force, which emulates Joule damping. In a strong magnetic field the turbulence attains a quasi-2D state with an enstrophy cascade inertial range of the normal flow components in the normal plane and a passive scalar inertial-convective range of the parallel component. Helicity in these runs remains zero. With increasing Reynolds number at constant magnetic field the enstrophy cascade becomes unstable and the power scaling in the normal plane changes from -3 to -7/3. The $k^{-7/3}$ spectrum is often associated with helicity cascade. Helicity is zero in pure 2D turbulence. However, near the 2D3C state the vorticity has a non-zero horizontal projection, which may cause helicity flux in the normal plane. We found that the flux of helicity Π_H is responsible for the observed spectrum, and the amplitude of the spectrum is proportional to $\Pi_H^{2/3}$.

Perpendicular and parallel helicity fluxes are shown in figure 1(a) . They have opposite signs and nearly compensate for one another in the total helicity flux. This result is not surprising, since the external forcing in our simulations does not inject helicity. Perpendicular and parallel helicity spectra are shown in figure 1(b). They are almost identical and seem to obey the $k^{-5/3}$ inertial range. The energy spectra compensated by $\Pi_H^{2/3} k^{-7/3}$ are shown in figure 1(c). They are nearly constant in the range of scales between forcing and dissipation. The enstrophy cascade is restored with an increasing magnetic field.

References

[1] Agoua W., Favier B., Delache A., Briard A. and Bos W. J. T., (2021), Spontaneous generation and reversal of helicity in anisotropic turbulence, *Phys. Rev. E,* 103, L061101 pp. 1-6.

[2] Sukoriansky S., Barami E., Feldman Y. and Zemach E., (2022), Anisotropization of quasistatic magnetohydrodynamic turbulence with an increasing magnetic field: Transition from three to two dimensions, *Phys. Rev. E*, 7, 074607, pp. 1-31.

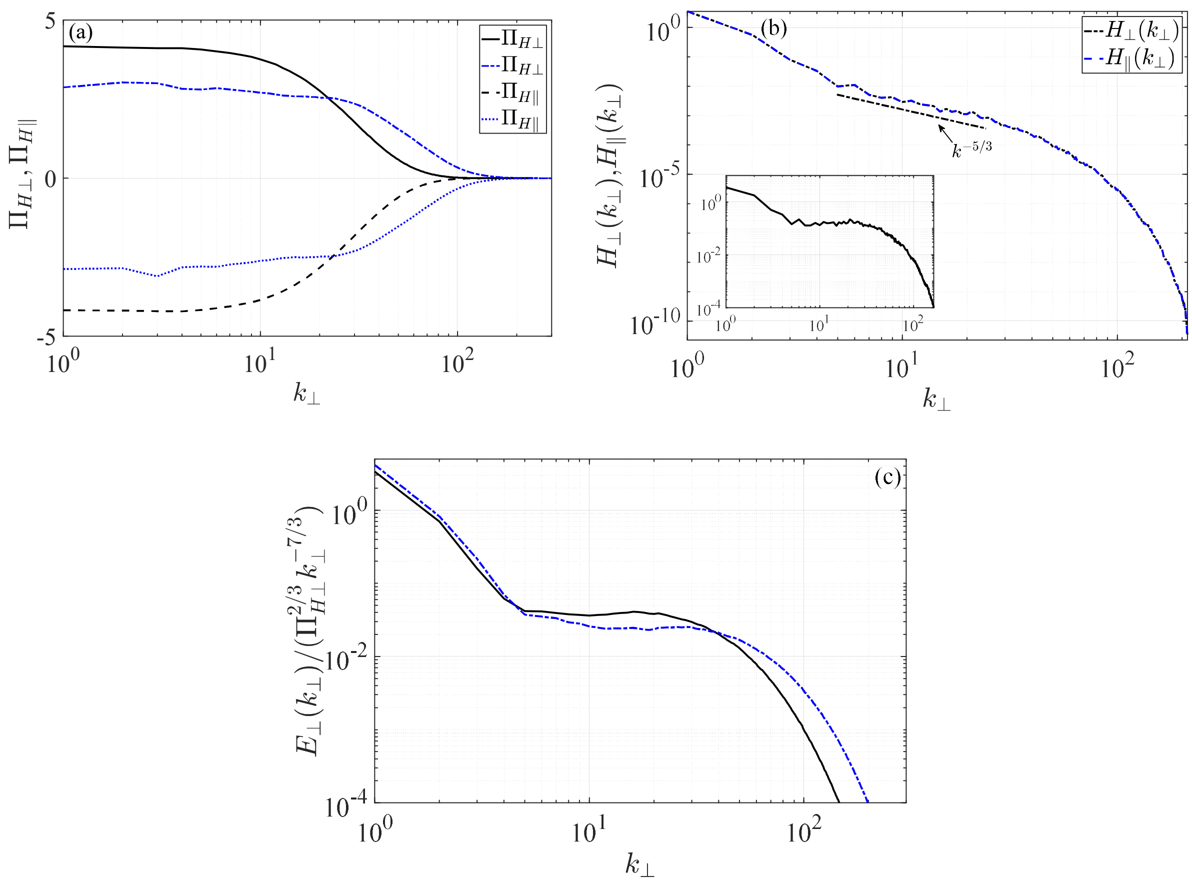

Figure 1: (a) *Perpendicular and parallel helicity fluxes,* (b) *helicity spectra* $H_\perp(k_\perp), H_\|(k_\perp)$ *and* (c) *compensated energy spectra for simulations with resolution* 512^3 *(solid and dashed black lines) and* 1024^3 *(dash-dotted and dotted blue lines). Details of simulations are given in reference* [2]. *Compensated spectrum* $H_\perp(k_\perp)/k_\perp^{-5/3}$ *is shown in the insert in* (b).

Near and far field development of the turbulent round jet derived from Galilean symmetry

Preben Buchhave[1] and Clara M. Velte[2]

[1] Intarsia Optics, Birkerød 3460, Denmark
[2] Dept. Civil and Mechanical Engineering, Technical University of Denmark, Kgs. Lyngby, Denmark

key-words: Galilean symmetry, Round turbulent jet, Evolving turbulence, Non-equilibrium turbulence

Abstract:
Based on the fundamental assumption of the existence of the Galilean Symmetry Group and a constant density Newtonian fluid, we have derived the average statistical properties of the free round turbulent jet. Using a small, recursive program that can conveniently run on a laptop and knowledge about the jet exit conditions, we can numerically predict the mean velocity profile all the way from the jet exit to beyond the self-similar region [1]. We can also predict the jet spreading angle, entrainment and transverse velocity component and we can show the influence of Reynolds number and turbulent dynamic viscosity on the jet properties.

From the knowledge gained from the recursive program, or simply physical reasoning, we can derive the equation that governs the current problem (*r* being the radial coordinate, *t* time, *u* the streamwise average velocity and ν the kinematic viscosity),

$$\frac{\partial u(r,t)}{\partial t} = \nu\left(\frac{1}{r}\frac{\partial u(r,t)}{\partial r} - \frac{\partial^2 u(r,t)}{\partial r^2}\right) \tag{1}$$

from which we have derived an analytical solution to the mean velocity profile. The above equation describes the diffusion of momentum, similarly to the heat conduction equation describing the diffusion of heat. As is common for such solutions, an error function-based description is expected and indeed found. The equation is similar to those presented and applied by [2] and [3], with the distinction that our equation describes the temporal development using a control volume in the form of a thin disc normal to the jet axis development, see Figure 1. The control volume analysis describes the momentum diffusion due to internal shear forces. In contrast, the equation of [2] uses a simplified boundary layer equation as a starting point, making it valid for the self-similar region only. Our equation covers both the developing turbulent flow as well as the flow in the self-similar region, unlike the solutions in [2] and [3].

To cover both the region very close to the jet exit, the intermediate developing region and the far self-similar region, we have made careful measurements on three jets of different sizes with highly similar jet exit conditions: 10 mm, 50 mm and 100 mm diameter by means of hot-wire and laser anemometry. We find excellent agreement between measurements and theory, as well as the numerical results, see Figure 2.

In addition to confirming some of the well-known properties of the jet in the far field, our small computer program also shows how the jet develops from the initial non-isotropic flow field and arrives at the equilibrium, self-similar state. The program also illustrates the importance of the initial turbulent structure and the value of the turbulent kinetic viscosity on the far field spreading angle of the jet. The results also confirm that the mean properties of the jet are rather independent of the jet Reynolds number.

Our investigation illustrates how basic properties of space and time asserts a profound influence on how "free flows" develop from their initial form and eventually assumes their final equilibrium state.

References

[1] Buchhave, P. and Velte, C. M., (2022), A similarity scaling model for the axisymmetric turbulent jet based on first principles, Physics of Fluids, vol. 34, no. 9, http://dx.doi.org/10.1063/5.0102809
[2] Pope, Stephen B., (2000): Turbulent Flows, Cambridge University Press.
[3] Schlichting, von H., (1933), Laminare Strahlausbreitung, ZAMM-Journal of Applied Mathematics and Mechanics / Zeitschrift für Angewandte Mathematik und Mechanik, vol. 13, pp. 260-263

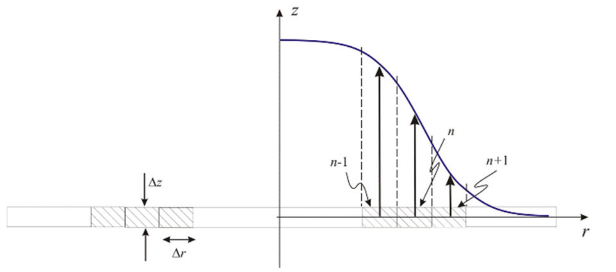

Figure 1: Mean velocity profile and ring-shaped control volume elements.

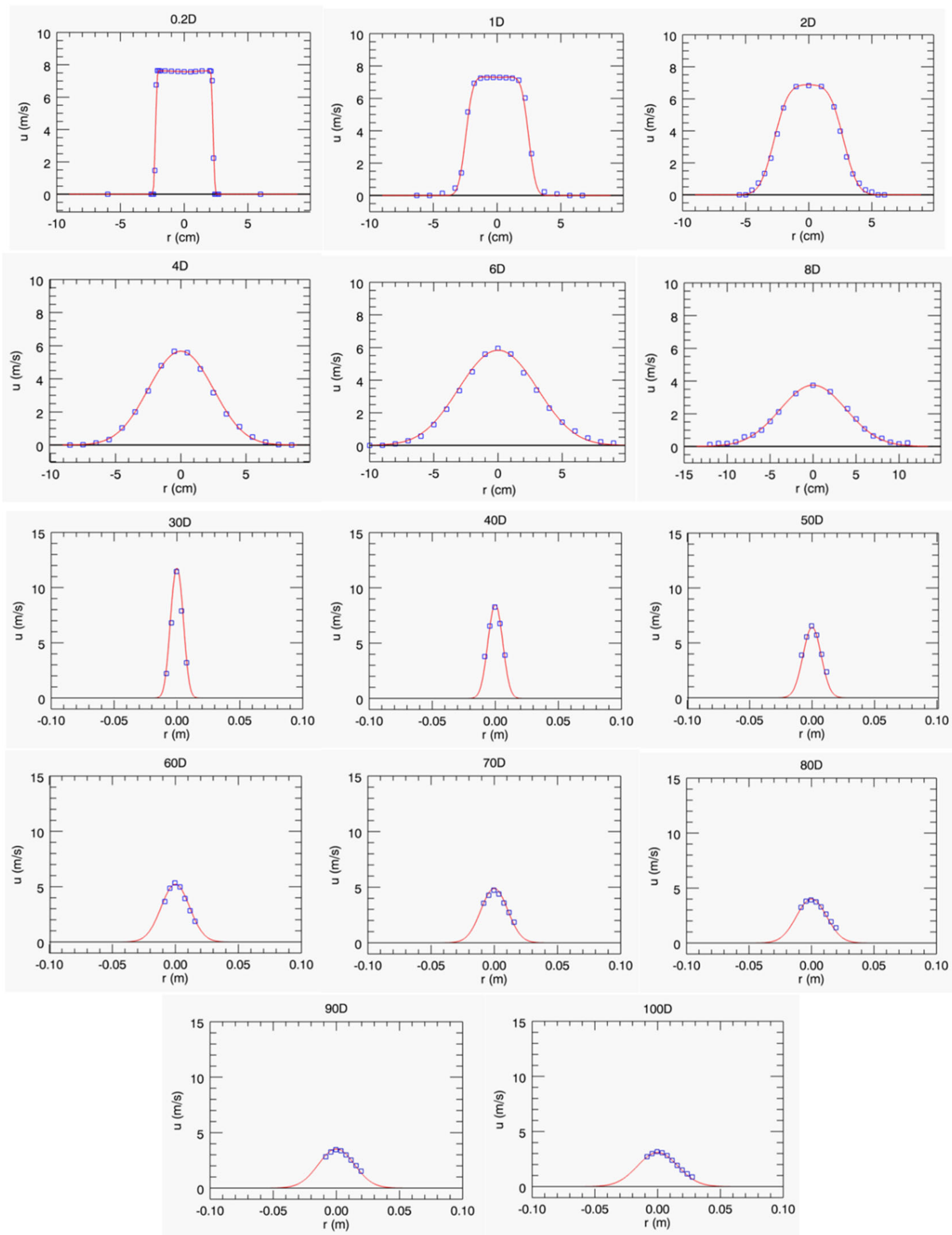

Figure 2: Average streamwise velocity profiles for downstream positions z/D = [0.2 - 100]. The blue squares represent LDA measurement results, the red and blue lines (perfectly overlapping) represent the analytical and numerical results, respectively.

Amplitude Modulation in Restricted Nonlinear Turbulence

Bianca Viggiano[1], Benjamin Minnick[2], and Dennice F. Gayme[3]

[1] Department of Mechanical Engineering, Polytechnique Montréal, Montréal, Québec, Canada
[2] Naval Surface Warfare Center Carderock Division, West Bethesda, MD, USA
[3] Mechanical Engineering Department, Johns Hopkins University, Baltimore, MD, USA

key-words: Wall-bounded turbulence, reduced-order modeling, amplitude modulation

Abstract:
The study of scale interactions has critically advanced understanding of the dynamical significance of coherent structures and their interactions in wall-bounded turbulent flows, see e.g., [1] and references therein. Evidence suggesting the modulation of small-scale velocity fluctuations imparted by large-scale fluctuations, in particular, has inspired the development of predictive models to readily provide useful statistics [2]. The importance of these interactions is underscored in literature demonstrating connections between such large/small-scale interactions to the widely studied attached eddy model [3]. The utility of the amplitude modulation for predicting statistical features and continuing discoveries exploiting these ideas motivates additional analysis of the critical mechanisms at play.

In this work we employ the recently proposed augmented restricted nonlinear (ARNL) modeling paradigm [4], whose decomposition of the flow into large scales coupled with dynamically restricted small scales provides a natural setting to investigate scale interactions. The large scale comprises the streamwise-averaged mean component in the RNL model augmented by a limited number of intermediate scale modes that are permitted to interact nonlinearly. This large scale is dynamically coupled with a limited set of small-scale streamwise varying modes whose nonlinear interactions are restricted to those contributing to the mean and the limited intermediate scale modes. The intermediate modes augmenting the large scale is on the order of the half-channel height, δ, while the small scales correspond to dissipative scales typically included in the RNL model. This ARNL model has been shown to provide more accurate predictions of low-order statistics than RNL models as the Reynolds number increases [4].

An ARNL channel flow at friction Reynolds numbers, $\mathrm{Re}_\tau = 550, 1000$ and 2000 is simulated using a modified version of the pseudo-spectral solver lesgo.jhu.me.edu. Figure 1 presents the resulting instantaneous velocity fluctuations at two different wall normal locations for $\mathrm{Re}_\tau = 550$. The snapshots demonstrate the influence of the streamwise varying intermediate mode, which allows the model to more accurately predict outer-layer dynamics [4], although the resulting flow is notably different than true multi-scale turbulence. To quantify the contributions of the small scale energy on the large scales, we employ a Hilbert transformation of the signals [5]. The small and large scale signal at $y^+ \approx 5$ and the filtered envelope are provided in figure 2. Here we note the trends present near the wall are well described by the filtered envelope, where large fluctuations of u_S^+ correlate often to a positive value for the envelope. These results suggest the ARNL model's ability to capture amplitude modulation and point to the utility of this framework in further evaluating key scale interactions.

References

[1] B.J. McKeon, (2017). The engine behind (wall) turbulence: perspectives on scale interactions. J. of Fluid Mech., 817, P1.

[2] I. Marusic, R. Mathis, and N. Hutchins, (2010): Predictive model for wall-bounded turbulent flow. Science 329(5988):193-6.

[3] C. Cheng and L. Fu, (2022): Consistency between the attached-eddy model and the inner–outer interaction model: a study of streamwise wall-shear stress fluctuations in a turbulent channel flow. J. Fluid Mech. 942:R9.

[4] B.A. Minnick, B. Viggiano and D.F. Gayme, (2023): Augmented Restricted Nonlinear (ARNL) Model for High Reynolds Number Wall-Turbulence Progress in Turbulence X: Proc. iTi Conf. on Turbulence

[5] W.J. Baars, N. Hutchines, and I. Marusic, (2017): Reynolds number trend of hierarchies and scale interactions in turbulent boundary layers, Phil. Trans. R. Soc. A 375: 20160077.

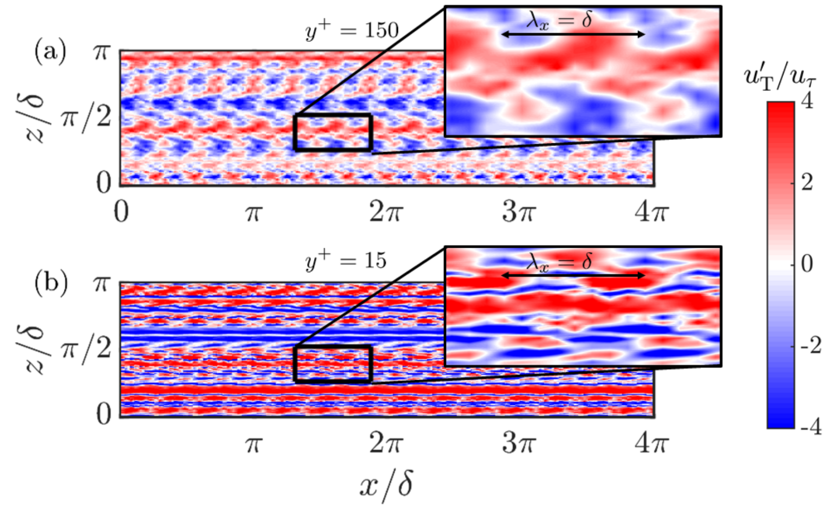

Figure 1: Instantaneous total streamwise velocity time-fluctuations from the ARNL model at $\mathrm{Re}_\tau = 550$ at wall-normal planes (a) $y^+ = 150$, and (b) $y^+ = 15$. Full spanwise extent, $L_z = 2\pi\delta$ not shown.

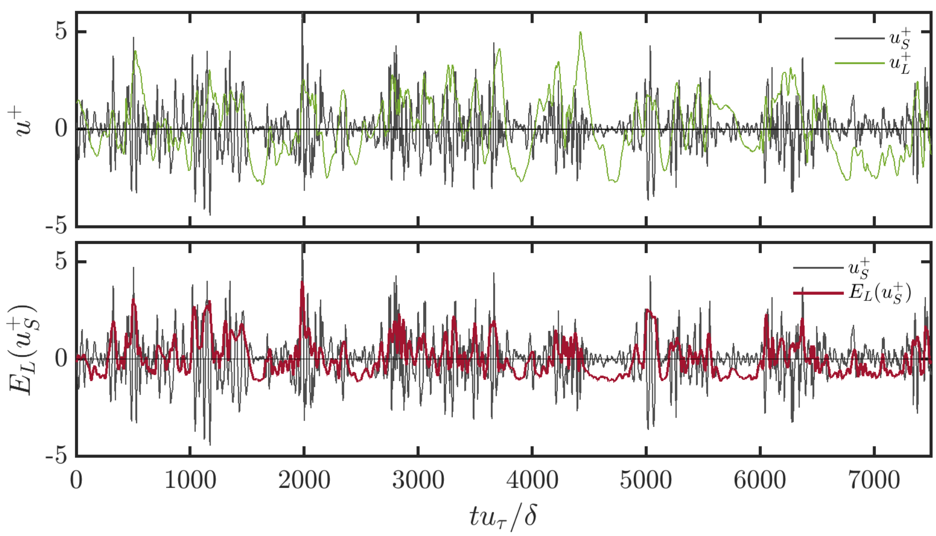

Figure 2: Decomposition of fluctuating signal into the small scale signal u_S^+, the large scale, u_L^+, and the filtered envelope $E_L(u_s^+)$.

Turbulent/turbulent entrainment in a planar wake

Oliver R.H. Buxton[1], and Jiangang Chen[2]

[1] Department of Aeronautics, Imperial College London, London, U.K.
[2] School of Aeronautics, Northwestern Polytechnical University, Xi'an, P.R. China

key-words: Entrainment, Experiments

Abstract:
Turbulent flows are typically separated from their backgrounds by a sharp, and well-defined interface. The rate at which turbulent flows expand is governed by the physics within these interfaces since they control the rate at which fluid is transported across the turbulent interface and subsequently mixed into the primary turbulent flow in processes that are collectively known as entrainment. The special case in which the background is irrotational, and hence the interface demarcating the primary turbulent flow from the background is a turbulent/non-turbulent interface (TNTI), has been extensively studied [1]. However the more general situation is one in which the primary turbulent flow is adjacent to a background that is itself turbulent, yet the study of turbulent/turbulent interfaces (TTIs) is far less advanced than that of TNTIs. Only recently have they been definitively shown to exist even in scenarios in which the turbulence intensity is comparable between the primary flow and the background [2], and their governing physics revealed [3] - a dominance of inertial vorticity stretching and a vanishingly small role for viscous diffusion.

In this abstract we examine how the fundamentally different physics of TTIs affect the entrainment fluxes of mass, momentum, and kinetic energy in a spatially developing planar turbulent wake produced by a circular cylinder of diameter d. Combined PIV and PLIF experiments are conducted in a hydrodynamics flume as depicted in figure 1a. Fluorescent dye (rhodamine 6G) is released into the wake of the cylinder mounted downstream of a turbulence-generating grid. Previous work has shown that the dye faithfully marks the extent of the wake when no grid is placed upstream such that the TNTI as defined by setting a threshold on the modulus of the gradient of the PLIF signal $|\nabla \phi|$ and the out-of-plane component of vorticity magnitude ω_z^2 coincide with one another. By varying the type of grid (fractal or regular) and the grid - cylinder spacing the cylinder is exposed to different "flavours" of freestream turbulence (FST) as characterised by the turbulence intensity/integral length scale $\{k^{1/2}/U_\infty, \mathcal{L}\}$ (see figure 1c). High-resolution experiments are conducted to measure the entrainment velocities/fluxes at five different measurement stations centred on streamwise locations $x/d = \{6.5, 10, 20, 30, 40\}$ to enable observation of the spatial evolution of the entrainment.

We now present sample results. Figure 2 shows the spatial evolution of the mean entrainment velocity, presented as both a function of the turbulence intensity of the FST and x. It can be seen that in the near wake the presence of FST can slightly enhance the mean entrainment velocity $\overline{v}_e$, whereas in the far wake there is a significant decrease in $\overline{v}_e$. Further, it is observed that for all FST flavours $\overline{v}_e$ decreases monotonically with x; an explanation for which is illustrated in figure 2b showing that in the far wake $\overline{v}_e$ seems to be asmymptoting towards scaling with the local Kolmogorov velocity scale u_η, which is observed to decrease with x. The importance of the local vorticity field in the vicinity of the TTI towards affecting the local entrainment velocity can be inferred from figure 3. When the mean enstrophy, conditioned on distance normal from the interface ξ_n, is further conditioned on the local entrainment velocity it can be seen that strong entrainment is accompanied by a steeper vorticity jump (and overshoot) whereas this is much less severe for cases conditioned on weak entrainment/detrainment; both for TNTIs and TTIs. The final presentation will offer explanations for these findings and further consider entrainment fluxes, whose behaviour are subtly different from just the entrainment velocities themselves.

References

[1] da Silva, C. B., Hunt, J. C. R., Eames, I., and Westerweel, J. (2014). Interfacial layers between regions of different turbulence intensity. *Annual Review of Fluid Mechanics*, 46(1):567–590.

[2] Kankanwadi, K. S. and Buxton, O. R. H. (2020). Turbulent entrainment into a cylinder wake from a turbulent background. *Journal of Fluid Mechanics*, 905:A35.

[3] Kankanwadi, K. S. and Buxton, O. R. H. (2022). On the physical nature of the turbulent/turbulent interface. *Journal of Fluid Mechanics*, 942:A31.

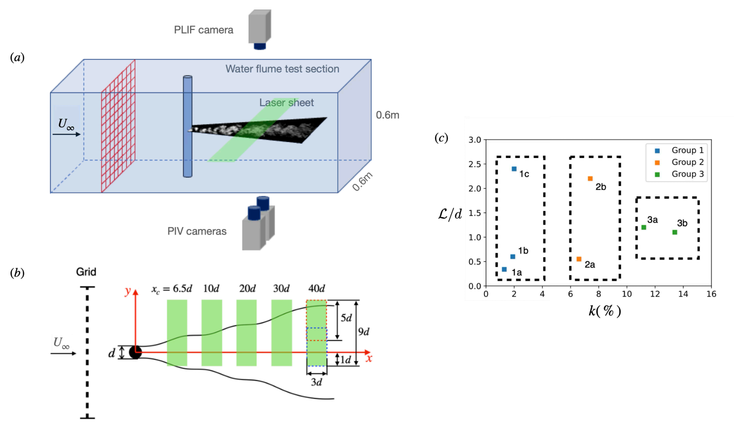

Figure 1: *(a) Experimental schematic, (b) location of PIV measurement stations, and (c) parameter space for various "'flavours" (cases) of FST studied.*

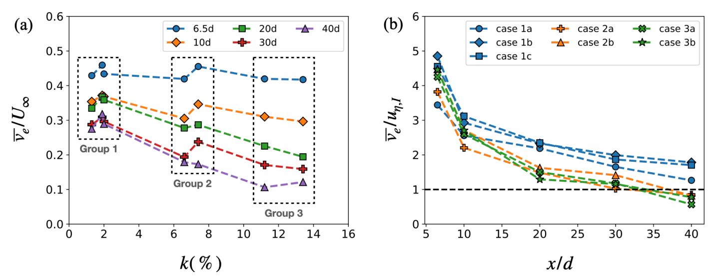

Figure 2: *Evolution of the entrainment velocity spatially and with difference cases of FST. (a) normalised by the invariant U_∞, (b) normalised by the local Kolmogorov velocity scale.*

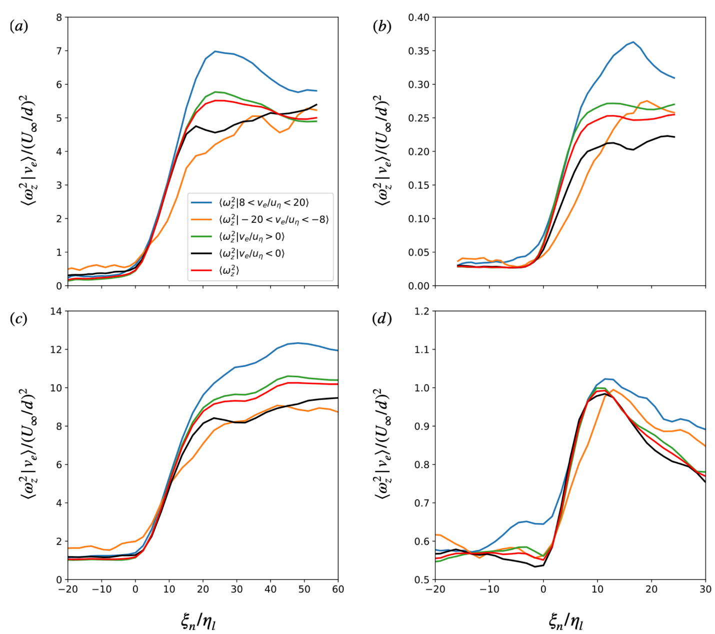

Figure 3: *Conditionally averaged enstrophy conditioned on different entrainment velocity ranges. (a) TNTI at $x/d = 6.5$, (b) TNTI at $x/d = 40$, (c) case 3b TTI at $x/d = 6.5$, and (d) case 3b TTI at $x/d = 40$.*

Coherent structures in the turbulent near-wake of a flapping wing

Y. Goodwin [1], G. Rigas [1] and J. F. Morrison [1]

[1] Department of Aeronautics, Imperial College London, United Kingdom

key-words: Shear Layer, Flapping Flight, Turbulent Wakes, Leading Edge Vortex

Abstract:

Leading edge vortex (LEV) generation promotes high transient lift across a wide range of unsteady flight conditions in nature [1]. A key regime is large vertebrate forward flight, in which Reynolds numbers can range from 10^3–10^5 while still sustaining LEVs for weight support and maneuvering [2]. The Rossby number Ro, a measure of the ratio of Coriolis to inertial accelerations along the wing, dictates the stability and attachment of the LEV [3].

In order to model this parameter space, we use a 6-axis articulated robotic arm (shown in Figure 1b) to actuate a flat plate of aspect ratio 2.17 in a closed-loop recirculating wind tunnel. The robot produces a canonical figure-of-8 stroke path where the angle of attack is varied from $-30^\circ \leq \alpha \leq 30^\circ$ continuously, and where the radius of revolution R is varied to produce $Ro = 12.8$ to infinity (where the plate moves in pure translation), an approach seen in [3], resulting in LEVs of varying stability. The Reynolds number is fixed at $Re = 15,000$, a transitional turbulent regime for this flow, such that the LEV is burst and incoherent. Stereo particle image velocimetry (PIV) datasets have been collected to capture the vorticity of the two extreme cases. We seek to understand how Ro affects the structure of the shear layer during formation, LEV bursting, and the subsequent turbulent wake shed from the plate. To identify coherent structures in these flowfields, proper orthogonal decomposition (POD) [4] and spectral POD (SPOD) [5] are used to characterise large-timescale and small-timescale structures respectively, some results of which are shown in Figure 2. The LEV formation cycle is identified as the dominant mode for the POD analysis during the upstroke phase, in agreement with existing literature. We further find through the SPOD analysis that the shear layer exhibits a range of high-frequency instabilities across the baseline (no flapping) and flapping cases, triggering small-scale vortex roll-up which is then fed into the forming LEV. However, this instability is less coherent for the $Ro = \infty$ and hence low LEV stability case. Further experiments are planned with longer acquisition times in order to provide further insight into this behaviour.

References

[1] Ellington CP, van den Berg C, Willmott AP, Thomas ALR. Leading-edge vortices in insect flight. Nature. 1996;384(6610):626-30.

[2] Muijres FT, Christoffer Johansson L, Winter Y, Hedenström A. Leading edge vortices in lesser long-nosed bats occurring at slow but not fast flight speeds. Bioinspiration & Biomimetics. 2014;9(2):025006.

[3] Lentink D, Dickinson MH. Rotational accelerations stabilize leading edge vortices on revolving fly wings. Journal of Experimental Biology. 2009 08;212(16):2705-19.

[4] Lumley JL. Stochastic tools in turbulence. New York: Academic Press; 1970.

[5] Towne A, Schmidt OT, Colonius T. Spectral proper orthogonal decomposition and its relationship to dynamic mode decomposition and resolvent analysis. Journal of Fluid Mechanics. 2018;847:821-67.

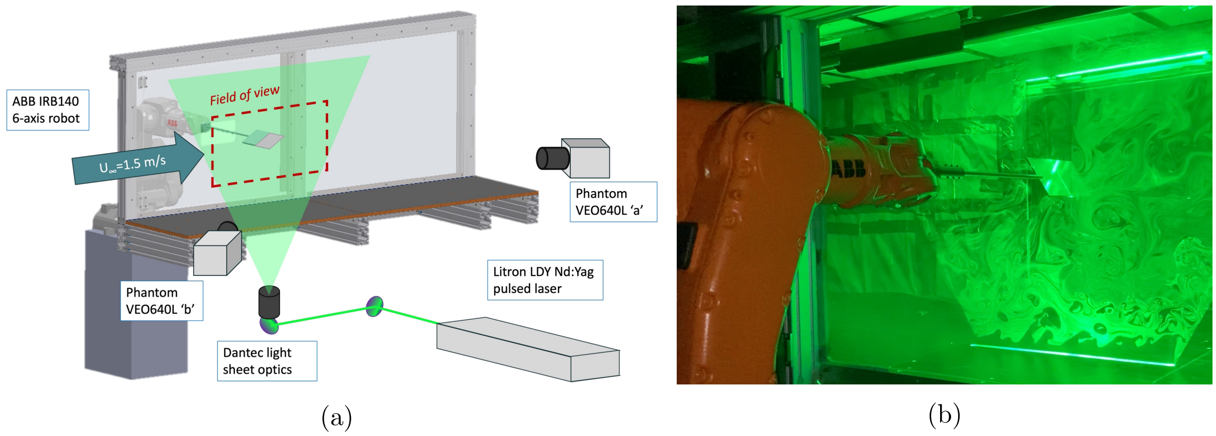

(a) (b)

Figure 1: (a) The experimental set-up for stereo-PIV, as shown via a stream-wise cross-section of the wind tunnel. (b) The robot arm with a Perspex plate mounted on the flange, performing a flapping procedure through the laser sheet with seeding.

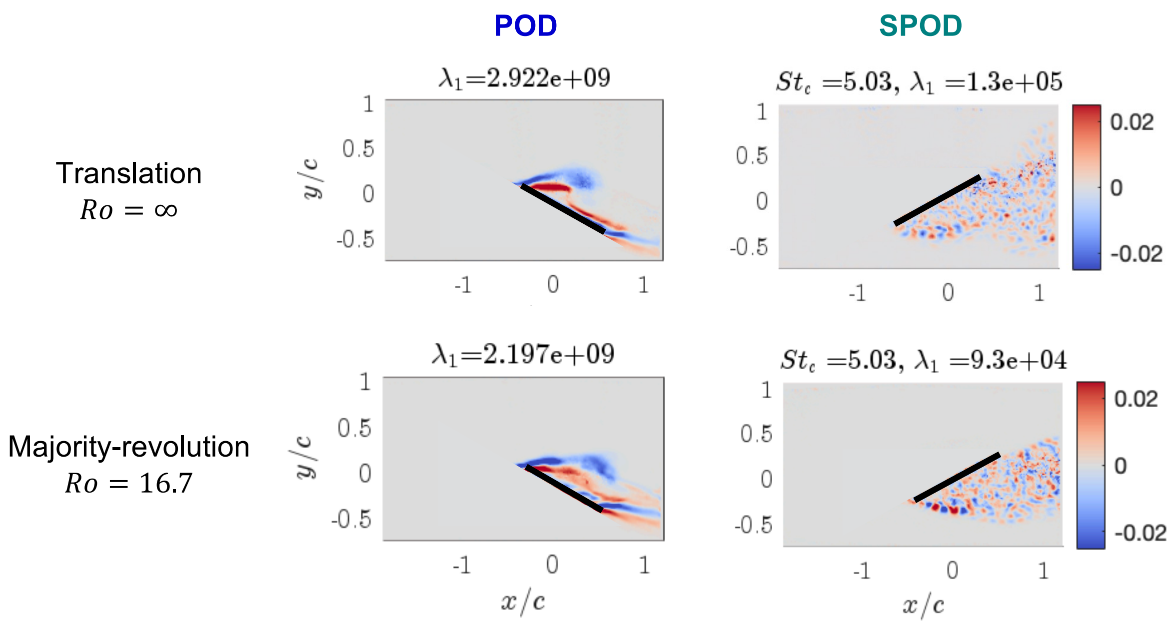

Figure 2: A comparison of the POD and SPOD results for two phases of the flapping procedures. The highest energy POD mode of the vorticity during the upstroke clearly shows the LEV formation stages across the two cases. The SPOD modes after the LEV sheds during the backstroke show stronger coherence and containment of high chord-based Strouhal number structures in the shear layer of the lower Ro case.

Turbulent wake resonance via oscillation of a solid plate

G. Xiangyu[1], and K. Steiros[1]

[1] Department of Aeronautics, Imperial College London, London, UK

key-words: Turbulent wake, vortex shedding, fluid-structure interaction

Abstract:
It has long been appreciated that the periodic forcing of a bluff body wake can induce significant alterations to both the large-scale (vortex shedding) structures that are emanating from the body and to the mean-flow wake topology. These effects are greatly accentuated at particular forcing frequencies which induce ‘flow-resonance’: For instance, the experiments of Tokumaru and Dimotakis [1] demonstrated that when a cylinder, exposed to a uniform stream, undergoes a forced rotary oscillation with a frequency equal to the natural vortex shedding one, a sharp decrease in body-drag can be observed, accompanied by a transformation of the momentum-deficit profile downstream of the cylinder (typical of wakes) into a momentum-excess profile (typical of jets). Unfortunately, the physics of this remarkable ‘flow-resonance’ phenomenon remain obscure. The aim of this work is to answer the following two questions. Firstly, is the above wake-jet transition exclusive to rotating cylinders, or can it be found in other types of oscillatory movements which are relevant to offshore floating structures, e.g., dynamic tilting of bluff bodies? Secondly (and more importantly), what is the cause of this phenomenon – in particular, can it be linked to the formation of near wake vortical structures?

To answer the above questions we conducted an extensive series of wind tunnel measurements of the turbulent wake of an oscillating solid disk. The disk was attached to a robotic arm (see figure 1) and in that way it could be dynamically pitched at various frequencies and amplitudes. Our experiments tested a parameter space that spanned (angular) amplitudes of 5, 10 and 20 degrees disk oscillation and six Strouhal numbers (characteristic oscillation frequencies) ranging from 0.047 to 0.23. In all cases the tunnel velocity was set to 2.95m/s, leading to a fully turbulent Reynolds number of 39000. Two ‘baseline’ cases were also tested: that of a steady disk wake, and that of the flow past an oscillating airfoil. The measurements were comprised of high-speed Particle Image Velocimetry at various downstream streamwise planes.

Our key-findings can be summarized as follows. First, the oscillatory titling of the disk performed at a frequency very close to that of the natural vortex shedding, produced downstream mean velocity profiles which resembled a jet (see figure 2), i.e., flow resonance was indeed observed. This jet flow started appearing approximately 5 disk diameters downstream of the body. Second, the cause of this phenomenon was found to be linked to the formation of a ‘reverse Karman street’, i.e., a vortex street which is identical to the regular Karman one, except from the fact that the vortices rotate in the opposite direction (see figure 3). Such ‘reverse’ Karman streets are known to exist in the wake of oscillating airfoils [2], but have not been hitherto observed in the wake of bluff bodies. The presentation will discuss in detail the above flow physics, and how they differ from the ‘off-resonance’ conditions.

References

[1] Tokumaru, P.T. and Dimotakis, P.E. (1991), Rotary oscillation control of a cylinder wake, Journal of Fluid Mechanics, 224, pp. 77–90.
[2] Koochesfahani, M.M. (1989), Vortical patterns in the wake of an oscillating airfoil, AIAA Journal, 27(9), pp. 1200–1205.

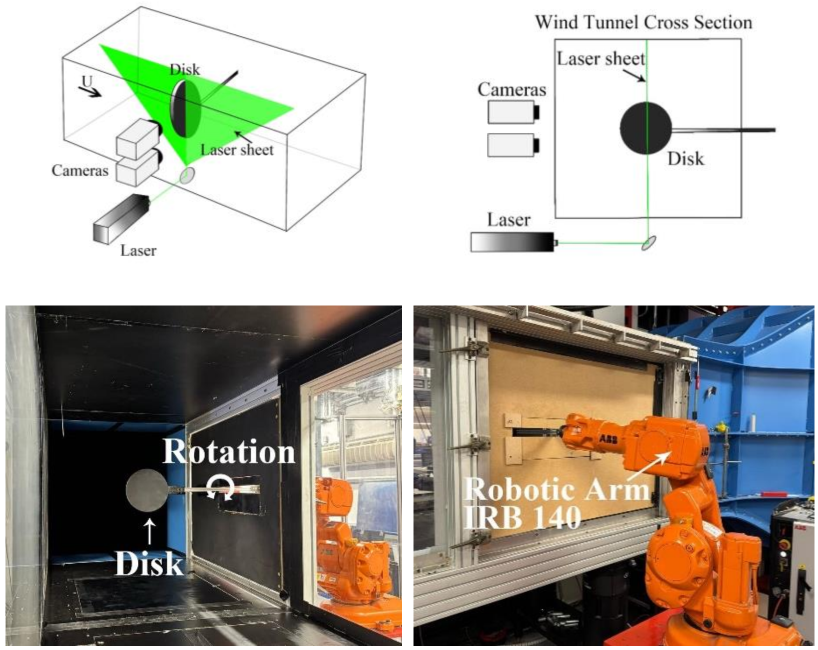

Figure 1: *Experiment setup*

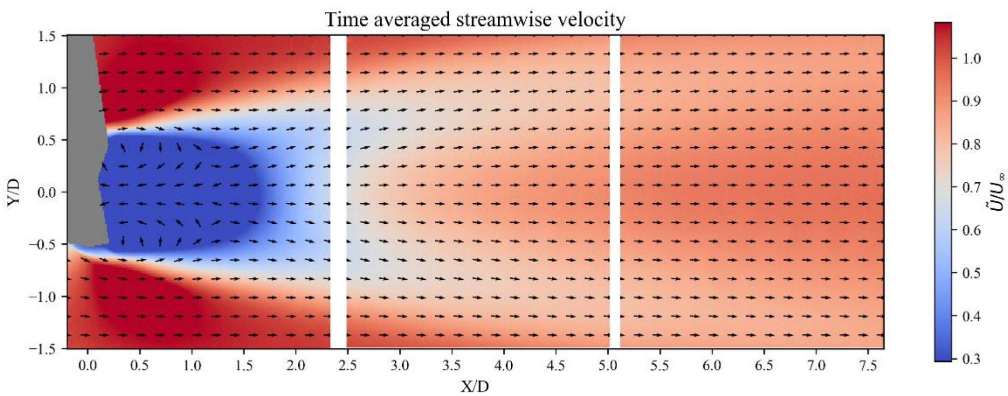

Figure 2: *Time-averaged streamwise velocity, normalized with the free stream velocity for the St = 0.186 and amplitude 20 degrees case. The arrows show the time-averaged velocity vectors.*

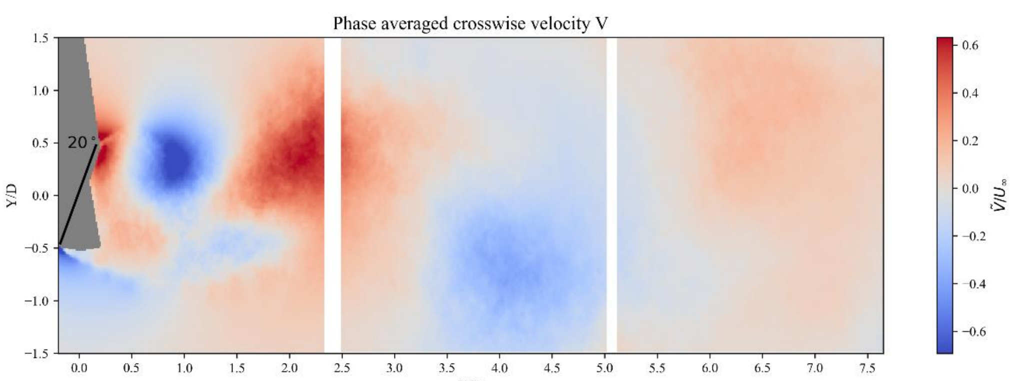

Figure 3: *Phase averaged crosswise velocity (at phase 20 degrees), normalized with the free stream velocity for the St = 0.186 and amplitude 20 degrees case. The alteration of velocity magnitude indicates the existence of a vortex street whose sense is opposite to the regular von-Karman one.*

A CFD Flow Control Study Using Plasma Actuation on the Leading Edge of a Bluff Body

Guglielmo Minelli [1], Rithvik Magal [1], Gabriele Bellani [1]

[1] Department of Industrial Engineering, Alma Mater Studiorum - Università di Bologna, I-47100 Forlì, Italy

key-words: CFD, LES, Flow-Control, Bluff body, wakes, plasma

Abstract:
The control of bluff-body wakes for reduced drag and enhanced stability has traditionally relied on the so-called direct-wake control approach, [1, 2, 3]. By the use of actuators or passive devices, one can manipulate the aerodynamic loads that act on the rear of the model. An alternative approach for the manipulation of the flow is to move the position of the actuator upstream, hence interacting with an easier-to-manipulate boundary layer. The present study will focus on a bluff-body flow solved via large-eddy simulations (LES) to investigate the effectiveness of an upstream plasma actuator (positioned at the leading edge) with regard to the manipulation of the wake dynamics and its aerodynamic loads. A rectangular cylinder with rounded leading edges, equipped with actuators positioned at the front curvatures, will be simulated at Re=40 000. Previous work [4] has shown that, by using a blowing and suction technique, super-harmonic frequencies of the natural vortex shedding is an effective way to tune the control device. In addition, the induced disturbances, penetrating downstream into the wake, significantly reduce drag and lateral instability, Fig. 1. This first study showed the potential of such a control, and in the present work a plasma actuation is implemented numerically, tested and its effect is compared with previous results.

References

[1] H. Choi, W. Jeon, and J. Kim, "Control of flow over a bluff body," *Annual Review of Fluid Mechanics*, vol. 40, pp. 113–139, 2008.

[2] R. Li, B. R. Noack, L. Cordier, J. Borée, and F. Harambat, "Drag reduction of a car model by linear genetic programming control," *Experiments in Fluids*, vol. 58, pp. 1–20, 2017.

[3] Y. Li, W. Cui, Q. Jia, Q. Li, Z. Yang, M. Morzyński, and B. R. Noack, "Explorative gradient method for active drag reduction of the fluidic pinball and slanted ahmed body," 2019.

[4] G. Minelli, T. Dong, B. Noack, and S. Krajnović, "Upstream actuation for bluff-body wake control driven by a genetically inspired optimization," *Journal of Fluid Mechanics*, vol. 893, 2020.

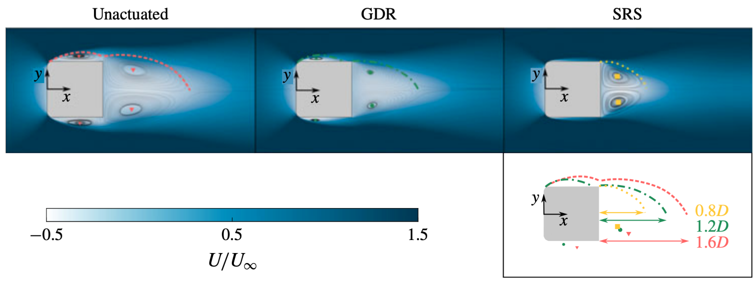

Figure 1: Comparison of the actuated wake topology: (red) unactuated case; (green) optimized actuated (GDR) case; (yellow) non optimized actuated (SRS) case, [4].

Turbulence: statistical approach versus coherent structures

J. Peinke[1]

[1]Institute for Physics, Carl-von-Ossietzky University, Oldenburg, Germany

The challenge of turbulence stems from its complexity. Taking different approaches to turbulence has led to the development of different schools of thought. On the one hand, the high degree of disorder obviously leads to a statistical approach. On the other hand, turbulent flows inspire one to see structures. This contribution presents a statistical, joint-multipoint characterisation of turbulence using a Fokker–Planck equation. The Fokker–Planck equation framework enables the application of concepts of non-equilibrium thermodynamics, such as the determination of entropy for each flow structure. According to fluctuation theorems, positive and negative entropy must be balanced mathematically. Interestingly, negative entropy events are linked to extreme velocity gradients, opening the possibility of defining coherent structures in a turbulent field using negative entropy values. In this approach, these structures are statistically entangled with the unstructured part of the field via the fluctuation theorem.

Entrainment and small-scale features in merging turbulent regions

Francisco A. Branco [1], Carlos B. da Silva [1]

[1] LAETA/IDMEC/Instituto Superior Técnico, Universidade de Lisboa, Lisboa, Portugal

key-words: Turbulent/Non-turbulent Interface, Shear-free Turbulent Merging

Abstract:

When turbulent flows develop within a non-turbulent environment, they are separated by a sharp and highly contorted boundary known as the turbulent/non-turbulent interface (TNTI) [1]. The flow dynamics at this region governs the fluxes of mass, momentum, and kinetic energy, that are fundamental to understand in detail the mechanisms by which turbulent regions grow in non-turbulent backgrounds.

In the present work, we investigate the small-scale characteristics of the turbulent/non-turbulent interface (TNTI) and of the turbulent entrainment using direct numerical simulations (DNS) in a novel flow configuration. In this setup, two turbulent fronts develop spatially separated by a non-turbulent background, without mean shear. A realistic inlet condition is implemented here, where planes of velocity fluctuations from homogeneous isotropic turbulence (HIT) simulations, computed with spectral accuracy using a separated temporal DNS code, are spatially advected. The non-turbulent region is generated by convolving these velocity fluctuations with a smoothing hyperbolic tangent profile, effectively eliminating velocity fluctuations in the inner region. A passive scalar is injected at this region, allowing to trace the non-turbulent flow. An example of the resulting flowfield is shown in Figure 1.

The two initially separated turbulent regions grow by entraining irrotational fluid, and eventually merge. At the merging point, turbulent kinetic energy, energy dissipation rate, and scalar mixing attain their maxima. The analysis of turbulent kinetic energy budgets ascertains turbulent transport to be the most significant source of turbulence in the non-turbulent core. Therefore, the TNTI develops in a substantially different configuration than in commonly analysed flows, such as jets or wakes, since the non-turbulent region is irrotational, but has non-negligible kinetic energy and energy dissipation rate. At the turbulent side of the TNTI, conditional enstrophy and the respective budgets collapse for the different streamwise positions analysed, once normalised by the local Kolmogorov micro-scales [2]. The exception are the enstrophy peaks that decrease along the streamwise direction (see Figures 2 and 3 – colour ranges from black to light grey, as the merging point is approached and sections downstream of the merging point are represented in fading red).

The local entrainment velocity, calculated from the enstrophy budgets at each point of the TNTI, following [3], is distributed in a non-Gaussian manner (Figure 4) and its average value, $\langle v_e \rangle \approx 0.1 - 0.2 u_\eta$, is found to be roughly independent of the streamwise location. However, extreme detrainment events, i.e., positive high values of v_e, are found to be less frequent for sections downstream, suggesting considerable changes in the geometry of the irrotational boundary as merging occurs.

It is stressed that the understanding of mutual interactions between merging turbulent fronts and their impact on small-scale motions and entrainment is particularly important in engineering contexts such as the merging wakes of turbines in wind farms, the development of boundary layers of consecutive blades in turbomachinery, and reacting flows in non-premixed conditions.

References

[1] da Silva C. B., Hunt J. C. R., Eames I. and Westerwell J., (2014), Interfacial layers between regions of different turbulence intensity, *Annual Review of Fluid Mechanics, vol. 46, pp. 567-590*

[2] Zecchetto M., da Silva C. B., (2021), Universality of small-scale motions within the turbulent/non-turbulent interface layer, *Journal of Fluid Mechanics, vol. 916, pp. A9*

[3] Wolf M., Lüthi B., Holzner M., Krug D., W. Kinzelbach W., Tsinober A., (2012), Investigations on the local entrainment velocity in a turbulent jet, *Physics of Fluids, vol. 24, pp. 105110*

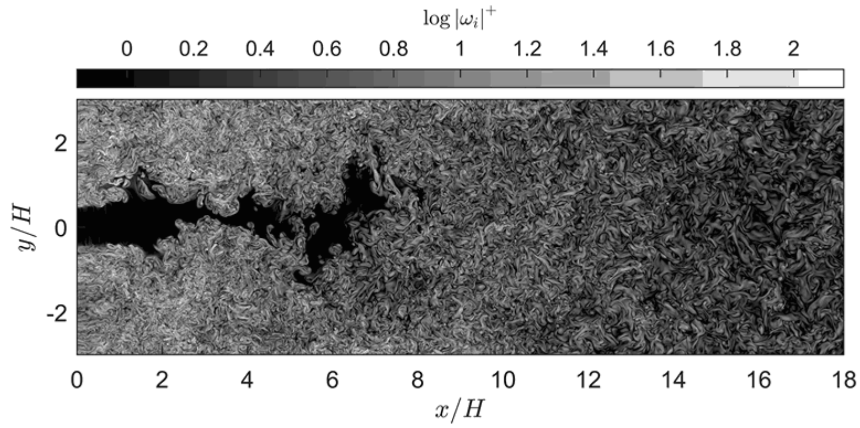

Figure 1: *Two-dimensional instantaneous snapshot of normalised vorticity magnitude, $|\omega_i|^+ = |\omega_i|/(U_\infty/H)$, in log scale.*

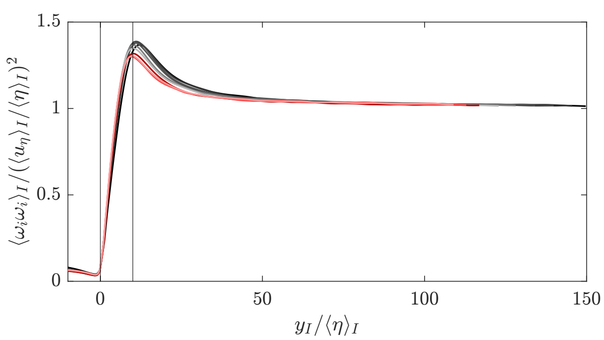

Figure 2: *Conditional profile of enstrophy, $\langle\omega_i\omega_i\rangle_I$, normalised by local Kolmogorov velocity, $\langle u_\eta\rangle_I$, and length scale, $\langle\eta\rangle_I$.*

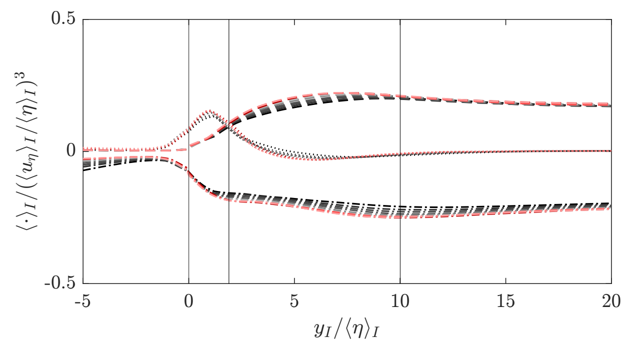

Figure 3: *Conditional profile of enstrophy budgets, normalised by local Kolmogorov velocity, $\langle u_\eta\rangle_I$, and length scale, $\langle\eta\rangle_I$.*

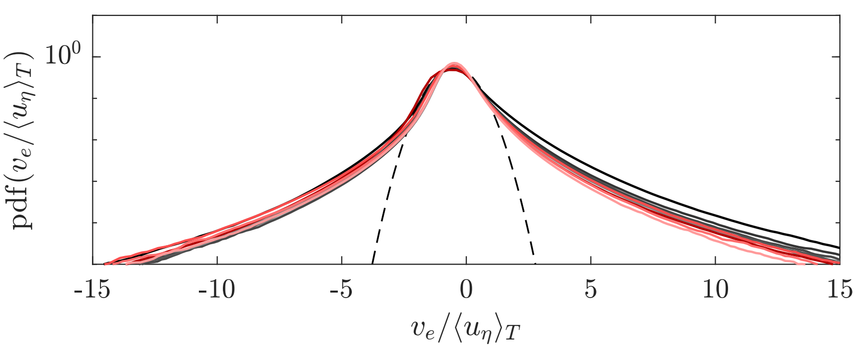

Figure 4: *Probability density function of the entrainment velocity, v_e, normalised by the Kolmogorov velocity scale at the turbulent core, $\langle u_\eta\rangle_T$. The dashed line represents a Gaussian distribution for comparison purposes.*

Multiscale circulation in wall-parallel planes of turbulent channel flows

Peng-Yu Duan[1], Xi Chen[1] and Katepalli R. Sreenivasan[2]

[1] Key Laboratory of Fluid Mechanics of Ministry of Education, Beihang University (Beijing University of Aeronautics and Astronautics), Beijing, PR China
[2] Tandon School of Engineering, Courant Institute of Mathematical Sciences, and Department of Physics, New York University, New York, USA

key-words: Circulation, Wall turbulence, Bifractal

Abstract:
Wall turbulence consists of various sizes of vortical structures that induce flow circulation around a wide range of closed Eulerian loops. Here we investigate the multiscale properties of circulation around such loops in statistically homogeneous planes parallel to the wall. Using a high-resolution direct numerical simulation database of turbulent channels at Reynolds numbers of $Re_\tau = 180$, 550, 1000 and 5200, circulation statistics are obtained in planes at different wall-normal heights. Intermittency of circulation in the planes of the outer flow ($y^+ \gtrsim 0.1 Re_\tau$) takes the form of universal bifractality as in homogeneous and isotropic turbulence. The bifractal character simplifies to space-filling character close to the wall, with scaling exponents that are linear in the moment order, and lower than those given by the Kolmogorov paradigm. The probability density functions of circulation are long-tailed in the outer bifractal region, with evidence showing their invariance with respect to the loop aspect ratio, while those in the inner region are closely Gaussian. The unifractality near the wall implies that the circulation there is not intermittent in character.

Noise-expansion cascade — a fundamental property of turbulence

Shijun Liao [1] and Shijie Qin [1]

[1] School of Ocean and Civil Engineering, Shanghai Jiao Tong University, Shanghai, China

key-words: Clean Numerical Simulation (CNS), DNS, Kolmogorov turbulence

Abstract:
It has been reported that turbulent flows governed by Navier-Stokes (NS) equation are chaotic. In addition, any numerical algorithms have artificial numerical noises. So, due to the butterfly-effect of chaos, numerical simulations of NS equations given by the direct numerical simulations (DNS) become badly polluted by artificial numerical noises quickly, as currently illustrated in [1] and [2].

In 2009 Liao proposed the so-called "Clean Numerical Simulation" (CNS) [3]. Unlike DNS, results given by CNS have rigorously negligible numerical noises in a finite but long enough interval of time [4], so that one can do "clean" numerical experiment for turbulence by CNS.

Randomness is one of the most important characteristics of turbulence, but its origin remains an open question. By means of a "thought experiment" via several clean numerical experiments based on the Navier-Stokes equations for two-dimensional turbulent Kolmogorov flow, we reveal a new phenomenon, which we call the "noise-expansion cascade" [5] whereby all micro-level noises/disturbances at different orders of magnitudes in the initial condition of Navier-Stokes equations enlarge consistently, say, one by one like an inverse cascade, to macro-level. More importantly, each noise/disturbance input may greatly change the macro-level characteristics and statistics of the resulting turbulence, clearly indicating that micro-level noise/disturbance might have great influence on macro-level characteristics and statistics of turbulence. Besides, the noise-expansion cascade closely connects randomness of micro-level noise/disturbance and macro-level disorder of turbulence, thus revealing an origin of randomness of turbulence. This also highly suggests that unavoidable thermal fluctuations must be considered when simulating turbulence, even if such fluctuations are several orders of magnitudes smaller than other external environmental disturbances. Hopefully, the "noise-expansion cascade" as a fundamental property of the NS equations could greatly deepen our understandings about turbulence, and besides is helpful for attacking the fourth millennium problem posed by Clay Mathematics Institute in 2000. For details, please refer to [5, 6].

References

[1] Qin, S. and Liao, S., (2022): Large-scale influence of numerical noises as artificial stochastic disturbances on a sustained turbulence, ,*J. Fluid Mech., vol. 948, pp. A7* (`doi:10.1017/jfm.2022.710`)

[2] Qin, S., Yang Y., Huang Y., Mei X., Wang L. and Liao, S., (2024): Is a direct numerical simulation (DNS) of Navier-Stokes equations with small enough grid spacing and time-step definitely reliable/correct?, *Journal of Ocean Engineering and Science, 9:293-310.*

[3] Liao, S., (2009): On the reliability of computed chaotic solutions of non-linear differential equations, *Tellus - A, vol. 61, pp. 550-564* .

[4] Liao, S., (2024): *Clean Numerical Simulation*, Taylor & Francis Groups, Boca Raton.

[5] Liao, S. and Qin, S. (2025): Noise-expansion cascade: an origin of randomness of turbulence, *J. Fluid Mech.* (accepted, `doi:10.1017/jfm.2025.140`)

[6] Liao, S. and Qin, S., (2025): Physical significance of artificial numerical noise of DNS for turbulenc, *J. Fluid Mech.* (accepted, `doi:10.1017/jfm.2025.200`)

Extending Kolmogorov Theory to Polymeric Turbulence

Alessandro Chiarini[1,2], Rahul K. Singh[2] and Marco E. Rosti[2]

[1] Dipartimento di Scienze e Tecnologie Aerospaziali, Politecnico di Milano, via La Masa 34, 20156 Milano, Italy

[2] Complex Fluids and Flows Unit, Okinawa Institute of Science and Technology Graduate University, Okinawa 904-0495, Japan

key-words: Polymers, Homogeneous and Isotropic Turbulence

Abstract:

The Kolmogorov phenomenology describes the nature of homogeneous and isotropic turbulence in flows of Newtonian fluids [1]. In his 1941 work, Kolmogorov showed that pth-order structure function must scale as $S_p \equiv \langle (\delta \boldsymbol{u} \cdot \boldsymbol{r}/r)^p \rangle \sim \langle \epsilon \rangle^{p/3} r^{p/3}$; $\delta \boldsymbol{u} = \boldsymbol{u}(\boldsymbol{x}+\boldsymbol{r}) - \boldsymbol{u}(\boldsymbol{x})$ and $r = |\boldsymbol{r}|$. In 1962, after the criticism by Landau, Kolmogorov and Oboukhov refined the similarity hypotheses (KO62) to account for the intermittent nature of turbulence, and relaxed the global averaging of dissipation $\langle \epsilon \rangle$ in favour of its locally averaged value over a scale r, $\langle \epsilon_r \rangle$, so that now $S_p \sim \langle \epsilon_r^{p/3} \rangle r^{p/3}$. In general, however, turbulent flows can be multiphase, and the added phase may modify the nature of turbulence in a non-trivial manner. A particularly interesting situation arises when polymers are added to a carrier flow: a small concentration of polymers in a turbulent flow modifies the way energy is distributed and transferred across scales and results in a variety of intriguing phenomena. Besides the Reynolds number Re, the nature of these polymeric flows is characterised by the Deborah number $De = \tau_p/\tau_L$, which quantifies the elasticity of the polymers via a typical polymer relaxation time τ_p relative to the largest time-scale of the flow $\tau_L \equiv L/u_{rms}$. Polymeric flows at large Re and unit De have recently been shown [2] to exhibit a novel, self-similar scaling with $S_2 \sim r^{\xi_2}$ where $\xi_2 \approx 1.3 \approx 4/3$, which departs significantly from the Kolmogorov exponent of $\xi_2 = 2/3$; see figure 1. It is thus clear that the addition of polymers drives turbulence statistics far away from the classical Kolmogorov predictions.

However, in this work we use an appropriate form of the Kármán-Howarth-Monin-Hill (KHMH) equation [3] to show that, with suitable modifications, turbulence statistics of polymeric flows can be actually cast within a K41-like phenomenology; see figure 2(a). We also show that the refined KO62 phenomenology accounts for appropriate corrections to the deviations from a K41-like behaviour, similar to classical Newtonian turbulence; see figure 2(b). At the conference, we will first set up the analytical framework, and then substantiate it with data from numerical simulations.

References

[1] Frisch, U., (1996): *Turbulence: The Legacy of A. N. Kolmogorov*, Cambridge University Press

[2] Zhang Y.-B.,Bodenschatz, E., Xu, H., Xi, H.-D. (2021), Experimental observation of the elastic range scaling in turbulent flow with polymer additives, *Sci. Adv., vol. 7, pp. eabd3525*

[3] Hill R.J. (2002), Exact Second-Order Structure-Function Relationships *J. Fluid Mech., vol. 468, pp.317-326*

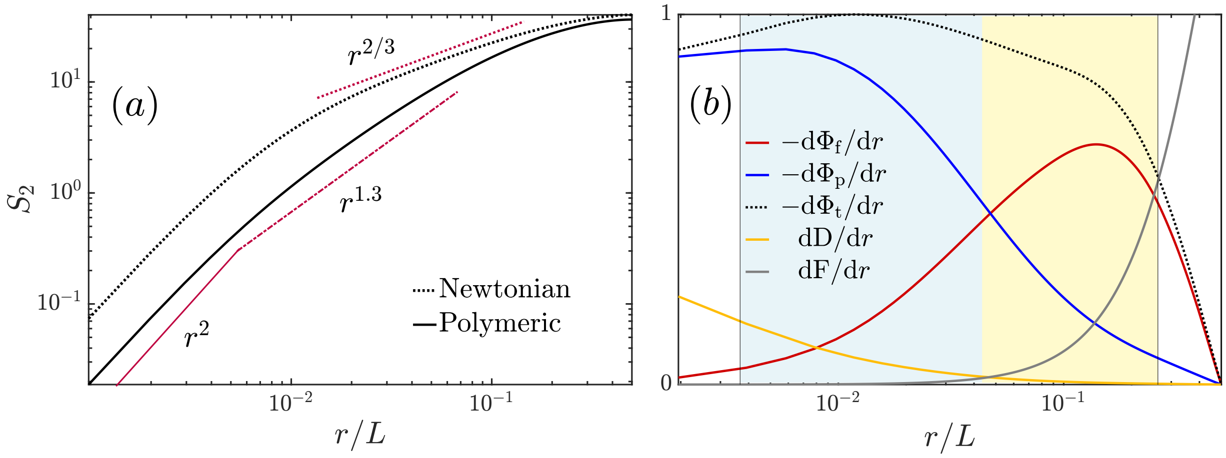

Figure 1: (a) Velocity structure functions S_2 in polymeric turbulence (solid curve) scale as $S_2 \sim r^{1.3}$, while in Newtonian turbulence (dashed curve) it scales as $S_2 \sim r^{2/3}$. (b) Terms of the KHMH equations for polymeric turbulence, i.e. $\mathrm{d}\Phi_f/\mathrm{d}r + \mathrm{d}\Phi_p/\mathrm{d}r = D(r) + F(r) - 4/3\langle\epsilon\rangle r$ where Φ_f and Φ_p denote the non-linear and polymeric fluxes, D is the viscous term which is relevant at the small scales and F is the forcing term that injects energy in the system at the large scales. This novel $r^{1.3}$ scaling holds in an intermediate range where fluid and polymeric flux contributions sum to a constant $\mathrm{d}\Phi_t/\mathrm{d}r = \mathrm{d}\Phi_f/\mathrm{d}r + \mathrm{D}\Phi_p/\mathrm{d}r$. We show in blue (yellow) the range of scales dominated by Φ_p (Φ_f). The dissipative D and forcing F contributions remain small in this entire range.

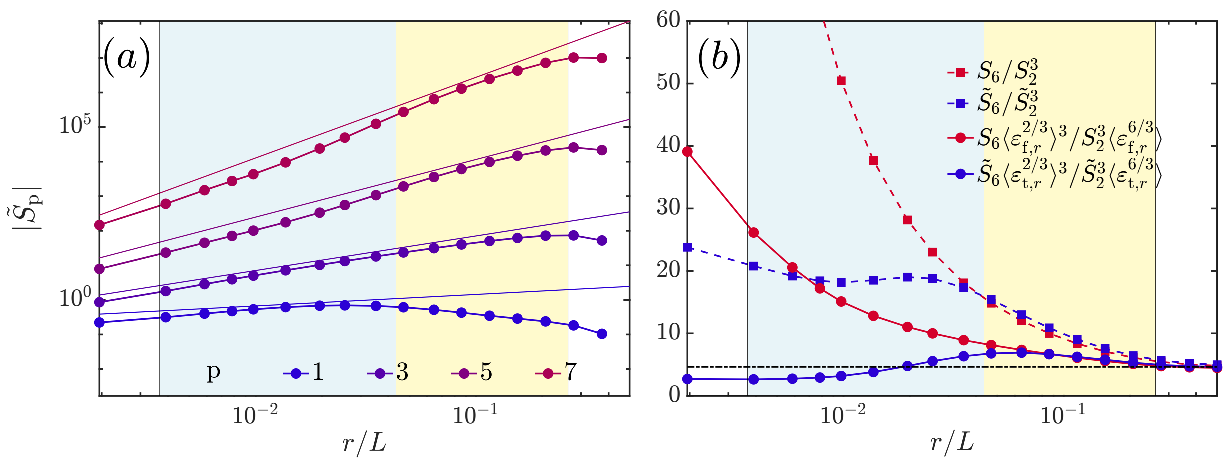

Figure 2: (a) The Extended Structure Functions $\tilde{S}_p$ (that we introduce in this work by using the KHMH equation) in polymeric turbulence exhibit a close to Kolmogorov behaviour $\tilde{S}_p \sim r^{p/3}$. Solid straight lines show $p/3$ scaling. The Extended Structure Function is defined as $\tilde{S}_p = \langle\widetilde{\delta V}_\parallel^p\rangle$, where $\widetilde{\delta V}_\parallel = (\delta u_\parallel \delta u_i^2 - 4\delta u_i T_{i\parallel}^*)^{1/3}$, with the subscript $\cdot_\parallel$ being the direction parallel to $\boldsymbol{r}$ and T_{ij} denoting the polymer stresses. (b) The flat compensated curve $\tilde{S}_6\langle\epsilon^{2/3}\rangle^3/\tilde{S}_2^3\langle\epsilon^{6/3}\rangle$ (blue circles) shows conformity to the Refined Kolmogorov similarity hypothesis. In comparison, the Newtonian compensated (solid lines, red circles) and the uncompensated (dashed line, red squares) ratios, as well as the uncompensated extended ratio (dashed blue curve, square markers), are strongly dependent on r.

Resolvent-Based Models for Wall-Modelled Large-Eddy Simulations

Z. Hantsis [1], M. Chan [2], N. Hoang[1], Beverley J. McKeon[3], and Ugo Piomelli[1]

[1] Department of Mechanical and Materials Engineering, Queen's University, Kingston (ON), Canada

[2] Graduate Aerospace Laboratories, California Institute of Technology, Pasadena (CA) USA

[3] Department of Mechanical Engineering, Stanford University, Stanford (CA), USA

key-words: Large-eddy simulations, Wall models

Abstract:

Large Eddy Simulation (LES) offers substantial computational savings over Direct Numerical Simulation (DNS). Wall-Modeled Large Eddy Simulation (WMLES), in which the near-wall is completely bypassed, makes the computations at high Reynolds-number and/or complex geometries computationally tractable. However, in WMLES one must model the small, unresolved scales everywhere in the domain, but also the dynamically important near-wall, small-scale turbulence. A consequence is reduced performance for flows in which near-wall flow phenomena dominate the outer flow, such as separation and relaminarization. WMLES is the topic of considerable research activity. Equation- and data-driven modelling approaches such as resolvent analysis and the family of proper orthogonal decompositions have given insight into reduced-order representations of a range of turbulent flows, but the findings have not been effectively integrated into LES models.

In this work, we exploit reduced but effective, scalable low-order models derived from the Navier-Stokes equations via resolvent analysis to simulate the effect of the unresolved turbulence in the wall layer. We embedd resolvent modes into WMLES and demonstrate that this approach can be used to improve the WMLES solution by populating the missing eddies in the vicinity of the first grid point.

In WMLES the near-wall is treated as a Reynolds-Averaged region, and only the mean flow is known. We present a framework to include the contribution of scales much smaller than the grid in the near-wall model in the form of modes derived from the resolvent analysis of the Navier-Stokes equations. A judicious choice of modes results in a model that, in addition to the (grid-averaged) wall stress, can account for wall-stress fluctuations, and allows the turbulent kinetic energy in the wall layer (which is unknown in standard wall models) to be determined. Figure 1 shows wall-stress contours, and highlights how the inclusion of resolvent modes results in smaller-scales (and more realistic) structures, and in an increase in the fluctuation magnitude. This is confirmed by examinning the streamwise-normal Reynolds stress. The inclusion of the resolvent modes in the near -wall layer results in a considerable increase in the inner-layer-velocity fluctuations; the addition of the contribution of the resolvent modes results in a total stress (–·–) in much with that obtained from the DNS, compared with a standard WMLES (–·–).

References

[1] M. Lee and R. D. Moser. Direct numerical simulation of turbulent channel flow up to $Re_\tau \approx 5,200$. *J. Fluid Mech.*, 774:395–415, 2015.

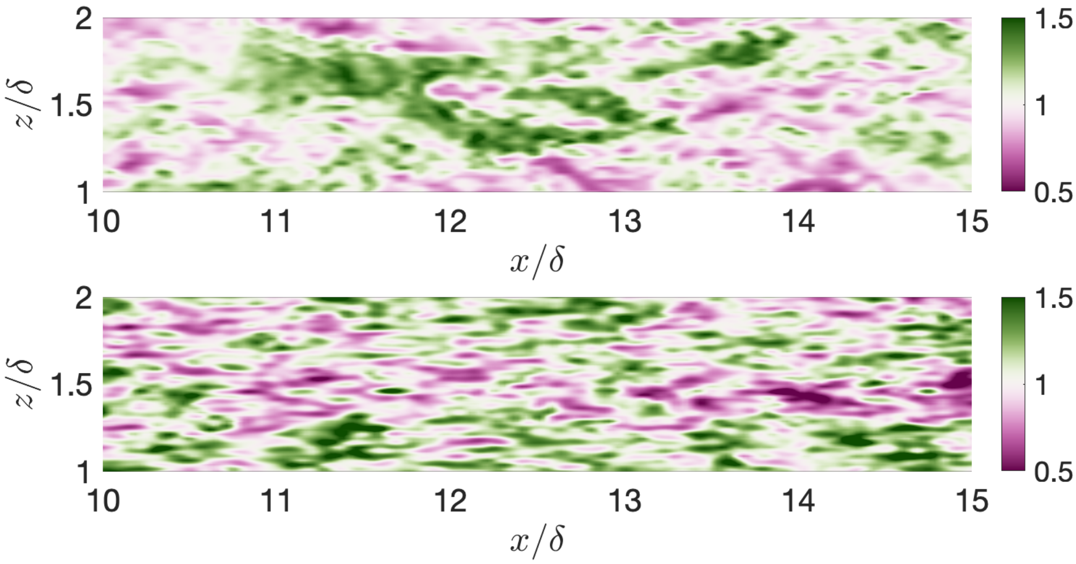

Figure 1: Contours of the wall stress. Left: standard WMLES; right: WMLES with resolvent modes.

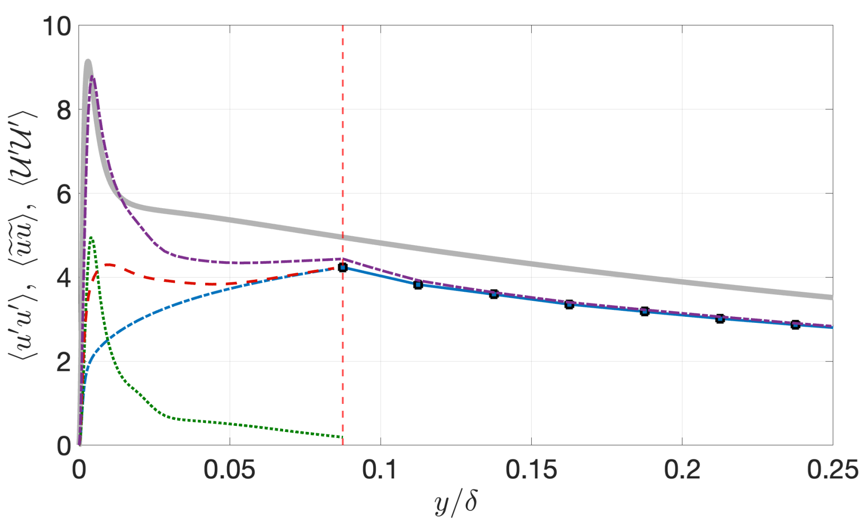

Figure 2: Profiles of the streamwise-normal Reynolds stress. ▬▬ DNS [1]; - - - : inner-flow averaged field; ······ resolvent-mode component; —— WMLES outer field; -·- total; -·- WMLES, no Resolvent modes, total.

Investigation of the physical role of backward scatter in minimal channel flow

Kazuhiro Inagaki [1]

[1] Department of Mechanical Engineering, Doshisha University, Kyoto, Japan

key-words: Turbulence modeling, Subgrid-scale model, Minimal channel

Abstract:
Subgrid-scale (SGS) models express a physical interaction between the resolved scale and SGS in large-eddy simulations (LESs) of turbulent flows. Recently developed data-driven modeling often produces a model by minimizing the error between a model expression and the true value calculated from instantaneous turbulent velocity fields [1]. Thus, we face the classical problem of numerical destabilization due to the backward scatter, which is observed for scale-similarity models [2].

To verify the necessity of backward scatter in LES, we investigate the dynamical aspect of turbulence via the minimal channel flow. Reynolds number based on the friction velocity u_τ is $\mathrm{Re}_\tau = u_\tau h/\nu = 200$ where h and ν denote the channel half width and kinematic viscosity, respectively. According to the typical size of near-wall structures [3], the domain size in the streamwise (x) and spanwise (z) directions are respectively set to be 400 and 200 when normalized by u_τ and ν. The grid points are $N_x \times N_y \times N_z = 64 \times 128 \times 64$. We employ the finite difference scheme. See Ref. [4] for details of the numerical scheme. The Fourier sharp-cut filter is employed only in the x and z directions. The cutoff wavelengths are set to be $(\lambda^+_{\mathrm{c},x}, \lambda^+_{\mathrm{c},z}) = (100, 50)$, and thus the typical near-wall structures are fairly involved in the resolved scale (see Ref. [3]).

The interaction between the resolved scale and SGS is represented by $\xi^{\mathrm{sgs}}_{ij} = -\tau^{\mathrm{sgs}}_{i\ell}|_{\mathrm{tl}}\partial_\ell \overline{u}_j - \tau^{\mathrm{sgs}}_{j\ell}|_{\mathrm{tl}}\partial_\ell \overline{u}_i$ where u_i and $\tau^{\mathrm{sgs}}_{ij} (= \overline{u_i u_j} - \overline{u}_i \overline{u}_j)$ respectively denote the velocity and SGS stress with the filter operation $\bar{\cdot}$, partial derivative in the ith direction ∂_i, and $A_{ij}|_{\mathrm{tl}} = A_{ij} - A_{\ell\ell}\delta_{ij}/3$. Figure 1 shows the orbit depicted in the two-dimensional plane of the energy transfer rate $\langle \xi^{\mathrm{sgs}}_{\ell\ell}/2 \rangle_V$ and the dissipation rate from SGS $\varepsilon^{\mathrm{SGS}}[= \langle u_i \nu \partial_j^2 u_i - \overline{u}_i \nu \partial_j^2 \overline{u}_i \rangle_V]$ where $\langle \cdot \rangle_V$ denotes the volume average. The energy transfer rate $-\langle \xi^{\mathrm{sgs}}_{\ell\ell}/2 \rangle_V$ occasionally exceeds the dissipation rate $\varepsilon^{\mathrm{SGS}}$, e.g. in $280 \leq t^+ \leq 360$, although it basically turns around the energy-balanced line. Hereafter, we focus on ξ^{sgs}_{zz} to discuss the spatial structure of turbulence (see Ref. [4]). Figure 2 shows that the backward scatter for the spanwise velocity $\langle \xi^{\mathrm{sgs}}_{zz}|_{>0} \rangle_V$ exhibits a large value in the period $280 \leq t^+ \leq 360$, which also corresponds to the time when the maximum value of the resolved scale Reynolds shear stress in the lower side of the channel becomes large. The flow visualization depicted in figure 3 suggests that the positive ξ^{sgs}_{zz} corresponds to the roll-up of a low-speed streak, which reminds us of a bursting process. Therefore, we infer that the backward scatter significantly contributes to the typical dynamics of wall-bounded turbulent flows.

References

[1] Duraisamy K., Iaccarino G. and Xiao H., (2019), Turbulence modeling in the age of data, *Annu. Rev. Fluid Mech., vol. 51, pp. 357–377*

[2] Beck A., Flad D. and Munz C.-D., (2019), Deep neural networks for data-driven LES closure models, *J. Comput. Phys., vol. 398, 108910*

[3] Jiménez J. and Moin P., (1991), The minimal flow unit in near-wall turbulence, *J. Fluid Mech., vol. 225, pp. 213–240*

[4] Inagaki K. and Kobayashi H., (2023), Analysis of anisotropic subgrid-scale stress for coarse large-eddy simulation, *Phys. Rev. Fluids, vol. 8, 104603*

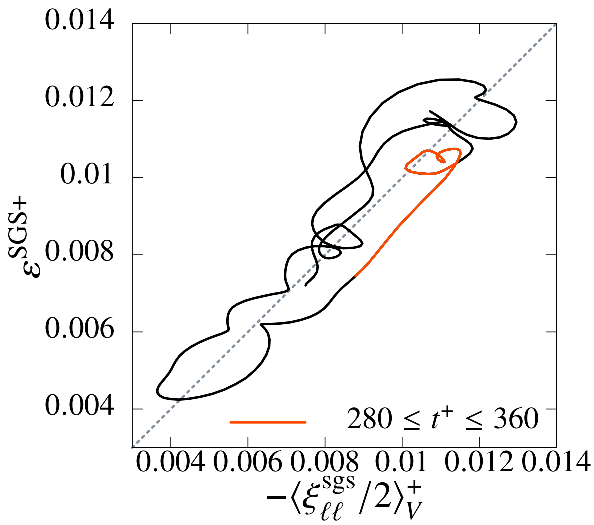

Figure 1: *Two-dimensional orbit of the energy transfer rate* $\langle \xi_{\ell\ell}^{\mathrm{sgs}}/2\rangle_V$ *and dissipation rate from SGS* $\varepsilon^{\mathrm{SGS}}$*. The elapsed time is* $t^+ = 500$*. The orbit turns anti-clockwise. The red line depicts the time range of* $280 \le t^+ \le 360$*. The linear dashed gray line corresponds to the balanced state, below which the SGS energy is accumulated.*

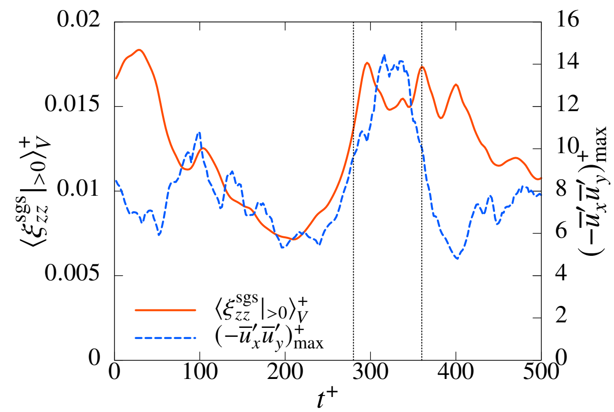

Figure 2: *Time history of the conditional average of* ξ_{zz}^{sgs} *for backward scatter* $\langle \xi_{zz}^{\mathrm{sgs}}|_{>0}\rangle_V$ *and maximum value of resolved scale Reynolds shear stress in the lower side the channel* $(-\overline{u}_x'\overline{u}_y')_{\max}$*. Note that* f' *denotes the deviation of* f *from the* x–z *plane average;* $f' = f - \langle f\rangle_{x\text{–}z\ plane}$*. Two vertical dotted lines depict the time* $t^+ = 280$ *and* 360*, respectively.*

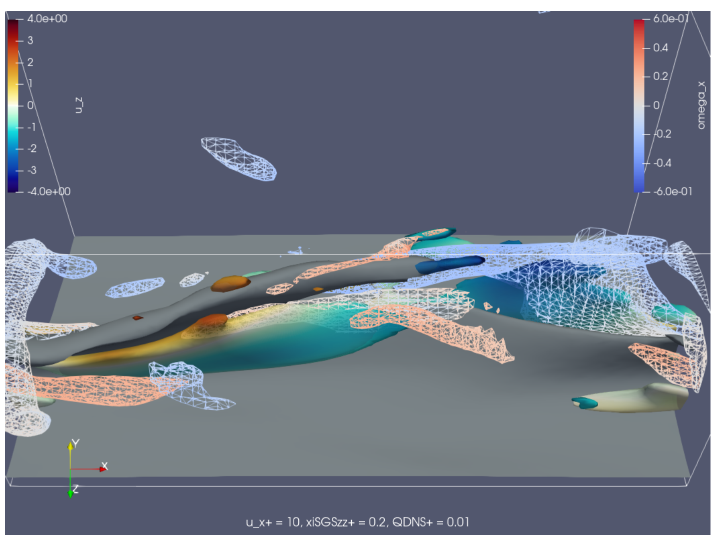

Figure 3: *Visualization of the streak* $\overline{u}_x^+ = 10$*,* $Q^+ = [-(\partial_j u_i)(\partial_i u_j)/2]^+ = 0.01$*, and backward scatter for the spanwise velocity* $\xi_{zz}^{\mathrm{sgs}+} = 0.2$ *at* $t^+ = 294$*. The gray sheet, elongated colored meshes, and colored surfaces depict the streak, Q, and backward scatter, respectively. Q is colored with the streamwise vorticity* $\omega_x^+ [= (\partial u_z/\partial y - \partial u_y/\partial z)^+]$*, whereas* ξ_{zz}^{sgs} *is colored with the spanwise velocity in the resolved scale* $\overline{u}_z^+$*: for both, warm and cool colors depict the positive and negative values, respectively. The direction of the mean flow is from left to right.*

Efficient Compressible Turbulent Flow Simulations: Entropy Projection and Correction for an ILES in a Discontinuous Galerkin solver

A. Crivellini [1], L. Alberti[1], E. Carnevali[1] and A. Colombo[2]

[1]Department of Industrial Engineering and Mathematical Sciences - Marche Politechnic University, Ancona, Italy
[2]Department of Engineering and Applied Sciences - University of Bergamo, Bergamo, Italy

key-words: Discontinuous Galerkin, ILES, entropy stability, entropy projection, transonic flow

Abstract:
It is well-known that Discontinuous Galerkin (DG) methods are very well suited to the Implicit Large Eddy Simulations (ILES) of turbulent flows. However, in the current literature, under-resolved DG simulations are usually performed at low Mach numbers [1] and the robustness of the approach under transonic/supersonic conditions is still questionable. In this contribution, we present the assessment of an entropy projection-correction method considering this more demanding situation. The approach proves to be an effective and efficient solution for undertaking scale-resolving simulations of turbulent transonic/supersonic flows. The projection operation of the discrete spatial operators onto the entropy variables space guarantees a robustness enhancement with respect to the baseline conservative scheme, enabling to account for both the discretization errors related to the under-resolution and the sharp variations of the thermodynamic state related to supersonic conditions. Furthermore, since the projected state is only used in the evaluation of the spatial operator, the non-stationary term retains its conservative form, hence both guaranteeing the formal conservation of the standard quantities and maintaining a computational cost comparable with the baseline standard (conservative) scheme. On top of this, the introduction of the explicit entropy correction [2] in such entropy-projected framework further guarantees the entropy stability of the numerical scheme. In this regard, we verified that the correction term does not introduce in the solution any spurious alteration or additional dissipation. The resulting framework enhances the robustness of the standard DG method and allows to successfully undertake highly challenging scenarios, ranging from high-Mach turbulent channel flows to configurations characterized by more complex geometries and flow discontinuities, i.e. shocks , such as the case of a transonic flow impinging on a sphere (Fig.2). The favourable dissipation/dispersion properties of the DG method are fully exploited to perform such simulations using a small fraction of the DOFs employed by the reference DNS [3, 4]. This, combined with the fact that the entropy stable framework is computationally inexpensive, allowed us to derive accurate solution on multi-scale problems by solely relying on the in-house computing facilities.

References

[1] Gassner, G. J. and Beck, A.D.: On the accuracy of high-order discretizations for underresolved turbulence simulations, *Theoretical and Computational Fluid Dynamics* **27**, 221–237 (2013).

[2] Abgrall, R., Öffner, P. and Ranocha, H.: Reinterpretation and extension of entropy correction terms for residual distribution and discontinuous Galerkin schemes: application to structure preserving discretization, *Journal of Computational Physics*, **453**, 110955 (2022).

[3] Modesti, D. and Pirozzoli, S.: Reynolds and Mach number effects in compressible turbulent channel flow, *International Journal of Heat and Fluid Flow*, **59**, 33–49 (2016).

[4] Nagata, T., Nonomura, T., Takahashi, S. and Fukuda, K.: Direct numerical simulation of subsonic, transonic and supersonic flow over an isolated sphere up to a Reynolds number of 1000, *Journal of Fluid Mechanics*, **904**, A36 (2020).

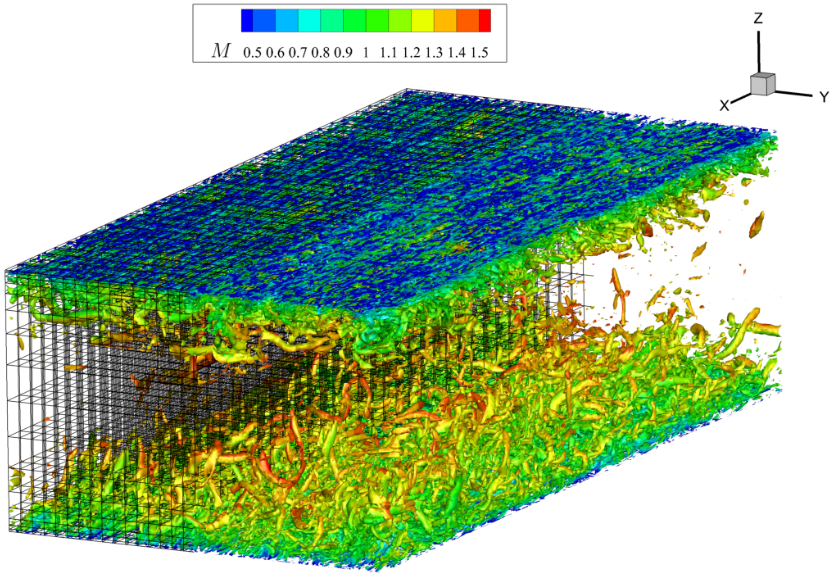

Figure 1: Compressible channel flow $Re_\tau = 1000$, $M_b = 1.5$. Instantaneous λ_2 isocontours coloured by Mach number. DG polynomial approximation $\mathbb{P}^8$.

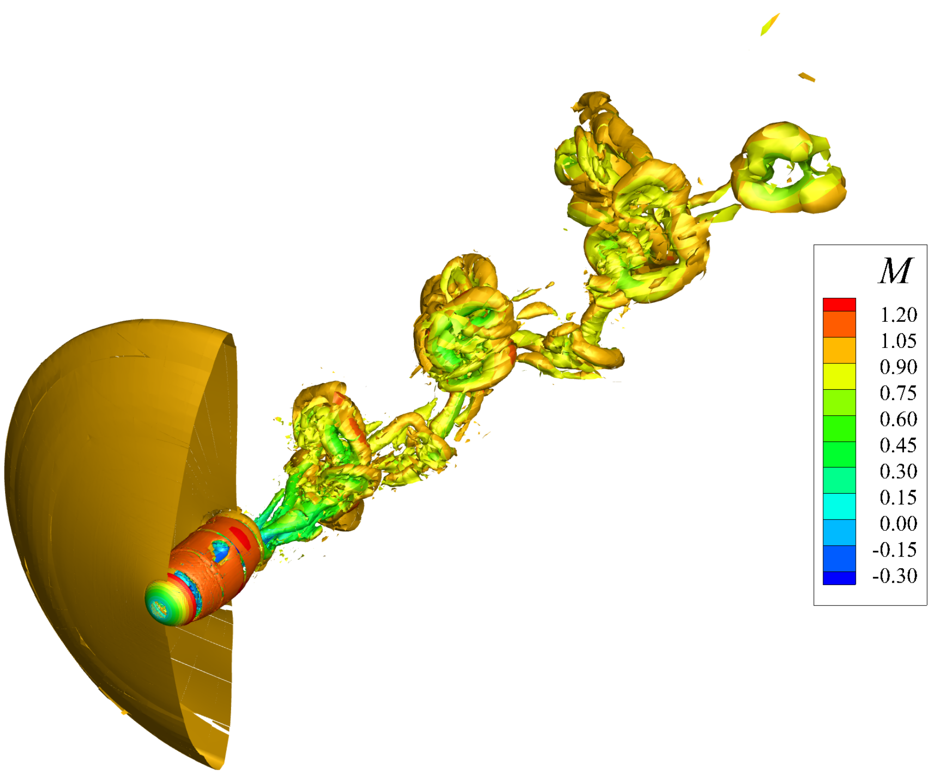

Figure 2: Transonic $M = 0.95$, $Re = 1000$ flow impinging a sphere. λ_2 isocontours coloured by Mach number with $M = 1$ isosurface. DG polynomial approximation $\mathbb{P}^6$.

Merging Filtering, Modeling and Discretization to Simulate Large Eddies in Burgers' Turbulence

Roel Verstappen

Bernoulli Institute, University of Groningen, Netherlands, r.w.c.p.verstappen@rug.nl

key-words: Large Eddy Simulation

Abstract:
Large-eddy simulation (LES) has developed into a valuable tool to study turbulent flow. However, the foundation of the method itself is not yet fully understood [1]. This concerns in particular the dividing line between physics and numerics, which is blurred by both the coupling filter-discretization and the interaction discretization-subgrid model. To get a better understanding of this, we consider the filtering, modeling and discretization as a whole, that is as being joint into a single entity. The basic idea is described in the simplest possible setting: a finite-volume discretization of 1D Burger's equation on a uniform grid with spacing h:

$$h\,\mathrm{d}_t\widetilde{\boldsymbol{u}}_{i-1/2} + \Phi_i - \Phi_{i-1} = -\tau_i + \tau_{i-1},$$

where Φ denotes the resolved flux and τ is the subgrid model. Both the flux and the model are evaluated at the faces of the volumes. Therefore this approach uses *two filters*: the average over the finite volume defines the first filter, the cell-to-face interpolation introduces the second filter:

$$\widetilde{u}_{i-1/2}(t) = \frac{1}{h}\int_{x_{i-1}}^{x_i} u(x,t)\,dx \qquad \overline{u}_i(t) = \frac{1}{2h}\int_{x_{i-1}}^{x_{i+1}} u(x,t)\,dx = \tfrac{1}{2}(\widetilde{u}_{i-1/2} + \widetilde{u}_{i+1/2}).$$

With these two filters the flux is approximated as usual by $\Phi_i = \overline{u}_i^2 - \nu(\widetilde{u}_{i+1/2} - \widetilde{u}_{i-1/2})/h$. The grid-filtered velocity is orthogonally decomposed. In matrix-vector notation: $\widetilde{\boldsymbol{u}} = \overline{\boldsymbol{u}} + \boldsymbol{u}^{\succ}$ with $\overline{\boldsymbol{u}} = \boldsymbol{L}\widetilde{\boldsymbol{u}}$, where $\boldsymbol{L}$ represents the cell-to-face interpolation, and $\boldsymbol{u}^{\succ} = \boldsymbol{S}\widetilde{\boldsymbol{u}}$ with $\boldsymbol{S} = \boldsymbol{I} - \boldsymbol{L}$. Importantly, $\overline{\boldsymbol{u}} \cdot \boldsymbol{u}^{\succ} = 0$; hence $\|\widetilde{\boldsymbol{u}}\|^2 = \|\overline{\boldsymbol{u}}\|^2 + \|\boldsymbol{u}^{\succ}\|^2$. So the total energy is broken up into $\|\boldsymbol{u}\|^2 = \|\overline{\boldsymbol{u}}\|^2 + \|\boldsymbol{u}^{\succ}\|^2 + \|\boldsymbol{u}'\|^2$, with the latter contribution being the subgrid energy, see also Fig. 1. To start, the leading-order term of $\boldsymbol{\tau}$ is determined using a Richardson extrapolation. This yields $\boldsymbol{\tau} \approx \boldsymbol{\tau}_{\mathrm{o}}$ [2]. Then, a novel scale-truncation model is added such that it approximately generates the minimal amount of dissipation needed to counteract the production of both $\boldsymbol{u}^{\succ}$ and $\boldsymbol{u}'$, i.e., $d_t\|\boldsymbol{u}^{\succ}\|^2 + d_t\|\boldsymbol{u}'\|^2 \leq 0$. This results into the model

$$\boldsymbol{\tau} = \boldsymbol{\tau}_{\mathrm{o}} - \alpha\,\nabla_S \boldsymbol{u}^{\succ} \qquad\qquad \alpha = \frac{(\nabla_S \boldsymbol{u}^{\succ} \cdot (\boldsymbol{\Phi} + \boldsymbol{\tau}_{\mathrm{o}}))_+}{\|\nabla_S \boldsymbol{u}^{\succ}\|^2},$$

where $\nabla_S = \nabla_h \boldsymbol{S}^{\top}$ and ∇_h is the difference operator, i.e., $(\nabla_h \boldsymbol{u})_i = u_{i+1/2} - u_{i-1/2}$.
The model is applied to a decaying burgulence test case [3]. Figure 2 shows a comparison of energy spectra. The DNS spectrum is computed using $N = 2^{14}$ gridpoints. The LES uses $2^7 - 2^{10}$ gridpoints. The DNS data is filtered using the above box filter with filter length $2h$. Note that its convolution kernel $\hat{G}_k = \sin(kh)/kh$ leads to the oscillatory behavior of the filtered spectrum. The LES spectrum matches that of the DNS very well for large scales of motion and coincides with the filtered DNS spectrum near the LES cut-off.

References

[1] Pope, S.B., (2004) Ten questions concerning large-eddy simulation of turbulence, *New Journal of Physics, vol. 6, pp. 1–124*

[2] Layton W.J. and Reboltz L., (2012): *Approximate Deconvolution Models of Turbulence*, Springer

[3] Maulik, R. and San, O., (2018) Explicit and implicit LES closures for Burgers turbulence, *Journal of Computational and Applied Mathematics, vol. 327, pp. 12–40*

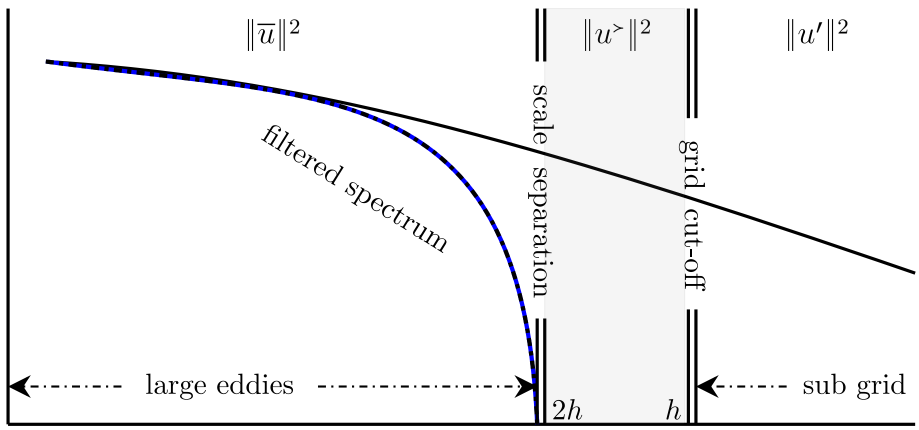

Figure 1: *Decomposition of the energy spectrum.*

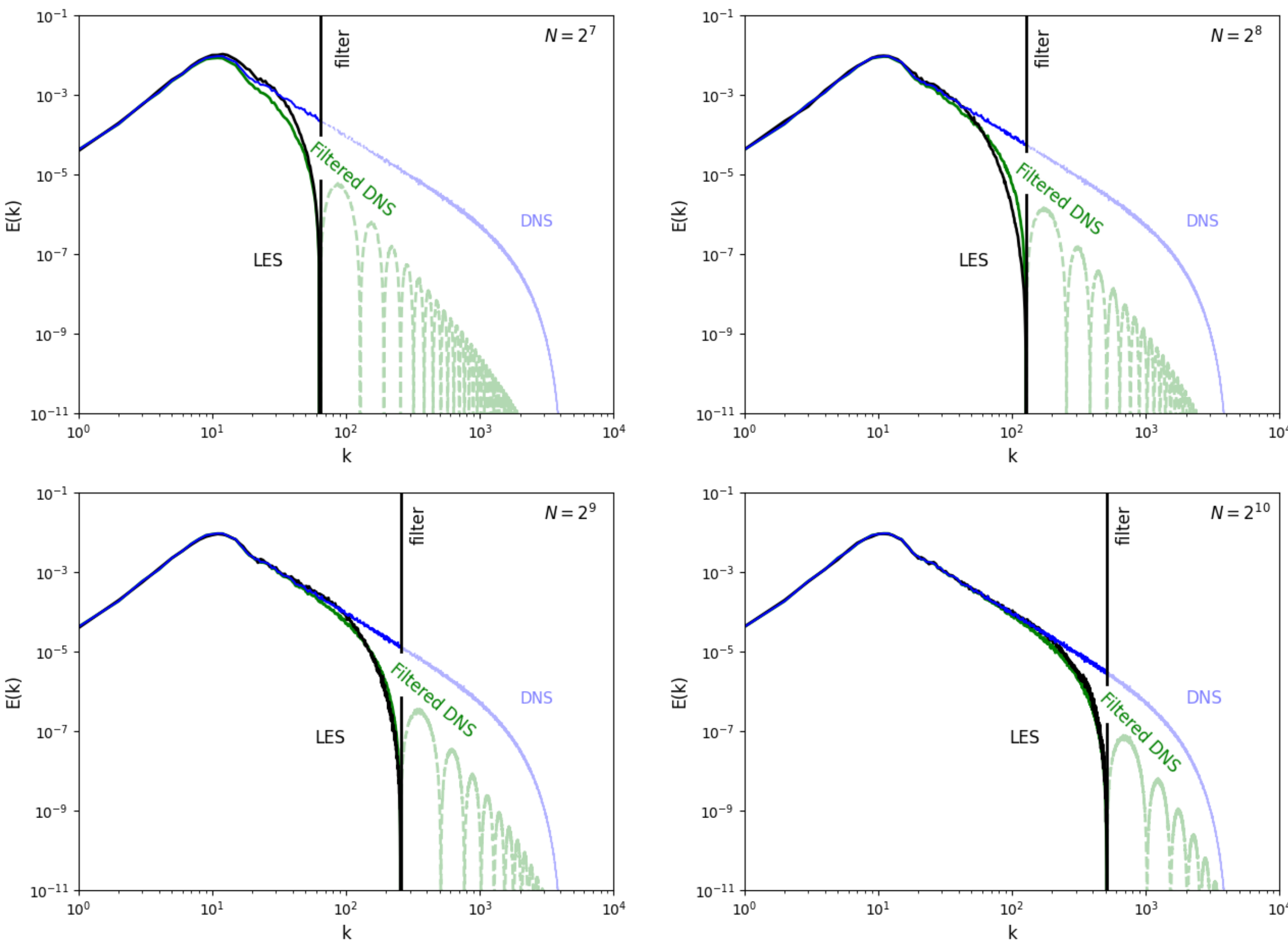

Figure 2: *Energy spectra for different resolutions*

Very low Ekman number turbulent rotating convection

E. Knobloch [1], A. van Kan [1]. B. Miquel [2], K. Julien [2] and G. Vasil [4]

[1] Department of Physics, University of California, Berkeley, CA94720, USA
[2] CNRS, École Centrale de Lyon, INSA Lyon, Université Claude Bernard Lyon 1, F-69134 Écully, France
[3] Department of Applied Mathematics, University of Colorado, Boulder, CO 80309, USA
[4] School of Mathematics, University of Edinburgh, Edinburgh, United Kingdom

key-words: Rapidly rotating convection, Geostrophic turbulence, Simulation

Abstract:
Direct numerical simulations (DNS) of turbulent rotating Rayleigh-Bénard convection are limited to moderately fast rotation (with Ekman numbers $\mathrm{Ek} = \mathrm{Ro}/\mathrm{Re} \geq 10^{-8}$ while astrophysical and geophysical applications are characterized by Ek orders of magnitude smaller (Figure 1). We present the *rescaled incompressible Navier-Stokes equations* [1] informed by the scalings valid in the asymptotic limit of $\mathrm{Ek} \to 0$ [2] which allow us to access previously unattainable parameter regimes, viz.,

$$D_t \mathbf{u}_\perp = -\hat{\boldsymbol{z}} \times \mathbf{U}_\perp + \nabla^2 \mathbf{u}_\perp, \qquad D_t w = -\partial_z p + (\widetilde{\mathrm{Ra}}/\mathrm{Pr})\theta + \nabla^2 w, \qquad \mathbf{U}_\perp = \varepsilon^{-1}(\mathbf{u}_\perp + \hat{\boldsymbol{z}} \times \nabla_\perp p),$$
$$D_t\theta + w(\partial_z \overline{\Theta} - 1) = \mathrm{Pr}^{-1}\nabla^2\theta, \quad \varepsilon^{-2}\partial_t\overline{\Theta} + \partial_z(\overline{w\theta}) = \mathrm{Pr}^{-1}\partial_{zz}\overline{\Theta}, \quad \nabla_\perp \cdot \mathbf{U}_\perp + \partial_z w = 0.$$

Here, $(\mathbf{u}_\perp, w)$ is the velocity field, with $\epsilon\mathbf{U}_\perp \equiv (\epsilon U, \epsilon V, 0)$ the ageostrophic velocity, and the temperature $T = \overline{\Theta} + \varepsilon\theta$; $D_t \equiv \partial_t + \mathbf{u}_\perp \cdot \nabla_\perp + \varepsilon w \partial_z$, $\nabla^2 \equiv \nabla_\perp^2 + \varepsilon^2 \partial_{zz}$. Control parameters are the Ekman number $\varepsilon \equiv \mathrm{Ek}^{1/3}$, the Prandtl number Pr, and the reduced Rayleigh number $\widetilde{\mathrm{Ra}} = \mathrm{Ra}\,\varepsilon^4$. Vertical (H) and horizontal $(\ell_\perp = \varepsilon H)$ coordinates are scaled anisotropically resulting in box aspect ratio $\varepsilon\Gamma \times \varepsilon\Gamma \times 1$. Impenetrable upper and lower boundaries are taken to be at fixed temperature and stress-free. Simulations for $\Gamma = 10\ell_c/\ell_\perp$ (in terms of the most unstable wavelength ℓ_c) access the parameter range $10^{-24} \leq \mathrm{Ek} \leq 10^{-1}$, $8.7 < \widetilde{\mathrm{Ra}} \leq 300$ [1, 3]. Figure 2 compares the Nusselt and Reynolds numbers $(\mathrm{Nu}, \mathrm{Re})$ at finite Ek with $(\mathrm{Nu}_\infty, \mathrm{Re}_\infty)$, the measured values in the asymptotic limit $\varepsilon \to 0$. Departure from the asymptotic limit is consistent with the predicted transitional value $\mathrm{Ek}_{t1} \propto \mathrm{Pr}^{3/2}\widetilde{\mathrm{Ra}}^{-15/4}$ [4]. For $\mathrm{Ek} < \mathrm{Ek}_{t1}$ geostrophic balance holds throughout the layer. Loss of balance within the thermal boundary layers for $\mathrm{Ek} > \mathrm{Ek}_{t1}$ results in the emergence of vertical gradient contributions to thermal and viscous dissipation and consequently enhancement of Nu, Re via their connection to dissipation rates: $\varepsilon_\nu = \mathrm{Ra}(\mathrm{Nu}-1)\mathrm{Pr}^{-2}$ and $\varepsilon_\vartheta = \mathrm{Nu}$. Loss of balance for the entire layer occurs for $\mathrm{Ek}_{t2} \propto \widetilde{\mathrm{Ra}}^{-3/2} > \mathrm{Ek}_{t1}$. The figure also confirms that cyclone-anticyclone asymmetry, measured by the depth-averaged (barotropic) vertical vorticity $\overline{\omega_z}$, disappears with decreasing Ek, as expected [2].

References

[1] Julien K., van Kan A., Miquel B., Knobloch E. and Vasil G., (2024), Rescaled equations of fluid motion for well-conditioned direct numerical simulations of rapidly rotating convection, *arXiv:2410.02702*, submitted to J. Comp. Phys.

[2] Julien K., Rubio A., Grooms I. and Knobloch E., (2012), Statistical and physical balances in low Rossby number Rayleigh-Bénard convection, *Geophys. Astrophys. Fluid Dyn., vol. 106, pp. 392–428*

[3] van Kan A., Julien K., Miquel B. and Knobloch E., (2024), Bridging the Rossby number gap in rapidly rotating thermal convection, *arXiv:2409.08536*, submitted to J. Fluid Mech.

[4] Julien K., Knobloch E., Rubio A. and Vasil G., (2012), Heat transport in low-Rossby-number Rayleigh-Bénard convection, *Phys. Rev. Lett., vol. 109, 254503*

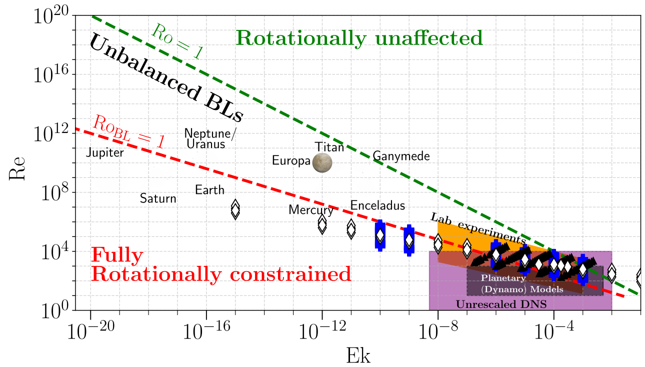

Figure 1: *Estimates of the nondimensional parameters for different celestial objects shown in the* $(\mathrm{Ek} \equiv \nu/2\Omega H^2, \mathrm{Re} \equiv w_{\mathrm{rms}}/\varepsilon)$ *plane (ν is the viscosity, Ω the rotation rate). Diamonds indicate the parameter values explored here. Parameters reached in previous laboratory experiments and simulations are indicated by shaded regions; dashed lines indicate transition Rossby numbers* Ro.

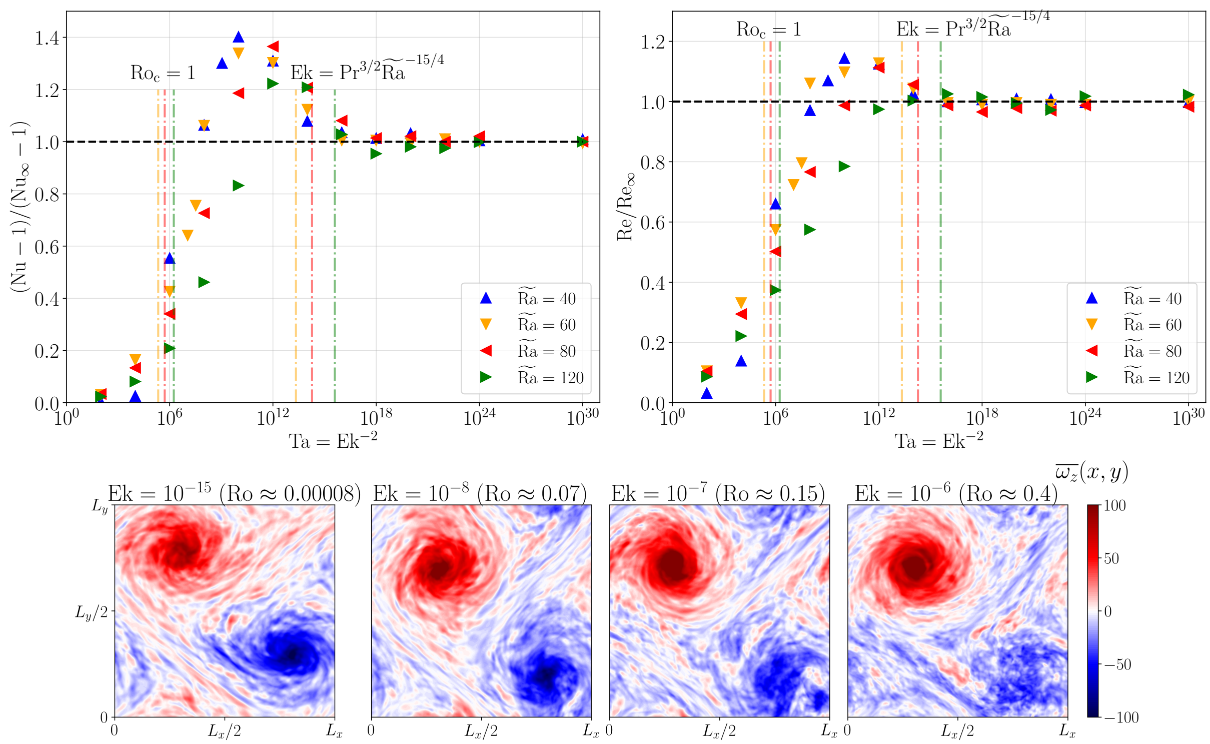

Figure 2: *Nusselt number* Nu *and Reynolds number* Re *vs* $\mathrm{Ta} \equiv \mathrm{Ek}^{-2} = \varepsilon^{-6}$ *at fixed* $\widetilde{\mathrm{Ra}}$, $\mathrm{Pr} = 1$. *Black dashed horizontal lines denote* Nu_∞, Re_∞*; vertical lines show* $\mathrm{Ek}_{\mathrm{t1}}$ *and* $\mathrm{Ek}_{\mathrm{t2}}$ *(*$\mathrm{Ek}_{\mathrm{t2}} > \mathrm{Ek}_{\mathrm{t1}}$*). Lower panels show the depth-averaged (barotropic) vertical vorticity* $\overline{\omega_z}(x,y)$ *for various* Ek.

Heat transfer fluctuations measurements with a heated thin foil

A Cuéllar [1], E Amico [2], J Serpieri [2], G Cafiero [2], W J Baars [3], S Discetti [1], A Ianiro [1]

[1] Department of Aerospace Engineering, Universidad Carlos III de Madrid, Leganés, Spain
[2] Department of Mechanical and Aerospace Engineering, Politecnico di Torino, Torino, Italy
[3] Faculty of Aerospace Engineering, Delft University of Technology, Delft, The Netherlands

key words: Turbulent channel flow, Infrared thermography

Abstract:
An experimental approach employing a heated thin foil and infrared (IR) thermography to take heat transfer fluctuations measurements in a channel airflow, characterised by small amplitude and high frequencies, is presented. The setup with a heated thin foil in which an electric current is discharged to apply the Joule effect enables signal amplification [1]. Compared with water medium [2], smaller fluctuations and higher characteristic frequencies might be found with air. This experimental campaign has been developed in the Channel Flow facility at Politecnico di Torino, at a Reynolds number $Re_\tau = 220$. The IR system was set to 180 Hz, with 5 and 10 μm foils at different input power levels.

The segment of the wall where measurements are taken is replaced by the foil, and the IR camera acquires temperature measurements on its external side, necessitating that it be thermally thin ($Bi \ll 1$). With these acquired maps, the energy balance of the thin foil (1) provides us with the convective heat transfer coefficient h_c between the fluid and the foil locally, considering also the Joule power input, conduction within the foil, radiation and external convection. To ensure that the foil can properly capture the thermal events in the channel flow, one must verify that the characteristic time of the foil is small enough with respect to that of the channel ($Fo \gg 1$) under the different parameters of the problem [3].

$$c_p \rho a \frac{\partial T_w}{\partial t} = \phi''_{\mathrm{J}} - \phi''_{\mathrm{cond}} - 2\phi''_{\mathrm{rad}} - \phi''_{\mathrm{conv,ext}} - h_c(T_w - T_{\mathrm{aw}}) \; . \tag{1}$$

The temperature sequence is characterised by a low signal-to-noise ratio. This data must be filtered before heat transfer is computed to enable a reasonable physical interpretation. To that end, the filtering procedure employs high-pass, 3D-Gaussian and POD filters. As shown in figure 1, the heat transfer map shows patterns with characteristic sizes as those expected in this type of channel flow [4].

Low levels of heating do not amplify the signal as needed. Natural convection cells on the external side of the foil, characterised by larger scales than those expected from this channel flow and significantly lower frequencies, were developed as a consequence of the heating of the foil. This thermal signature increases with the level of heating, but it can be removed with the filtering procedure.

The thermal inertia and conduction difference between the 5 and 10 μm foils results in a lower sensitivity and a longer response time to temperature changes for the thicker foil. Although these patterns still resemble representative of the physics in the channel, peaks are attenuated and noise is increased with respect to the thinner foil.

References

[1] Nakamura, H. and Yamada, S., (2013), Quantitative evaluation of spatio-temporal heat transfer to a turbulent air flow using a heated thin-foil, *Int. J. Heat Mass Tran.*, **64**, 892–902.

[2] Foroozan, F. et al., (2023), Synchronized measurement of instantaneous convective heat flux and velocity fields in wall-bounded flows, *Meas. Sci. Tech.*, **34**(12), 125301.

[3] Astarita, T. and Carlomagno, G. M., (2013): *Infrared thermography for thermo-fluid-dynamics*, Springer, Berlin, Heidelberg.

[4] Del Álamo, Juan C and Jiménez, Javier, (2003), Spectra of the very large anisotropic scales in turbulent channels *Phys. Fluids*, **15**(6), L41–L44.

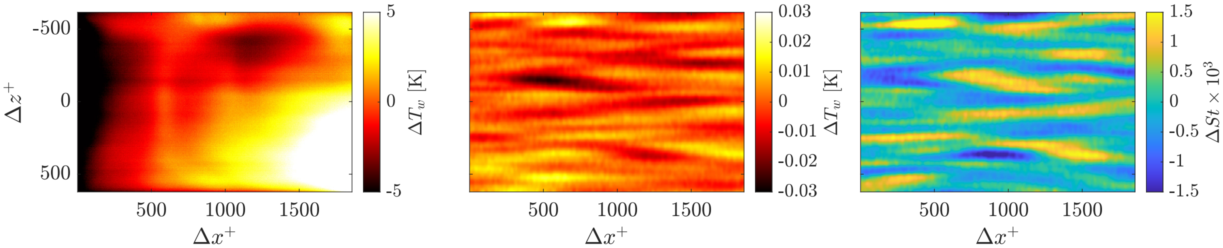

Figure 1: Filtering example for an instantaneous snapshot employing a 5 μm foil: from left to right, original ΔT_w map, filtered ΔT_w map and heat transfer map employing the Stanton number (ΔSt). These quasi-streamwise-aligned patterns have characteristic sizes of 500–1000 Δx^+ and 50–100 Δz^+.

Acknowledgements A.C. acknowledges financial support from the Spanish Ministry of Universities under the FPU programme 2020. This activity is part of the project EXCALIBUR (Grant No PID2022-138314NB-I00), funded by MCIU/AEI/10.13039/501100011033 and by "ERDF A way of making Europe".

Validation of helicity turbulence model and its application to stellar convection

Nobumitsu Yokoi [1],

[1] Institute of Industrial Science, University of Tokyo, Tokyo, Japan

key-words: Helicity, Turbulence modelling, Stellar convection

Abstract:
Helicity, a measure of broken reflectional symmetry, contributes to the turbulence dynamics and statistical properties [1]. The two-point two-time velocity correlation of homogeneous isotropic but non-mirror-symmetric turbulence is written in mathematically generic form as

$$\begin{aligned}\tilde{R}_{ij}(\mathbf{r};t,t') &\equiv \langle u'_i(\mathbf{x};t)u'_j(\mathbf{x}';t')\rangle = \langle u'_i(\mathbf{0};t)u'_j(\mathbf{r};t')\rangle \\ &= f\frac{r_i r_j}{r^2} + g\left(\delta_{ij} - \frac{r_i r_j}{r^2}\right) + h\epsilon_{ij\ell}\frac{r_\ell}{r},\end{aligned} \tag{1}$$

where $r = |\mathbf{r}| = |\mathbf{x'} - \mathbf{x}|$, $\mathbf{u}'$ is the fluctuating velocity, and $\langle\cdots\rangle$ is an appropriate averaging. Here, f is the longitudinal correlation, g is the transverse correlation, and h is the cross-flow correlation as depicted in Figure 1. As this natural consequence, the turbulent momentum transport will be affected by the turbulent helicity defined by $H \equiv \langle\mathbf{u}' \cdot \boldsymbol{\omega}'\rangle$ ($\boldsymbol{\omega}'(= \nabla \times \mathbf{u}')$: fluctuating vorticity) [2]. Such a helicity contribution comes from the cross-flow correlation h in (1). This gives a stark contrast to the eddy-viscosity which comes from the transverse and longitudinal velocity correlations.

On the basis of the theoretical analysis of the turbulent momentum flux [3, 4], the subgrid-scale (SGS) stress is modelled as [5]

$$\begin{aligned}\tau_{ij} &\equiv \overline{u_i u_j} - \overline{u}_i\overline{u}_j \\ &= \frac{2}{3}K_{\mathrm{S}}\delta_{ij} - \nu_{\mathrm{S}}\overline{s}_{ij} + \eta_{\mathrm{S}}\left[\frac{\partial H_{\mathrm{S}}}{\partial x_i}\overline{\omega}_{*j} + \frac{\partial H_{\mathrm{S}}}{\partial x_j}\overline{\omega}_{*i} - \frac{2}{3}\delta_{ij}(\overline{\boldsymbol{\omega}_*}\cdot\nabla)H_{\mathrm{S}}\right],\end{aligned} \tag{2}$$

where $K_{\mathrm{S}} \equiv (\overline{\mathbf{u}^2} - \overline{\mathbf{u}}^2)/2$ is the SGS energy and $H_{\mathrm{S}} \equiv \overline{\mathbf{u}\cdot\boldsymbol{\omega}} - \overline{\mathbf{u}}\cdot\overline{\boldsymbol{\omega}}$ is the SGS helicity. The SGS viscosity is expressed by the Smagorinsky model $\nu_{\mathrm{S}} = (C_{\mathrm{S}}\Delta)^2|\overline{\boldsymbol{s}}|$ (C_{S}: Smagorinsky coefficient, Δ: filter width). In addition to the usual Smagorinsky model (the first term), we have an additional contribution of the SGS helicity (the second term). This model is called the helicity SGS model.

where $K_{\mathrm{S}} \equiv (\overline{\mathbf{u}^2} - \overline{\mathbf{u}}^2)/2$ is the SGS energy and $H_{\mathrm{S}} \equiv \overline{\mathbf{u}\cdot\boldsymbol{\omega}} - \overline{\mathbf{u}}\cdot\overline{\boldsymbol{\omega}}$ is the SGS helicity. The SGS viscosity is expressed by the Smagorinsky model $\nu_{\mathrm{S}} = (C_{\mathrm{S}}\Delta)^2|\overline{\boldsymbol{\mathcal{S}}}|$ (C_{S}: Smagorinsky constant, Δ: filter width). In addition to the usual Smagorinsky model (the first term), we have an additional contribution of the SGS helicity (the second term). This model is called the helicity SGS model.

In order to validate the helicity SGS model, we perform a series of direct numerical simulations in a triple periodic box with helical forcing [5]. The inhomogeneous turbulent helicity is injected by external forcing. The scattering plots of the DNSs and the two models (Smagorinsky and helicity models) are shown in Figure 2. While the Smagorinsky model never properly represent the DNS results, the helicity SGS model improves the correlation with the DNSs very much. This clearly shows that even in the homogeneous isotropic turbulence, the second term of (2) should be implemented in the SGS model for helical turbulence.

In the context of astrophysical and geophysical flows, the helicity model is applied to the problem of angular-momentum transport in the stellar convection zone [6]. In the solar convection turbulence, there are some unsolved problems called the convection conundrum. One of them is how to reproduce the prograde angular velocity (differential rotation) profile observed in helioseismology by the numerical simulations of solar convection zone with the solar parameters (rotation, luminosity, etc.). Here we stress that the radial and colatitudinal distribution of turbulent helicity coupled with the large-scale azimuthal vorticity associated with the meridional circulation can contribute to the realisation of the Reynolds stress, which plays key roles for the large-scale flows (differential rotation and meridional circulation) in the Sun. Some recent results with the aid of the helicity turbulence model and DNSs of spherical shell mimicking the Sun are presented (Figures 3 and 4). These results indicate the inhomogeneous helicity effect may be relevant to the stellar angular-momentum transport.

References

[1] Pouquet, A. and Yokoi, N., (2022) Helical fluid and (Hall)-MHD turbulence: a brief review, *Phil. Trans. R. Soc. A, vol. 380, 20210087*

[2] Yokoi, N., (2024) Transport in helical fluid turbulence, in *Helicities in Geophysics, Astrophysics, and Beyond, Geophysical Monograph 283, First Edition. (Eds.) K. Kuzanyan, N. Yokoi, M.K. Georgoulis, and R. Stepanov. John Wiley & Sons, Inc. pp. 25-50*

[3] Yokoi, N. and Yoshizawa, A., (1993) Statistical analysis of the effects of helicity in inhomogeneous turbulence, *Phys. Fluids A, vol. 5, pp. 464-477*

[4] Yokoi, N. and Brandenburg, A. (2016) Large-scale flow generation by inhomogeneous helicity, *Phys. Rev. E, vol. 93, 033125*

[5] Yokoi, N., Mininni, P., Pouquet, A., Rosenberg, D., and Marino, R. Validation of the helicity subgrid-scale model, *Phys. Fluids, submitted*

[6] Yokoi, N. and Miesch, M.S. (2025) Kinetic helicity effects in stellar angular-moment transport, *Geophys. Astrophys. Fluid Dyn. in press*

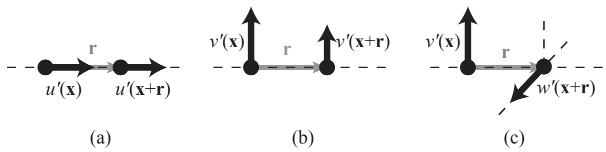

Figure 1: *Velocity correlations: (a) longitudinal, (b) transverse, and (c) cross-flow correlations*

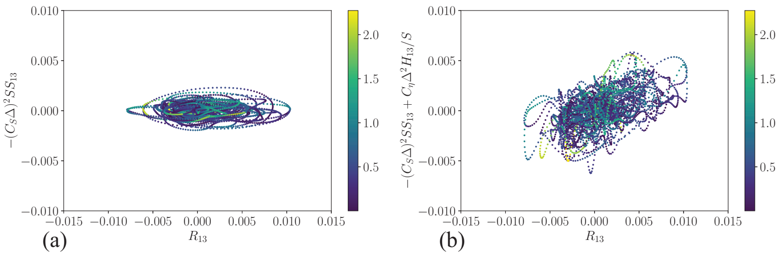

Figure 2: *Scatter plots of SGS stress: (a) Smagorinsky model (b) Helicity SGS model*

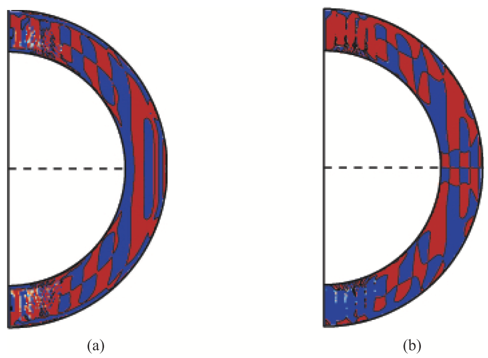

Figure 3: *Helicity effects: (a) r-ϕ component (b) θ-ϕ component*

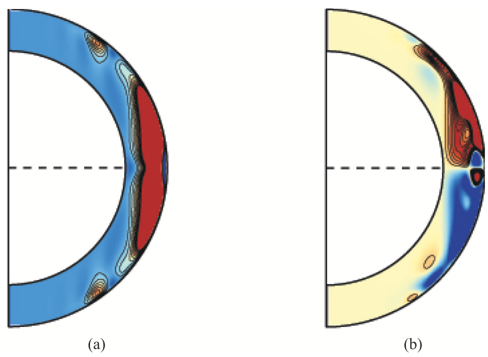

Figure 4: *Reynolds stresses: (a) r-ϕ component (b) θ-ϕ component*

Richtmyer-Meshkov induced turbulent mixing in a shock tube

Jérôme Griffond [1], Olivier Soulard [1], Yannick Bury [2] and Stéphane Jamme [2]

[1] CEA, DAM, DIF, F-91297 Arpajon, France

[2] Institut Supérieur de l'Aéronautique et de l'Espace (ISAE-SUPAERO), Université de Toulouse, 31055 TOULOUSE Cedex, France

key-words: Turbulent mixing, Experiments

Abstract:
Experiments devoted to the study of turbulent mixing at an interface between air and helium are conducted in a shock-tube set-up at ISAE-SUPAERO. The shape of the interface, just before shock front arrival, stems from the opening of a series of rotating blades initially separating both gases. The vorticity deposit induced by the first interaction with the incident shock wave of Mach number 1.2 leads to the occurence of a mixing zone which is subsequently hit by the transmitted shock front reflected at the aft-end of the tube. This event is referred to as "reshock" and its effect on the mixing zone structure and growth is the main scope of this study.

Three kinds of diagnostics have been employed in the present air/helium configuration. High-speed camera Schlieren photography, as shown in figure 1, allows to follow the upper and lower edges of the mixing zone during most of the time from the first shock-crossing to the post-reshock period, see [1]. High-resolution stereoscopic particle image velocimetry (PIV) at three instants (shortly after shock-crossing, just before the arrival of the reshock and soon after the interaction of the reshock with the mixing zone), as shown in figure 2, gives access to details of the flow field, see [2]. Planar tomoscopy allows to characterize the 2D-concentration field around the rotating blades just after complete opening (before any interaction with a shock wave), see [3].

The latter are then used to initialize the 3D-simulations of the experiments illustrated in figure 3. Comparisons between measurements and computations comprise the mixing zone width from Schlieren photography and the integral or Taylor microscales from PIV.

References

[1] Rasteiro dos Santos, M., Bury, Y., Jamme, S. & Griffond, J. (2023) On the effect of characterised initial conditions on the evolution of the mixing induced by the Richtmyer–Meshkov instability, *Shock Waves, 33:117-130*

[2] Rasteiro dos Santos, M. (2022) Comment les conditions initiales affectent-elles la transition turbulente du mélange induit par l'instabilité de Richtmyer-Meshkov ? *PhD thesis, Université de Toulouse.*

[3] Bury, Y., Graumer, P., Jamme, S. & Griffond, J. (2020), Turbulent transition of a gaseous mixing zone induced by the Richtmyer-Meshkov instability, *Physical Review Fluids, 5(2):024101.*

Figure 1: *Schlieren photography of the interface between air (left) and helium (right) at three times : shortly after shock-crossing, just before the arrival of the reshock and soon after the interaction with the reshock.*

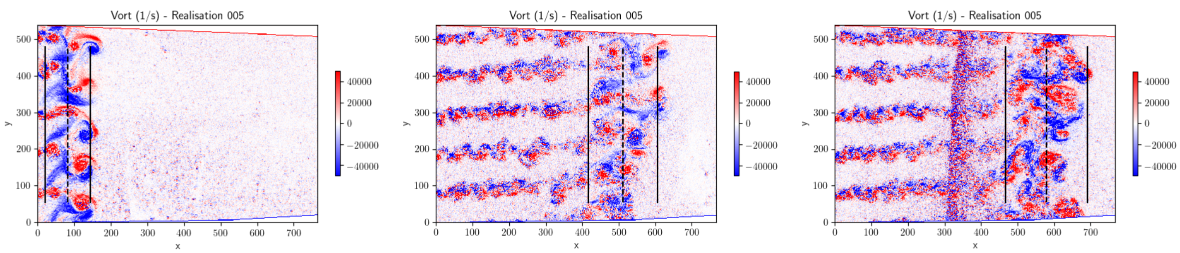

Figure 2: *Vorticity fields from PIV measurements at the same three times as in figure 1*

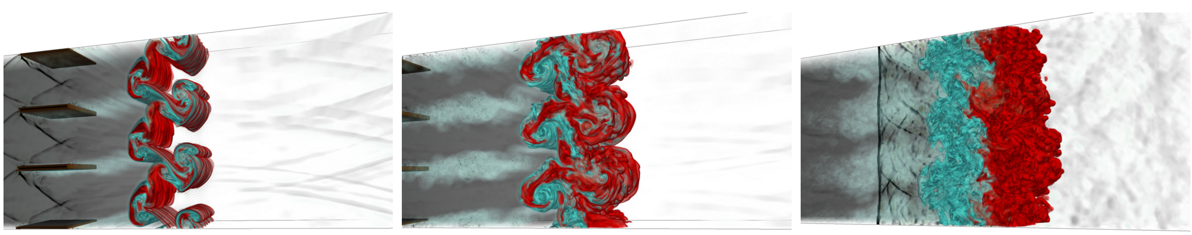

Figure 3: *Volume rendering of a numerical simulation of the experiment*

Learning to Backtrace Turbulent Scalar Fields

M. Carbone[1,2], L. Piro[3,2], R. Heinonen[3,2], L. Biferale[3,2] and M. Cencini[1,2]

[1] Istituto dei Sistemi Complessi–CNR, Rome, Italy
[2] INFN "Tor Vergata", Rome, Italy
[3] Department of Physics, University of Rome "Tor Vergata", Rome, Italy

key-words: Olfactory search, machine learning

Abstract:
Olfactory search is fundamental for living organisms to locate nutrients or mates and plays a major role in robotic search-and-rescue operations, where chemical sources must be promptly localized. The searcher (agent) navigates through a turbulent flow field, where odors emitted from a source (target) are subject to stretching and diffusion, leading to sparse and intermittent odor detections [1]. Existing navigation strategies often rely on the Bayesian update of a probability map on the entire domain used to determine an optimal action within a discretized action space [2]. While robust and efficient, these methods are memory-intensive.
Here we propose a backtracing-based approach for odor source localization in turbulent environments, inspired to simpler heuristics, such as casting and surging [3], which do not require a probability map on the entire domain. The agent learns the spatiotemporal dynamics of the turbulent flows in which it typically moves. Specifically, it infers the time-dependent probability distribution of an odor particle's position at an earlier time given an odor detection at the current time and agent's position, conditional on the local fluid velocity and possibly other local observables. Learning this probability density does not require measuring the odor field. When engaged in source localization, the agent samples the learned probability distribution through an associated Fokker-Planck equation, which includes an explicitly time-dependent drift, a component parallel to the probability gradient, and an orthogonal component. These contributions correspond to a surge in the probability gradient direction and a cast perpendicular to it, mirroring natural olfactory search strategies. We evaluate this algorithm for a passive scalar emitted from a point source and advected by a two-dimensional turbulent flow. We show that the agent can effectively backtrace odor detections, reconstructing trajectories that resemble passive scalar plumes, thus efficiently localizing the source.
We acknowledge financial support under the National Recovery and Resilience Plan (NRRP), Mission 4, Component 2, Investment 1.1, Call for tender No. 104 published on 2.2.2022 by the Italian Ministry of University and Research (MUR), funded by the European Union – NextGenerationEU – Project Title Equations informed and data-driven approaches for collective optimal search in complex flows (CO-SEARCH), Contract 202249Z89M – CUP B53D23003920006 and by the European Research Council (ERC) under the European Union's Horizon 2020 research and innovation program (Grant Agreement No. 882340).

References

[1] Celani A., Villermaux E. and Vergassola M., (2014), Odor Landscapes in Turbulent Environments, *Physical Review X, vol. 4, pp. 041015*

[2] Vergassola M., Villermaux E. and Shraiman B. I., (2007), 'Infotaxis' as a strategy for searching without gradients, *Nature, vol. 445, pp. 406-409*

[3] Balkovsky E. and Shraiman B. I., (2002), Olfactory search at high Reynolds number, *Proceedings of the National Academy of Science U.S.A, vol. 99, pp. 12589-12593*

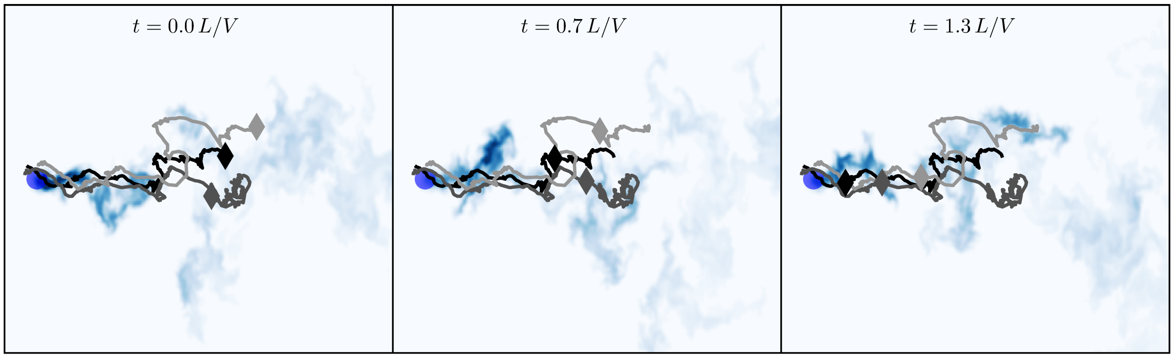

Figure 1: *Trajectories of three independent agents and snapshots of the scalar field at three times. Diamonds denote the agents' positions, while the blue circle marks the area where agents can detect and reach the source. The reference length scale L is of the order of the domain size, and V is the mean flow velocity in the horizontal direction.*

On the flow statistics and dynamics of axial rotating turbulent pipe flows: A DNS study

Lei Yang [1], Jie Yao [1]

[1] Advanced Research Institute of Multidisciplinary Sciences, Beijing Institute of Technology, Beijing, China

key-words: pipe flow, rotating turbulence

Abstract:
Rotating turbulence often occur in many industrial applications such as rotary machinery, food processing, turbines, and pumps, and understanding the characteristics and behaviour of flow in these systems can provide the fundamental principles governing fluid flow and turbulence, which can in turn contribute to the development of better turbulent models. This study conducts direct numerical simulation of turbulent flow in a $10\pi R$ (R is the pipe radius) long pipe with axial rotation, considering Reynolds numbers Re_τ up to 1000 and rotation numbers $N = \Omega R/U_b$, where Ω is the rotational angular velocity and U_b is the bulk velocity. The results show that the friction factor under the effect of rotation number is complicated. For larger $Re_{\tau,0}$ (e.g., 550 and 1000), the friction factor decreases with increasing rotation number, while for $Re_{\tau,0} = 180$, the minimum Reynolds number considered, the friction factor decreases first and then increases with the rotation number, achieving the minimum at $N = 0.5$. Scaling laws for the mean centerline axial velocity, mean axial, azimuthal velocity, and the minimum azimuthal velocity are proposed, which also take the effect of rotation into consideration and are in contrast to the usual inner-scaled laws. And the new scaling laws all show a better agreement with the DNS data. The analysis of energy flux box reveals that rotation enhances the production of the fluctuating field of axial velocity from the mean field of axial velocity, and also the convection between u'_r and u'_θ. In addition, the mean azimuthal velocity is no longer 0. The azimuthal velocity under rotation is only maintained by the production from u'_r and u'_θ. As for dissipation, rotation enhances the dissipation of U_θ and u'_θ, and reduces the dissipation of U_z, u'_r, and u'_z. Examination of the turbulent structures highlights the role of rotation in widening, elongating, and inclining the streaks structures. At high rotation numbers, clear strengthening of turbulence is observed in the core part of the flow, with a obvious outer peak in the pre-multiplied spectra which indicates very-large scale motions (VLSMs) emerge under the influence of rotation.

Momentum and heat transfer in turbulent channels with drag-increasing riblets

S. Cipelli [1], N. Rapp [1], B. Frohnapfel [1] and D. Gatti [1]

[1] Institute of Fluid Mechanics, Karlsruhe Institute of Technology (KIT), Karlsruhe, Germany

key-words: riblets, friction, Reynolds analogy

Abstract:
Of the many different kinds of surface roughness, riblets stand out not only for their drag-reducing regime at low viscous sizes [1] but also for their divergence from the typical k-roughness regime at high l_g^+ values, where l_g^+ is the square root of the groove cross-section. Von Deyn, Gatti & Frohnapfel [2] demonstrated that these anisotropic surfaces exhibit a peak in friction drag at approximately 50 wall units, after which their drag increase relative to a smooth surface becomes independent of the geometry size.
On the one hand, it seems reasonable that this type of surface should not behave exactly like a canonical random rough surface due to the absence of pressure drag resulting from homogeneity along the streamwise direction. However, the physical reason behind this behavior remains unclear, necessitating a numerical investigation to gain deeper insight into the underlying physics.
In this context, we perform Direct Numerical Simulations of turbulent channel flows with riblets in the drag-increasing regime, spanning a range of riblet sizes between $l_g^+ = 20$ and 200 to replicate the behavior observed experimentally by von Deyn, Gatti & Frohnapfel [2]. The riblet geometry, in terms of cross-section shape, is fixed, with a height-to-spacing ratio of $k/s = 0.38$ and a tip angle of $\alpha = 60°$. The riblet size in outer units (l_g) ranges from 0.05 to 0.24, and different l_g^+ values are obtained by varying the friction Reynolds number between 200 and 900. Preliminary results include four different geometries with sizes $l_g = (0.12, 0.12, 0.24, 0.24)$ and $l_g^+ = (30, 50, 50, 100)$, respectively. The implementation of a passive scalar also allows for a heat transfer analysis in the context of forced convection with a unitary Prandtl number. Simulations are run for 80 large-eddy turnover time units.
In Figure 1, we plot the friction curve in terms of shift in the mean velocity profile, ΔU^+. In this case, ΔU^+ is calculated from the friction coefficients (C_f) of the smooth and ribbed cases, for a proper comparison to the experimental results. However, directly comparing the mean velocity profiles would yield very similar results. As expected, while the $l_g^+ = 30$ case follows the prediction of the k-roughness regime, the cases at $l_g^+ = 50$, and especially 100, significantly deviate from it. Friction appears to be largest at $l_g^+ \approx 50$, while it decreases slightly for the $l_g^+ = 100$ case, perfectly matching the experimental data. Further ongoing simulations will confirm whether ΔU^+ reaches a constant value for increasingly larger viscous sizes. The current understanding of this behavior is that, as the Reynolds number increases, the buffer layer is compressed on the wall surface. As the riblet walls grow larger in viscous units, they may be perceived as locally smooth by wall turbulence. This, combined with the absence of pressure drag, may explain why further increases in the Reynolds number do not lead to increases in ΔU^+.
When considering ribbed surfaces, Rouhi et al.[3] showed that certain geometries have the ability, to some extent, to favorably break the Reynolds analogy. This means that in some cases, heat transfer (measured as C_h, the Stanton number) can be increased more than friction, offering interesting prospects for industrial applications. It was also demonstrated that this capability is linked to the emergence of Kelvin-Helmholtz rollers in the near-wall region. Preliminary results, plotted in Figure 2, show that the simulated geometries are very close to the Reynolds analogy prediction $RA = RA_0$, where $RA = 2C_h/C_f$. The one case that stands out is the one at $l_g^+ = 50$, which features a ratio of $RA/RA_0 \approx 1.02$, favourably breaking the Reynolds analogy. Further analysis will explore the physics of this phenomenon in more detail, supported by ongoing parametric simulations.

References

[1] Bechert D.W., Bruse M., Hage W., Van Der Hoeven J.G.T. & Hoppe G., (1997), Experiments on drag-reducing surfaces and their optimization with an adjustable geometry, *Journal of Fluid Mechanics, vol. 338, pp. 59-87*

[2] von Deyn L.H., Gatti D. & Frohnapfel B., (2022), From drag-reducing riblets to drag-increasing ridges, *Journal of Fluid Mechanics, vol. 951, A16*

[3] Rouhi A., Endrikat S., Modesti D., Sandberg R.D., Oda T., Tanimoto K,. Hutchins N. & Chung, D., (2022), Riblet-generated flow mechanisms that lead to local breaking of Reynolds analogy, *Journal of Fluid Mechanics, vol. 951, A45*

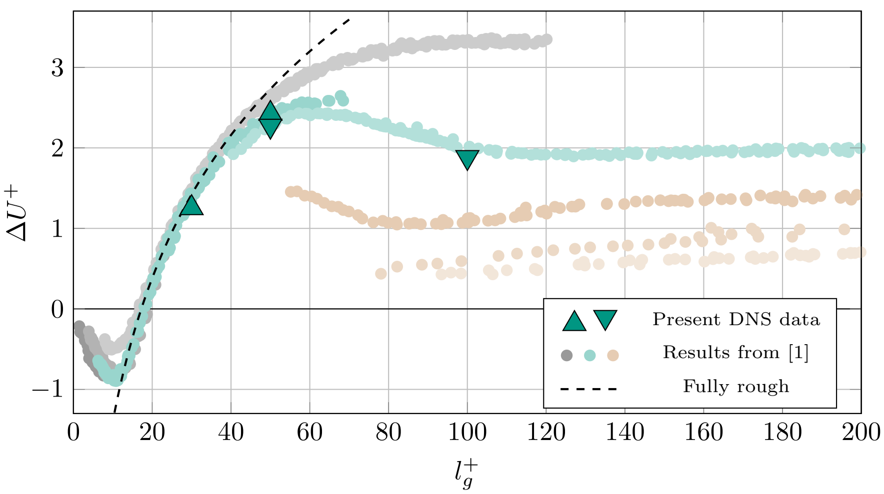

Figure 1: *ΔU^+ values from present DNSs are compared to the experimental data from von Deyn, Gatti & Frohnapfel [2]. Green markers indicate geometries with the same cross-section shape as the simulated ones, brown markers represent different trapezoidal geometries, and gray markers correspond to triangular riblets. The dashed line represents the fully rough regime.*

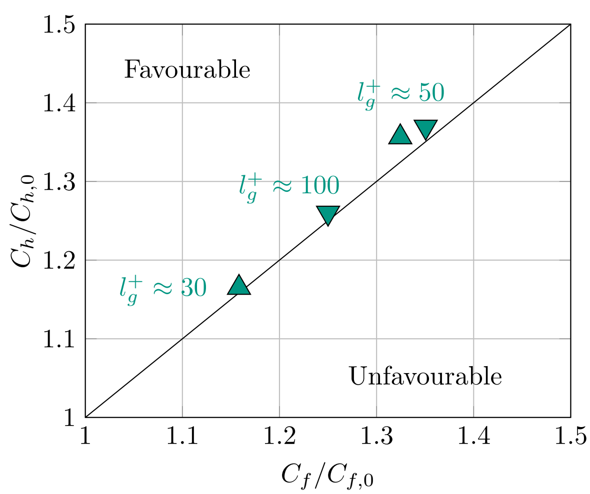

Figure 2: *Changes in Stanton numbers (C_h) are compared to changes in friction coefficients (C_f) relative to the reference smooth channel data ($\cdot_0$). The line with unitary slope represents the Reynolds analogy line, dividing the domain into two regions: one where the increase in heat transfer exceeds the increase in friction (favorable breaking of the Reynolds analogy) and another where friction increases more than heat transfer (unfavorable breaking).*

Identity variation of turbulent spots in pipe flow associated with multigenerational splits, reconnect and re-splits

X. Wu[1], P. Moin[2] and R.J. Adrian[3]

[1] Department of Mechanical & Aerospace Engineering, Royal Military College, Kingston, Canada
[2] Center for Turbulence Research, Stanford University, Stanford, USA
[3] Aerospace & Mechanical Engineering, Arizona State University, Tempe, USA

key-words: Pipe Flow, Turbulent Spot, Transition, Split, Turbulence

Abstract:
The development of turbulent spots dictates the nature of pipe flow transition in the theoretically important Reynolds number range $2000 < Re < 3000$, based on the diameter $2R$ and the bulk velocity V. At these low Reynolds numbers, some turbulent spots may split into two units with the child spot appearing downstream of the parent (Lindgren [1]). Research in this field has been centered around the notion of equilibrium puff [2]. It is widely believed that an equilibrium puff translates through the pipe as a frozen eddy until a Reynolds-number-dependent probability dictates it to either split or decay; and the competition between split and decay governs whether turbulence spreads or not at low Reynolds numbers [3]. We present direct simulation results on short-duration, wedge-type and plug-type, inlet disturbances developing spatially through a 1000 radii-long fully-developed laminar pipe flow at $Re = 2150, 2300$ and 2500. The computational mesh size is $32768 \times 200 \times 256$ in the axial, radial, and azimuthal directions, respectively. We seek answers to the following questions: (1) What does an equilibrium puff do while waiting for its turn to split? Is split a sudden memoryless event or a gradual process with some unknown hysteresis effect? How is puff identity affected by such a hysteresis effect, if it does exist? (2) Is decay a totally separate factor from split? (3) What is the representative type of vortex inside a pipe turbulent spot? We found that the representative constitutive structure of these spots (puffs at lower Re and slugs at higher Re) is reverse hairpin vortex. Rather than waiting passively as translating frozen eddies between splits, puffs are discovered here to constantly undergo a quasi-cyclic process as manifested by a mini life cycle localized in their frontal elongated zone (potential child embryo), a result of sustained zonal axial velocity differential. This is accompanied by a quasi-cyclic oscillation in their front propagation speed, which has been masked in the prevailing statistical view of constant equilibrium puff length and speed. Decay is found to be an integral part of split rather than a totally independent factor. Most importantly, spot identity varies frequently due to a previously unknown composite process of puff development including, sequentially, multi-generational splits, reconnect, and re-splits (Figure 1 and Figure 2). This unexpected hysteresis effect of split and the associated composite process carry implications to theoretical studies modeling the critical Reynolds number at which turbulence starts to spread in pipe flow: Puff life-time and split waiting-time statistics used in theoretical predictions may be less accurate if such spot identity reset, due to reconnect and re-splits, is not tracked and included in the sampling procedure. A set of movies documenting these composite processes with remarkable clarity has been constructed.

References

[1] Lindgren E.R., (1959), Liquid flow in tubes III. *ARKIV FYSIK, vol. 16, pp. 101-112.*

[2] Wygnanski I., Champagne F.H., (1973), On transition in a pipe. Part 1. The origin of puffs and slugs and the flow in a turbulent slug. *J. Fluid Mech. vol. 59, pp. 281-335.*

[3] Song B., Barkley D., Hof B., Avila M., (2017), Speed and structure of turbulent fronts in pipe flow. *J. Fluid Mech. vol. 813, pp. 1045-1059.*

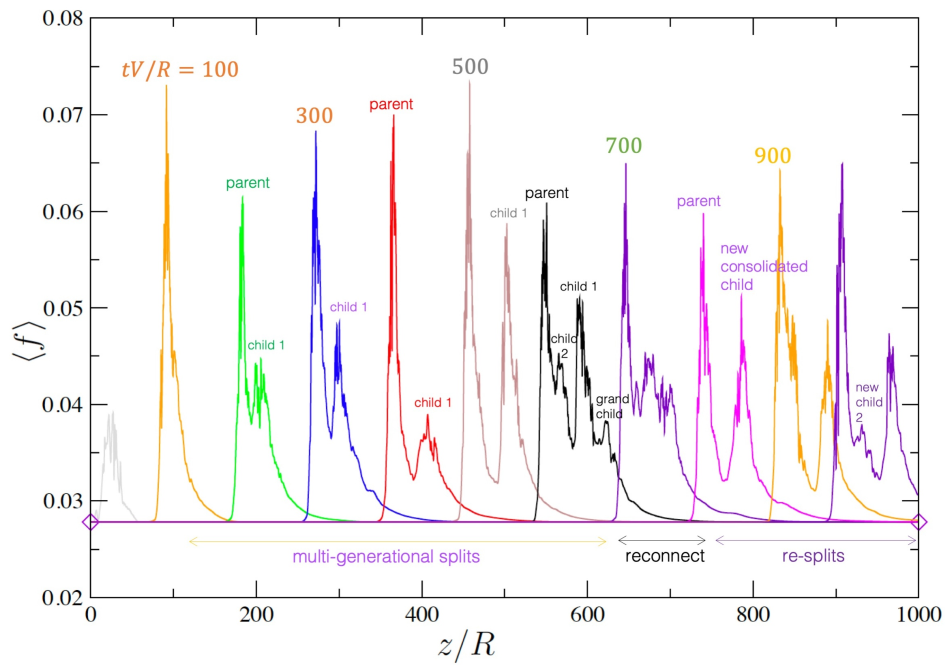

Figure 1: Circumferentially-averaged friction factor $\langle f \rangle$ as a function of axial distance z and time t at $Re = 2300$. Diamond symbol: fully-developed laminar pipe solution $f = 64/Re$. The new child at $tV/R = 800$ is a consolidation of several upstream spots as a result of the splits, reconnect and re-split composite process. Hence, the identity of this new child spot is not the same as the upstream children or the grandchild. For accurate spot life-time statistics sampling, such identity reset must be tracked.

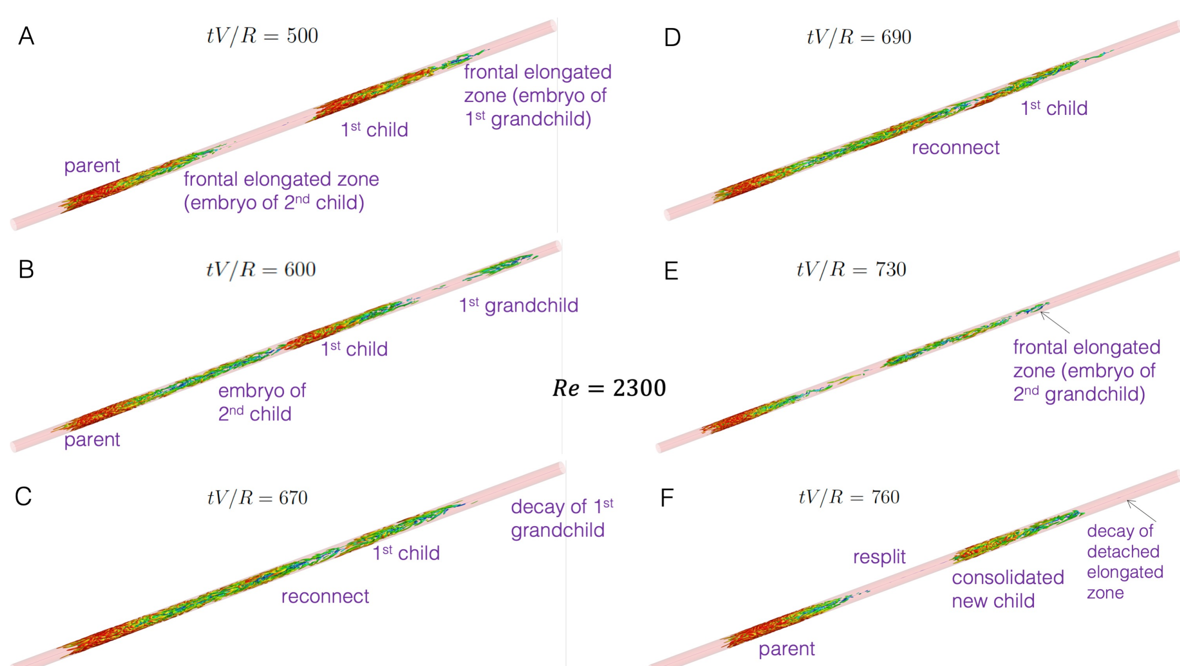

Figure 2: Multi-generational splits, reconnect and re-split composite process revealed by the iso-surfaces of swirling strength, corresponding to the skin-friction results in Figure 1. The mini life cycle of frontal elongated zone including growth, detach and decay reflects the quasi-cyclic nature of puff in low-Reynolds-number pipe flow. It is evident that puffs are not translating frozen eddies while waiting to split; they have a vivid mini life cycle; split is not a sudden mysterious event, decay is an integral part of split; spot identities are frequently reset as a result of the composite process.

Direct Numerical simulations of Taylor-Couette flows with extreme small radius inner rotating cylinders

P. Orlandi [1], and S. Pirozzoli [1]

[1] Dipartimento di Ingegneria Meccanica e Aerospaziale, Sapienza Università di Roma, Italy

key-words: Taylor-Couette, Simulation

Abstract:
The effect of the radius of curvature on the turbulent flow between two concentric cylinders, azimuthally oriented has been investigated by direct numerical simulations, at bulk Reynolds number $R_b \approx 5000$. By varying the inner radius from $r_i/\delta = 0.025$ to 95.5, (δ is the gap width) four flow regimes have been identified namely: 1) mild curvature for $r_i/\delta > 14.5$; 2) moderate curvature for $1.5 < r_i/\delta \leq 14.5$; 3) strong curvature for $0.25 < r_i/\delta \leq 1.5$; 4) extreme curvature for $r_i/\delta \leq 0.25$. For all values of curvature a region of negative turbulent kinetic energy production arises due to the displacement between the locations of zero shear and turbulent stress. While the peak of negative production is negligible for mild curvatures, it becomes increasingly pronounced as curvature intensifies, with the peak shifting closer to the inner wall. Negative TKE production is associated with an energy transfer from the small scales of turbulence to the largest scales of motion. In turbulent flows, the pressure field tends to be more coherent at larger scales compared to the velocity field. As a result, pressure fluctuations are expected to exhibit greater coherence near the inner wall, particularly for strong curvature. Indeed, flow visualisations of azimuthal flows revealed spanwise coherence in fluctuating pressure, which interacts with the fluctuating radial velocity. A misalignment between these spanwise structures leads to a strong negative correlation between pressure and radial velocity fluctuations.

The increased correlation between radial velocity and pressure results in a completely different distribution of terms in the TKE transport equation, which has never been observed in wall-bounded turbulent flows. In the region near the inner wall of strongly curved channels, the production term becomes negligible, and TKE is gained instead through pressure-velocity correlations. This significant energy gain is partially transferred away from the inner wall by triple velocity correlations, and is locally dissipated by total dissipation. It is important to note that this complete redistribution of TKE budgets occurs only under conditions of extreme curvature, where the mean TKE is higher near the inner wall than near the outer wall.

This study was mainly of academic interest, being almost impossible to reproduce in practice the set-up considered. Taylor-Couette flow largely studied in the past both experimentally and numerically is a configuration close to the one of academic interest. To our knowledge the minimum radius, up to now considered, was approximately $r_i/\delta = 0.53$ corresponding to the strong curvature regime. Since the more interesting regime is that with extreme curvature in the present study we would like to conduct numerical experiments of Taylor-Couette flow with internal radii as small as 0.025δ, to assess whether the same behaviour of the TKE budget observed in azimuthal flow is found.

To show that the azimuthal flow structures and consequently the statistics depend on the radius of the inner rotating cylinder contour lines of the radial velocity v_r are shown in figure 1. When the radius r_i is equal to the gap the structures in figure 1 d extends from the inner to the external cylinder, when r_i reduces smaller structures appear and interact with large structures in figure 1 c. The latter start to disappear at $r_i = 0.0075$ (figure 1 b) and are evanescent at $r_i = 0.0025$ (figure 1 a). These visualization have been presented at an intermediate value of Reynolds number, namely $Re = 1600$. At higher Re a fully turbulent status is characterised by smaller velocity structures.

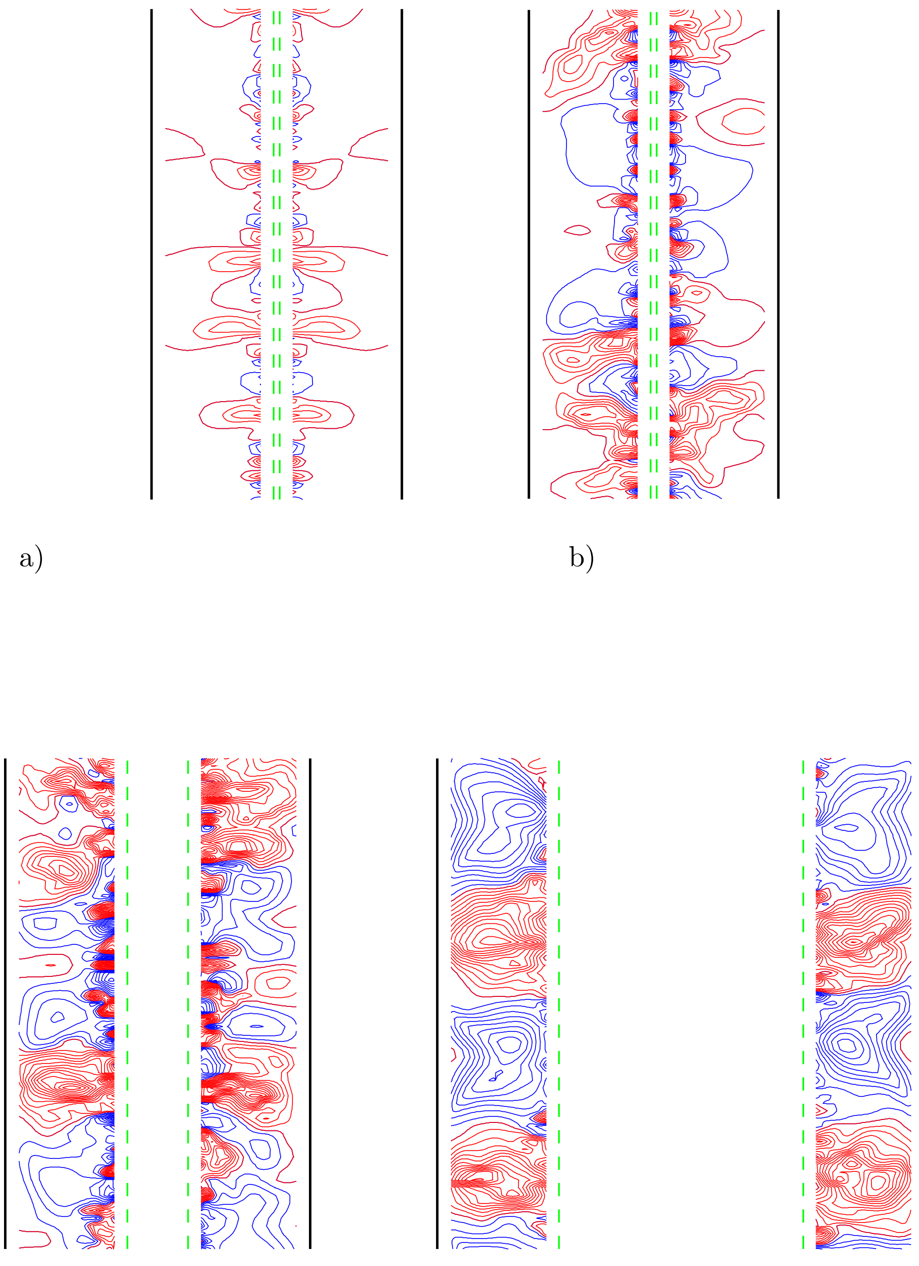

a) b) c) d)

Figure 1: *Radial velocity contours with increment* $\Delta = 0.025$*: red positive, blue negative in a cross* $x - z$ *plane, the green lines represent the inner rotating, the black the stationary cylinder; a)* $r_i = 0.0025$*, b)*$r_i = 0.0075$*, c)* $r_1 = 0.5$ *and d)* $r_i = 1$

Experimental and numerical investigations of laminarization via preconditioning in turbulent pipe flows

S. Nozarian [1], M. J. Rincón [1,2], P. Forooghi [1], M. Reclari [2] and M. Abkar [1]

[1] Department of Mechanical and Production Engineering, Aarhus University, 8200 Aarhus N, Denmark
[2] Metrology and Accreditation Department, Kamstrup A/S, 8660 Skanderborg, Denmark.

key-words: PIV, LES

Abstract:
Water utility networks are vital to modern life but face a critical challenge: substantial energy loss, primarily due to friction in extensive water pipe systems. Approximately 95% of this energy loss arises from friction [1], contributing to about 10% of global electric energy consumption [2]. Addressing this issue is pivotal for optimizing energy efficiency and enhancing sustainability in water distribution systems.

Turbulence is the main cause of frictional drag in pipe flows due to intensified momentum transport from the walls. Reducing or eliminating turbulence can greatly lower drag. Kühnen et al. (2018) [3] demonstrated that targeted velocity profile distortions can suppress turbulence, reducing friction losses by up to 90%. Practical methods to achieve this include injecting fluid through an annular gap near the walls or installing specially designed screens (here referred to as "flow preconditioners"). This research focuses on the latter approach due to its simplicity in experimental implementation and the successful proof-of-concept results.

Our experimental investigations leverage Particle Image Velocimetry (PIV) and high-precision pressure transducers to evaluate the performance of these preconditioners in achieving laminarization of turbulent flows. Figure 1 presents a schematic representation of the PIV setup alongside the measured mean streamwise velocity profiles at various sections immediately downstream of the preconditioner. Notably, these profiles exhibit an M-shaped configuration, which is a hallmark of the laminarization mechanism under study. This characteristic pattern aligns with observations reported in previous literature [2, 3], further verifying the underlying phenomena.

To complement the experimental investigations, large-eddy simulations (LES) are utilized to examine the flow dynamics both in the immediate vicinity of the preconditioner and along the extended length of the pipe. Conducted at Re $= 3800$ with a pipe length exceeding $l = 105D$, the simulations demonstrate laminarization (see Fig. 2) in both qualitative and quantitative agreement with the experimental results. These simulations offer valuable insights into the underlying mechanisms of turbulence suppression, particularly the disruption of turbulence regeneration cycles. Such understanding plays a crucial role in optimizing the design of preconditioners and assessing their scalability for broader applications.

Furthermore, to extend the applicability of this work and bridge the existing gap in the literature, this research aims to experimentally assess the effect of roughness by comparing flow behavior in smooth and rough pipes after preconditioning. The study will evaluate the potential for drag reduction in the presence of rough walls and explore the influence of wall roughness on preconditioner performance.

References

[1] Yang X. I., Pirozzoli S., and Abkar M. (2020): Scaling of velocity fluctuations in statistically unstable boundary-layer flows, *J. Fluid Mech., 886., A3*

[2] Kühnen J., Song B., Scarselli D., Budanur N. B., Riedl M., Willis A. P., Avila M., and Hof B. (2018): Destabilizing turbulence in pipe flow, *Nature Phys., 14(4)., pp.386–390*

[3] Kühnen J., Scarselli D., Schaner M. and Hof B. (2018): Relaminarization by steady modification of the streamwise velocity profile in a pipe, *Flow Turbul. Combustion, 100(4)., pp.919–943*

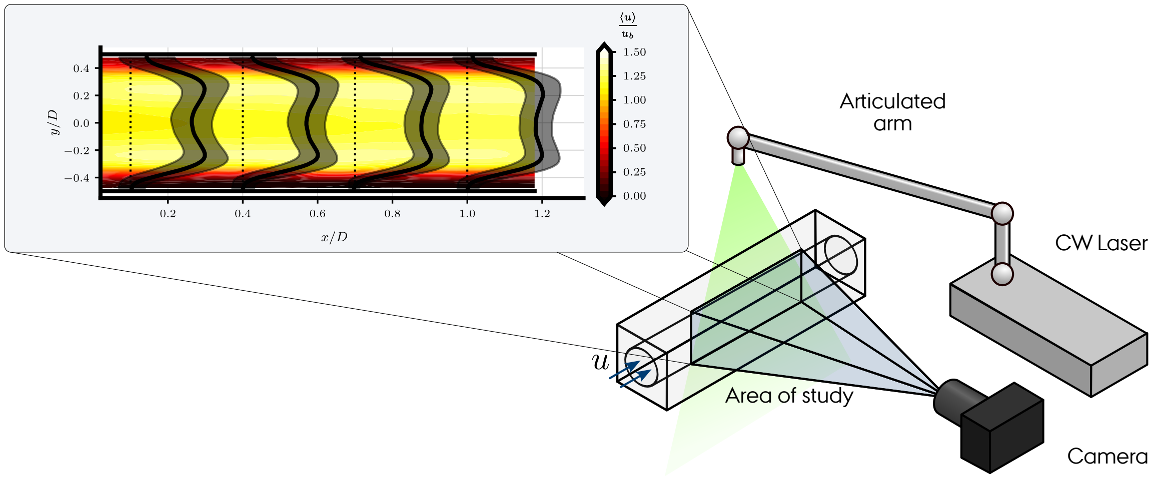

Figure 1: Schematic of the PIV setup along with PIV measurements of the normalized mean streamwise velocity profile $\langle u \rangle / u_b$ at various sections immediately downstream of the preconditioner, illustrating the M-shaped velocity profile.

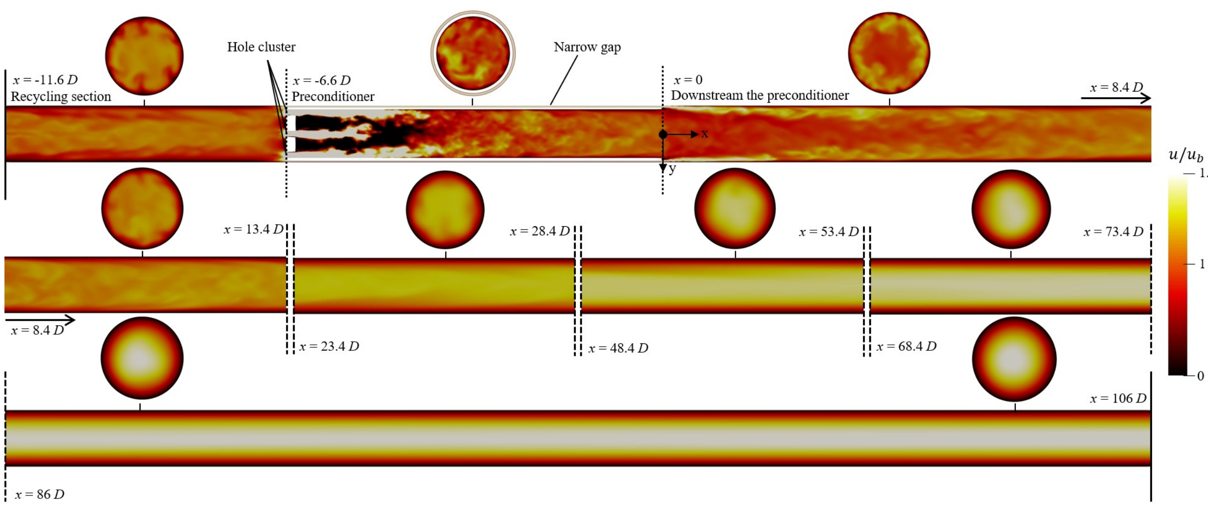

Figure 2: Visualization of the instantaneous streamwise velocity, normalized by the bulk velocity (u/u_b) in various sections of the pipe, highlighting the laminarization process resulting from preconditioning.

High Reynolds number trends of centerline mean velocity and normal stress in pipe flow

Hassan Nagib[1], Lorenzo Lazzarini[2] , Gabriele Bellani[2] and Alessandro Talamelli[2]

[1] Mechanical, Materials and Aerospace Engineering Department, ILLINOIS TECH, Chicago, USA
[2] Department of Industrial Engineering, University of Bologna, Forli, Italy

key-words: High Reynolds Number, Pipe Flow, Centerline Trends

Abstract:

The CICLoPE facility at the University of Bologna in Forli, Italy, is a unique facility providing fully developed pipe flow up to Reynolds numbers near Re_τ of 50,000 with exceptional spatial resolution and stable operating conditions as described by Fiorini [1] and Mascotelli [2], and illustrated here in figure 1. Measurements obtained over the last two years, on the centerline of the pipe in the fully developed test section, with pitot probes for streamwise mean velocity (+/- 0.2% accuracy) and hot wires for the streamwise normal stress (+/- 5% accuracy) are reported here and compared to other data.

Figure 2 compares the measurements to earlier data from CICLoPE by Fiorini [1] and Mascotelli [2], to the superpipe data of McKeon et al. [3], and to the DNS results of Pirozzoli [4]. The large amount of data obtained with several pressure transducers and repeated over one year provide a reliable correlation of the centerline velocity to equal (1/0.44) $\mathrm{Ln}(Re_\tau)$ + 7.9, providing a Kármán coefficient for pipe flow of 0.44.

Figures 3 and 4 reveal high Reynolds number trends of the streamwise normal stress to be constant and equal to 0.85, the skewness to equal -0.5 and the kurtosis to equal 3.5, all with high degree of certainty.

References

[1] Fiorini, T. (2017*). Turbulent pipe flow-high resolution measurements in ciclope,* PhD thesis, University of Bologna.

[2] Mascotelli, L. (2020*). High Reynolds number experiments in the long pipe at CICLoPE,* PhD thesis, University of Bologna.

[3] McKeon, B.J., Zagarola, M.V. & Smits, A.J., (2005), *A new friction factor relationship for fully developed pipe flow, J. Fluid Mech. 538, 429–443.*

[4] Pirozzoli S., (2024), On the streamwise velocity variance in the near-wall region of turbulent flow, *Journal of Fluid Mechanics, vol. 989: A5.*

[4] Hultmark, M., Vallikivi, M., Bailey, S. C. and Smits, A. J. (2012), *Turbulent pipe flow at extreme Reynolds numbers. Physical Review Letters 108, 094501.*

[5] Ono, M., Furuichi, N. and Tsuji, Y. (2023), *Reynolds number dependence of turbulent kinetic energy and energy balance of 3-component turbulence intensity in a pipe flow. J. Fluid Mech. 975: A9.*

Figure 1: *CICLoPE facility*

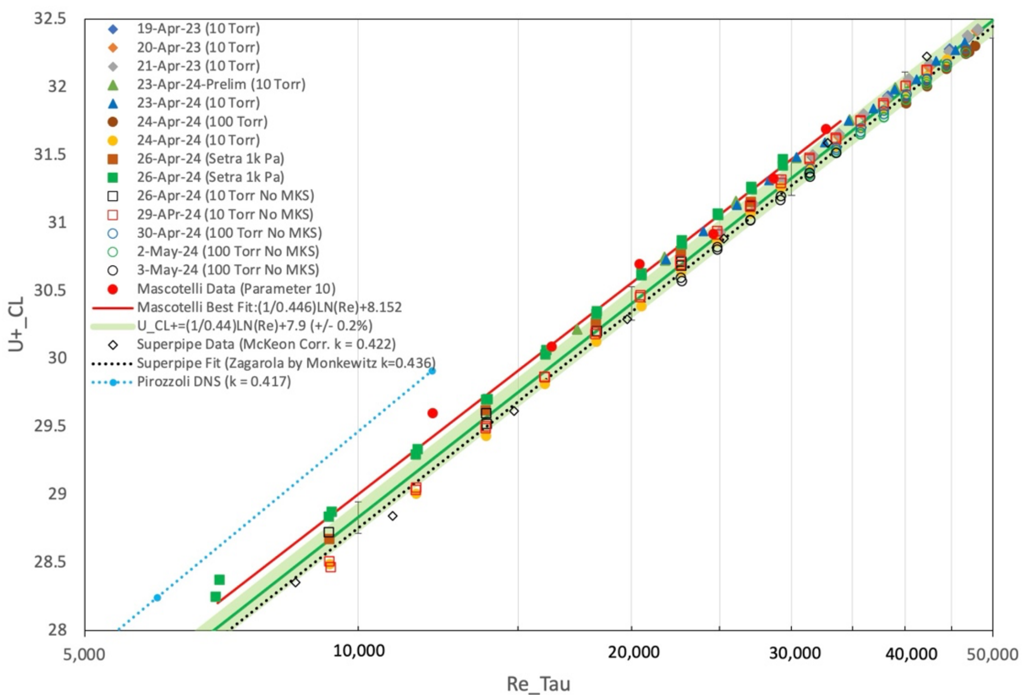

Figure 2: *Centerline mean velocity from CICLoPE compared to other data*

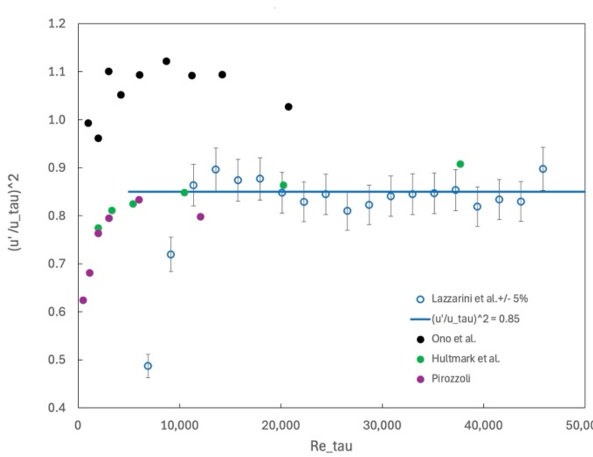

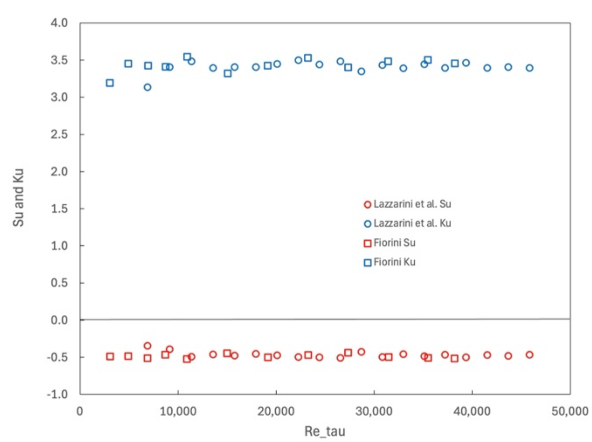

Figure 3: *Centerline normal stress with comparison*

Figure 4: *Skewness and kurtosis from CICLoPE*

On the inertial sublayer of the mean velocity profile in turbulent wall-flows

Joe Klewicki and Jimmy Philip

Department of Mechanical Engineering, University of Melbourne, Parkville, Australia

key-words: Turublent Wall-Flows, Logarithmic Law, Inertial Sublayer

Abstract:
The notion of an inertial sublayer in turbulent flows has proven useful relative to both wavenumber and physical space representations, e.g. [1]. In wall-bounded flows (say, fully-developed channel flow), the inertial sublayer is manifest in physical space as an interior domain between the wall and centreline. This domain resides sufficiently far from the wall such that the flow dynamics are dominated by inertia, but remains well-interior to the centreline such that the direct influences of the overall boundary conditions are negligible. Under a number of classical wall-flow descriptions the inertial sublayer is co-located with the position of the logarithmic mean velocity profile, while the inertial sublayer traits just described are connected to the conditions for the existence of a log profile, e.g. [1]. The mean momentum equation-based analyses used in this study also directly associate the inertial sublayer with the log layer. An advantage of this framework, however, is that it provides guidance for estimating the upper and lower bounds of the inertial sublayer by using the analytical properties associated the existence of a log profile.

Studies seeking to describe wall-flow structure often involve the estimation of properties on the inertial sublayer. To obtain high fidelity estimates that accurately convey scaling trends toward the asymptotic state, it is thus advantageous to have precisely defined bounds for the inertial sublayer. Toward this aim, inertial sublayer inner and outer bounds are developed for the canonical wall-flows. These Reynolds number dependent bounds are independently founded in the properties of the mean dynamical equation and thus for any given flow are objectively determinable prior to estimating the statistical quantities of interest. Enjoying support from both analytical and empirical results, the inner bound is directly connected to the onset of the domain where the viscous force in the mean dynamical equation loses leading order [2]. While, in principle, the present theoretical framework provides a specification for the outer bound, practical issues associated with data uncertainty must also be considered. This is because the outer bound depends on the Reynolds stress profile curvature, which becomes very small with increasing distance from the wall. In this regard, figure 1 shows a sequence of inertial sublayer upper bound estimates with increasing Reynolds number. These estimates reflect a fixed precision in measuring the profile curvature of the Reynolds stress, $\langle uv \rangle$. With increasing Reynolds number, the inner bound is shown to move to increasing y^+, while as depicted in figure 1 the outer bound moves to decreasing y/δ, where $y^+ = yu_\tau/\nu$ and y/δ are the inner and outer normalized wall-distances, respectively. With the bounds specified, mean profile properties are estimated and assessed on the inertial sublayer using available direct numerical simulation (DNS) and high-quality physical experiment data over a range of friction Reynolds numbers, $\delta^+ = \delta u_\tau/\nu$. For example, figure 2 shows estimates from channel flow DNS for the key parameter in the mean profile similarity solution, ϕ_c, plotted as a function of δ^+.

The present theory yields a similarity solution in the form of a log-linear mean velocity profile on the inertial sublayer [3]. As such, the present results are compared with, and discussed relative to, a recent adaptation of the two-length-scale matched asymptotic approach that also yields a log-linear profile [4].

References

[1] Tennekes H. and Lumley J.L., (1972): *A First Course in Turbulence*, MIT Press.

[2] Wei T., Fife P., Klewicki J. and McMurtry P., (2005), Properties of the mean momentum balance in turbulent boundary layer, pipe and channel flows, *Journal of Fluid Mechanics, vol. 522, pp. 303.-327.*

[3] Klewicki J., (2021), Properties of turbulent channel flow similarity solutions, *Journal of Fluid Mechanics, vol. 915, pp. A39.*

[4] Monkewitz P.A. and Nagib H.M, (2023), The hunt for the Karman 'constant' revisited, *Journal of Fluid Mechanics, vol. 967, pp. A15.*

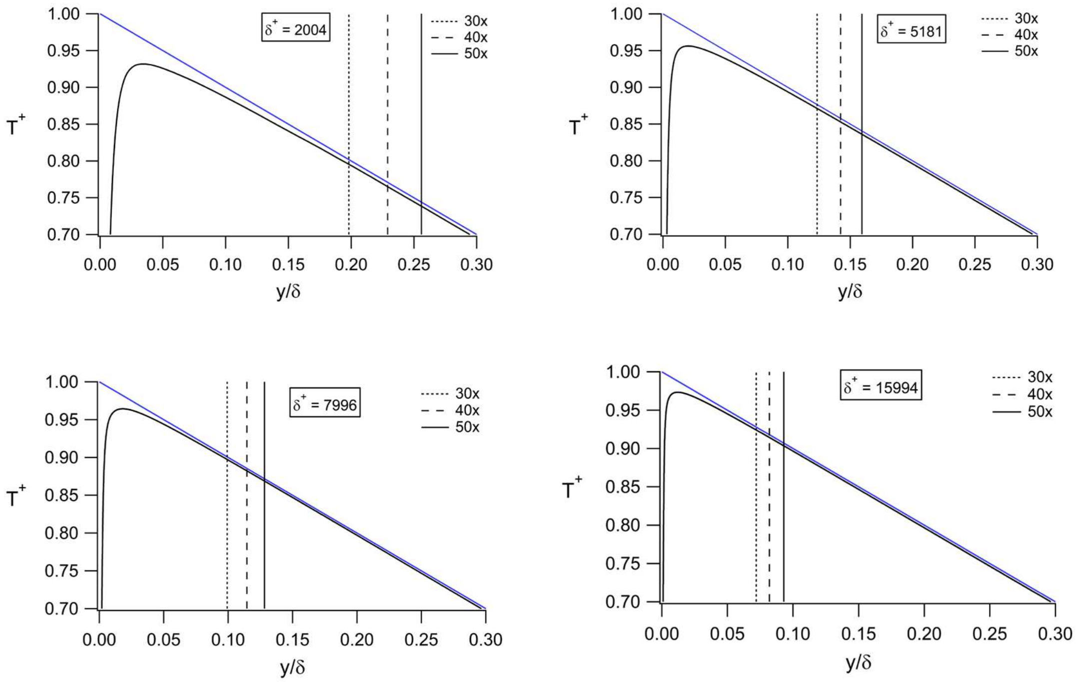

Figure 1: *Outer layer profiles of the Reynolds shear stress $T^+ = \langle uv \rangle^+$ in turbulent channel flow for various Reynolds numbers. Vertical lines denote criteria indicating the position where the ratio of the constant term in the equation for dT^+/dy^+ is thirty, forty or fifty times greater than the variable term that accounts for the curvature of the Reynolds stress. Data are from the DNS of Hoyas and Jimenez (2006), Lee and Moser (2015), Yamamato and Tsuji (2018,2024) and Hoyas et al. (2022).*

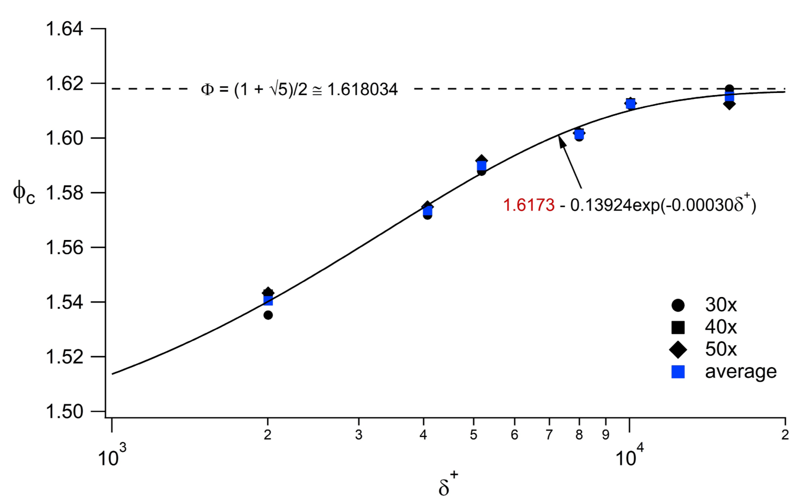

Figure 2: *Estimates of ϕ_c on the inertial sublayer in turbulent channel flow as a function of δ^+. This parameter, which is predicted to attain constancy as $\delta^+ \to \infty$, becomes apparent when generating the invariant form of the mean momentum equation that leads to the resulting log-linear similarity solution for the mean velocity profile.*

High-order moment scaling of near-wall turbulence for arbitrary velocities: Extendeding the symmetry approach

M. Oberlack [1,2], S. Hoyas [3], and S. Görtz [1,2]

[1] Chair of Fluid Dynamics, Technische Universität Darmstadt, Germany
[2] Graduate School of Computational Engineering, Technische Universität Darmstadt, Germany
[3] Instituto Universitario de Matemática Pura y Aplicada, UP València

key-words: Fundamentals, wall-bounded turbulence, turbulent scaling laws, symmetry theory

Abstract:
We derive and validate scaling laws for arbitrary turbulent one-point velocity moments in wall-bounded flows. The scaling laws are derived using a symmetry analysis of the underlying set of Navier-Stokes equations from which the infinite moment hierarchy is derived in [1] and are therefore first principle-based. They are validated using new DNS data for a channel flow, revealing a hidden Reynolds number dependency and the fact that scaling is determined by the lowest order moment.
The higher order scaling laws are given for both the wall-near logarithmic as well as the core region of the channel flow. For one-point velocity moments of higher order, we obtain for the logarithmic region

$$\overline{U^n_{[i]}}^{+} = C_{[i]_{\{n\}}} \left(x_2^+ + A\right)^{\omega(n-1)} + B_{[i]_{\{n\}}} + L_{[i]_{\{n\}}} x_2^+, \qquad \text{for } n \geq 2, \tag{1}$$

and for the core region in deficit form

$$\frac{\overline{U^n_i}^{(0)} - \overline{U^n_i}}{u^n_\tau} = C'_{i,n} \left(\frac{x_2}{h}\right)^{n(\sigma_2-\sigma_1)+2\sigma_1-\sigma_2}, \tag{2}$$

where the bar denotes ensemble averaging. For the validation in the current work, we focus on the velocity moments in wall-normal and spanwise direction with $i = 2, 3$ without any influence of the mean flow, thus these moments are more sensitive to errors. For a similar validation of the logarithmic law for the averaged mean velocity, see [2] where the von Kármán constant is obtained to $\kappa = 0.394$. The scaling laws (1) and (2) are validated using new DNS data of a plane turbulent channel flow, with a Reynolds number of $Re_\tau = 10^4$ using the code LISO with a grid of about 80 billion points. For further details on this simulation, the reader is referred to [2]. However, for the current comparison, the length of the DNS was doubled again compared to the aforementioned work. Figures 1 and 2 show excellent agreement comparing the data with the scaling law (1) for the logarithmic region, where the value $\omega = 0.1$ has been taken from the U_1 moments and is also the perfect fit for the U_2 and U_3 moments. Consequently, the prediction of this group parameter being directionally independent meets the data. Considering the core region, the same holds for the values $\sigma_1 = 1.95$ and $\sigma_2 = 1.94$ in (2), which were obtained in [1] for U_1 moments and are also the optimal fit for the U_2 and U_3 moments as the comparison with the DNS data in Figures 3 and 4 shows. Having validated the scaling laws, we present an approach to the Reynolds-dependency of the group parameters in the logarithmic region. We show by means of asymptotic methods how viscosity and thus Reynolds number influences the boundary condition for the scaling laws. This is exemplary shown in Figures 5 and 6 for the second order moment in streamwise direction. Currently, we are limited to streamwise velocities because only these data are available over a wide range of Reynolds numbers.

References

[1] Oberlack, M., Hoyas, S., Kraheberger, S., Alcántara-Ávila, F. and Laux, J., (2022), Turbulence Statistics of Arbitrary Moments of Wall-Bounded Shear Flows: A Symmetry Approach, *Phys. Rev. Lett., vol. 128, pp. 024502-024508*

[2] Hoyas, S., Oberlack, M., Alcántara-Ávila, F., Kraheberger, S., Laux, J., (2022), Wall turbulence at high friction Reynolds numbers, *Phys. Rev. Fluids, vol. 7, pp. 014602-014612*

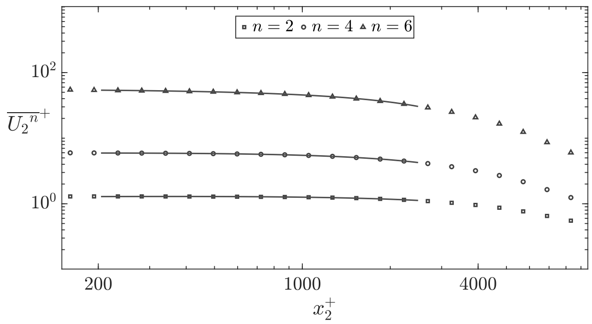

Figure 1: *Comparison between DNS data and scaling law* (1) *for velocity moments* $\overline{U_2^n}$ *in the log-region.*

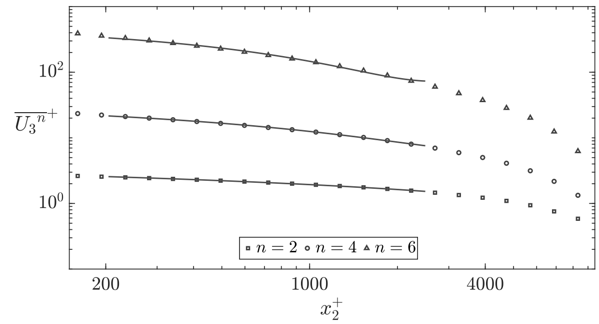

Figure 2: *Comparison between DNS data and scaling law* (1) *for velocity moments* $\overline{U_3^n}$ *in the log-region.*

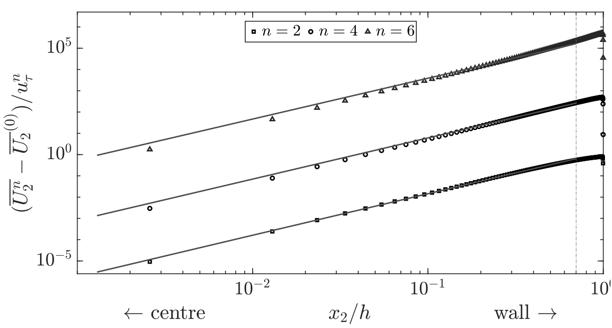

Figure 3: *Comparison between DNS data and scaling law* (2) *for velocity moments* $\overline{U_2^n}$ *in the core region.*

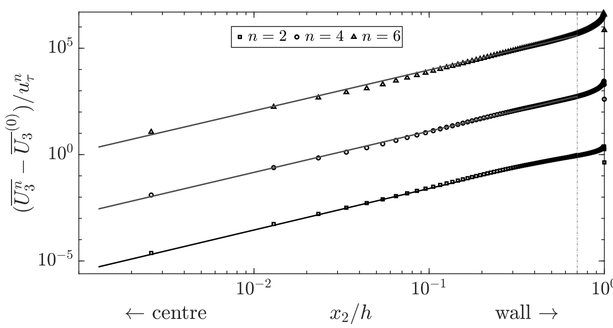

Figure 4: *Comparison between DNS data and scaling law* (2) *for velocity moments* $\overline{U_3^n}$ *in the core region.*

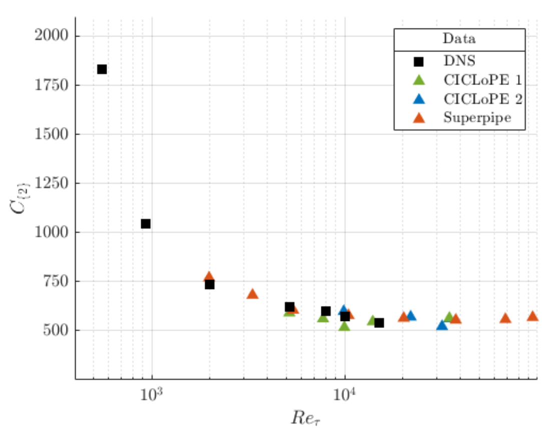

Figure 5: Values for scaling prefactor $C_{[1]_{\{2\}}}$ from eq. (1) fitted for $Re_\tau = 180 \dots 9.4 \cdot 10^4$

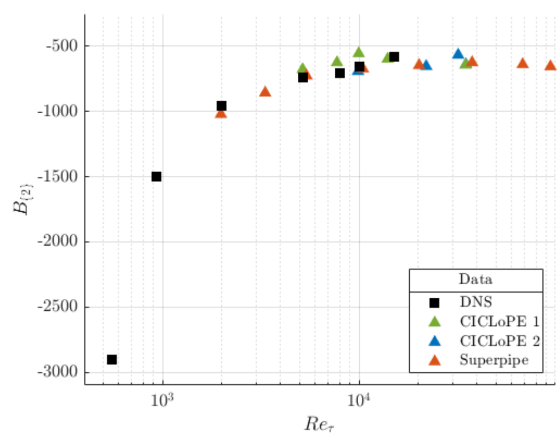

Figure 6: Values for constant $B_{[1]_{\{2\}}}$ from eq. (1), fitted for $Re_\tau = 180 \dots 9.4 \cdot 10^4$

iTi Conference on Turbulence X

July 27- 30, 2025 | Bertinoro, Italy

Poster Presentation

Generalized Scaling of Wall-Bounded Turbulent Flow Structure

T.-W. Lee[1] and J.E. Park[1]

[1] Aerospace and Mechanical Engineering, SEMTE, Arizona State University, Tempe, AZ, USA, attwl@asu.edu

key-words: Theory, scaling, wall-bounded flows

Abstract:
An alternative set of scaling properties for wall-bounded flows is presented. For Reynolds stresses (u'^2, v'^2, $u'v'$), if we take the gradients then generalizable, self-similar structure emerges, as shown in Fig. 1 for channel (CF) and boundary-layer flows over a flat plate (FP). In Fig. 1, the profiles are "bi-normalized", by the peak magnitude of the near-wall maximum and far-field minimum, respectively. This gradient scaling can be extended to adverse pressure-gradient flows (Fig. 2) and compressible (Fig. 3), with minor modifications. The physical origins of the self-similarity in the first- or second-gradient space will be discussed during the presentation, and in the final version of the paper.

For the mean velocity, an inverse operation of taking a running integral (Eq. 1) leads to a near-universal scaling, for different types of turbulent flows (incompressible, compressible and adverse pressure gradient). An example of this transformation from the mean to the integral velocity profiles is shown in Fig. 4, for compressible channel flow.

$$I(U^+) = \int_0^{y+} U(y^+)dy^+ \tag{1}$$

The collapse of the integrated velocities near the wall is evidently from the use of inner coordinate (y^+), which summarizes the effect of viscosity relative to the mean momentum (shear stress). However, this effect persists through the boundary layer, as the additive momentum is also scaled by y^+. As noted above, the same property for the integrated mean velocity is found for compressible and adverse pressure-gradient flows. These scaling characteristics have been validated using DNS data by Lee and Moser [1], Soria et al. [2], and Gerolymos and Vallet [3].

References

[1] Lee, M. and Moser, R. D. (2015) Direct numerical simulation of turbulent channel flow up to Re_t ~ 5200, *Journal of Fluid Mechanics* 774:395-415.
[2] Soria, J., Atkinson, C., Kitsios, V., Sekimoto, A., Senthil, S., Jimenez, J. (2019) Statistics and TKE Budgets of Beta = 0, 1, 39 Turbulent Boundary Layer DNS. https://doi.org/10.26180/5d1f2b59e66ea https://bridges.monash.edu/articles/dataset/Statistics_of_Beta_0_1_39_Turbulent_Boundary_Layer_DNS/8790785/4
[3] Gerolymos, G.A. and Vallet, I. (2023) Scaling of pressure fluctuations in compressible plane channel flows, Journal of Fluid Mechanics, Vol. 958, A19.

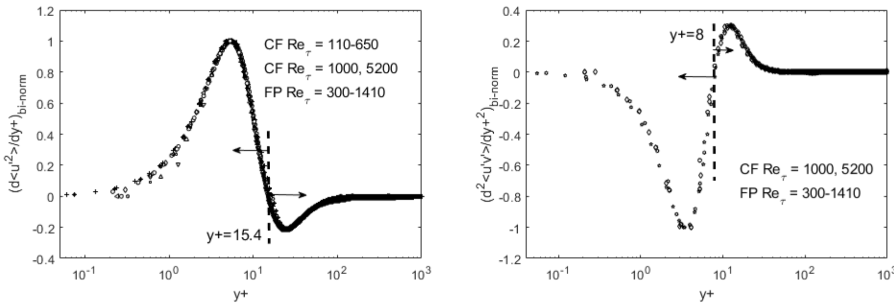

Figure. 1. The gradient scaling of $d<u'^2>/dy^+$ profiles in incompressible channel flows. The DNS data from Lee and Moser [1] for CF are used.

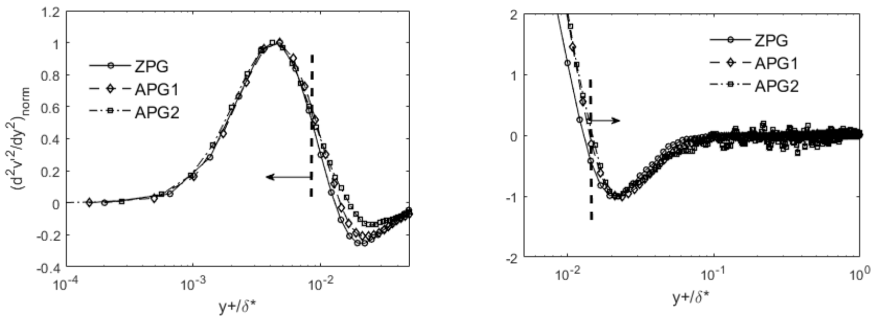

Figure 2. Scaling of the $d^2< v'^2>/dy^{+2}$ profiles for the near-wall (left) and outer region (right) for adverse pressure-gradient flows. DNS data from Soria et al.[2]are used.

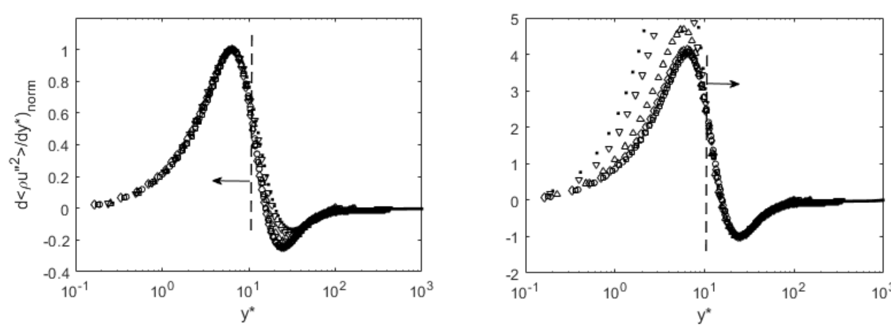

Figure 3. Scaled $d^2<\rho v''^2>/dy+^2$ structure for the near-wall (left) and far regions (right), in compressible channel flows. The DNS data from Gerolymos and Vallet [3]are used.

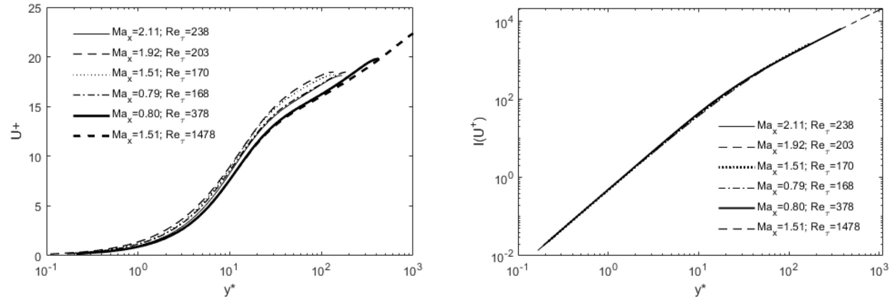

Figure 4. Mean velocity (left) and integrated U^+ (right) profiles for compressible channel flows. The DNS data from Gerolymos and Vallet [3]are used in Eq. 1.

Structures and cascades for each wall-normal mode in wall-less models of wall-bounded turbulent flows

M. Takaoka [1]

[1] Department of Mechanical Engineering and Science, Doshisha University, Kyotanabe, Kyoto, Japan

key-words: Wall-bounded flow, Laminar-turbulent transition, Stripe structures, Local-flux vectors

Abstract:
Relationship between large-scale structures in real space and local-flux vectors in wavenumber space is investigated in laminar-turbulent transition in wall-less models of wall-bounded turbulent flows. Eliminating near wall region, Mizuno and Jiménez [1] claim the effect from near wall region to outer layer is mainly modifying length scales. Waleffe [2] showed the self-sustaining process of streaks may be reproduced by periodic flow obtained by Galerkin approximation with free-slip boundary conditions. Chantry *et al* [3] demonstrated that the model Waleffe flow exhibits its transition belongs to 2+1 directed percolation universality class. These results suggest that the laminar-turbulent transition in wall-bounded turbulent flow may be examined under periodic boundary conditions without walls. Recently, we[4],[5] have introduced **local flux vectors** of invariants to reveal anisotropic structures of their cascades in wavenumber space.

We have performed numerical simulations of the trigonometric-mode model of a planar shear flow by employing the poloidal-toroidal plus mean-mode representation as done by Chantry *et al* [3]. The velocity is decomposed into a sum of wall-normal (y-direction) mode as $\boldsymbol{u}(\boldsymbol{x},t) = \sum_n (u_n(x,z,t)\mathrm{CsSn}(ny), v_n(x,z,t)$ $\mathrm{SnCs}(ny), w_n(x,z,t)\mathrm{CsSn}(ny))$, where $\mathrm{CsSn}(2ny) = \cos(2n\beta y)$, $\mathrm{CsSn}((2n-1)y) = \sin((2n-1)\beta y)$, $\mathrm{SnCs}(2ny) = \sin(2n\beta y)$, $\mathrm{SnCs}((2n-1)y) = \cos((2n-1)\beta y)$, and $\beta = \pi/(2H)$. The relationship between the structures of velocity-fluctuation field on streamwise(x)-spanwise(z) plane and the focus wavenumber of energy cascade on (k_x, k_z)-plane for each $n\beta y$-mode are studied. Figures 1, 3, 5, and 7 provide examples of instantaneous structures of representative-speed field, $\overline{U}_n(x,z,t) = \sqrt{u_n^2 + v_n^2 + w_n^2}$, in (x,z)-plane for each $n\beta y$-mode with $n = 0, 1, 2$, and 3 respectively. Figures 2, 4, 6, and 8 respectively show anisotropic structures observed in the local-flux vectors (LFVs) of averaged energy cascade for corresponding each $n\beta y$-mode. In these right figures, where shown are the low-wavenumber range, we can see that the energy flows into localized wavenumber region, which is called **focus wavenumber** here. It is found that for each $n\beta y$-mode the focus wavenumber is consistent with the real space structure of $\overline{U}_n$ as expected. By changing the Reynolds number, I will report the consistency between focus wavenumbers and real space strucure for each stage of laminar-turbulent transition. Since $\mathrm{CsSn}(ny)$ and $\mathrm{SnCs}(ny)$ take large value at different y-position, I will discuss the energy flux in y-direction by comparing the distribution of energy for different $n\beta y$-modes.

References

[1] Mizuno Y. and Jiménez J., (2013), Wall turbulence without walls, *J. Fluid Mech., vol. 723, pp.429-455*

[2] Waleffe F., (1997), On a self-sustaining process in shear flows, *Phys. Fluids, vol. 9, pp. 883-900*

[3] Chantry M., Tuckerman L.S. and Barkley D., (2016) Turbulent-laminar patterns in shear flow without walls, *J. Fluid Mech., vol. 791, R8*, *Id.* (2017) Universal continuous transition to turbulence in a planar shear flow, *J. Fluid Mech., vol. 824, R1*

[4] Yokoyama N. and Takaoka M., (2021) Energy-flux vectors in anisotropic turbulence: application to rotating turbulence, *J. Fluid Mech., vol. 908, A17*

[5] Takaoka M., Yokoyama N. and Sasaki E., (2022) Local-flux vectors of conserved quantities in wave number space: Anisotropic structures in Charney-Hasegawa-Mima turbulence, *Phys. Rev. Fluids, vol. 7, L012601*

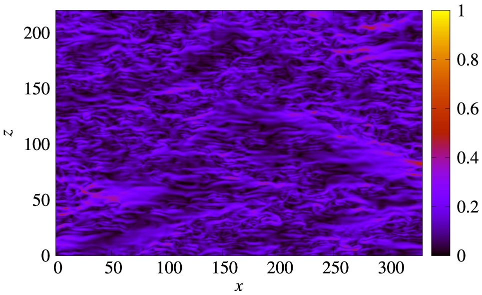

Figure 1: *Instantaneous structures of* $\overline{U}_0$ *field for* $0\beta y$*-mode*

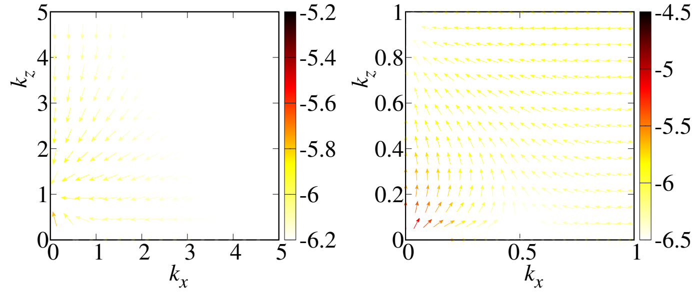

Figure 2: *Averaged energy LFV for* $0\beta y$*-mode in the first quadrant of* (k_x, k_z)*. Right: its low-wavenumber range.*

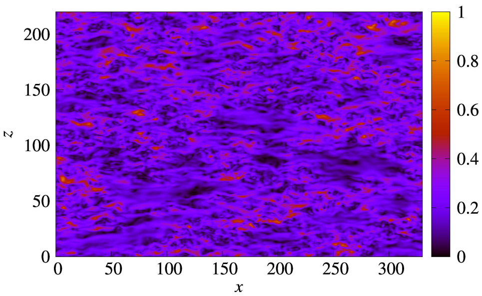

Figure 3: *Instantaneous structures of* $\overline{U}_1$ *field for* $1\beta y$*-mode*

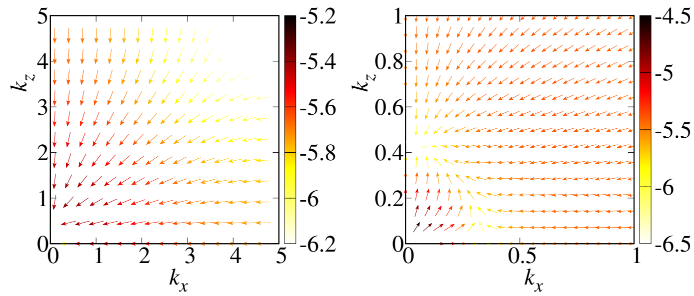

Figure 4: *Averaged energy LFV* $1\beta y$*-mode in the first quadrant of* (k_x, k_z)*. Right: its low-wavenumber range.*

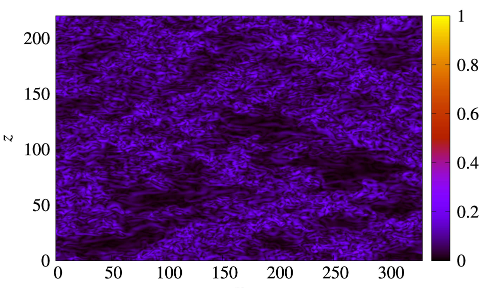

Figure 5: *Instantaneous structures of* $\overline{U}_2$ *field for* $2\beta y$*-mode*

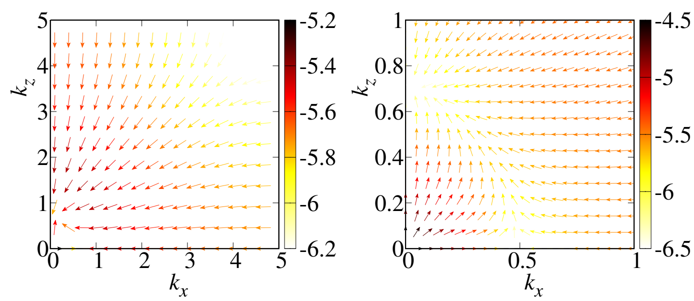

Figure 6: *Averaged energy LFV for* $2\beta y$*-mode in the first quadrant of* (k_x, k_z)*. Right: its low-wavenumber range.*

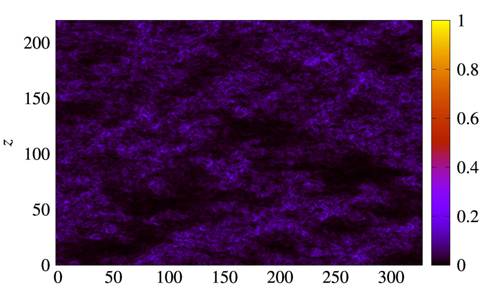

Figure 7: *Instantaneous structures of* $\overline{U}_3$ *field for* $3\beta y$*-mode*

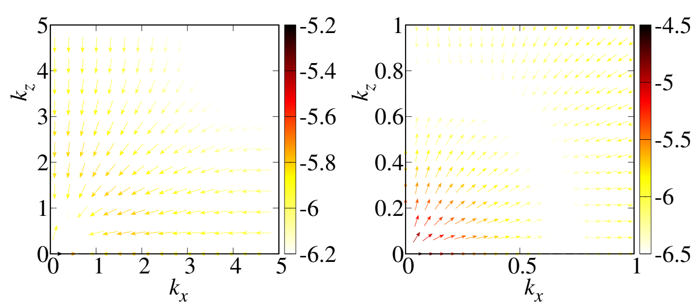

Figure 8: *Averaged energy LFV for* $3\beta y$*-mode in the first quadrant of* (k_x, k_z)*. Right: its low-wavenumber range.*

Angular momentum transport scaling in Very wide gap turbulent Taylor-Couette flow ($\eta = 0.1$).

Mohammed Hussein Hamede[1], Sebastian Merbold [2] and Christoph Egbers[1]

[1] Department of Aerodynamics and Fluid Mechanics, BTU Cottbus-Senftenberg, Cottbus, Germany
[2] Institute of Electrified Aero Engines, German Aerospace Center (DLR), Cottbus, Germany

Keywords: Taylor-Couette flow, Ultimate turbulent Regime

Abstract:

Flow between two coaxial, independently rotating cylinders has been utilized as a model to study various phenomena for several decades. These phenomena include shear flow instabilities, transitions to turbulence, and flow patterns [1]. The so-called Taylor-Couette (TC) flows have a simple geometry defined by the radius ratio $\eta = r_1/r_2$, where r_1 and r_2 are the inner and outer cylinder radii, the gap width $d = r_2 - r_1$, and the aspect ratio $\Gamma = L/d$, where L is the length of the system. The kinematics of the system are defined by the rotation ratio $\mu = \omega_2/\omega_1$, with ω_1 and ω_2 being the inner and outer cylinder rotation velocities respectively, and the shear Reynolds number introduced by Dubrulle et al. [2]:

$$Re_s = \frac{2r_1 r_2 d}{(r_1 + r_2)\nu}|\omega_2 - \omega_1| \tag{1}$$

where ν is the fluid kinematic viscosity.

This experimental study aims to ascertain the existence of turbulent flow boundary layers in a turbulent Taylor-Couette flow within a very wide geometry $\eta = 0.1$. In this study, the outer cylinder was maintained in a static position while the inner cylinder underwent rotation, thereby yielding a rotation ratio of $\mu = 0$. The flow covers a parameter range of Re_s from 5×10^3 to 1.5×10^4. The flow in the planar sheet was scanned at different heights using the High-Speed Particle Image Velocimetry (Hs-PIV) system. This process resulted in measuring the radial (u_r) and azimuthal (u_ϕ) velocity components at different heights. The angular momentum flux is determined by the measured velocity components and is expressed in terms of the quasi-Nusselt number (Nu_ω). For low Re_s flows (≤ 7000), a shaft-to-shaft torque sensor is employed to ascertain the torque applied on the inner cylinder, thereby maintaining a constant rotation speed. This quantity is also utilized to calculate the Nu_ω. The results show that for a critical value of shear Reynolds number $Re_{s,cr} = 2.5 \times 10^4$ a change in the scaling exponent occurs between the Nusselt number and the shear Reynold number, where for $Re_s \geq 2.5 \times 10^4$, a scaling of $Nu_\omega \sim Re_s^{0.76}$ is found as shown in figure 1. The transition to this scaling exponent has already been studied for other TC geometries as an indicator of the transition of the flow boundary layer from the laminar to the turbulent state, or in other words, the transition of the flow from the classical turbulent regime (where the flow is turbulent in the bulk but laminar in the boundary layer) to the ultimate regime (where both bulk and boundary layer are turbulent) [3, 4, 5]. A comparative study is conducted to examine the flow in both regimes. A clear dependence on the flow regime is exhibited in the radial profiles of mean angular momentum; conversely, the angular velocity profiles demonstrate the same behavior in both regimes. To further explore this phenomenon, a spectral analysis is performed on the investigated cases. This analysis aims to examine the variation of the pre-multiplied azimuthal energy co-spectra with respect to different wave numbers. In the classical regime, the energy manifests two peaks: one for small-scale structures and another for large-scale structures. As Re_s approaches $Re_{s,cr}$, the amplitude of the small structures decreases until they are no longer observable for $Re_s \geq Re_{s,cr}$. In the ultimate regime, only the peak corresponding to large-scale structures is observed.

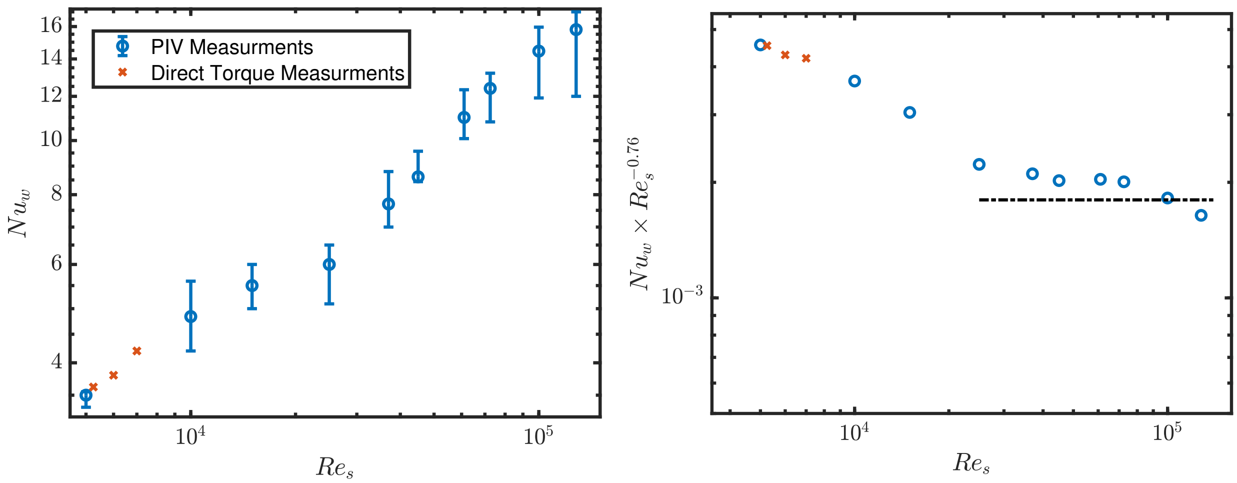

Figure 1: Left: The radial averaged quasi-Nusselt number as a function of shear Reynolds number for flow with stationary outer cylinder. The blue circles present the values calculated from the measured velocity field using HS-PIV, while the orange crosses present the values obtained using direct torque measurements. Right: presents the compensated Nusselt number $Nu_\omega Re_s^{-0.76}$ as a function of the shear Reynolds number. The dash-dot line is used to indicate the value$Nu_\omega \sim Re_s^{0.76}$.

References

[1] Taylor G.I., (1923), Stability of a viscous liquid contained between two rotating cylinders, *Phil. trans. Roy. Soc. London*, 223.

[2] Dubrulle B., Dauchot O., Daviaud F., Longaretti P.-Y., Richard D. and Zahn J.-P., (2005), Stability and turbulent transport in Taylor-Couette flow from analysis of experimental data., *Phys. Fluids*, 17, 118–149.

[3] Huisman S. G., van Gils D. P.M., Grossmann S., Sun C. and Lohse D. , (2012), Ultimate Turbulent Taylor-Couette Flow, *Phys. Rev. Lett*, 108, 024501.

[4] Ostilla-Monico R., van der Poel E. P., Verzicco R., Grossmann S. and D. Lohse , (2014), Boundary layer dynamics at the transition between the classical and the ultimate regimes, *Phys. Fluids*, 26, 015114.

[5] Hamede M. H., Merbold S. and Egbers C., (2023), Transition to the ultimate turbulent regime in a very wide gap Taylor-Couette flow (η = 0.1) with a stationary outer cylinder, *Europhysics Letters*, 143, 23001.

Connecting the Kramers-Moyal coefficients of turbulent flows with the turbulence dissipation constant C_ε

Finn Köhne [1], Felix Schmitt [1] and Joachim Peinke [1]

[1] Physics, Univ. Oldenburg, Oldenburg, Germany

key-words: Stochastic processes, Dissipation

Abstract:
The description of turbulent flows can be approached in a number of ways, which can be roughly divided into two categories. The first category is physics-based and the second category uses stochastic processes for this purpose. For the latter category, a promising approach to analyse turbulent flows that satisfy the Markov property is to describe them using the Fokker-Planck equation (FPE) in scale, which is governed by the first two Kramers-Moyal coefficients (KMCs), the drift $D^{(1)}(u_r, r)$ and the diffusion coefficient $D^{(2)}(u_r, r)$. Here, u_r describes the velocity increments of the flow on the physical scale r. Thus, the KMCs contain all necessary information to describe the general multipoint statistics of a turbulent flow [2]. More specifically, $D^{(1)}(u_r, r)$ describes the deterministic part of the system, while $D^{(2)}(u_r, r)$ describes the intrinsic noise amplitude. This stochastic description can also be related to Kolmogorov's theory from 1962 (K62) [1].
In [3] it is shown that the KMCs depend on the Reynolds number Re of the flow. Similarly, the KMCs can be expected to depend on the intermittency coefficient μ of K62 [1]. Recently, a scaling behaviour, which still holds in the case of non-ideal turbulence, has been found that connects the intermittency coefficient, which can be taken as a typical stochastic quantity, with the dissipation constant C_ε, which is a physical quantity [4].
Inspired by this work, this contribution analyses the dependency of the KMCs as a function of μ and C_ε. It is shown that the statistical description of turbulent flows using the FPE and KMCs can be connected to a more physics based description of turbulence using C_ε. In figure 1 first results show that the quadratic contribution d_{22} to $D^{(2)}$, which is the multiplicative noise contribution that causes intermittency, is depending on C_ε, while figure 2 shows the dependency on μ.
For this contribution we plan to analyse more than 300 velocity time series, acquired by 1D-hot-wire anemometry, are analysed capturing both homogeneous isotropic and non-ideal turbulence. The underlying turbulent flows cover planar and axisymmetric turbulent wakes, grid-generated turbulence and an axisymmetric jet.

References

[1] Friedrich R. and Peinke J., (1997), Description of a Turbulent Cascade by a Fokker-Planck Equation, *Physical Review Letters , vol. 78, pp. 863-866.*

[2] Peinke J., Tabar M.R.R. and Wächter M., (2019), The Fokker–Planck Approach to Complex Spatiotemporal Disordered Systems, *Annual Review of Condensed Matter Physics , vol. 10, pp. 107-132.*

[3] Reinke N., Fuchs A., Nickelsen D. and Peinke J., (2018), On universal features of the turbulent cascade in terms of non-equilibrium thermodynamics, *Journal of Fluid Mechanics, vol. 848, pp. 117-153.*

[4] Schmitt F., Fuchs A., Peinke J. and Obligado M., (2025), A Universal Relation Between Intermittency and Dissipation in Turbulence, *arXiv preprint arXiv:2407.15953*

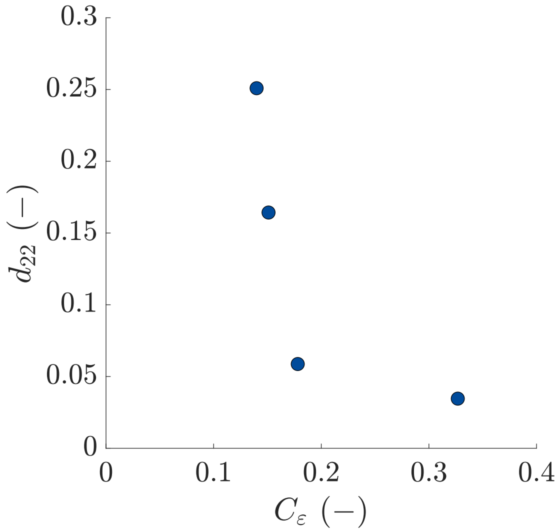

Figure 1: *The quadratic contribution d_{22} to the second Kramers-Moyal coefficient $D^{(2)}$ versus the turbulence dissipation constant C_ε, shown for four different datasets.*

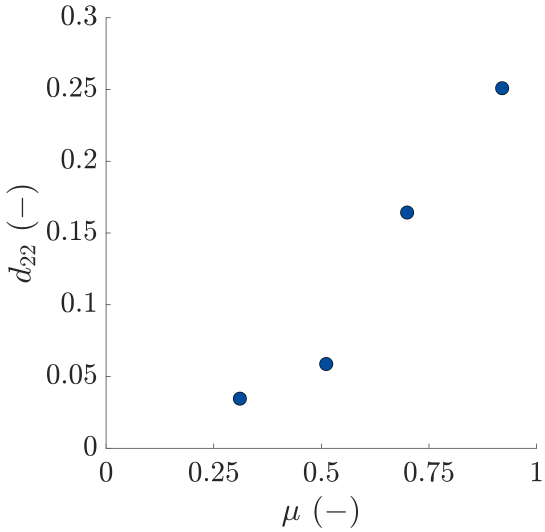

Figure 2: *The quadratic contribution d_{22} to the second Kramers-Moyal coefficient $D^{(2)}$ versus the intermittency coefficient μ, shown for four different datasets.*

Correlating large-scale turbulent structures and wind turbine loads within LES Simulations

M. Bock[1], D. Moreno[1] and J. Peinke[1]

[1] ForWind – Institute of Physics, University of Oldenburg, Germany

key-words: Simulation, Large-Scale Structures, Load-correlation

Abstract:
To model the loads on wind turbines there is a need to describe the incoming turbulent flow. Synthetic turbulence models are efficient method to create realistic wind fields, which represent the atmospheric turbulence. For the wind energy sector, such models are predefined by the IEC standard [1] for the design of wind turbines, namely the Mann model [2, 3] and the Kaimal model [4]. Wind fields from such models are created from parameters that describe the statistics of the atmospheric turbulence. Values for those parameters are defined by the standard or can be extracted form measured data.
A typical approach in the industrial development of a new wind turbine is to use a synthetic wind field from the prescribed models in a Blade Element Momentum (BEM) simulation. As the wind turbines continue to improve, this approach reaches its limits i.e., the correlation between the simulated loads and the observed loads is different. Research is currently being conducted on both aspects of the development strategy. On the one hand, the existing models for generating the wind fields are being improved and, on the other, turbines are being analyzed using high-resolution Large Eddy Simulation (LES) simulations in order to identify the weaknesses of BEM.
A new proposal to characterize a flow field is the Center of Wind Pressure (CoWP) introduced by Schubert et al. [5]. This property reduces the loading of a wind field slice to a single point at which the aggregated thrust force is acting on. In the work of [5] and [6] this characteristic point was used to correlate the flow with the loads on a wind turbine by means of BEM simulations.
BEM models are a low order method, where the flow field is not calculated. This raises the question: To what extent is the concept of the Center of Wind Pressure valid in LES and if a load correlation is feasible even with a high resolution model. Therefore, a LES with a turbulent inflow and a wind turbine modeled with an actuator line is investigated (Figure 1). The behavior of the turbulence in LES after the inflow is analyzed with classical methodologies by one and two-point statistics. Additionally the Center of Wind Pressure as a new characteristic parameter for the description of the flow is analyzed and compared to the other quantities. First results show, that the concept of the Center of Wind Pressure could be applied to correlate wind turbine loads in LES (Figure 2).

References

[1] International Electrotechnical Commission, Wind Energy Generation Systems –Part 1: Design Requirements (IEC, Geneva, Switzerland, 2019), Standard No. IEC 61400-1:2019-02.

[2] Mann, J. (1994). The spatial structure of neutral atmospheric surface-layer turbulence. Journal of fluid mechanics, 273, 141-168.

[3] Mann, J. (1998). Wind field simulation. Probabilistic engineering mechanics, 13(4), 269-282.

[4] Kaimal, J. C., Wyngaard, J. C. J., Izumi, Y., & Coté, O. R. (1972). Spectral characteristics of surface-layer turbulence. Quarterly Journal of the Royal Meteorological Society, 98(417), 563-589.

[5] Schubert C, Moreno D, Schwarte J, Friedrich J, Wächter M, Radons G and Peinke J 2023 Introduction of the center of wind pressure. Wind Energy Science Conference 2023.

[6] Moreno, D., Schubert, C., Friedrich, J., Wächter, M., Schwarte, J., Pokriefke, G., ... & Peinke, J. (2024, June). Dynamics of the virtual center of wind pressure: An approach for the estimation of wind turbine loads. In Journal of Physics: Conference Series (Vol. 2767, No. 2, p. 022028). IOP Publishing.

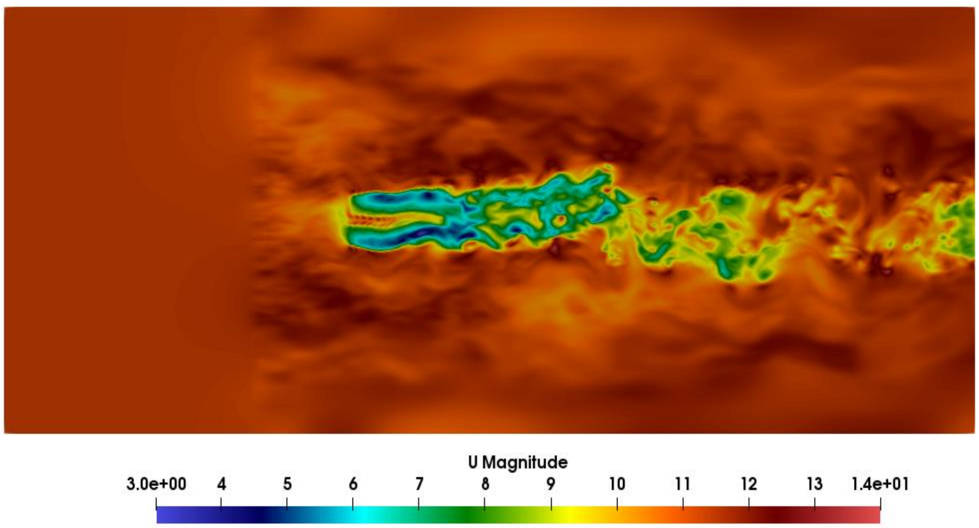

Figure 1: Cutting plane of the LES domain with turbulent inflow and a wind turbine modeled with an actuator line

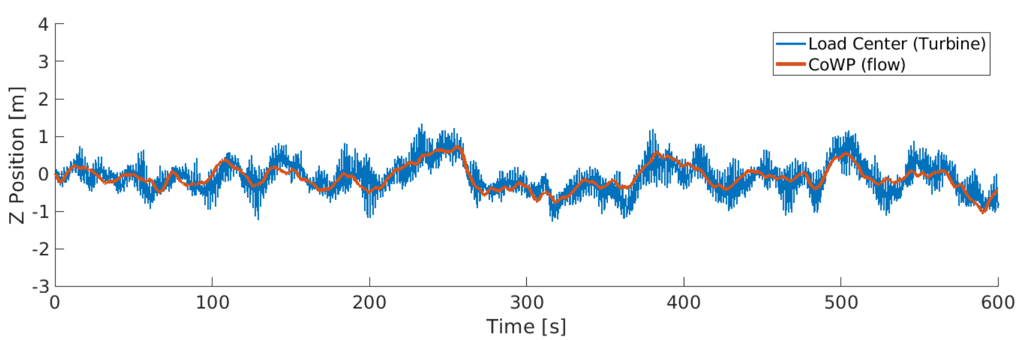

Figure 2: Time series of the load center and the Center of Wind Pressure of a load center

Spatio-temporal linear stability of plane Couette flow

K. Wilhelm[1,2], M. Oberlack[1,2], S. Görtz[1,2], J. Conrad[1,2], L. De Broeck[1,2] and Y. Wang[1]

[1] Chair of Fluid Dynamics, Technical University of Darmstadt, 64287 Darmstadt, Germany
[2] Centre for Computational Engineering, Technical University of Darmstadt, 64293 Darmstadt, Germany

key-words: spatio-temporal linear stability theory, plane Couette flow, Squire's theorem

Abstract:
Plane Couette flow is proven to be linearly stable at all Reynolds numbers for temporally evolving modes. However, oblique structures and turbulence transition are observed in experiments at moderately low Reynolds numbers. This research aims to close this gap by analyzing the linear stability of spatio-temporally evolving modes for plane Couette flow.

Squire's theorem extended:
The Orr-Sommerfeld equation (OSE) governs the wall-normal perturbations in parallel shear flows as

$$\left[(-i\omega + i\alpha U)\left(\frac{\mathrm{d}^2}{\mathrm{d}y^2} - (\alpha^2+\beta^2)\right) - i\alpha\frac{\mathrm{d}^2U}{\mathrm{d}y^2} - \frac{1}{Re}\left(\frac{\mathrm{d}^2}{\mathrm{d}y^2} - (\alpha^2+\beta^2)\right)^2\right]\tilde{v} = 0, \tag{1}$$

where the normal mode approach $v'(t,x,y,z) = \tilde{v}(y)exp[i(\alpha x+\beta z-\omega t)]$ has been employed with frequency ω and streamwise and spanwise wave numbers α and β, and where $U = U(y)$ describes the laminar base flow and Re is the Reynolds number.

The key idea of Squire was that the OSE has a similar structure in 2D and 3D. This allows an equivalence transformation between 2D and 3D modes. Introducing indices for 2D and 3D quantities and with the Reynolds number ratio $\phi := Re_{3D}/Re_{2D}$, we derive the relationships

$$Re_{3D} = \phi Re_{2D}, \quad \alpha_{3D} = \alpha_{2D}/\phi, \quad \omega_{3D} = \omega_{2D}/\phi, \quad \beta = \pm\sqrt{1-1/\phi^2}\,\alpha_{2D}. \tag{2}$$

When Squire considered temporally evolving modes, $\omega \in \mathbb{C}, \alpha, \beta \in \mathbb{R}$, he observed that this parameter choice implies $\phi > 1$ to keep β real, or reformulated as Squire's classic finding, $Re_{2D} < Re_{3D}$.

When extending this to spatio-temporally evolving modes, $\omega, \alpha, \beta \in \mathbb{C}$, the equivalence transformation is identical to (2) but has two branches for β, since complex roots of (2) are now allowed

$$\beta = \begin{cases} \pm\sqrt{1-1/\phi^2}(\alpha_{2D,r} + i\alpha_{2D,i}) & \text{for } \phi > 1, \\ \pm\sqrt{1/\phi^2-1}(\alpha_{2D,i} - i\alpha_{2D,r}) & \text{for } \phi < 1. \end{cases} \tag{3}$$

Key results are: (i) critical Reynolds numbers may be smaller in 3D than in 2D (that is for $\phi < 1$); (ii) the complex β gives rise to structures that can grow obliquely to the base flow. With those equivalence transformations (2, 3), the linear stability problem can be analyzed in 2D and scaled to 3D.

Plane Couette flow modes:
The spatio-temporally evolving modes are investigated for plane Couette flow. To understand the behavior of these modes, the time-asymptotic responses to an impulse and to a time-periodic forcing are analyzed by inverting the temporal and spatial Fourier transformations (i.e. the normal mode approach) in the complex ω-plane and the complex α-plane. By following the paths of singularities of the system in the complex plane and manipulating the contours associated with the inverse transformations, the spatio-temporal growth of modes is characterized [1]. In the last step, the spatio-temporal modes are then transformed to oblique modes using the extended Squire theorem (3).

References

[1] Huerre, P., Monkewitz, P. A., (1990), Local and Global Instabilities in Spatially Developing Flows, *Annu. Rev. Fluid Mech., vol. 22, pp. 473-537*

On the impact of tip speed ratio and free-stream turbulence on blade dynamics of a wind turbine

Francisco J. G. de Oliveira [1], Zahra Shariff Khodaei [1] and Oliver R. H. Buxton [1]

[1] Department of Aeronautics, Imperial College London, London, UK

key-words: Wind turbine blades, fluid-structure interaction, free-stream turbulence

Abstract:

Wind turbines are often arranged in wind farms, and as a result, subsequent machines are often subjected to free-stream turbulence (FST) inflow conditions generated by the wakes of upstream wind turbines [1]. As these systems are scaled to meet current and future energy demands, understanding the impact of FST on the life-span of wind turbine components is crucial. To this end, we have developed an experimental rig to assess the impact of inflow FST and the operating conditions of a 0.5m radius (R) wind turbine model on the experienced blade dynamics, shedding light on the fluid-structure interaction mechanisms underpinning the failure of these components. The turbine rotor was designed with conventional blade element momentum theory, and the spanwise chord length and twist angles were set based on a design tip speed ratio λ_r of 3.5. The rotor speed (Ω) is controlled with a perpendicularly mounted DC electric motor working as a generator, with an inline optical encoder. The tests are conducted in the large section of the 10x5 wind tunnel at Imperial College London, with a cross section of $5.7 \times 2.8\text{m}^2$, and length 18m. The blade structural dynamics are retrieved with Rayleigh backscattering sensors (RBS) [2]. To recover the optical signal from the rotating blades, we use a fibre optic slip ring, located at the root of the driving shaft (see fig. 1 *a*)). The wind turbine model is set in the middle of the test section, and a 6 hot wire rack and traverse system extending for 7m in streamwise extent is set in the turbine's wake - see fig. 1 *b*)-. The hot wires are used to measure the near-wake dynamics along the spanwise direction from $y/R = [1.8, -1.4]$ (encompassing 15 spanwise measurement locations), and streamwise at locations $x/R = [1.4, 2.4, 3.4, 4.4, 5.4]$ at hub height. The 6 hot wires are sampled concurrently with the RBS using a Dantec Streamline Pro, at an acquisition frequency of $10,000$ Hz. Cross-correlations with the RBS data are performed by downsampling in post processing the hot-wire data to the RBS acquisition frequency. The averaged incoming free-stream wind speed was set to $U_\infty = 3.5$ m/s for all the tested cases, setting the Reynolds number based on the turbine's diameter to $\approx 240,000$. Preliminary experiments at 3 low tip speed ratios have been conducted ($\lambda = [0.4, 0.8, 1.2]$), for 3 different FST "flavours" detailed in fig. 1 *c*). These were generated by manipulating the distance between an upstream regular turbulence generating grid and the wind turbine, generating inflows characterised by turbulence intensity (TI), and inflow integral length scale ($\mathcal{L}_{11}/R$), defined as in [2]. Case 1a represents the scenario in which no grid was placed upstream of the turbine. Fig. 1 *d*) presents the spanwise evolution of the TI acquired by the hot wire rack for the different λ and FST conditions tested, at $x/R = 2.4$. As expected, the profiles of TI broaden with the increase of λ and respective decreased porosity of the turbine. Fig. 1 *e*) presents the cross-power spectral density (CPSD) between the fluctuating strain and the fluctuating velocity field at the blade's tip passing region ($y/R = 1$) and $x/R = 1.4$ for the three preliminary tested tip speed ratios, and FST conditions 1a. The multi-scale character of the turbine's wake is imprinted into the blades represented by the multiple peaks at the harmonics of the rotor frequency for the different tested λ. The correlation between the fluctuating velocity field at this particular spanwise location and the strain fluctuations at the tip region of the blade exhibits the largest energy at the tip vortices characteristic frequency ($St = 3$, Strouhal number defined as $St = f/\Omega$), detailing the interaction between the formation of these flow structures and their impact on the blade. To assess the impact of the generated FST inflows and λ on the tip vortices contribution to the blade dynamics, the CPSDs are integrated for each case over a window of frequencies centred on $St = 3$, averaged within the spanwise region where these flow structures develop ($\pm y/R = [0.8, 1.2]$) for each streamwise station, defined by Φ in fig. 1 *f*). As x/R increases, Φ decreases in line with the respective flow structure's spatial decay. As λ and TI increase, so does Φ, except for $\lambda = 0.4$ suggesting that at sub-optimal operating conditions, increased TI helps to break down the contribution of tip-vortices to the blade dynamics while at closer to optimal conditions, enhanced TI yields a stronger correlation between the coherent motions shed into the wake and the mechanical response of the blades.

References

[1] Thomsen K. and Sørensen P., (1999), Fatigue loads for wind turbines operating in wakes, *Journal of Wind Engineering and Industrial Aerodynamics, vol. 80 pp. 16*

[2] G. de Oliveira, F. J. *et al.*, (2024), Simultaneous measurement of the distributed longitudinal strain and velocity field for a cantilevered cylinder exposed to turbulent cross flow, *Exp. in Fluids, vol. 65*

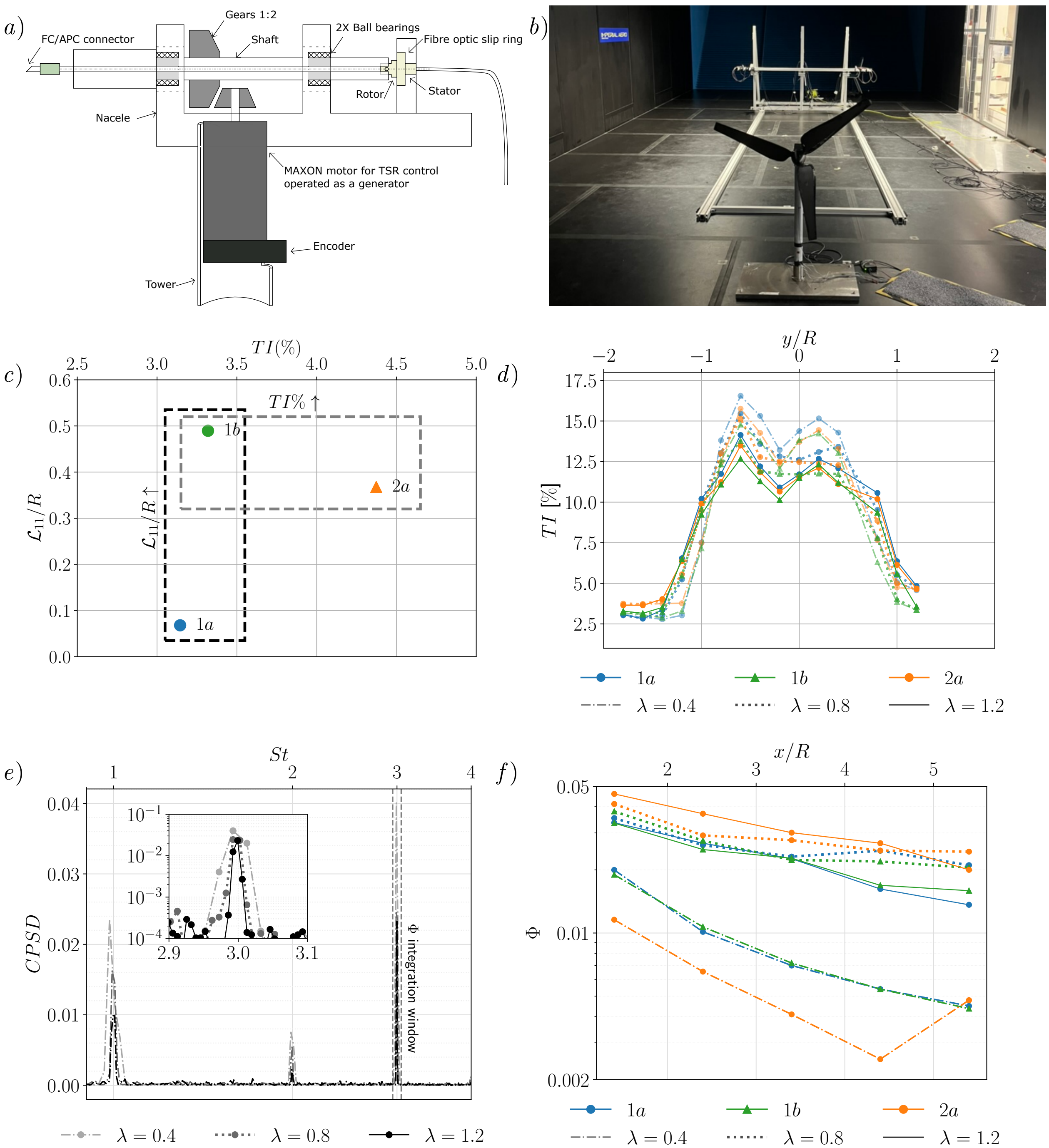

Figure 1: a): Detailed view of the wind turbine model nacelle layout. An in-line optical slip ring is set at the base of the shaft allowing the optical signal used to instrument the blades to pass through the rotating device. b): Wind tunnel installation and instrumentation set-up. c): Generated FST conditions and respective nomenclature. d): Turbulence intensity profiles along the spanwise extent of the wind turbine at $x/R = 2.4$, for each λ and FST case. e): averaged cross-power spectral density (CPSD) between the fluctuating velocity field acquired at $y/R = 1$, and fluctuating strain acquired at the tip region of the blade, under different operating λ. In the final manuscript, we will explore how the different coexisting flow dynamics in the wake of the wind turbine imprint themselves on the mechanical response of different sections of the blade. f): streamwise evolution of the contribution of the tip vortices ($St = 3$) to the CPSD averaged over the developing wake shear-layers.

Effects of pressure gradient sequences on wall shear stress in turbulent boundary layers at $Re_\tau = 1500$

Marco Mattei [1] and Theresa Saxton-Fox [1]

[1] Aerospace Engineering Department, University of Illinois Urbana-Champaign, Urbana, Illinois, United States of America

key-words: Turbulent boundary layers, pressure gradient effects, wall shear stress

Abstract:

Turbulent boundary layers (TBLs) under spatially varying pressure gradients deviate from canonical zero pressure gradient cases, exhibiting flow history effects [1]. In our experiments, we investigate six sequential favorable and adverse pressure gradients (FAPG) over a flat plate, measuring wall shear stress at $Re_\tau = 1500$. A false ceiling (figure 1) induces steady but spatially varying pressure gradients, with local strength quantified by the pressure coefficient and acceleration parameter [3], ranging from 0 to -0.86 and 0 to 5.97×10^{-6}, respectively. Three flush-mounted capacitive shear sensors (DirectShear$^{\mathrm{TM}}$ CS-0210) capture time-resolved streamwise data in the APG region at $x'/L = (0.61,\ 0.66,\ 0.72)$, spanning 1.04 boundary layer thicknesses with a sampling window of at least 15,000 turnover times [2].

Figures 2 and 3 show the $\overline{C_f}$ and normalized fluctuations of wall shear stress ($\tau_w'^+ = \tau_{w,rms}'/\overline{\tau_w}$) as functions of the strength of the FAPG. For the ZPG case (PG1) at $Re_\tau = 1500$, the measured $\overline{C_f}$ is within 2% of the value reported in [4] and the expected $\tau_w'^+$ value is 0.44 [5]. It is known that an FPG suppresses turbulent fluctuations. The trends of $\overline{C_f}$ and $\tau_w'^+$ suggest that flow history effects from the earlier FPG persist and propagate into the downstream APG. We observe that these effects vary in space and that an increase in $\overline{C_f}$ due to the strengthening of the FAPG sequence correlates with a decrease in $\tau_w'^+$ at the furthest upstream and downstream sensors, while minimal variations occur at $x'/L = 0.66$. Additionally, a non-monotonic trend is observed from PG1 to PG3, while for stronger FAPG conditions, $\overline{C_f}$ increases linearly and τ_w^+ decreases linearly at $x'/L = 0.61$ and $x'/L = 0.72$, with the latter experiencing the highest $\overline{C_f}$ and lowest $\tau_w'^+$ compared to upstream locations at the same FAPG conditions. In the final paper, we will thoroughly investigate the effects of spatially varying pressure gradient sequences on wall shear stress in the APG region, focusing on mean skin friction, normalized fluctuations of wall shear stress, the coherence spectrum, and longitudinal cross-correlation.

References

[1] Monty J.P. et al., (2011), A parametric study of adverse pressure gradient turbulent boundary layers, *International Journal of Heat and Fluid Flow, vol. 32(3), pp. 575-585.*

[2] Mathis, R. et al., (2009), Large-scale amplitude modulation of the small-scale structures in turbulent boundary layers, *Journal of Fluid Mechanics, vol. 628, pp. 311-337.*

[3] Parthasarathy, A. & Saxton-Fox, T., (2022), A novel experimental facility to impose unsteady pressure gradients on turbulent boundary layers., *Experiments in Fluids, vol. 63(6) pp. 107.*

[4] Willert, C.E. et al., (2018), Experimental evidence of near-wall reverse flow events in a zero pressure gradient turbulent boundary layer., *Experimental Thermal and Fluid Science, vol. 91, pp. 320-328.*

[5] Wu, X. & Moin, P., (2010), Transitional and turbulent boundary layer with heat transfer., *Physics of Fluids, vol. 22(8).*

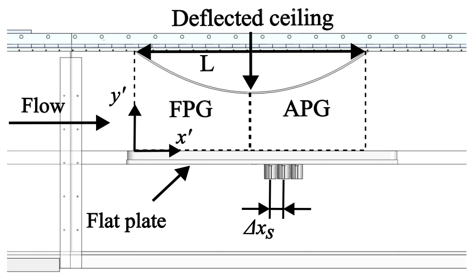

Figure 1: *Schematic of the test region featuring a deflected ceiling (not to scale). (x', y') is centered at the beginning of the ceiling. Dashed boxes indicate the favorable (FPG) and adverse (APG) pressure gradient regions. L is the ceiling length.* Δx_s *is the streamwise probe spacing.*

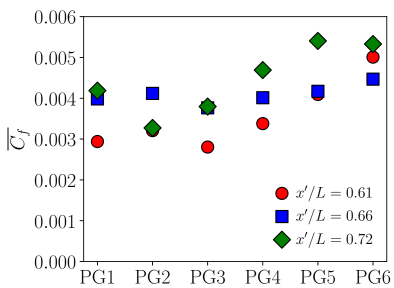

Figure 2: *Skin friction coefficient* ($\overline{C_f}$) *as a function of pressure gradient sequences at three streamwise sensor locations for* $Re_\tau = 1500$.

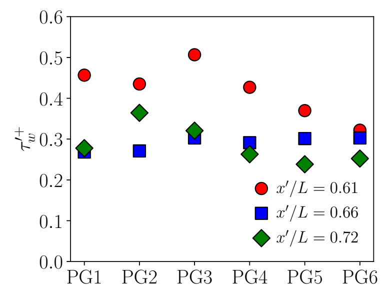

Figure 3: *Turbulent fluctuations* ($\tau_w'^+$) *as a function of pressure gradient sequences at three streamwise sensor locations for* $Re_\tau = 1500$.

Acknowledgments:
This research is supported by ONR Grant #N00014-21-1-2648 and NSF Grant #2339655.

Coherent structures and pressure fluctuations in axisymmetric turbulent boundary layer

Chunxiao Xu[1], Yikai Xu[2] and Weixi Huang[3]

[1] AML, Department of Engineering Mechanics, Tsinghua University, Beijing, PR China
[2] AML, Department of Engineering Mechanics, Tsinghua University, Beijing, PR China
[3] AML, Department of Engineering Mechanics, Tsinghua University, Beijing, PR China

key-words: Coherent structures, Pressure fluctuations, Axisymmetric turbulent boundary layer

Abstract:

Relationships between fluctuating pressure and coherent structures are investigated within a spatially-developed turbulent boundary layer along a slender cylinder with curvature parameter $\delta/a = 7\sim13$ and $au_\tau/v = 40\sim42$, where δ is the boundary layer thickness, a is the cylinder radius, u_τ is the friction velocity and v is the kinematic viscosity. We divide the vortical structures within the boundary layer into two sections according to the transitional and turbulent part of boundary layer shown in Figure 1. Within the transition section, the vortex structures consist of many clusters within which a profusion of arc-shaped small-scale structures are attached to the primary backbone structures. In the turbulent section, different types of vortex structures spread over different radial regions. According to the Poisson equation of pressure fluctuations[2][3] and the distribution of vortex structures (identified by Q-criterion[1]) shown in equation (1), we extract several individual structures in transition section and show their net contributions to pressure fluctuations in the flow field. Similarly, we divide flow domain in turbulent section along the radial direction into several subparts, each comprising different kinds of structures acting as sources and calculate the pressure fluctuations separately with each source term.

$$\nabla^2 p = -\nabla \cdot (\vec{u} \cdot \nabla\vec{u}) \tag{1}$$

It turns out that the contributions of vortex structures to pressure fluctuations are getting weaker and the induced pressure fluctuating scales are getting larger as the distance from the wall increases in turbulent sections. Furthermore, the extracted individual structures within the transition section and their impacts on pressure fluctuations are also assessed (shown in Figure 2). The vortex structures tend to induce low-pressure fluctuations around themselves and high-pressure fluctuations in the interstices, while the shear structures behave inversely. The superimposition of their effects culminates in the distributions of pressure fluctuations within the turbulent boundary layer (shown in Figure 3). With the analysis, we could obtain the net contributions from certain structures to the pressure fluctuations in the whole field clearly and immediately, which are of great importance in the flow-control and sound-related applications in future work.

References

[1] J.C.R. Hunt., A.A. Wray., P. Moin., (1988), Eddies, streams, and convergence zones in turbulent flows, *Proceeding of the Summer Program in Center for Turbulence Research, N89-24555:193-208.*

[2] Kim J., (1989), On the structure of pressure fluctuations in simulated turbulent channel flow, *Journal of Fluid Mechanics, 205: 421–451.*

[3] Peter A. Chang., Ugo Piomelli. and William K. Blake., (1999), Relationship between wall pressure and velocity-field sources, *Physics of Fluids, 11 (11): 3434–3448.*

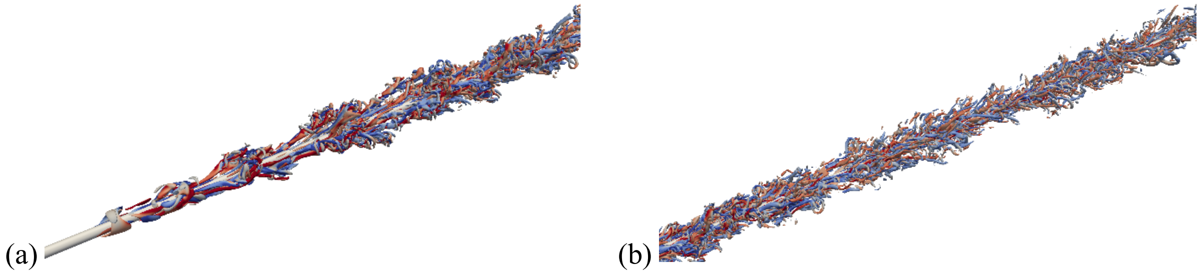

Figure 1: *Vortex structures in (a) transition sections and (b) turbulent sections identified by* $\bar{Q}$*=1.5.*

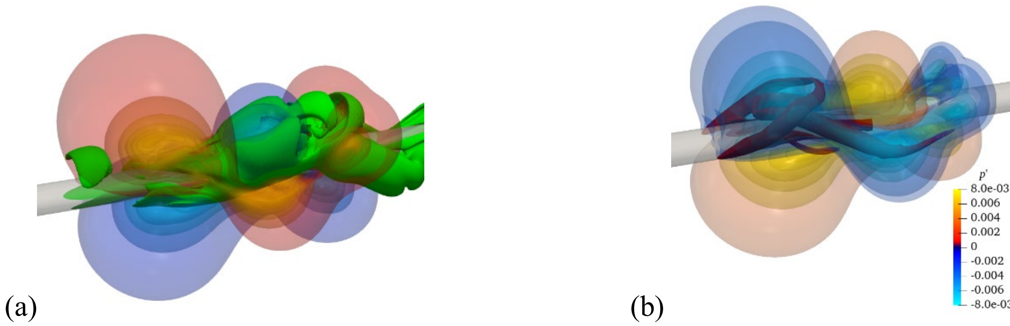

Figure 2: *Distributions of pressure fluctuations (blue and yellow iso-surfaces) caused by (a)shear and (b)vortical structures. Green: shear structures indentified by* $\bar{Q}=-1.5$*; Red: vortical structures identified by* $\bar{Q}$*=1.5.*

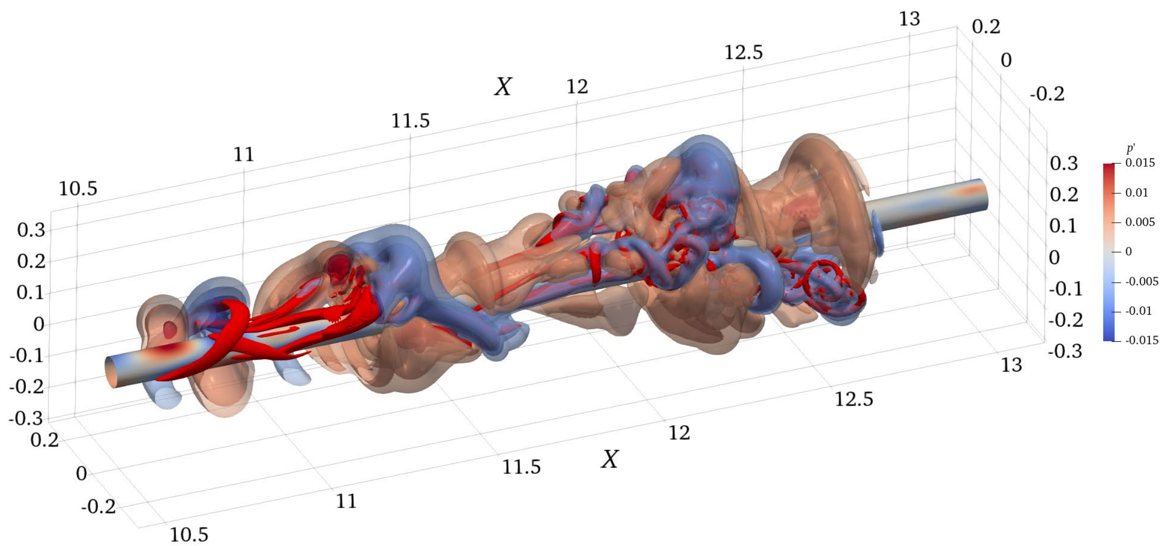

Figure 3: *Distributions of pressure fluctuations (blue and red iso-surfaces) caused by the superimposing effects of vortical and shear structures. Red solid parts: vortical structures identified by* $\bar{Q}$*=1.5.*

Experimental Investigation of Turbulent Thermal Diffusion in Inhomogeneous and Anisotropic Turbulence

E. Elmakies, O. Shildkrot, N. Kleeorin, A. Levy, I. Rogachevskii

The Pearlstone Center for Aeronautical Engineering Studies, Department of Mechanical Engineering, Ben-Gurion University of the Negev, Beer-Sheva, Israel

key-words: Turbulent Thermal Diffusion, Inhomogeneous Turbulence, Particle Transport, Stratified Flows

Abstract:

Turbulent transport and mixing of particles in fluid flows play a fundamental role in atmospheric sciences, industrial processes, and astrophysical applications. One such transport mechanism is turbulent thermal diffusion, which leads to the accumulation of particles in regions of minimum mean temperature. In this study, we present results of an experimental study of turbulent thermal diffusion of small particles in inhomogeneous and anisotropic turbulence produced by a single oscillating grid. The experiments were conducted under both stably stratified and forced convective turbulence conditions. Particle Image Velocimetry (PIV) was used to measure velocity fields and determine turbulence characteristics, including mean and turbulent velocities (see Fig. 1 and 2), two-point correlation functions, and integral turbulence scales. Temperature distributions were measured using an array of 12 E type thermocouple probes, and particle distributions were analyzed using PIV and the effect of Mie light scattering by the particles (see Fig. 3 and 4)**.** Our results demonstrate that particles accumulate in the vicinity of the temperature minimum due to turbulent thermal diffusion, with the particle number density being correlated to turbulence intensity and the temperature field. A key finding of our study is the quantification of the effective turbulent thermal diffusion coefficient, which was determined from measured normalized mean number density of particles and temperature distributions. We observe that turbulence intensity decreases in stably stratified turbulence, leading to a reduction in the effective turbulent thermal diffusion coefficient, whereas in forced convective turbulence, the increase in turbulence intensity enhances the effective turbulent thermal diffusion coefficient. These results are in agreement with theoretical predictions.

References

Elmakies, E., Shildkrot, O., Kleeorin, N., Levy, A., Rogachevskii, I., & Eidelman, A. (2022). Experimental study of turbulent thermal diffusion of particles in inhomogeneous and anisotropic turbulence. Physics of Fluids, 34(5), 055125. https://doi.org/10.1063/5.0088982

Elmakies, E., Shildkrot, O., Kleeorin, N., Levy, A., & Rogachevskii, I. (2023). Experimental study of turbulent thermal diffusion of particles in an inhomogeneous forced convective turbulence. Physics of Fluids, 35(9), 095123. https://doi.org/10.1063/5.0163878

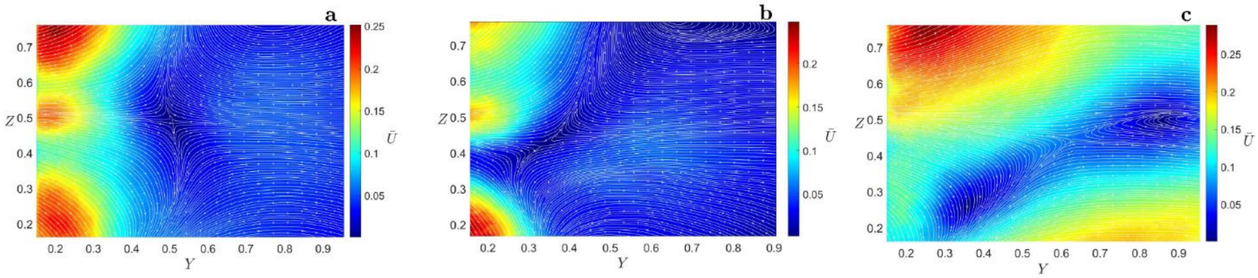

FIG. 1. Mean velocity field $\bar{U}$ in the core flow for (a) isothermal turbulence; (c) stably stratified turbulence; (b) convective turbulence. The velocity is measured in m/s.

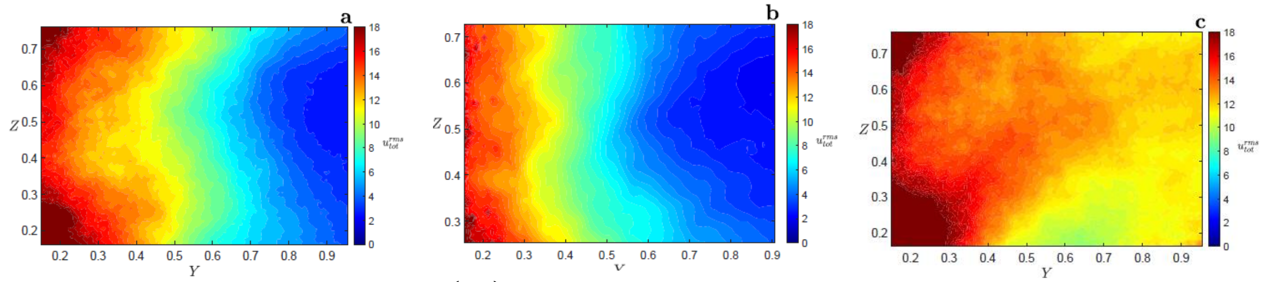

FIG. 2. Distributions of the turbulent velocity $u_{tot}^{(rms)}$ for (a) isothermal turbulence; (b) stably stratified turbulence and (c) convective turbulence. The velocity is measured in cm/s.

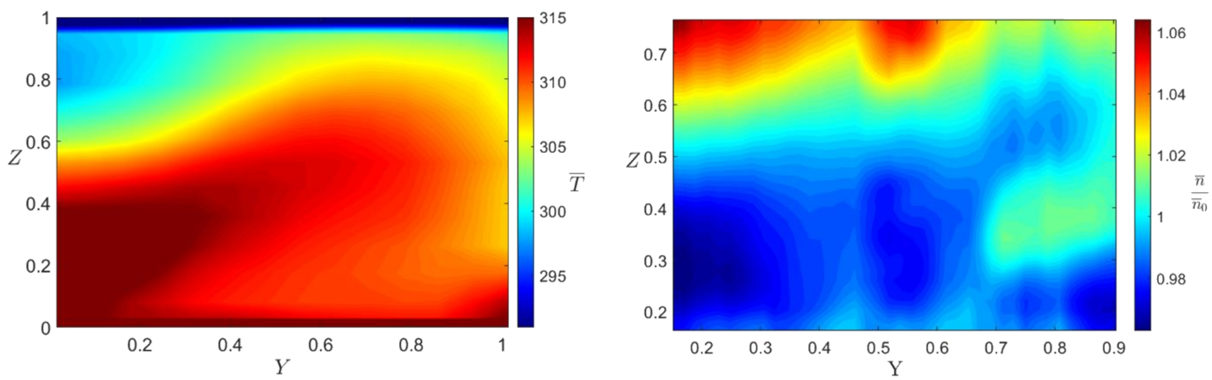

FIG. 3. Distributions of the mean temperature $\bar{T}$ (left panel) and normalized mean particle number density $\bar{n}/n_0$ (right panel) for forced convective turbulence. Temperature is measured in K and coordinates are normalized by $L_z = 26\ cm$.

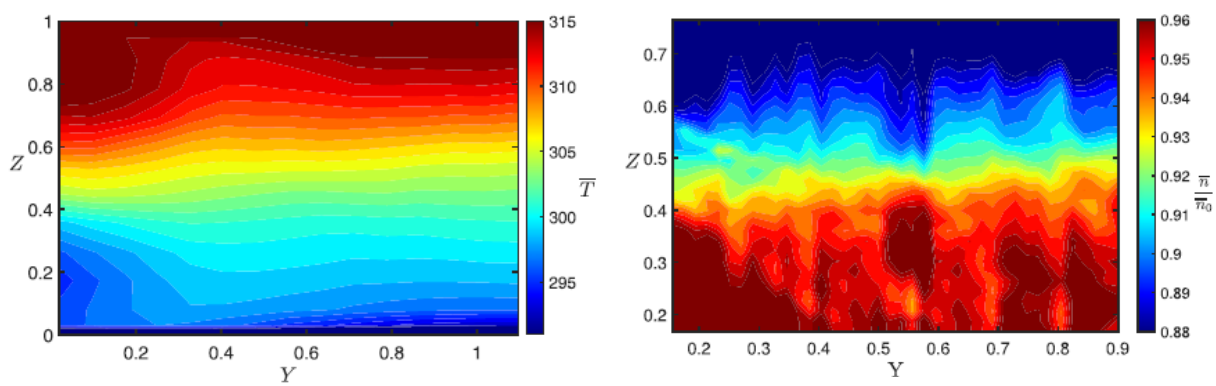

FIG. 4. Distributions of the mean temperature $\bar{T}$ (left panel) and normalized mean particle number density $\bar{n}/n_0$ (right panel) for temperature stably-stratified turbulence.

A Lie-symmetry-based approach for the self-similar profiles of velocity moments in the turbulent round jet

N. Benedikt [1], M. Oberlack [1,2] and C.T. Nguyen [1,2]

[1] Chair of Fluid Dynamics, Technische Universität Darmstadt, Germany

[2] Graduate School of Computational Engineering, Technische Universität Darmstadt, Germany

key-words: Self-similarity, round jet

Abstract:
The turbulent round jet is one of the prime examples of self-similarity in turbulence. While there are many approaches to understand the scaling of velocity moments with the downstream distance z, there has been considerably less research to determine how the self-similar profiles of the moments depend on the similarity invariant

$$\eta = \frac{r}{z - z_0}. \tag{1}$$

We extend the work of [1], who used the invariant function method from Lie-symmetry theory [2] to derive the profiles

$$\widetilde{\overline{U_z^n}}(\eta) = \mathrm{e}^{-\gamma_n \eta^2} \tag{2}$$

and

$$\widetilde{\overline{U_r U_z^{n-1}}}(\eta) = \left(\eta - \frac{(n-2)}{2\gamma_n \eta}\right) \mathrm{e}^{-\gamma_n \eta^2} + \frac{(n-2)}{2\gamma_n \eta}, \tag{3}$$

which provide an excellent fit to the data [1], as shown in Figures 1 and 2. The family of functions (2) especially contains the Gaussian radial profile for the mean velocity for $n = 1$, which has already been observed empirically [3]. We show that these profiles are based on a new type of scaling symmetry of the multipoint moment equations (MPME) that is linked to intermittency [4] and another new translation symmetry. The empirical fit for the exponent of the Gaussian profiles results to be non-linear in n, which deviates from the perfectly dimensional linear scaling in n. This effect causes the Gaussian profiles to be wider than expected and can also be understood as a consequence of intermittency along the edge of the jet.

References

[1] Nguyen, C.T., Oberlack, M., (2025), Hidden intermittency in turbulent jet flows, *Flow, Turbulence and Combustion, under review*

[2] Bluman, G. W., Cheviakov, A. F., Anco, S. C., (2010): *Application of Symmetry Methods to Partial Differential Equations*, Springer

[3] List, E. J., (1982), Turbulent Jets and Plumes, *Annual Review of Fluid Mechanics, vol. 14, pp. 189-212*

[4] Wacławczyk, M., Staffolani, N., Oberlack, M., Rosteck, A., Wilczek, M., Friedrich, R., (2014), Statistical symmetries of the Lundgren-Monin-Novikov hierarchy, *Phys. Rev. E, vol. 90, pp. 13-22*

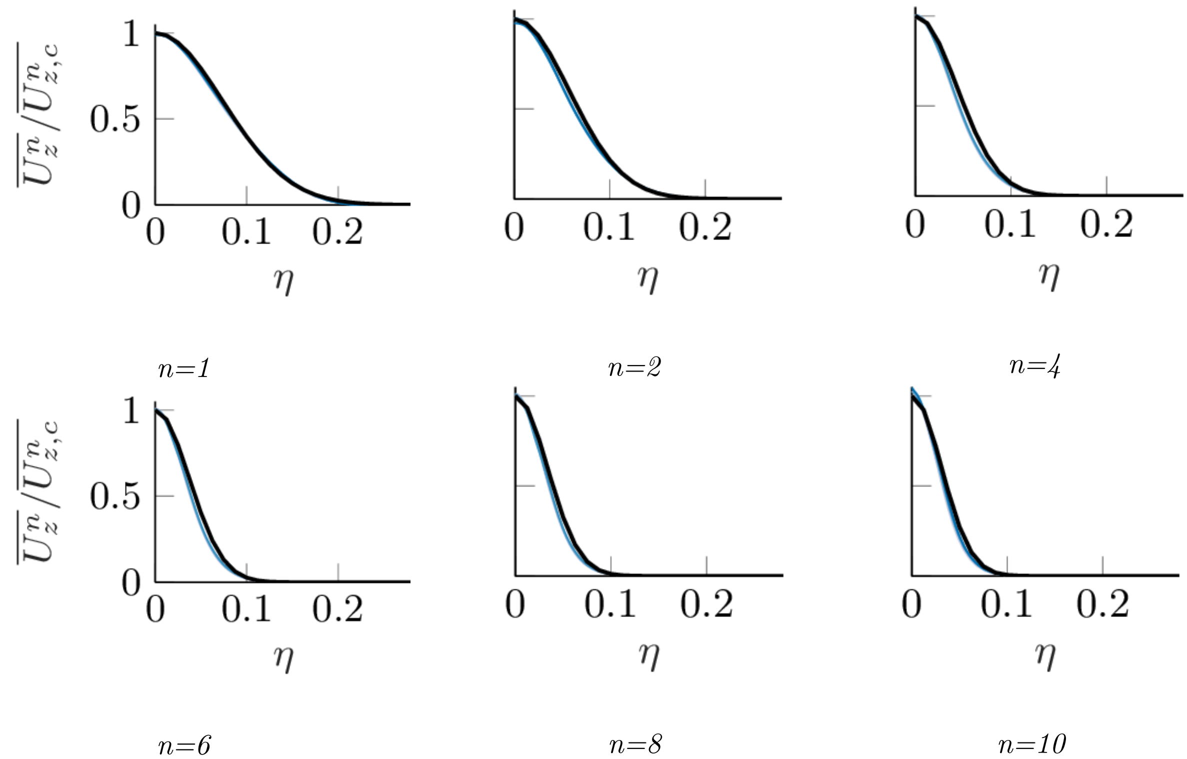

Figure 1: *The normalized radial profiles of the n^{th} axial moment at different distances from the orifice: z/D = 25, 35, 45, 55, 65 (blue lines). The black solid lines indicate the Gaussian behavior from equation (2) using the fitted exponent γ_n. Figure taken from [1].*

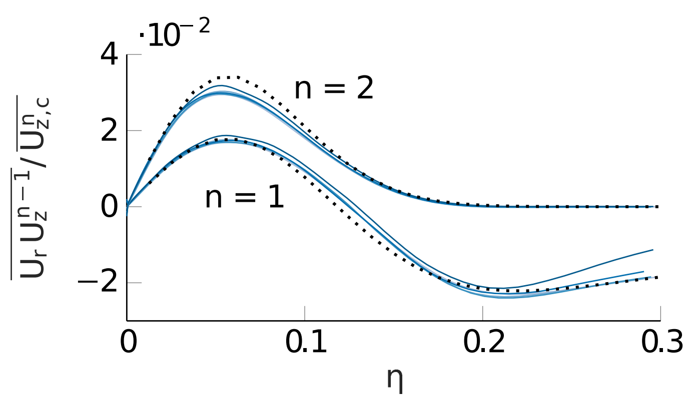

Figure 2: *The radial profiles of $\overline{\widetilde{U_r U_z^{n-1}}}$ at different distances $z/D = 25$, 35, 45, 55 and 65 from the orifice (blue lines) compared to the solution in equation (3) using the fitted exponent γ_n (black dotted lines). Figure taken from [1].*

Experimental investigation of wind turbine wakes exposed to freestream turbulence

Martin Bourhis [1], Thomas Messmer [2,3], Michael Hölling [2,3] and Oliver R. H. Buxton [1]

[1] Department of Aeronautics, Imperial College London, London SW7 2AZ, United Kingdom

[2] Carl von Ossietzky Universität Oldenburg, School of Mathematics and Science, Institute of Physics, 26129 Oldenburg, Germany

[3] ForWind - Center for Wind Energy Research, Küpkersweg 70, 26129 Oldenburg, Germany

key-words: Wakes, Freestream Turbulence, Wind Turbine, Entrainment

Abstract:

Predicting the evolution of wind turbine wakes exposed to freestream turbulence (FST) is essential for designing efficient wind farm layouts, where most turbines operate within the wake of upstream units. Wind turbine wakes grow by mixing with a very complex ambient flow, characterised by a wide range of FST intensity, TI_∞, and integral length scale, $\mathcal{L}_x$. Typically, standard wind turbine wake models assume that wakes are wider and grow faster with increasing TI_∞, often omitting the influence of $\mathcal{L}_x$ and C_T. However, recent experiments with bluff bodies [1] and porous discs [2]—commonly used as wind turbine surrogates in wind tunnel experiments—have shown that C_T, TI_∞, and $\mathcal{L}_x$ each play distinct and significant roles in wake evolution, with spatially evolving contributions. Specifically, in the "far wake" of bluff and porous bodies (below a given porosity threshold), increasing TI_∞ has been shown to reduce the entrainment rate of mass into the wake, a result that contrasts with the current state of the art on wind turbine wakes. Hence, to bridge this knowledge gap, we conducted an extensive experimental study in a large wind tunnel (3 m $\times$ 3 m $\times$ 30 m), systematically measuring the wake of a wind turbine exposed to various turbulent inflows, and operating at different thrust coefficients: $C_T \approx 0.5$, $C_T \approx 0.7$ and $C_T \approx 0.9$. Eight turbulent inflows, with varying TI_∞ and $\mathcal{L}_x$, were generated using an active turbulence-generating grid. The incoming wind speed was set at $U_\infty = 6.5$ m.s^{-1}, resulting in a diameter-based Reynolds number of Re $\approx 3 \times 10^5$ ($D = 0.58$ m). The 24 wakes were scanned horizontally from $1D$ to $20D$ downstream using 21 single hot-wire probes. A schematic of the experimental setup and the envelopes $\{TI_\infty, \mathcal{L}_x\}$ of the 8 FST "flavours" are shown in Figure 1.

Global integral mass-fluxes were calculated according to $\dot{m} = 2\pi\rho \int_0^{\delta(x)} \overline{U}(x,r) r\mathrm{d}r$, where $\delta(x)$ is the radial location r at which the time-averaged velocity deficit ($\overline{U} - U_\infty$) is 10% that of the maximum (Figure 2). Mass entrainment rates were then determined as $\mathcal{E} = \mathrm{d}\dot{m}/\mathrm{d}x$ [2], for two streamwise intervals: one in the "near wake" for $x/D \in [2, 7]$, and one in the "far wake" for $x/D \in [15, 20]$ (Figure 3). A significant observation in Figure 2 is the sharp change in the slope of $\dot{m}$ occurring after several diameters, particularly for highly turbulent cases (L7, L8). For all $\{C_T, \mathrm{FST}\}$ combinations, the mass-flux initially increases quasi-linearly, with higher TI_∞ and C_T resulting in both increased mass-fluxes and entrainment rates $\mathcal{E}_{[2D-7D]}$ (Figure 3a). However, further downstream, an opposite trend is observed, namely a reduction in the entrainment rate, $\mathcal{E}_{[15D-20D]}$, as TI_∞ increases (Figure 3a). In the "near wake", increasing $\mathcal{L}_x$, although having a secondary effect, seems to reduce both $\dot{m}$ and $\mathcal{E}_{[2D-7D]}$, thereby delaying the onset of wake recovery (*e.g.*, comparing Group 2 cases, $\dot{m}_{\mathrm{M5,S4}} \geq \dot{m}_{\mathrm{L3,L6}}$ and $\mathcal{E}_{[2D-7D],\mathrm{M5,S4}} \geq \mathcal{E}_{[2D-7D],\mathrm{L3,L6}}$). These results raise important questions about the validity of current wind turbine wake models, while bridging the gap between entrainment behaviours observed in wind turbine and bluff body wakes. The underlying physics will be explored in greater detail in the final presentation through a more in-depth analysis of turbulence statistics and dynamics across the different wakes.

References

[1] Kankanwadi, K. & Buxton, O., (2020), Turbulent entrainment into a cylinder wake from a turbulent background, *J. Fluid Mech., 905, A35.*

[2] Bourhis, M. & Buxton, O., (2024), Influence of freestream turbulence and porosity on porous disk-generated wakes, *Phys. Rev. Fluids, 9(12), 124501.*

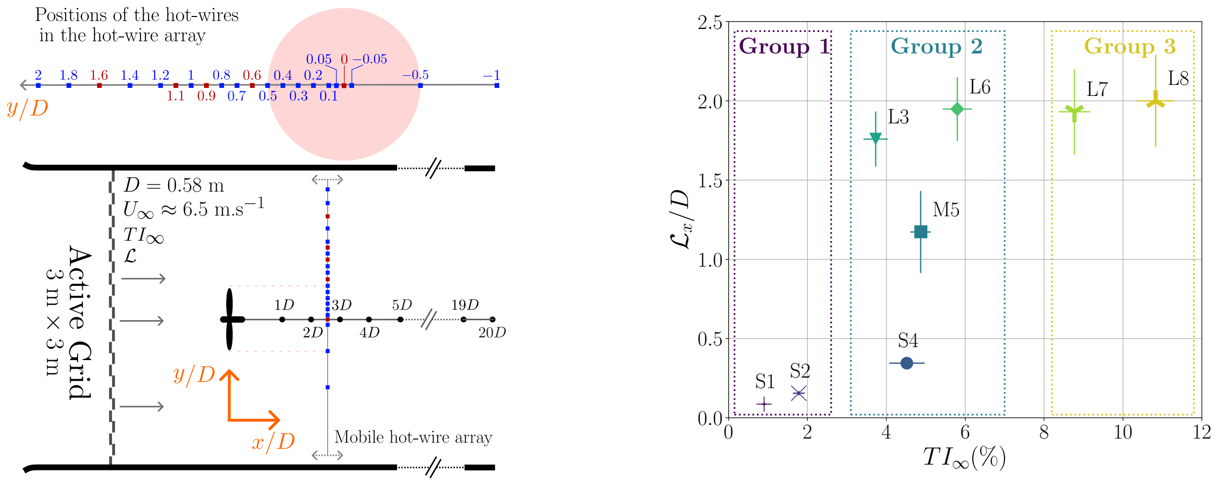

(a) (b)

Figure 1: *(a) Schematic of the experimental setup. (b) Envelopes of the FST "flavours". FST cases are classified by a letter indicating the levels of $\mathcal{L}_x$ (**S**mall, **M**edium, and **L**arge) and numbered hierarchically by increasing TI_∞ from #1 to #8.*

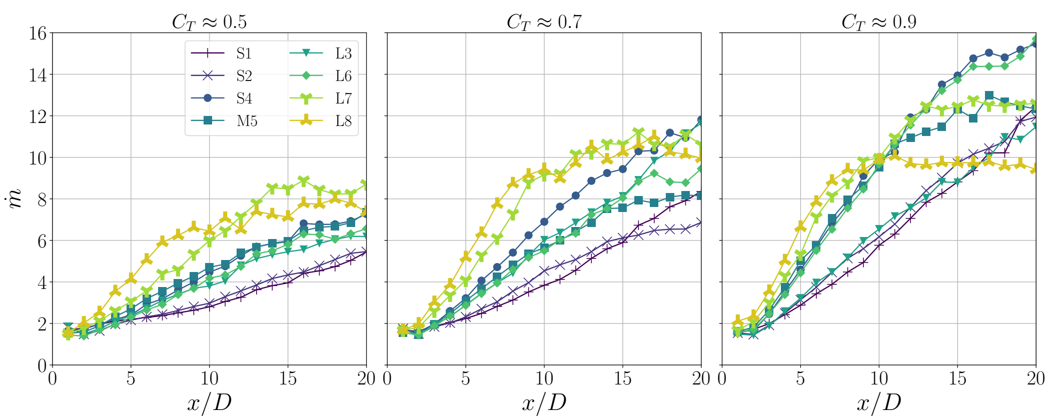

Figure 2: *Streamwise evolution of the global integral mass-flux, $\dot{m}$.*

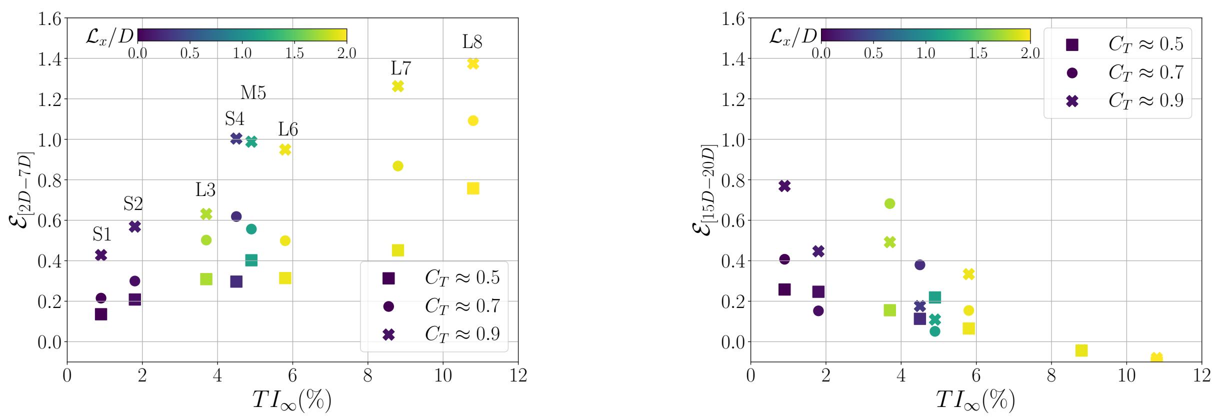

(a) (b)

Figure 3: *Entrainment rates of mass, $\mathcal{E} = \mathrm{d}\dot{m}/\mathrm{d}x$, computed for (a) $x/D \in [2, 7]$, and (b) $x/D \in [15, 20]$.*

A new definition for the turbulent boundary layer thickness based on streamwise velocity skewness

Mitchell Lozier, Rahul Deshpande, Ahmad Zarei, Luka Lindić, Wagih Abu Rowin and Ivan Marusic

Department of Mechanical Engineering, The University of Melbourne, Parkville VIC, Australia

Key-words: turbulent boundary layers, large-scale experiments

Abstract:
Determining a characteristic outer length scale for a turbulent flow is critical for characterising its state and describing its development. Here, we focus on the turbulent boundary layer (TBL) where the outer length scale is referred to as the TBL thickness, δ. Rigorously quantifying the TBL thickness has remained persistently difficult due to the complex stochastic interface bounding the TBL. This has led to the use of various statistical approaches for estimating the TBL thickness [1], such as δ_{99}. However, many approaches commonly used in the literature have ambiguities relating to the use of thresholds, and shortcomings related to applicability (especially for non-canonical TBLs) [2]. To overcome these limitations, we propose the following definition: $\overline{\overline{u^3}}(z = \delta_S) = 0$, where the local mean TBL thickness is defined as the wall-normal location where the skewness of streamwise velocity fluctuations changes sign from negative to positive, in the outer region of the TBL [2].

A representative skewness profile for a canonical TBL, demonstrating this sign-change, is shown in figure 1(a). Green symbols (and dotted lines) indicate wall-normal locations where the skewness is equal to zero, while red and blue symbols indicate locally positive and negative skewness, respectively. In figure 1(b), a population of 2000 local kinetic energy (LKE) interfaces are shown alongside a contour of zero-skewness. While the interface occasionally exceeds this zero-skewness contour, it acts as a nominal indicator of the uppermost extent of the interface, on average. In figure 1(c), the background colour represents the instantaneous streamwise velocity, while arrows represent vectors of instantaneous streamwise/wall-normal velocity fluctuations, and the solid black line represents a single LKE interface. Fluctuations above the interface are weak, but the instantaneous velocity is typically equal to, or slightly greater than the freestream velocity, owing to local flow acceleration above the interface. Below the interface, there are strong turbulent fluctuations, and the instantaneous velocity is typically lower than the freestream velocity. Figure 1(d) schematically relates this wall-normal variation in flow features with the characteristic wall-normal profile of skewness. Wall-normal profiles of skewness from several canonical datasets are compiled in figure 2 to demonstrate similarity in the outer skewness profile over a wide range of flow/measurement parameters. The TBL thickness, δ_S, estimated using the above definition is used to normalise the wall-normal distance, z. A compilation of datasets will be used to critically assess the applicability of this new definition, and compare it directly with previously proposed definitions in the literature.

References

[1] Griffin, K. P., Fu, L. and Moin, P., (2021), General method for determining the boundary layer thickness in nonequilibrium flows, *Physical Review Fluids, vol. 6, 024608*

[2] Lozier, M. and Deshpande, R.and Zarei, A. and Lindić, L. and Abu Rowin, W. and Marusic, I., (2025), Defining the mean turbulent boundary layer thickness based on streamwise velocity skewness, *arXiv preprint arXiv:2502.00157*

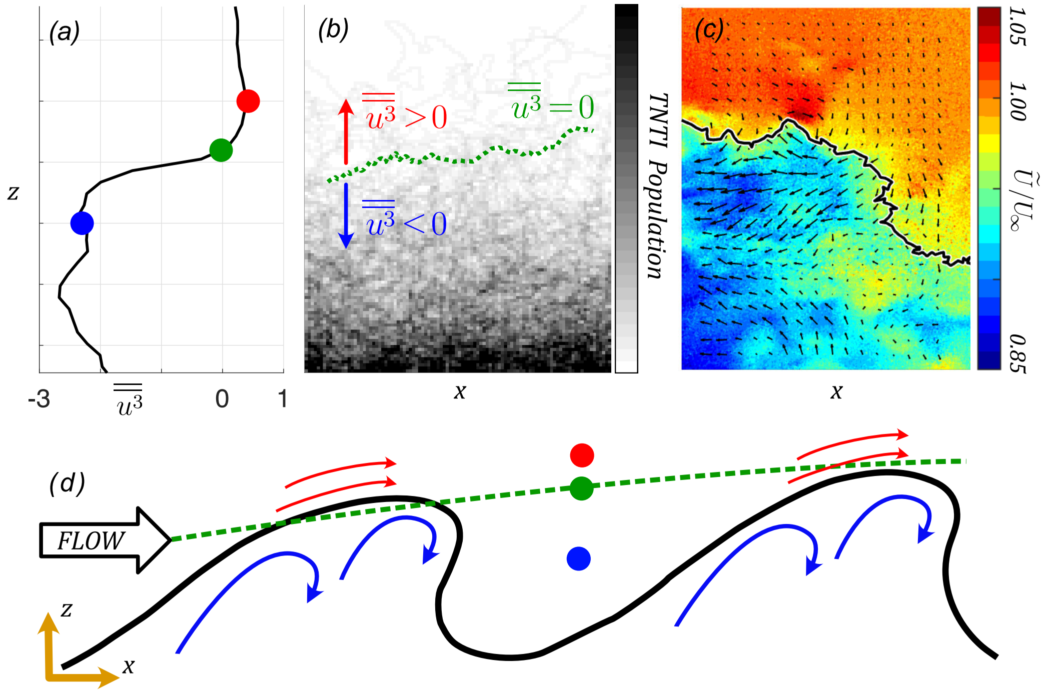

Figure 1: Representative (a) profile of streamwise velocity skewness and (b) TNTI population for a ZPG TBL. (c) Instantaneous TNTI (black line) imposed on instantaneous fields of streamwise velocity (colours) and velocity fluctuations (arrows). (d) Schematic of instantaneous flow phenomenology characteristic of (a,b,c).

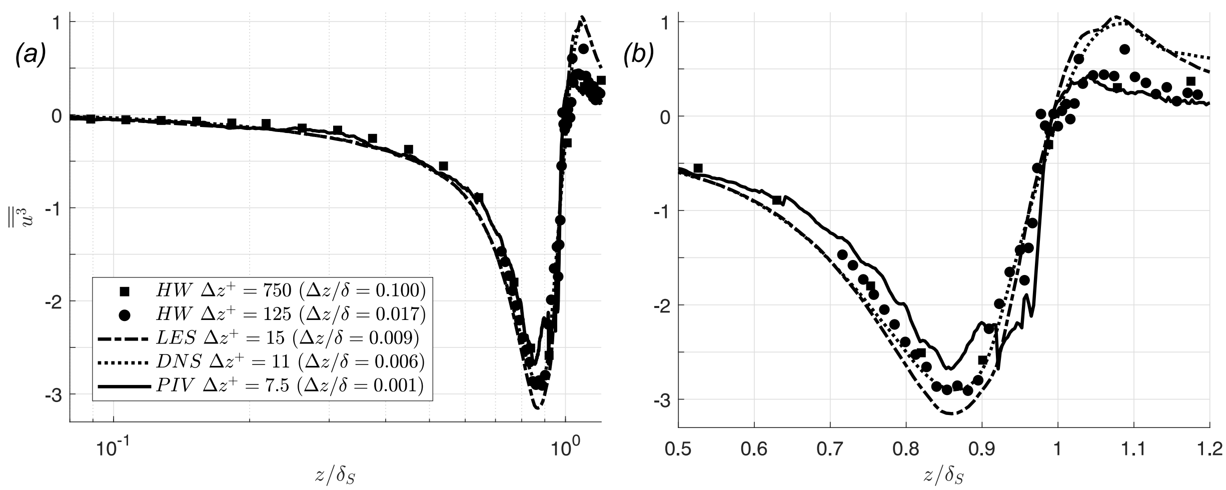

Figure 2: Compilation of various experimental and numerical ZPG TBL skewness profiles described in [2], normalised by δ_S with (a) logarithmic scaling and (b)linear scaling.

Reducing the rough wall pressure drag via imposition of spanwise wall oscillations

Rahul Deshpande, Aman G. Kidanemariam and Ivan Marusic

Department of Mechanical Engineering, University of Melbourne, Parkville, VIC 3010, Australia

key-words: Rough wall boundary layers, drag reduction, flow control

Abstract:
Wall-bounded turbulent flows are common in a wide range of engineering applications, such as flows over ships and submarines, and in pipes. In such cases, the bounding walls generally have a 'rough' surface topography, which adds a drag penalty in the form of pressure drag [1]. This drag is generated from the local flow separation and subsequent wake formation behind the protruding roughness elements, similar to that noted for bluff bodies. An increase in the size of surface roughness increases the relative contributions of the pressure drag to the total drag, but reduces the relative viscous drag contributions [1]. The latter is associated with obliteration of the drag-producing near-wall cycle, by roughness, thereby making pressure drag the dominant contributor to the total drag in the 'fully-rough' regime. These fundamental differences in smooth and rough wall drag-generating mechanisms pose a significant challenge for shipping as well as piping industries, wherein the exposed surfaces degrade from a hydraulically smooth to fully-rough regime in their operation cycle. In such cases, a drag reduction strategy that can attenuate both smooth and fully-rough wall drag-generating mechanisms is required, and this forms the focus of the present study. Here, we will refer to a fully-rough scenario as when the total drag almost entirely comes from the pressure drag.

The present study tests the efficacy of the well-known viscous drag reduction strategy of imposing spanwise wall oscillations [2] to reduce pressure drag contributions in a transitional- and fully-rough turbulent wall flow. This is achieved by conducting a series of direct numerical simulations of a turbulent flow over two-dimensional (spanwise aligned) semi-cylindrical rods, placed periodically along the streamwise direction with varying streamwise spacing (figure 1a; setup inspired from [3]). Surface oscillations, imposed at fixed viscous-scaled time periods optimum for smooth wall drag reduction, are found to yield substantial drag reduction ($\gtrsim$25%) for all the rough wall cases (figure 1b), maintained at matched roughness Reynolds numbers. While the total drag reduction is due to a drop in both viscous and pressure drag in the case of transitionally-rough flow (i.e. with large inter-rod spacing), it is solely associated with pressure drag reduction for the fully-rough cases (relatively small inter-rod spacing; figure 2), with the latter being reported for the first time. The study finds that pressure drag reduction in all cases is caused by the attenuation of the vortex shedding activity in the roughness wake, in response to wall-oscillation frequencies that are of the same order as the vortex shedding frequencies.

References

[1] Chung, D. and Hutchins, N. and Schultz, M.P. and Flack, K.A. (2021), Predicting the drag of rough surfaces, *Annual Review of Fluid Mechanics 53(1): 439-471*

[2] Jung, W.-J. and Mangiavacchi, N. and Akhavan, R., (1992) Suppression of turbulence in wall-bounded flows by high-frequency spanwise oscillations, *Physics of Fluids A: Fluid Dynamics, 4(8), 1605–1607.*

[3] Leonardi, S. and Orlandi, P. and Smalley, R.J. and Djenidi, L. and Antonia, R.A. (2003), Direct numerical simulations of turbulent channel flow with transverse square bars on one wall, *Journal of Fluid Mechanics 491: 229-238*

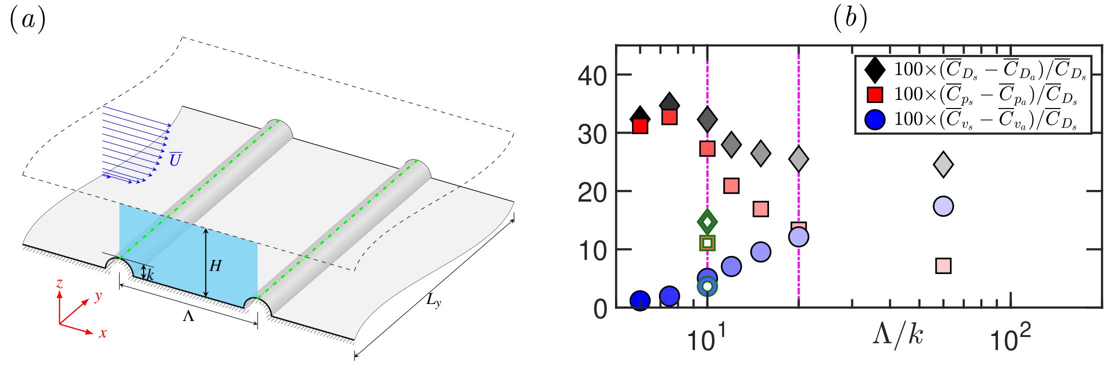

Figure 1: (a) Schematics of an open-channel flow (height H) of an incompressible fluid over a rough wall, made up of spanwise-aligned semi-cylindrical rough elements. The shaded light blue region shows the extent of the domain over what is referred to as the streamwise periodic unit ($0 \leq x/\Lambda \leq 1$). (b) Total percentage drag reduction ($\overline{C}_D$; in diamonds), percent drag reduction due to decrease in pressure drag ($\overline{C}_p$; in squares), and due to decrease in viscous drag ($\overline{C}_v$; in circles), on imposition of wall oscillations at a fixed viscous-scaled time period 100. In (a,b), fully and partially filled symbols correspond to simulations with $k = 0.1H$ and $0.2H$ respectively.

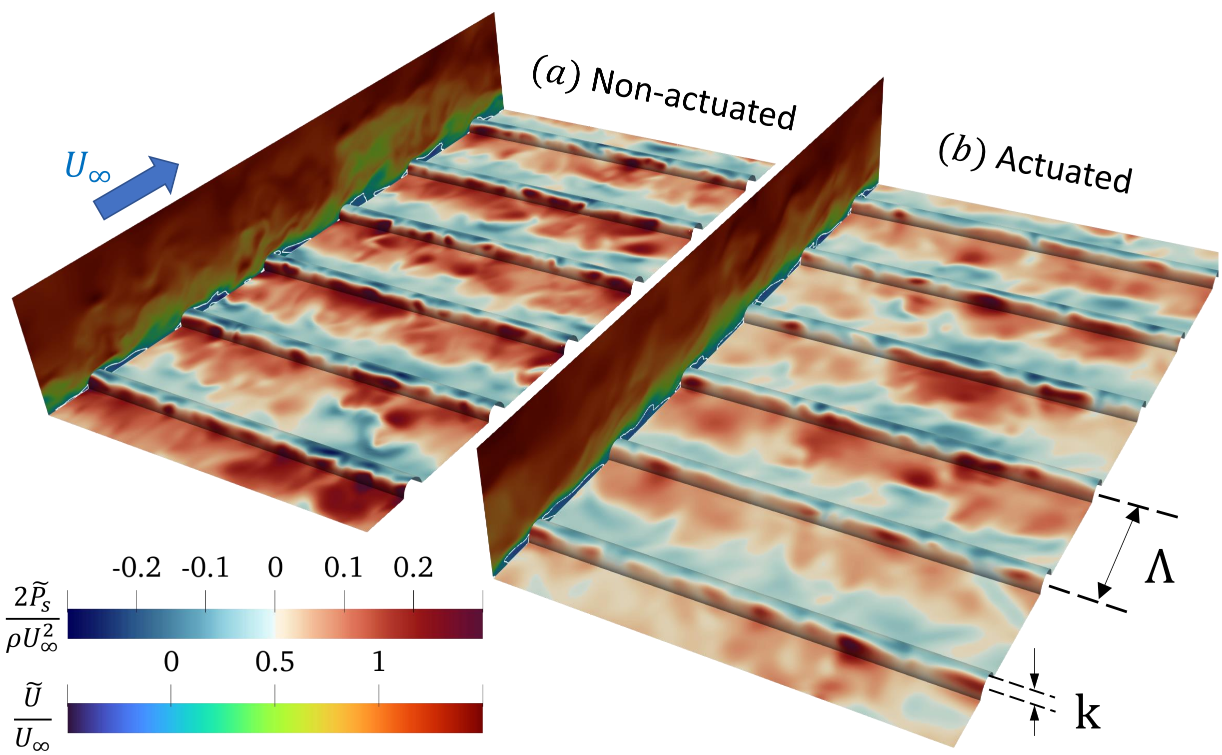

Figure 2: (a) Instantaneous surface pressure ($\tilde{P}_s$) and streamwise velocity ($\tilde{U}$) plotted in an open channel flow with semi-circular rods (radius k) positioned on the wall at various streamwise offsets, Λ. Flow in (a) corresponds to a non-actuated wall while that in (b) is after imposition of time-periodic spanwise oscillations[1] on the wall. U_∞ and ρ are bulk velocity and density.

Influence of Adverse Pressure Gradients on the Outer Region of High Reynolds Number Wall Turbulence

Luka Lindić [1], Rahul Deshpande [1], Wagih Abu Rowin [1] and Ivan Marusic [1]

[1] Department of Mechanical Engineering, University of Melbourne, Melbourne, Australia

key-words: Adverse Pressure Gradient, Particle Image Velocimetry, Canonical Turbulent Boundary Layers, High Reynolds number, Turbulent/Non-Turbulent Interface

Abstract:

Adverse pressure gradient (APG) turbulent boundary layers (TBLs) play a crucial role in various engineering applications, including aircraft aerodynamics, ship hydrodynamics, and turbomachinery. However, their behavior at high Reynolds numbers remains inadequately understood. This study presents new experimental results on a high-friction Reynolds number (Re_τ) canonical inflow APG TBL, wherein history effects are minimized, thereby addressing a key limitation of previous studies.

The experimental setup, implemented in a large-scale wind tunnel at the University of Melbourne (Figure 2(a)), and described in Deshpande et al. [2], ensures well-controlled APG inflow conditions, mitigating history effects and enabling high Reynolds number investigations. High-fidelity particle image velocimetry (PIV) measurements (see Figure 1) extend recent studies, offering insights into the evolution of velocity profiles, turbulent entrainment, and vorticity.

A primary focus of this study is the evolution of mean velocity and turbulence characteristics, with particular emphasis on the outer flow region and the turbulent/non-turbulent interface (TNTI) (Figure 2(b)). Recent studies have revealed interesting flow physics when comparing the outer regions of ZPG and APG TBLs [3]. Additionally, the increasing height of wind turbines, both as standalone structures and as components of tall buildings, has heightened the likelihood of encountering TNTI-like behavior in atmospheric turbulent boundary layers. Accurately characterizing and predicting interface heights may aid in designing wind turbines that operate within the atmospheric surface layer/boundary layer interface, thereby optimizing performance and resilience under varying flow conditions [5].

Here, TNTI is analyzed using the modified local kinetic energy (LKE) and vorticity-based methods, leveraging PIV datasets as outlined in Lindić et al. [4] for zero-pressure gradient (ZPG) and mild APG flows. The findings contribute to a more comprehensive understanding of APG flows, particularly with respect to interface height variations. The TNTI exhibits fractal-like behavior at high Re_τ under both ZPG and APG conditions, while the introduction of a mild APG leads to a reduction in the normalised TNTI height relative to the boundary layer thickness.

References

[1] Clauser, F. H. "Turbulent boundary layers in adverse pressure gradients." *Journal of the Aeronautical Sciences*, vol. 21, no. 2, 1954, pp. 91–108.

[2] Deshpande, R., van den Bogaard, A., Vinuesa, R., Lindic, L., & Marusic, I. (2023). Reynolds-number effects on the outer region of adverse-pressure-gradient turbulent boundary layers. *Physical Review Fluids*, *8*, 124604.

[3] Deshpande, R., & Vinuesa, R. (2024). Streamwise energy-transfer mechanisms in zero- and adverse-pressure-gradient turbulent boundary layers. *Journal of Fluid Mechanics*, *997*, A16. Cambridge University Press.

[4] Lindić, L., Abu Rowin, W., Deshpande, R., & Marusic, I. (2025). Investigation of turbulent/non-turbulent interfaces in high Reynolds number adverse pressure gradient boundary layers. *International Journal of Heat and Fluid Flow* (under review).

[5] Neuhaus, L., Wächter, M., & Peinke, J. (2023). The fractal turbulent/non-turbulent interface in the atmosphere. *Wind Energy Science Discussions*, *2023*, 1–19.

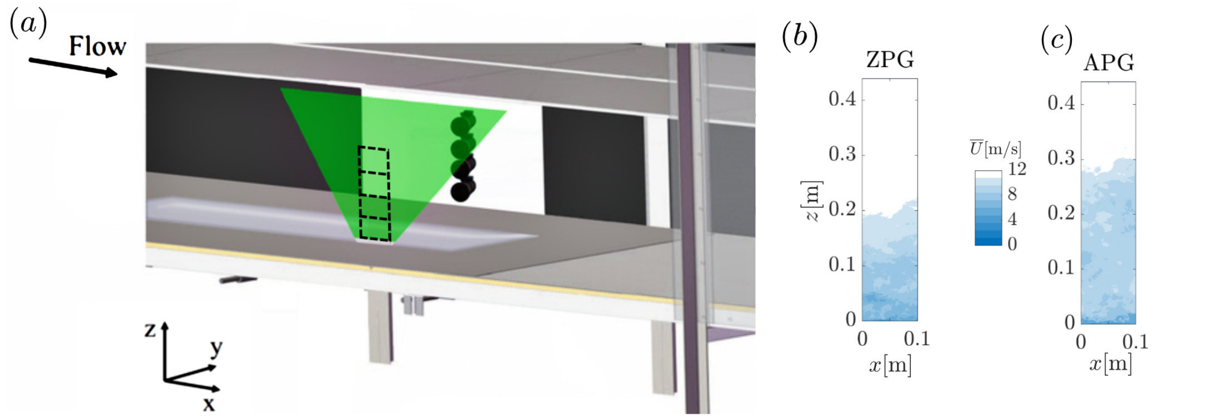

Figure 1: *(a) Experimental setup with tower planar PIV cameras arranged in the HRNBLWT. The four black high-resolution cameras at the back of the tunnel create a large FOV, which covers the entire turbulent boundary layer with high and consistent resolution. (b-c) The plots of the FOV show instantaneous flow for ZPG (b) and APG (c) cases.*

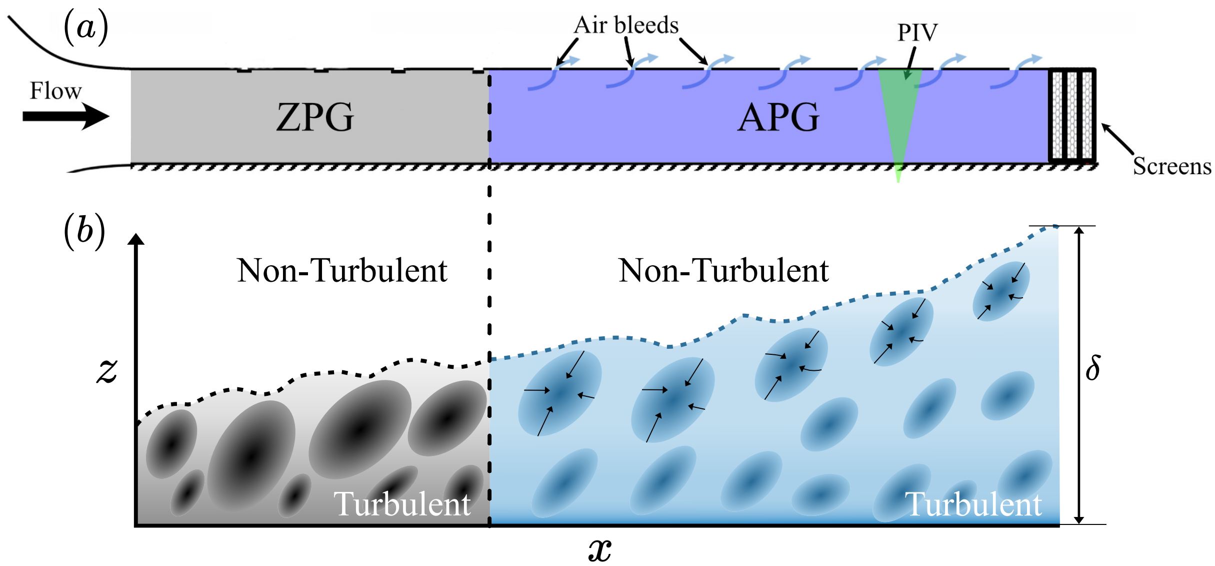

Figure 2: (a) Schematic of the test section for the APG case, showing three meshes located at the outlet of the test section. A canonical ZPG inflow is maintained until $x \approx 8$ m, followed by the APG section for $x > 8$ m. The green sheet and dashed line indicate the PIV measurement location at $x \approx 17.5$ m. (b) Schematic of the boundary layer thickness along the test section.

The fractal atmospheric turbulent-non-turbulent interface: characterization and experimental reproduction

Matthias Wächter, Lars Neuhaus, Michael Hölling, Kerstin Avila, and Joachim Peinke

Carl von Ossietzky Universität Oldenburg, School of Mathematics and Science, Institute of Physics
ForWind – Center for Wind Energy Research, Küpkersweg 70, 26129 Oldenburg, Germany

Keywords: Atmospheric turbulence, turbulent-non-turbulent interface, fractal analysis, wind tunnel experiments

Abstract:

Wind turbines are constantly increasing in size, with their upper blade tips reaching currently up to about 300 m, and are expected to grow even further. In these heights, they are influenced by wind conditions that have not yet been studied in detail. With increasing height, a transition from turbulent to quasi-laminar conditions becomes more and more likely. In this contribution we report results about the presence of a turbulent–non-turbulent interface (TNTI) in the atmosphere and the reproduction of its key features in a wind tunnel using an active grid.

For the first aim, three different on- and offshore measurement sites are investigated. Our fractal scaling analysis leads to typical values of the fractal dimension D_f known from ideal laboratory and numerical studies [1, 2], namely $D_f \approx 0.36$ for a 1D time series. The height distribution of the probability of the TNTI is determined and shows a frequent occurrence in the height range of the rotor of multi-megawatt turbines, cf. Fig. 1. The indicated universality of the fractal TNTI allows the use of simplified models in laboratory and numerical investigations.

For the second aim, an active grid was designed and realized which covers only the lower part of our 3×3 m wind tunnel cross section, see Fig. 2. In Fig. 3 the separation of the flow within the TNTI into laminar (white) and turbulent (black) flow phases is shown based on PIV measurements. For the separation a threshold is applied to the normalized TKE over the pseudo distance $x \propto -t \cdot \langle u \rangle$, using Taylor's hypothesis of frozen turbulence. Laminar patches in the turbulent phase can be recognized. For the two different cases shown (based on different active grid motion protocols and resulting TI at lower part, 3% for (a) and 4% for (b)), a different behavior can be recognized. For the high TI case (Fig. 3 (b)), the interface is found on a larger height range. Consequently, also the structures recognized are larger compared to the low TI case (Fig. 3 (a)). First analyses show the similarity between lab and field TNTI with respect to their fractal dimensions.

Future research includes, from the application side, investigation of the possible impact of such TNTI inflow on loads and power output of wind turbines. A more fundamental question is the dynamic evolution of such atmospheric TNTI flow, namely, how turbulent and laminar flow regions interact. The newly developed wind tunnel setup provides a basis for investigating these questions.

References

[1] Lars Neuhaus, Matthias Wächter, and Joachim Peinke (2024), The fractal turbulent–non-turbulent interface in the atmosphere, *Wind Energy Science, vol. 9(2), pp. 439-452*

[2] Charitha M de Silva, Jimmy Philip, Kapil Chauhan, Charles Meneveau, and Ivan Marusic (2013), Multiscale geometry and scaling of the turbulent-nonturbulent interface in high reynolds number boundary layers, *Physical review letters, vol. 111(4), pp. 044501*

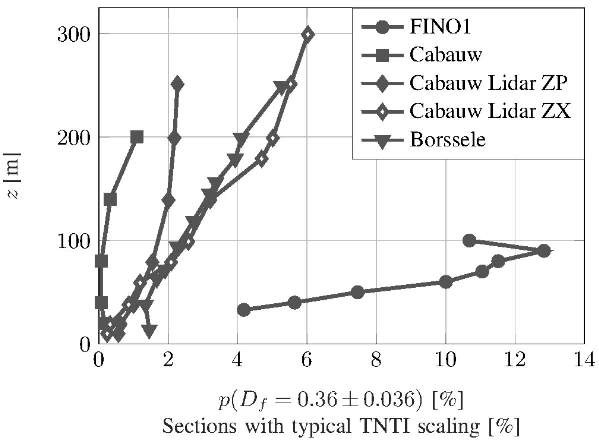

Figure 1: *Percentage of data exhibiting a typical TNTI fractal dimension for different measurement sites (cf. [1] for a complete description).*

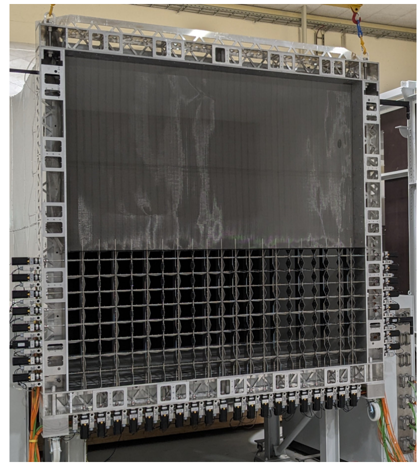

Figure 2: *Half active grid, with an active grid part in the bottom to produce turbulent flows, and fine metal mesh in the upper part to generate quasi-laminar flows.*

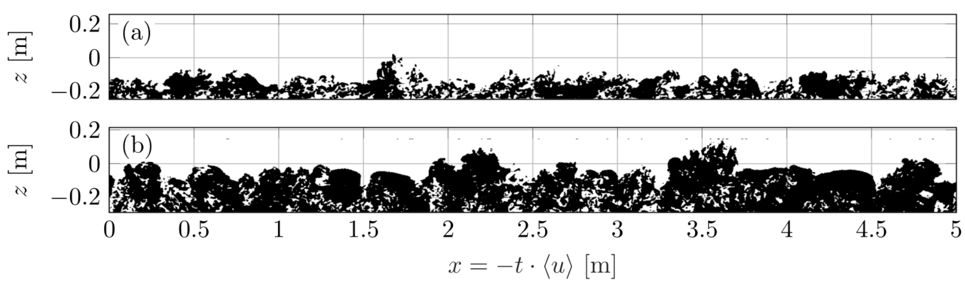

Figure 3: *Turbulent structures (black) recorded by PIV for two different flow cases over height and for pseudo downstream distance x, estimated by the mean wind speed $\langle u \rangle$ and shifted negative time, using Taylor's hypothesis of frozen turbulence. White color corresponds to quasi-laminar flow. The TI in the lower part of the wind tunnel is 3% for (a) and 4% for (b).*

Drag reduction of a turbulent boundary layer by imposing a square-wave type spatial spanwise forcing

Max W. Knoop[1], Rahul Deshpande[2], Bas W. van Oudheusden[1]

[1] Faculty of Aerospace Engineering, Delft University of Technology, 2629 HS Delft, The Netherlands
[2]Department of Mechanical Engineering, The University of Melbourne, Parkville, VIC 3010, Australia

key-words: Turbulent boundary layer, Drag reduction, Wall-based forcing, Experiment, Workshop

Abstract:
We experimentally investigate the drag reduction (DR) of a turbulent boundary layer (TBL) by a spatially imposed spanwise wall-forcing, which is a well-established method to achieve DR [1]. Our particular interest in the spatial type forcing is motivated by it (i) having received only sparse attention in the literature so far (especially experimentally) [1], and (ii) being the closest equivalent to a potential passive counterpart. We investigate a square-wave (SqW) type discretization of the traditionally studied (steady) spanwise wall velocity: $W_w(x) = A\sin(2\pi x/\lambda_x)$[2], where A and λ_x represent forcing amplitude and wavelength, respectively. The square-waveform is realized by an experimental setup, which comprises an array of 48 streamwise-spaced belts (fig. 1 a,b), following the methodology of Knoop *et al.* [3]. Unique to this setup, the forcing amplitude A (*i.e.* belt speed) can be varied independently from the wavelength λ_x by the number of belts comprising one waveform, which is otherwise challenging to achieve in the case of time-oscillating forcing setups, where these parameters are commonly coupled. We investigate the influence of wavelength on DR, at $\lambda_x^+ = 471$ (sub-optimal), 942 (near-optimal), and 1884 (post-optimal conditions), with a fixed forcing amplitude, $A^+ = 12$, at friction Reynolds number, $Re_\tau = 960$ (based on the inflow TBL thickness $\delta_0 = 70\,\text{mm}$), by utilizing particle image velocimetry (PIV; fig. 1 c).

Fig. 2 highlights the phase-wise evolution of the skin-friction coefficient (C_f; the method is detailed below) in FOV2 where the forcing effect is fully established. The FOV captures, respectively, 4, 2, and 1 complete (physical) waveforms for the three increasing λ_x^+. The (sub-)optimal cases (green, blue), reveal a streamwise homogeneous response, with a significant reduction of C_f with respect to the non-actuated baseline (black). Interestingly, the post-optimal case (red) is characterized by a continual decline of C_f over the half-phase, followed by a significant increase when the direction of spanwise forcing reverses ($x/\delta_0 \sim 10.75$). In addition to this workshop, we aim to elucidate these underlying flow mechanics in our conference contribution. We obtain streamwise velocity profiles, $\langle\overline{U}\rangle_x$, by streamwise averaging over λ_x. For our DR estimate, we rely on indirectly determining the skin-friction velocity U_τ (similarly as for C_f in fig. 2), by fitting $\langle\overline{U}\rangle_x$ to a composite profile [4], which was modified to allow for a log-layer offset ΔB while retaining $\kappa = 0.384$. Using this description, we found that the transition between the viscous sublayer and logarithmic region held valuable information, allowing us to determine U_τ with reasonable accuracy. To give the reader an idea of the accuracy of the method, fig. 3(a,b) compares the streamwise velocity profiles scaling with the non-actuated $U_{\tau 0}$ and the 'drag-reduced' actual U_τ, respectively, signfied by the inner-layer similarity in fig. 3(b). The variation of DR with λ_x^+ in fig. 3(c), is qualitatively in line with the observed ΔB shift, and is consistent with the literature, reflecting an optimum of DR $\approx 38\%$.

References

[1] P. Ricco, M. Skote, and M. A. Leschziner, "A review of turbulent skin-friction drag reduction by near-wall transverse forcing," *Prog. Aerosp. Sci.*, vol. 123, p. 100713, 2021.

[2] C. Viotti, M. Quadrio, and P. Luchini, "Streamwise oscillation of spanwise velocity at the wall of a channel for turbulent drag reduction," *Phys. Fluids*, vol. 21, 2009.

[3] M. W. Knoop, F. H. Hartog, F. F. J. Schrijer, O. W. G. van Campenhout, M. van Nesselrooij, and B. W. van Oudheusden, "Experimental assessment of square-wave spatial spanwise forcing of a turbulent boundary layer," *Exp. Fluids*, vol. 65, no. 5, p. 65, 2024.

[4] K. A. Chauhan, P. A. Monkewitz, and H. M. Nagib, "Criteria for assessing experiments in zero pressure gradient boundary layers," *Fluid Dyn. Res.*, vol. 41, no. 2, p. 021404, 2009.

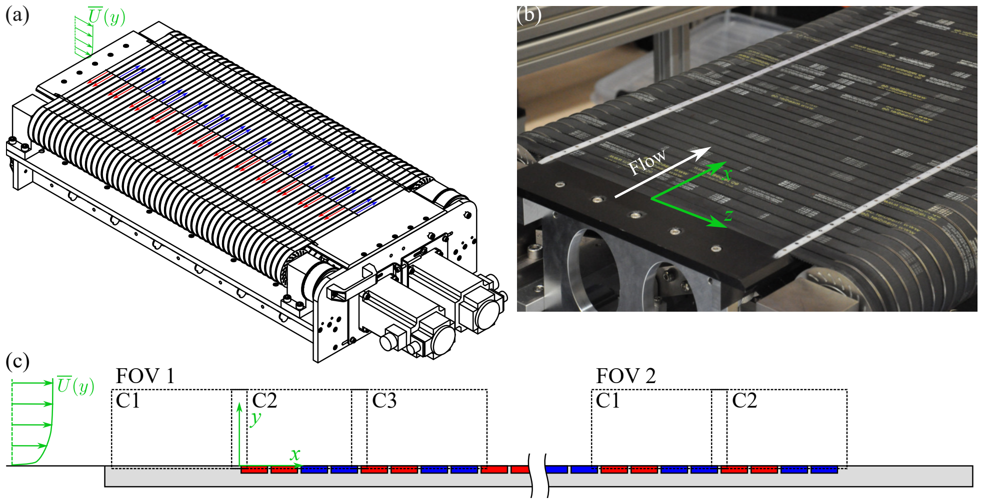

Figure 1: (a) Schematics of the experimental apparatus, of which (b) shows a photograph. (c) Arrangement of the multi-camera PIV (2D-2C) experiment, conducted at the initiation of forcing (FOV1) and in the fully-established forcing region (FOV2). Coloured arrows in (a) and belts in (c) indicate respective positive (red) and negative (blue) W_w for the case $\lambda_x^+ = 942$.

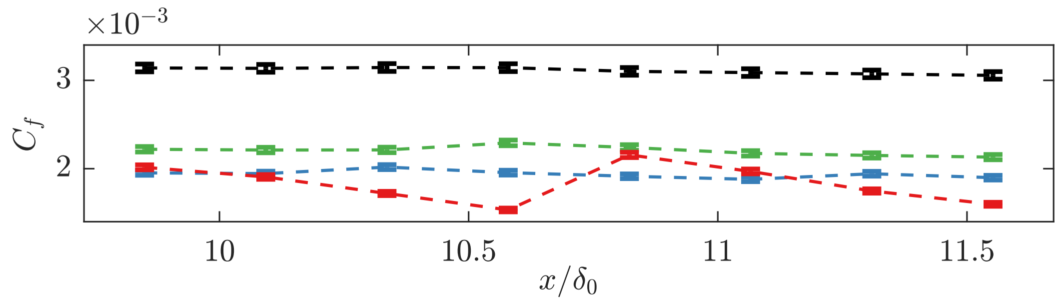

Figure 2: Streamwise evolution of C_f in FOV2 at $A^+ = 12$, for respectively, $\lambda_x^+ = 471$ (green; sub-optimum), $\lambda_x^+ = 942$ (blue; near-optimum), $\lambda_x^+ = 1884$ (red; post-optimum), as well as the non-actuated reference (black).

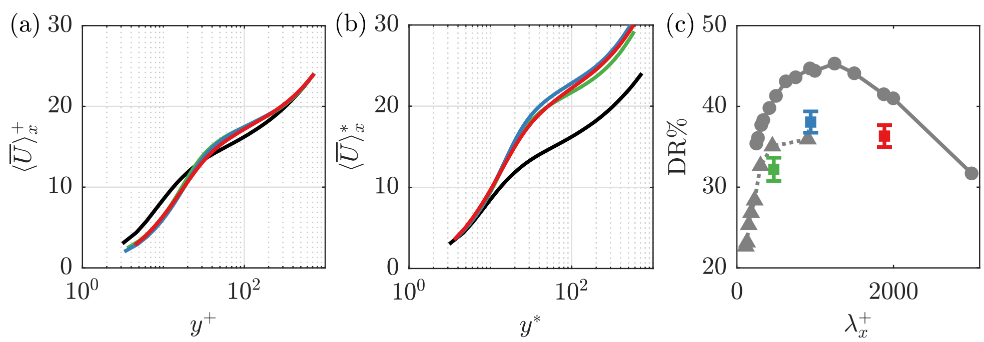

Figure 3: (a,b) Mean streamwise velocity profiles averaged over λ_x in FOV2, normalized by (a) non-actuated ($U_{\tau 0}$) and (b) actual (U_τ) flow conditions. (c) Drag reduction as a function of λ_x^+ for the SqW forcing scenarios investigated experimentally (in colored symbols), at $A^+ = 12$. Also considered for comparison are DR% estimates from channel DNS considering SinW forcing: Viotti et al. (Phys. Fluids, 2009) at $Re_\tau = 200$ (solid) and Gatti and Quadrio (J. Fluid Mech., 2016) at $Re_\tau = 906$ (dashed).

Non-uniform heating effects in turbulent pipe flows

J. Neuhauser [1], D. Gatti [1] and B. Frohnapfel [1]

[1] Institute of Fluid Mechanics, Karlsruhe Insitute of Technology, Karlsruhe, Germany

key-words: Heat transfer, Simulation

Abstract:
Liquid metals are a promising working fluid for concentrated solar power plants (CSPs) due to their high thermal diffusivity and melting point, allowing for elevated process temperatures and thus higher efficiency. The design of such plants require accurate modeling of the heat transfer and distribution of thermal loads, but established correlations for heat transfer in turbulent flows are not well-suited for low-Pr fluids such as liquid metals. Azimuthally non-uniform heat flux, as usually encountered in CSPs, adds further complexity as models are not calibrated for this case.

So far, numerical studies assessed the influence of thermal boundary conditions on the fluid domain [1]. These boundary conditions cannot capture the effect of the heat exchange between the flow and the surrounding solid. Hence, we present data on conjugate heat transfer (CHT) in turbulent pipe flow, including azimuthally inhomogeneous heating over a range of Re numbers, a setup for which recent experimental work is available [2]. The thermal development region is also considered in the dataset (for lower Reynolds numbers), see also Figure 1 for an overview of the configuration. The data has been acquired and cross-validated using two separate numerical codes. The presented results are obtained from a second-order finite differences code based on [3], while the spectral element code NekRS was used for cross-validation.

Our database shows that the mean heat transfer for given Pr and Re number depends mainly on the ratio of thermal conductivities $G_2 = \lambda_\mathrm{s}/\lambda_\mathrm{f}$ (see Figure 2). Furthermore, we show that the mean heat transfer (Nusselt number) only depends on the mean heat flux, but not its distribution around the circumference. This result is exactly true for laminar flow, but also holds well for turbulent flow, conjugate heat transfer and the thermal inlet region.

We investigate how conjugate heat transfer and inhomgeneous heating affects higher order turbulent statistics such as the temperature covariance. Based on the energy spectra of temperature, we explore how the concept of the turbulent convection velocity [4] can be applied to the temperature field, including the solid domain. Both information are required for an estimate of the thermal stresses induced by temperature fluctuations.

Until the conference, we plan to extend this dataset to cases of higher Re, allowing for direct comparison with the available experimental data [2].

References

[1] Straub S., Forooghi P., Marocco L., et al. (2019), The influence of thermal boundary conditions on turbulent forced convection pipe flow at two Prandtl numbers, *International Journal of Heat and Mass transfer, vol. 144, 118601*

[2] Laube T., Dietrich B., Marocco L., Wetzel T., (2024) Conjugate heat transfer of a turbulent tube flow of water and GaInSn with azimuthally inhomogeneous heat flux, *International Journal of Heat and Mass Transfer, vol. 221, 125027*

[3] Pirozzoli S., Romero J., Fatica M., et al. (2022), DNS of passive scalars in turbulent pipe flow, *Journal of Fluid Mechanics, vol. 940:A45*

[4] Del Álamo, JC., Jiménez J., (2009) Estimation of turbulent convection velocities and corrections to Taylor's approximation, *Journal of Fluid Mechanics, vol. 640, pp. 5-26*

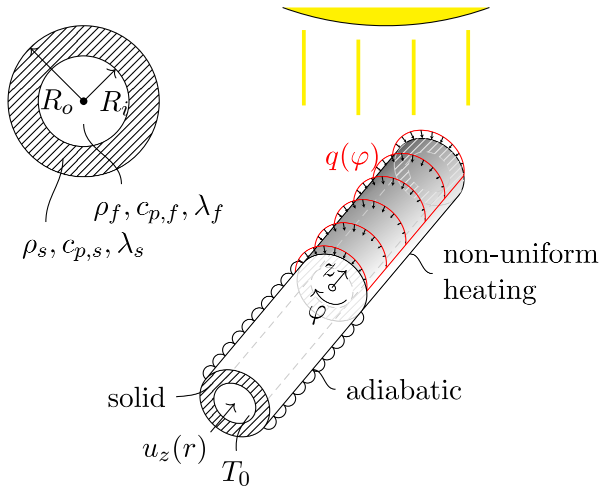

Figure 1: Sketch of the considered configuration. The fluid enters into the pipe at a constant temperature, and is heated starting at $z = 0$; the heat flux is independent of z, but varies with φ. The thermally fully-developed state is present sufficiently far away from $z = 0$.

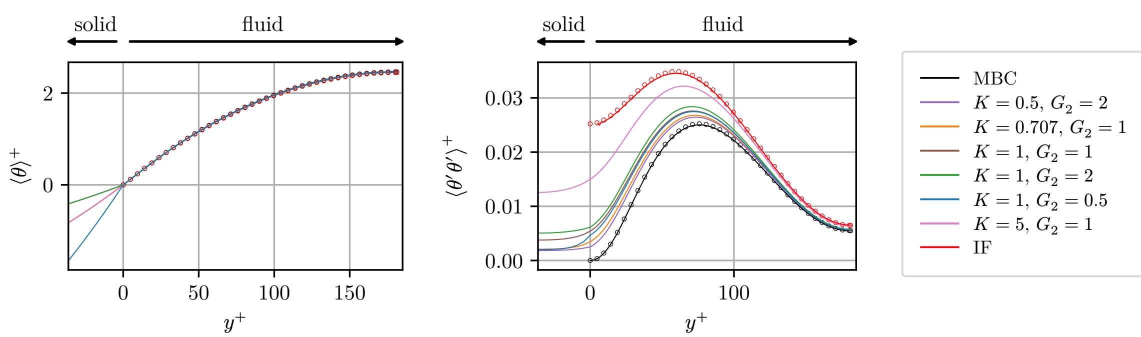

Figure 2: Fully developed temperature statistics for q = const., $Re_\tau = 180$, $Pr = 0.025$. The mean temperature depends on $G_2 = \lambda_s/\lambda_f$ while the temperature covariance is goverened by the thermal activity ratio $K = \sqrt{\rho_f c_{p,f} \lambda_f}/\sqrt{\rho_s c_{p,s} \lambda_s}$. The limiting cases (mixed boundary condition MBC and constant heat flux IF on the fluid) are given for reference.

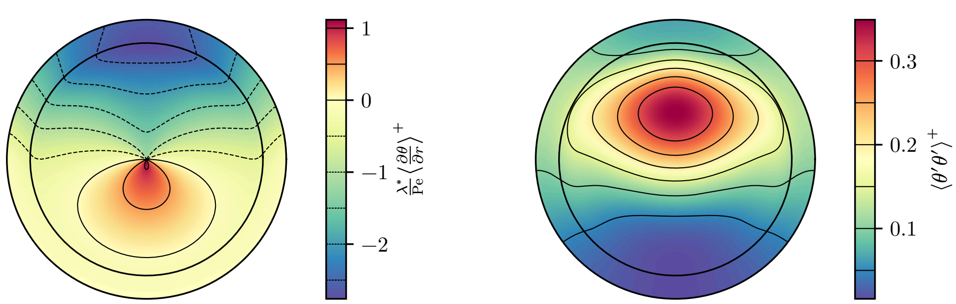

Figure 3: Radial heat flux and temperature covariance for a non-uniformly heated pipe. Half-sinusoidal heating (as in Fig. 1). $Re_\tau = 180$, $G_2 = 1$, $K = 5$, $Pr = 0.025$. Non-uniform heating increases the absolute level of temperature variance significantly, and a high value of K leads to temperature variances penetrating deeper into the pipe.

Balancing of MHD turbulence imbalance in strong shear flows

M. Kavtaradze [1,2], G. Mamatsashvili [2,3] and G. Chagelishvili [2]

[1] Department of Physics, Tbilisi State University, Tbilisi 0179, Georgia
[2] Georgian National Astrophysical Observatory, Abastumani 0301, Georgia
[3] Helmholtz-Zentrum Dresden-Rossendorf, Bautzner Landstr. 400, D-01328 Dresden, Germany

key-words: MHD turbulence – shear flows – transient growth – DNS

Abstract:
We study the degree of imbalance of MHD turbulence in magnetized shear flows using numerical simulations. Unlike previous studies of MHD turbulence energetically supplied by external forcing [1, 2], we consider a more natural case: MHD turbulence in shear flows without any forcing. In this case, there are key processes driven by shear that govern turbulence sustenance and dynamics: linear nonmodal, or transient growth, which provides perturbations with energy extracted from the flow, and nonlinear transverse cascade, which gives feedback to the nonmodal growth [3]. The self-sustenance of the turbulence is achieved through the subtle interplay of the nonmodal growth and the transverse cascade. Furthermore, in the classical case without shear, the degree of imbalance of MHD turbulence remains constant. Here we demonstrate that the flow shear reduces the imbalance and at strong enough shear, turbulence becomes essentially balanced. This finding is consistent with observational data, which indicates that in a solar wind, Alfvénic fluctuations are in a balanced state as the shear increases [4].

There are three main types of modes in the flow: Pseudo-Alfvén and Shear-Alfvén modes with different polarizations characterized by the Elsasser variables $Z_p^{\pm}$ and $Z_s^{\pm}$, respectively, and the hydrodynamic basic mode, which is uniform in the streamwise (y) and shearwise (x) directions and varies in the vertical (z) direction. The basic mode, carrying the largest fraction of the kinetic energy, gives its energy to Alfvén modes through nonlinear transfers, while shear enables an efficient energy exchange between the oppositely propagating Alfvén modes (Fig. 1). As a result of the combined action of strong shear and the basic mode, the MHD turbulence becomes balanced: the ratios $f_p = \left\langle (Z_p^+)^2 - (Z_p^-)^2 \right\rangle /D$, $f_s = \left\langle (Z_s^+)^2 - (Z_s^-)^2 \right\rangle /D$, where $D = \left\langle (Z_p^+)^2 + (Z_p^-)^2 + (Z_s^+)^2 + (Z_s^-)^2 \right\rangle$ ($\langle \cdot \rangle$ denote volume average), which quantify the imbalance of these modes, rapidly become close to zero even in an initially fully imbalanced case (Fig. 2).

References

[1] Lithwick, Y., Goldreich, P., and Sridhar, S. (2007). Imbalanced strong MHD turbulence. *The Astrophysical Journal, 655(1), 269–274.*

[2] Perez, J. C., and Boldyrev, S. (2010). Numerical simulations of imbalanced strong magnetohydrodynamic turbulence. *The Astrophysical Journal Letters, 710(1), L63–L66.*

[3] Mamatsashvili, G. R., Gogichaishvili, D. Z., Chagelishvili, G. D., and Horton, W. (2014). Nonlinear transverse cascade and two-dimensional magnetohydrodynamic subcritical turbulence in plane shear flows. *Physical Review E, 89(4), 043101.*

[4] Soljento, J. E., Good, S. W., Osmane, A., and Kilpua, E. K. J. (2023).Imbalanced turbulence modified by large-scale velocity shears in the solar wind. *The Astrophysical Journal Letters, 946(1), L19.*

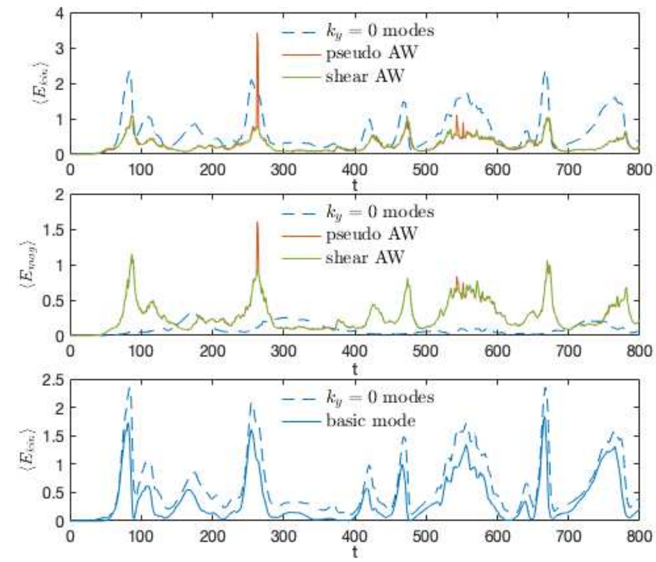

Figure 1: *Evolution of the volume-averaged kinetic, $\langle E_k \rangle$ (top), and magnetic, $\langle E_m \rangle$ (middle) energies of $k_y = 0$ (blue), where k_y is the streamwise wavenumber, Pseudo-Alfvén (red) and Shear-Alfvén (green) modes. The bottom panel shows the evolution of the volume-averaged kinetic energy of hydrodynamic $k_y = 0$ (dashed) and the basic (solid) modes. Note that the "bursts" of the basic mode precede that of Alfvén waves, indicating that the former transfers energy to the latter. The imbalanced condition: $\langle (Z_p^+)^2 \rangle \neq 0$ and $\langle (Z_p^-)^2 \rangle, \langle (Z_s^+)^2 \rangle, \langle (Z_s^-)^2 \rangle = 0$ was imposed at $t = 25$.*

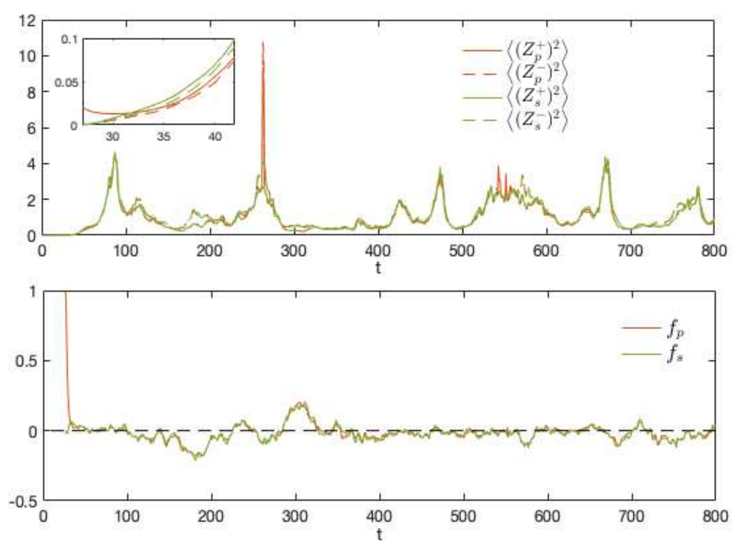

Figure 2: *Top: Evolution of the volume-averaged squared Elsasser variables of Pseudo- $\langle (Z_p^+)^2 \rangle$ (red solid) and $\langle (Z_p^-)^2 \rangle$ (red dashed) as well as Shear- $\langle (Z_s^+)^2 \rangle$ (green solid) and $\langle (Z_s^-)^2 \rangle$ (green dashed), Alfvén wave modes for the same run as in Fig. 1. Bottom: Evolution of f_p (red) and f_s (green), which characterize the degree of imbalance in MHD turbulence. The initially imbalanced case with $f_p = 1$ (i.e., $\langle (Z_p^+)^2 \rangle \neq 0$) shortly becomes on average balanced – f_p decreases, f_s slightly increases and both quickly settle down to small fluctuations around 0.*

Scalings for transition of the boundary layer on a rotating slender cone in axial flow

K. Kato[1], K. Yamada[1], K. Takahara[1], F. Iwashita[1], P. H. Alfredsson[2] and M. Matsubara[1]

[1] Department of Mechanical Systems Engineering, Shinshu University, Nagano, Japan
[2] FLOW, Engineering Mechanics, KTH Royal Institute of Technology, Stockholm, Sweden

key-words: reflective-flake flow visualization, three-dimensional boundary layer

Flows on rotating cones have been studied as a simple model of three-dimensional boundary layers [1], whose geometry is defined by the cone half-apex angle ψ alone. The flow develops from laminar (near the apex) to turbulent along the surface, where the x-coordinate is defined along the generating line with the origin at the apex.

Kobayashi et al. [2] studied the flow on rotating slender cones in axial flow and reported transition axial Reynolds number based on x^* and the velocity U_e^* at the outer edge of the boundary layer (* indicates dimensional quantities). They show that transition is promoted by increasing the angular velocity Ω^*, but delayed by increasing U_e^*, and suggested that transition is controlled by a velocity ratio $S = \Omega^* r^*/U_e^*$ for a given ψ, where $r^* = x^* \sin\psi$ denotes the local radius of the cone. Here we revisit this flow using flow visualization in a towing tank.

The experiments were made as shown in Fig. 1, where a cone with $\psi = 7.5°$ was rotated around its central axis. Experiments were conducted with various combinations of the towing speed U_∞^* and the cone angular velocity Ω^*. Pearl-flake pigment (Iriodin111, Merck Ltd.) was distributed in the water and illuminated by a laser sheet with a thickness of 2 mm, approximately 1 mm away from a generating line of the cone. The reflective flake patterns were recorded by a camera fixed on the trolley through an optical window at the water surface. The averaged root-mean-square of the light intensity I_{rms} just above the generating line was extracted from the recorded movies and used as a qualitative measure of the flow status.

Figure 2 shows the development of the transitional flow with (a) and without (b) axial flow. The top and bottom panels show the same data but as functions of (i) x^* and (ii) x where x is a non-dimensional distance $x = \sqrt{x^* r^* \Omega^*/\nu^*}$ (ν^* is the kinematic viscosity), which can also be seen as the square root of the local rotational Reynolds number. Close to the apex, I_{rms} is relatively low (except very close to the apex) indicating the development of a laminar boundary layer. As x^* increases, I_{rms} increases due to vortex structures developed through a centrifugal instability. Further downstream, I_{rms} saturates and decreases gradually, indicating turbulence.

Overall, increasing U_∞^* and decreasing Ω^* shift transition to larger x^*. However, the data in Fig. 2(ai) were chosen to have a constant global non-dimensional axial velocity $U_g = U_\infty^*/\sqrt{\Omega^*\nu^*} \approx 26.5$, and as can be seen collapse onto a single curve in Fig. 2(aii). Thus, U_g seems to be a more useful scaling as compared to S, since it is independent of space, can be determined *a priori* and used in still fluid seamlessly (see Fig.2(bii)).

References

[1] Alfredsson, P.H., Kato, K., Lingwood, R.J. (2024), Flows over rotating disks and cones, *Annu. Rev. Fluid Mech., vol. 56, pp. 45–68*

[2] Kobayashi, R., Kohama, Y., Arai, T., Ukaku, M. (1987), The boundary-layer transition on rotating cones in axial flow with free-stream turbulence, *JSME Int. J., vol. 30, pp. 423–429*

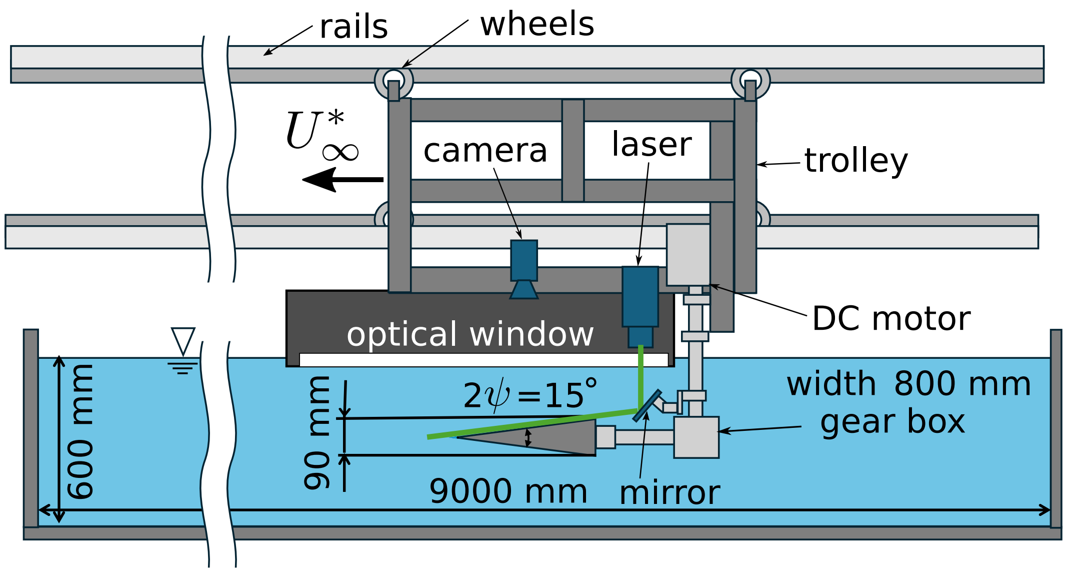

Figure 1: *Experimental setup with the rotating cone in the towing tank. The cone is moving from right to left.*

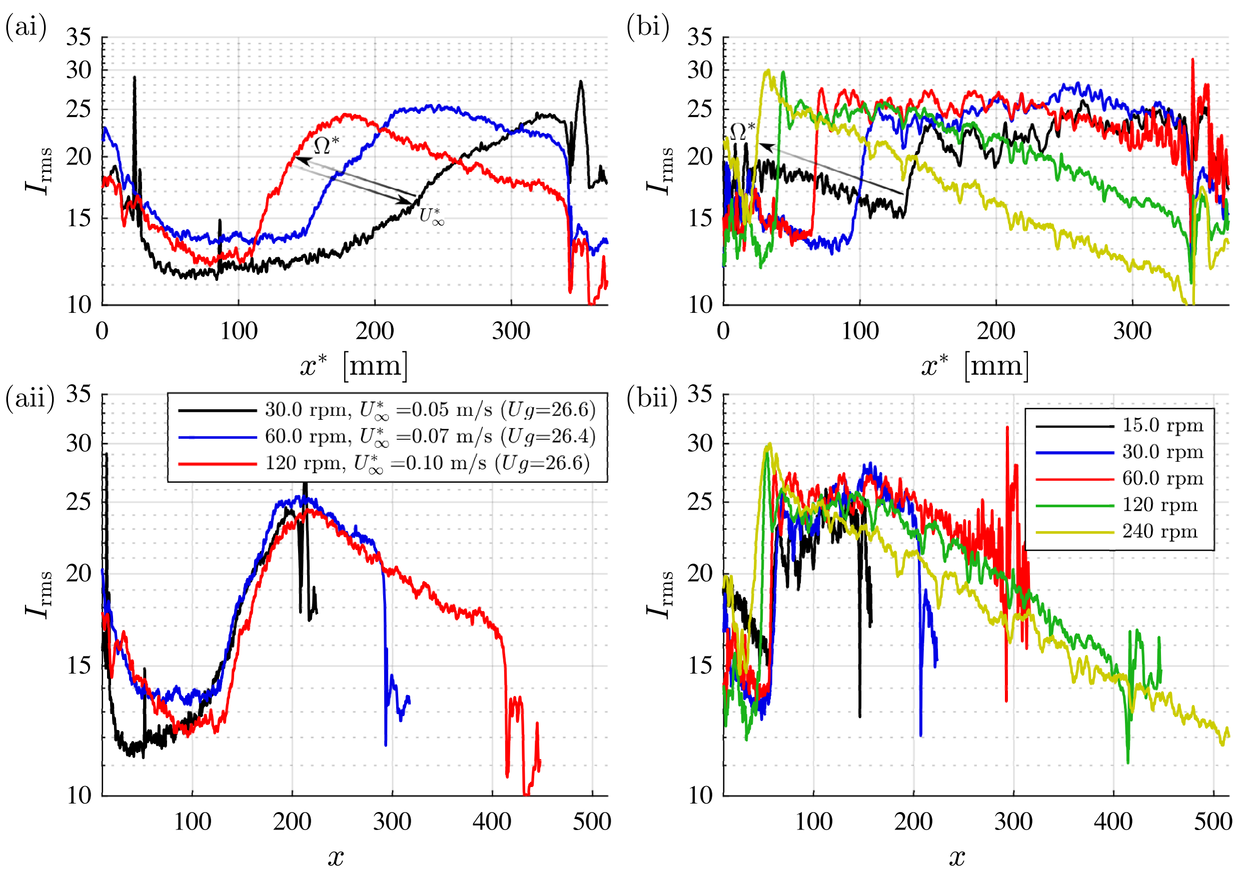

Figure 2: *Root-mean-square of the light intensity I_{rms} as a function of (i) x^* and (ii) x. The left and right columns show data for $U_g = U^*_\infty/\sqrt{\Omega^*\nu^*}$ (a) around 26.5 and (b) 0 (still fluid), respectively.*

Direct Numerical Simulations of turbulent channel flow roughened with 2D triangular bars: on the Effective Distribution parametrization

Federica Bruno[1], Stefano Leonardi[2] and Mauro De Marchis[3]

[1] Department of Architecture and Engineering, University of Enna "Kore", Enna, Italy
[2] Department of Mechanical Engineering, University of Texas at Dallas, Richardson, TX, USA
[3] Department of Engineering, University of Palermo, Palermo, Italy.

key-words: Turbulent Flow, Roughness Effects

Abstract:
Roughness plays a fundamental role in physics, engineering, and environmental science. Many studies have investigated the effects of different roughness shapes and distributions. Efforts aim to find a statistical descriptor of roughness geometry to replace the classical equivalent sand grain roughness k_s, a hydraulic property estimable from the mean velocity profile. Surface affects the flow depending on factors like size, distribution, density, shape, and slope of features. Despite advances in understanding flow over rough walls, a knowledge gap remains in parametrizing drag and roughness function. To this aim, DNS of turbulent channel flows have been performed with periodic boundary conditions in streamwise and spanwise directions and a no-slip condition in the wall-normal direction. The computational domain, with dimensions $6.4h \times 2.2h \times \pi h$, is discretized using a grid of $512 \times 256 \times 256$ points to ensure high resolution near the wall. The Reynolds number is set to $Re = 4300$, corresponding to a friction Reynolds number of $Re_\tau = 240$. Two sets of simulations have been conducted, varying roughness height while keeping a fixed pitch-to-height ratio of $w/k = 4$. The first set features 16 triangular transverse bars with a roughness height of $k/h = 0.1$ ($A1_1$), and the second set doubles the roughness height to $k/h = 0.2$ ($A1_2$). Other cases modified the baseline to highlight features like protuberances and wakes affecting downstream roughness. The correlation between roughness configurations and flow characteristics has been investigated, focusing on drag, roughness function, and turbulent intensities. Fig.2 shows that ES alone exhibited significant variation, about 30-40%. Results indicated that geometrical parametrization must consider the contribution of elements in larger elements' wake to drag, pattern and distance effects of roughness elements, and the impact of flat regions between rough elements on velocity distribution. These factors have been included in a new parametrization, Effective Distribution (ED), revising ES. The ED improved drag correlation by accounting for peaks above mean roughness, wake regions from the highest elements, and distances between elements. To further analyze this behavior, turbulent intensities have been investigated. The color contour plots of streamwise turbulent intensities for select cases, shown in Fig.3, highlight the impact of roughness geometry on turbulent flow. Comparing the uniform triangular roughness configuration ($A1_1$, Fig.3a) with a configuration including a taller element ($B1_1$, Fig.3b), a significant increase in u'_{rms} is observed near the stagnation point of the tallest element. This increase is attributed to stronger velocity gradients and enhanced turbulence near the windward side of the element, extending downstream into the wake. The localized increase in turbulence in $B1_1$ suggests higher turbulent mixing and greater energy fluctuations than in $A1_1$. A similar amplification of turbulence and mixing is observed when comparing $A1_2$ and $B1_2$ (Fig.3c and d). These findings underscore the influence of roughness element positioning on drag and flow physics, even when geometric statistics like mean roughness height and ES remain constant. The rms of flow fluctuations behind the pinnacles is notably low, with turbulence intensity approaching zero within the wake, indicating that surface perturbations have a localized effect. The ED improves the correlation between roughness and turbulence characteristics.

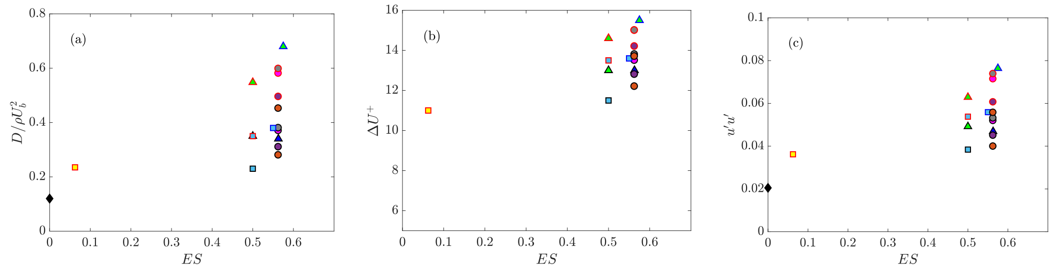

Figure 1: Effective slope dependence on the Drag, roughness function, and streamwise turbulent intensities of the rough wall.

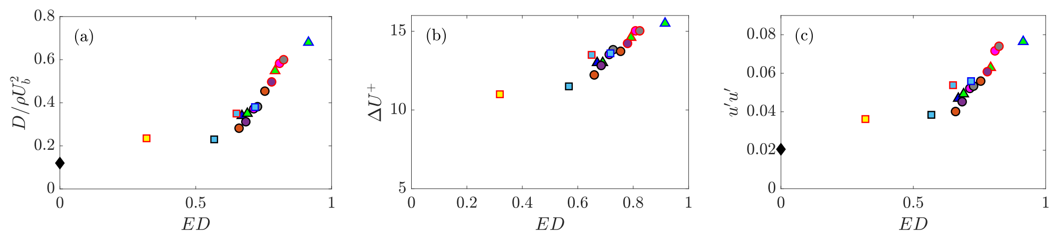

Figure 2: Effective Distribution dependence on the Drag, roughness function, and streamwise turbulent intensities of the rough wall.

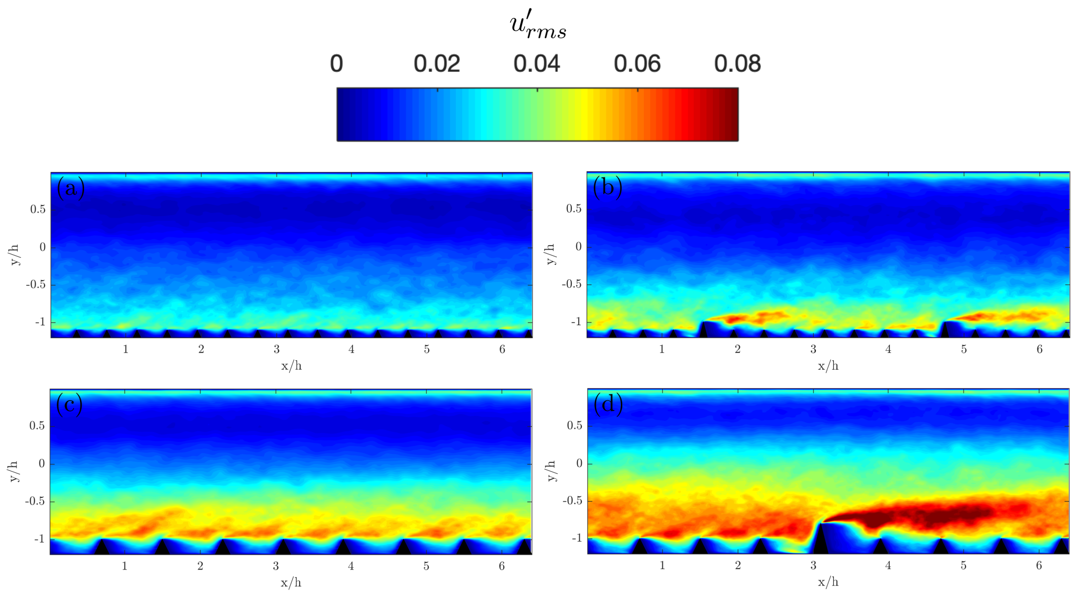

Figure 3: Color contours of streamwise turbulent intensities: (a) $A1_1$, (b) $B1_1$, (c) $A1_2$, (d) $B1_2$.

Anisotropic turbulence in transition phenomena of Taylor–Couette–Poiseuille flow

Yuki Matsukawa [1], Ryo Araki [1] and Takahiro Tsukahara [1]

[1] Department of Mechanical and Aerospace Engineering, Tokyo University of Science, Noda-shi, Japan

key-words: Anisotropy, Taylor–Couette–Poiseuille flow

Abstract:
There are two routes for a laminar flow to be turbulent: by supercritical and subcritical transitions. In the supercritical transition scenario, a linearly unstable base flow becomes turbulent continuously. The Taylor–Couette flow with inner cylinder rotation ($Re_{\rm in} \equiv u_{\rm in}h/\nu$) is one typical example; it reaches a turbulent state via the Taylor vortex (TVF), wavy Taylor vortex (WVF), and modulated wavy Taylor vortex (MWV). On the other hand, the subcritical transition is nonlinearly unstable to finite disturbances even in the linearly stable Reynolds number regime. Many wall-bounded shear flows belong to the subcritical transition. They exhibit localized turbulence near the global turbulence maintenance lower limit and form geometric patterns.

In this study, we performed direct numerical simulations of the Taylor–Couette–Poiseuille flow (TCPF, Fig. 1), a Taylor–Couette flow geometry with an axial pressure gradient drive, and investigated its turbulent transition process. Since a TCPF is a combined shear flow in multiple orthogonal directions, its three-dimensional velocity distribution makes the flow structure complex [1]. When we apply an axial drive to the TVF- and WVF-based cases ($Re_{\rm in} = 130$ and 150), the flow structures disappear. If the axial driving force is even greater, the flow becomes re-unstable and exhibits the helical turbulence characteristic of subcritical transitions (Fig. 2). The axial drive triggers a continuous turbulent transition with the MWV ($Re_{\rm in} = 1300$), suggesting the supercritical transition. Here, we do not observe any laminarization or localized turbulence. To further investigate this peculiar behavior, we adopted the Lumley triangle based on the second and third invariants (II and III) of the anisotropy tensor to evaluate the anisotropy of the flow structure [2]. The triangle's vertices indicate one-, two-component, and isotropic turbulent flow ($\mathbf{x}_{1c}$, $\mathbf{x}_{2c}$, and $\mathbf{x}_{3c}$). In the TVF and WVF, the invariants are distributed along the two-component limit ($\mathbf{x}_{1c}$–$\mathbf{x}_{2c}$). However, in the helical turbulence, they deviate from the limit line near the gap center (figures are not shown). On the other hand, in the MWV-based case, we can see an approach to the lines $\mathbf{x}_{2c}$–$\mathbf{x}_{3c}$ and $\mathbf{x}_{1c}$–$\mathbf{x}_{3c}$. In addition, as the axial driving increases, the distribution of the invariant map changes continuously, and it approaches the vertex of three-component turbulence and acquires high isotropy (Fig. 3). This acquiring isotropy is similar to the characteristics seen in a high Reynolds number turbulent channel flow.

In summary, we observed different turbulent transition processes depending on $Re_{\rm in}$ in TCPF and a continuous turbulent transition, which we investigated by evaluating the Lumley triangle representing the anisotropy of the flow. In the presentation, we will also discuss the turbulent transition process from the perspective of the energy balance of the Reynolds stress.

References

[1] Matsukawa Y. and Tsukahara T., (2022), Subcritical transition of Taylor–Couette–Poiseuille flow at high radius ratio, *Physics of Fluids, Vol. 34(7), 074109.*

[2] Lumley J. L. and Newman G. R., (1977), The return to isotropy of homogeneous turbulence, *Journal of Fluid Mechanics, Vol. 82(1), pp. 161–178.*

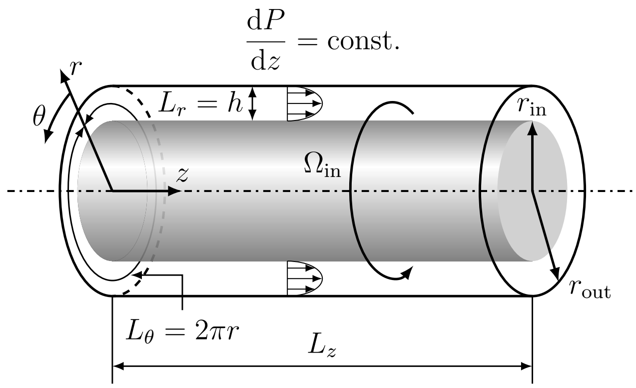

Figure 1: Configuration of a Taylor–Couette–Poiseuille flow (TCPF). The outer cylinder is stationary ($\Omega_{\text{out}} = 0$).

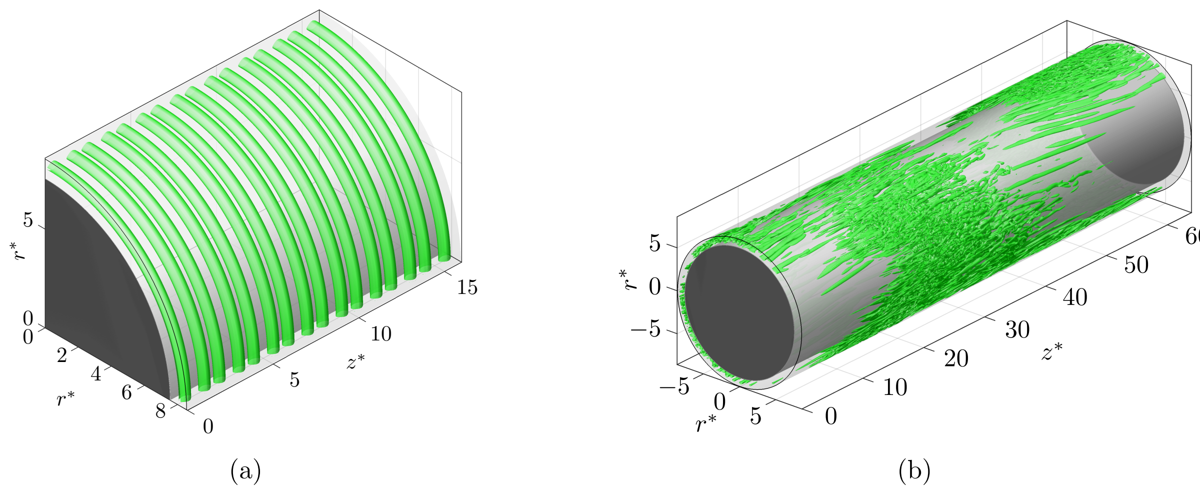

Figure 2: Three-dimensional visualizations of second invariant of velocity gradient tensor Q: (a) $Re_{\text{in}} = 130, Re_{\tau,z} = u_{\tau,z}h/2\nu = 0, Q = 0.005$ (Taylor vortex in the supercritical transition) and (b) $Re_{\text{in}} = 130, Re_{\tau,z} = 49.4, Q = 1$ (helical turbulence in the subcritical transition).

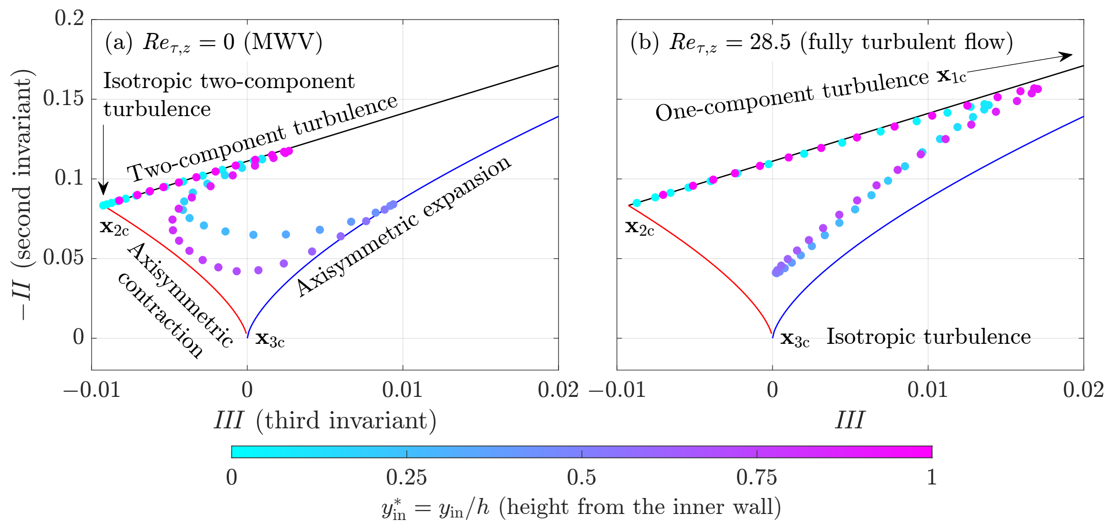

Figure 3: Diagram of anisotropy invariant map at $Re_{\text{in}} = 1300$ (MWV-based case), represented by the Lumley triangle. The color of the data corresponds to the height from the inner cylinder wall y^*_{in}.

Turbulent channel flow manipulations by sinusoidal riblets - a numerical study

E. Amico [1], A. Busse[2], F.A. Portela[3], G. Cafiero [1]

[1] Department of Mechanical and Aerospace Engineering, Politecnico di Torino, Torino, Italy

[2] James Watt School of Engineering, University of Glasgow, Glasgow, G12 8QQ, UK

[3] Ecole Centrale de Lyon, CNRS, Universite Claude Bernard Lyon 1, INSA Lyon, LMFA, UMR5509, 69130, Ecully, France

key-words: Wall bounded flows, Simulation

Abstract:

Reducing drag in wall-bounded turbulent flows is a crucial challenge in fluid dynamics, with significant implications in aerospace, naval, and automotive applications. Among passive control techniques, modifying surface textures by adding riblets—streamwise-aligned grooves—has been widely studied and demonstrated to effectively reduce skin friction [1].

Recent advancements propose an alternative approach by introducing sinusoidal riblets, characterized by a periodic streamwise waviness. This solution has been suggested as a robust alternative to conventional riblets, offering similar or greater drag-reduction potential while exhibiting lower sensitivity to flow misalignment [2]. Experimental studies have demonstrated the efficacy of such designs in modifying near-wall turbulence structures, leading to increased aerodynamic efficiency [3].

In this work, we perform direct numerical simulations (DNS) of a turbulent channel flow at a friction Reynolds number $Re_\tau = 540$ with sinusoidal riblets embedded on both walls. The riblet configuration is defined by a height-to-spacing ratio of $h/d = 0.7$ and an amplitude of $a = 0.15$, consistent with the experimental work of Cafiero and Iuso [2]. The near-wall flow structures are analyzed through phase-conditional averaging to assess their impact on turbulence dynamics.

As in the case of stream-wise-aligned riblets, mean-flow vortical structures aligned with the streamwise direction develop just above the riblets' crests [3]. These coherent vortical structures play a crucial role in modifying the near-wall dynamics by redistributing momentum and influencing the overall shear stress at the wall. Our DNS data allows us to directly visualize those vortical structures, which, in the present case of sinusoidal riblets, appear with alternating vorticity in the stream-wise direction.

This alternation in vorticity is a direct consequence of the sinusoidal modulation of the riblets, which introduces a periodic variation in the local surface curvature and alters the way the boundary layer interacts with the wall. As shown in figure 1, the structures are generated at locations where the amplitude of the sine wave is maximum (corresponding to $\Phi = \pi/2$). This suggests that the flow locally adapts to the changing surface geometry by forming vortices whose size and strength vary periodically along the streamwise direction.

Once generated, these vortices exhibit a distinct growth pattern, increasing in size (radius r^+) as they migrate from the center of the groove ($\Theta = 0^o$) toward the riblet's crest ($\Theta = \pi/2$). This growth is indicative of an interaction between the near-wall low-speed streaks and the modified surface topology, which influences the dynamics of turbulence production and dissipation. The observed movement of the vortices from the groove center to the riblet crest suggests a redistribution of turbulent kinetic energy in the near-wall region, potentially altering the classical buffer-layer dynamics typically observed in smooth-wall turbulent flows.

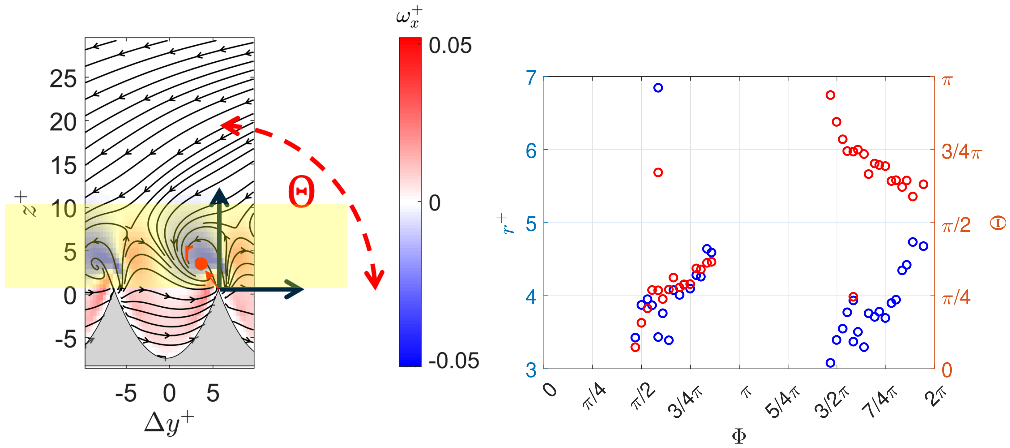

Figure 1: Instantaneous visualization of the streamwise vorticity in the spanwise (y^+), wall-normal (z^+) plane (left), with indication of the vortex trajectory in terms of the radius and polar coordinate (right).

References

[1] R. García-Mayoral and J. Jiménez, "Drag reduction by riblets," *Philosophical Transactions of the Royal Society A: Mathematical, Physical and Engineering Sciences*, vol. 369, no. 1940, pp. 1412–1427, 2011. DOI: 10.1098/rsta.2010.0359.

[2] G. Cafiero and G. Iuso, "Drag reduction in a turbulent boundary layer with sinusoidal riblets," *Experimental Thermal and Fluid Science*, vol. 132, p. 110723, 2022. DOI: 10.1016/j.expthermflusci.2022.110723.

[3] D. Modesti, S. Endrikat, N. Hutchins, and D. Chung, "Dispersive stresses in turbulent flow over riblets," *Journal of Fluid Mechanics*, vol. 915, A23, 2021. DOI: 10.1017/jfm.2021.310.

Geometric and Statistical Characterization of the Turbulent/Non-Turbulent Interface in a Turbulent Bounday Layer Flow Identified Using Uniform Momentum Zone Concepts

B. Sun , C. Atkinston and J. Soria

[1] Laboratory for Turbulence Research in Aerospace and Combustion, Department of Mechanical and Aerospace Engineering, Monash University, Melbourne, Australia 3800

key-words: Turbulent Boundary Layer Flow, TNTI

Abstract:
The turbulent/non-turbulent interface (TNTI) refers to the region that separates the irrotational, non-turbulent part of the flow from the turbulent region. The entrainment process occurring at this interface is of significant interest for both industrial applications and turbulence research. However, detecting the TNTI remains challenging due to the absence of a universally accepted physical definition[2]. Uniform momentum zones (UMZs) are regions within the turbulent boundary layer where the streamwise velocity remains relatively uniform[3]. It has been demonstrated that there is a jump in velocity across UMZ edges [4], which is also a property shared with TNTI. Therefore, the outmost UMZ edge is natually a candidate for TNTI identification.

In the identification process of the turbulent/non-turbulent interface (TNTI), for each plane in the spanwise direction a sliding window of size 1δ in streamwise direction, and 2δ in wall normal direction is used and moved downstream. The boundary layer thickness in the window size corresponds to the value at the center of the window. Thus, the sliding window increases in size as it progresses downstream, ensuring that the proportion of the turbulent and non-turbulent parts of the flow remains approximately constant throughout its streamwise extent. A histogram of the instantaneous streamwise velocity is computed within the sliding window. The local minimum in the probability density function (PDF) that separates the peak representing the freestream velocity from the rest of the turbulent flow is identified as the edge velocity, u_{edge}. The velocity isocontour corresponding to u_{edge} is then defined as the TNTI within the window. As the window moves downstream, new values of u_{edge} are determined through the same process, and the TNTI location is updated accordingly. The identification process is illustrated in the figure 1.

The analysis of the geometric properties of the interface will be presented at the conference. Additionally, conditional turbulent statistics, including mean velocity, Reynolds stress, as well as mean and fluctuating vorticity profiles, will also be presented.

Acknowledgement:
The authors would like to acknowledge the funding of this research by the Australian Research Council through a Discovery Grant. The authors also acknowledge the computational resources provided by the Pawsey Supercomputing Centre supported by the Australian and Western Australian Governments, and the National Computational Infrastructure (NCI), supported by the Australian Government through computational grants awarded by the National Computational Merit Allocation Scheme (NCMAS) funded by the Australian Government. Bihai Sun gratefully acknowledges the support provided by a Monash Graduate Scholarship (MGS).

References

[1] Chauhan, K., Philip, J., de Silva, C. M.,Hutchins, N., and Marusic, I., (2014), The turbulent/non-turbulent interface and entrainment in a boundary layer, *Journal of Fluid Mechanics, vol. 742, pp. 119–151*

[2] Adrian, R. J. ,Meinhart C. D. and Tomkins, C. D., (2000), Vortex organization in the outer region of the turbulent boundary layer, *Journal of Fluid Mechanics, vol. 422, pp. 1-54.*

[3] de Silva, C. M., Hutchins, N., and Marusic, I., (2016), Uniform momentum zones in turbulent boundary layers, *Journal of Fluid Mechanics, vol. 786, pp. 309–331.*

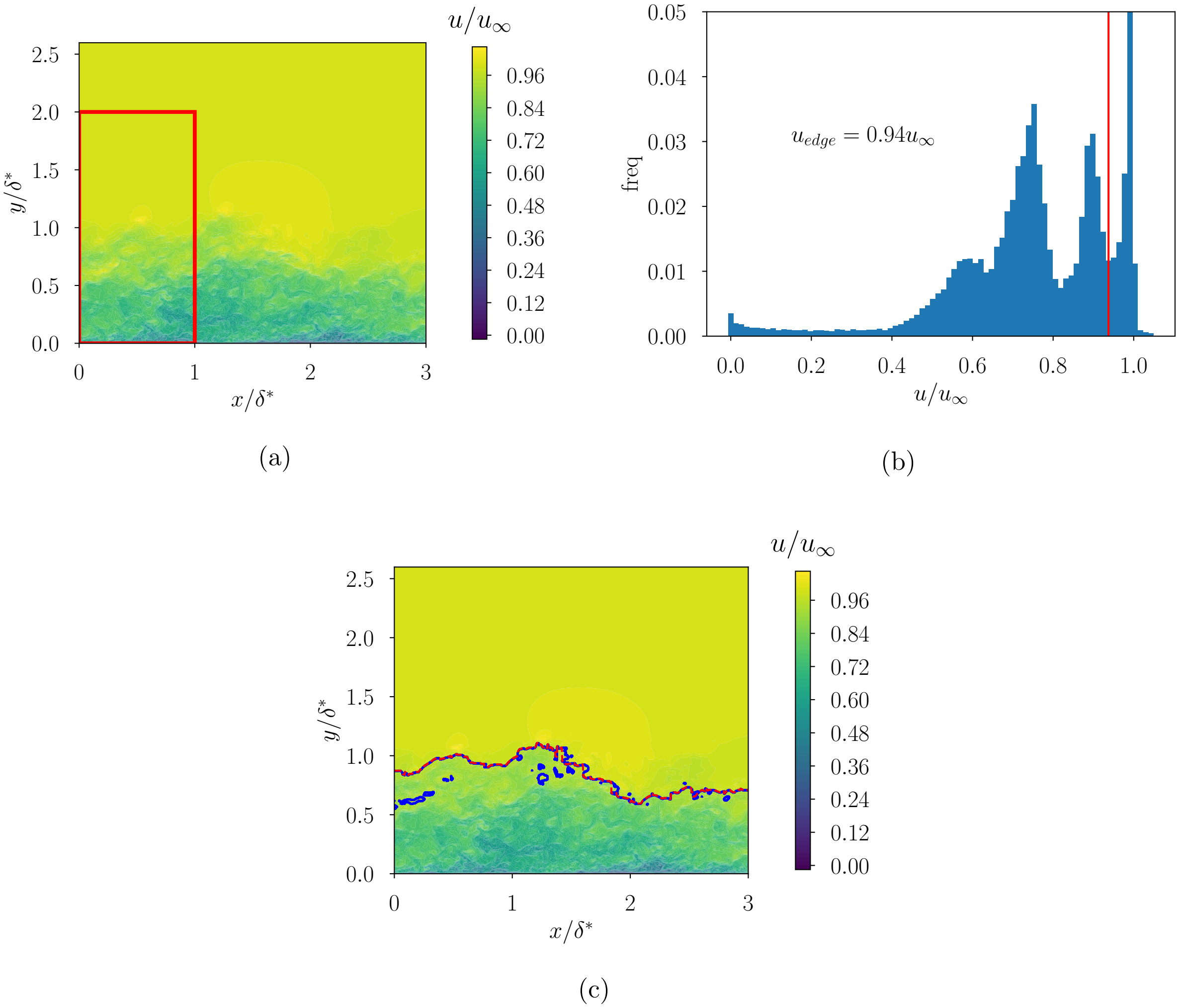

Figure 1: *(a) Contour of an example instantaneous velocity field with the moving window for TNTI identification highlighted in red (b) PDF of velocity within the window, with the verticle line representing u_{edge} (c) The identified TNTI (—) and interface height (y_{TNTI}, - - -) overlayed on the instantaneous velocity contour.*

Structure of the momentum and temperature fields in a turbulent boundary layer perturbed by an effusion film

D. Burnett [1], J. F. Morrison [1]

[1] Department of Aeronautics, Imperial College London, UK

key-words: Turbine blade cooling, turbulent mixing

Abstract:

Despite the vast research into gas turbine blade cooling systems, few studies focus on detailed characterisation of the velocity and temperature fields, although the transport of heat and momentum determine the surface heat transfer rate. Measurements of these fields will improve what is a currently poor understanding of the heat transfer mechanisms [1] and highlight the current shortcomings of RANS models. This lack of understanding also leads to use of higher injection-to-freestream velocity ratios (VR) in current state-of-the-art designs, which reduces engine efficiency and power output [1]. In previous studies, boundary layer measurements have been limited to outside of the viscous region and a small number of VR cases have been studied [2, 3].

The current work presents three-component velocity measurements extending down to the viscous sublayer using laser Doppler anemometry. Simultaneous temperature and velocity measurements are acquired with an x-wire and an adjacent cold-wire for turbulent heat flux measurements. Independent skin friction measurements are obtained with oil film interferometry. The geometry of a turbine blade with effusion cooling is idealised with injection of lower temperature air into a large turbulent boundary layer, through a flat porous plate that consists of a staggered array of small holes with diameters $D = 16\,\text{mm}$. The large-scale 'big and slow' experiment benefits from high resolution and allows for larger δ/D ratios than previously used in the literature, which is characteristic of next-generation effusion cooling or 'quasi-transpiration' designs. Wall-normal profiles are measured at a fixed streamwise location on the effusion plate at two spanwise locations: one the centreline of the holes, and one between two columns of holes (where there is no immediate effect of injection). The velocity ratio is varied in the range $0 < VR < 0.37$.

The results show rapid departures from canonical viscous scaling, occurring for $y^+ > 20$ (Figure 1). In the overlap region, the boundary layers become heavily perturbed with distinct plateaus in the streamwise velocity profiles forming by $VR = 0.37$. No evidence of logarithmic scaling is apparent and therefore traditional modelling strategies are shown to be inadequate, particularly the mixing length model. The turbulence structure is significantly modified, with an outer peak forming for each orthogonal velocity variance (Figure 2). A key result is the change in boundary layer scaling observed about a critical velocity ratio $VR_c \approx 0.2$ - a much lower threshold than indicated by previous studies. An example is that the spanwise velocity fluctuations begin to dominate the near-wall turbulence on the hole centreline for $VR > VR_c$. A large dissimilarity between the momentum and temperature fields is observed. Turbulent transport of both turbulence kinetic energy and temperature variance is large across the boundary layer, so the local equilibrium hypothesis is not valid. In the outer region, structure parameters such as a_1 and $a_{1\theta}$ are approximately constant and similar to the unperturbed values. The turbulent Prandtl number assumes an approximately constant value $1 < Pr_t < 1.4$ in this region, although large departures from Reynolds' analogy and counter-gradient transport of heat are observed near the wall.

References

[1] J. Han, "Fundamental gas turbine heat transfer," *Journal of Thermal Science and Engineering Applications*, vol. 5, no. 2, 2013, 021007.

[2] S. Yavuzkurt, R. J. Moffat, and W. M. Kays, "Full-coverage film cooling. Part 1. Three-dimensional measurements of turbulence structure," *Journal of Fluid Mechanics*, vol. 101, no. 1, pp. 129–158, 1980.

[3] A. Kohli and D. G. Bogard, "Turbulent transport in film cooling flows," *Journal of Heat Transfer*, vol. 127, no. 5, pp. 513–520, 2005. [Online]. Available: https://dx.doi.org/10.1115/1.1865221

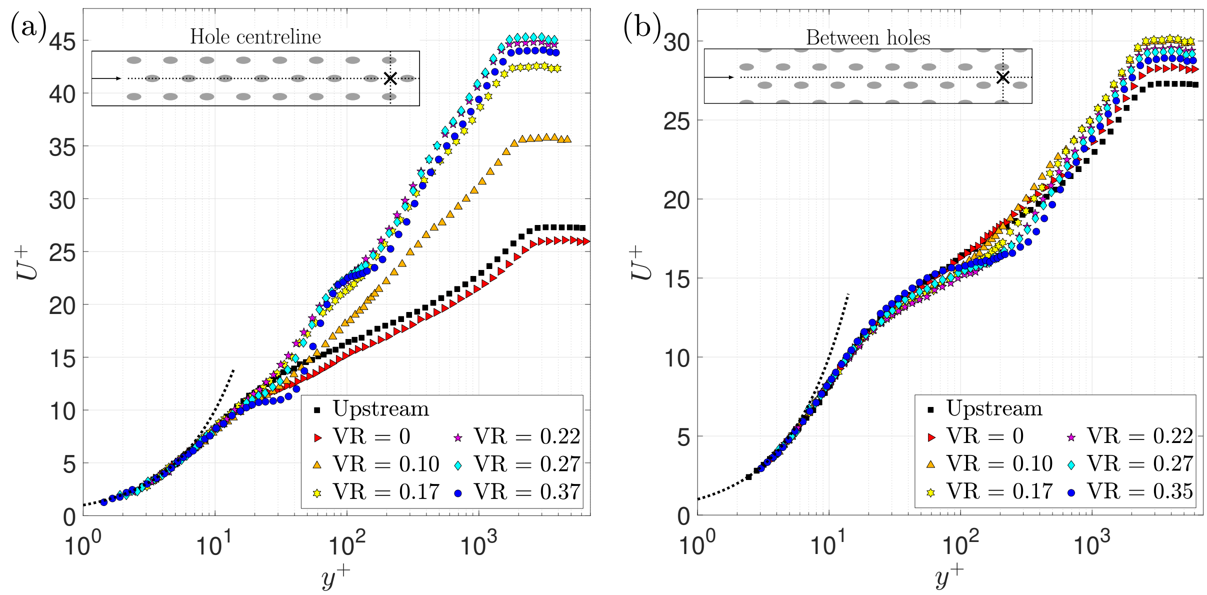

Figure 1: Mean streamwise velocity profiles on (a) the hole centreline, and (b) between holes, presented in inner scaling. Dotted lines correspond to $U^+ = y^+$.

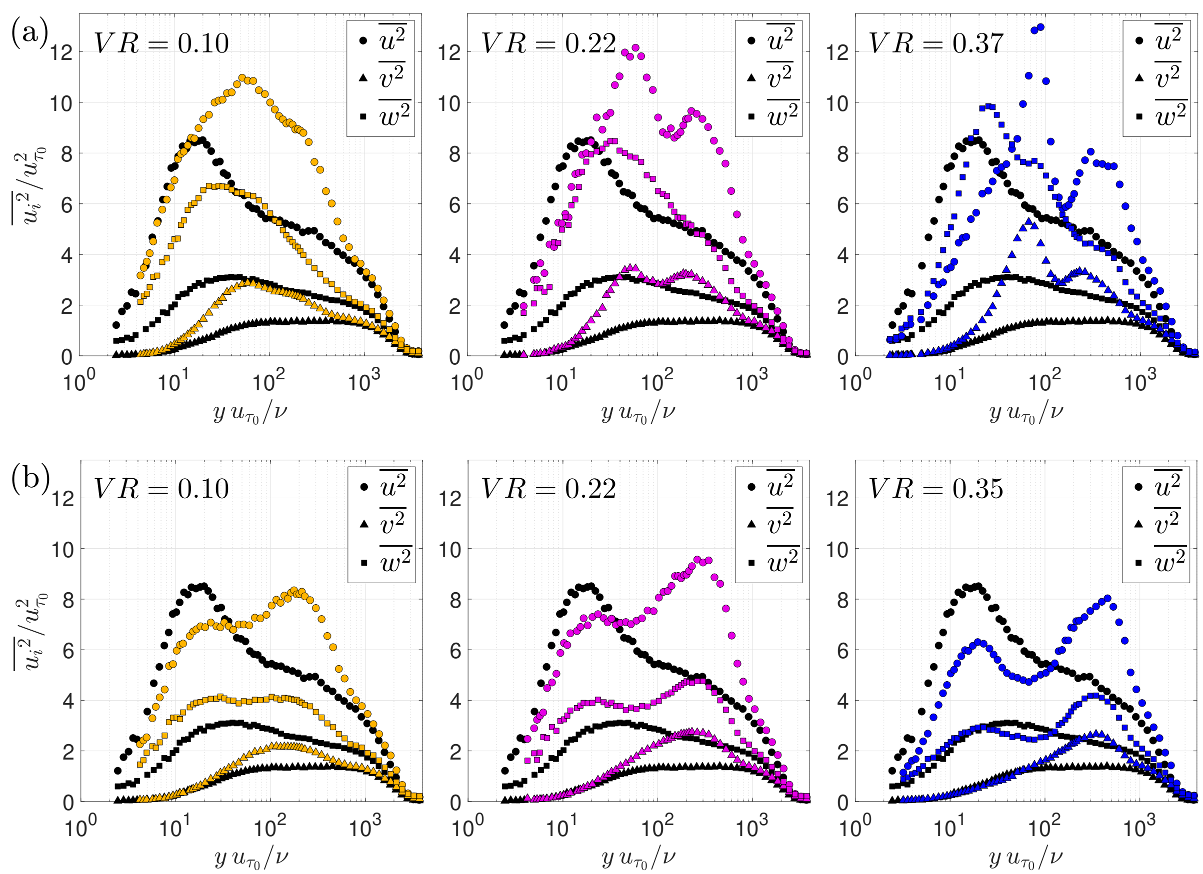

Figure 2: Turbulent momentum flux distributions in the three orthogonal directions for (a) on the hole centreline and (b) between holes. The velocity ratio is indicated in the top left-hand corner of each plot. Each plot shows the comparison with the baseline unperturbed case (black symbols).

Direct Numerical Investigation of Flow Dynamics in Karst Conduits

Ismail El Mellas [1], Juan Hidalgo and Marco Dentz

[1] Groundwater and Hydrogeochemistry, Idaea-Csic, Barcelona, Spain

key-words: Karst conduit, Transitional flow, Simulation

Abstract:
Karst aquifers, with their extensive and intricate conduit networks, are essential for groundwater flow and contaminant transport [1]. The complex geometry, characterized by branching conduits, varied cross-sections, and remarkable wall roughness (k/D $\simeq 10^{-1}$), add further challenges to predicting flow patterns, friction losses, and turbulence onset.
This work examines flow behaviour in representative karst conduits to identify key geometrical and fluid mechanical parameters, such as average cross-sectional areas, cave centrelines, friction factors, and velocity distributions, using direct numerical simulations over a broad range of flow conditions (Re $= 1 - 10^3$). These variables are critical for upscaling methods as can be used to simulate the entire karst networks without resolving every conduit in detail. In this study a combination of finite-volume and spectral element methods has been employed: finite-volume for resolving laminar flows in more complex geometries and spectral element methods for capturing turbulent flows at higher Reynolds numbers. Conduit geometries for the simulations are reconstructed from high-resolution LiDAR scans of real karst formations, with point cloud data maintaining all features such as rough walls, branching, and variable cross-sections. An immersed boundary model [2] together with a ray-tracing algorithm allows accurate boundary representation and correct forcing of boundary conditions within these intricate geometries.
The validation of the numerical framework was first performed on classical problems, including laminar and turbulent flow in a straight circular pipe. The immersed boundary method reproduced excellent friction factors and velocity profiles matching both laminar and turbulent reference data. Tests conducted in a wavy channel geometry (see Fig. 1(a)) suggest that laminar flow conditions hold in certain conduit sections, leading to smooth centerline velocities and predictable friction losses. Due to the irregularities in the conduit, the flow field is significantly disrupted, resulting in spatial variations that differ from those observed in smooth-channel conditions. Moreover, the simulations reveal that the flow transitions to a transitional or turbulent regime at Reynolds numbers lower than those predicted by standard empirical correlations (Re $\leq$ 1000). The result suggests that the conventional friction factor estimations, often based on the Moody chart [3] and Darcy-Weisbach formulations [4], may not fully capture the effects of the complex, heterogeneous conditions typical of karst systems (see Fig. 1(b)). As illustrated in Fig. 2, the intricate geometry and roughness of karst conduits appear to significantly change the flow dynamics, causing deviations from classical behaviour. Furthermore, extracting relevant quantitative data, such as velocity profiles, turbulence statistics, and friction factors remains challenging due to the complexity of these geometries. As a result, alternative approaches are needed to effectively capture the key flow characteristics in karst conduits.

References

[1] Parise M., Gunn J., (2007), Natural and anthropogenic hazards in karst areas: an introduction, *Geol. Soc., 279, pp. 1-3*

[2] Fadlun E. A., Verzicco R., Orlandi P. and Mohd-Yusof J., (2000): Combined Immersed-Boundary Finite-Difference Methods for Three-Dimensional Complex Flow Simulations, *J. Comput. Phys., 161, pp. 35-60*

[3] Moody L. F., (1944): Friction factors for pipe flow, *Transitions of the ASME, 66, pp. 671-684*

[4] White Frank M. , (2011): *Fluid Mechanics*, *Mcgraw-Hill, 7th ed.*

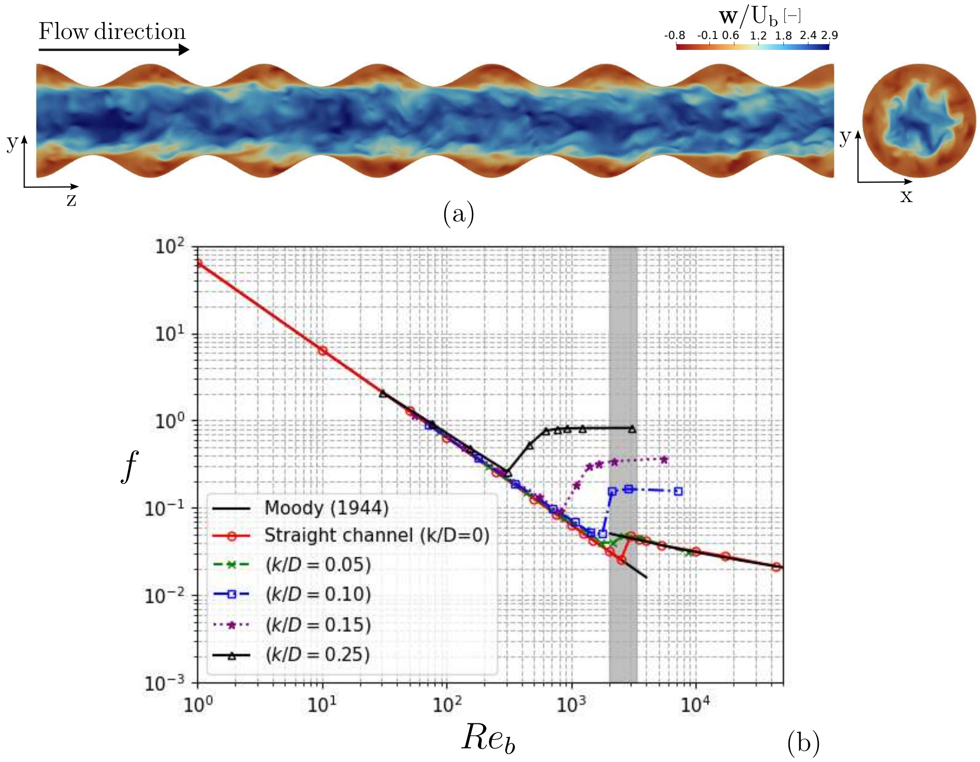

Figure 1: *a) Velocity contours of the main velocity component* (w/U_b) *on the streamwise* ($y-z$) *and cross-stream* ($x-y$) *planes, for the wavy-channel case* $k/D = 0.25$ *and* $\mathrm{Re} = 1500$. *b) Friction factor* ($f = 2D\Delta p/U^2\rho L$) *versus Reynolds number for various roughness ratios.*

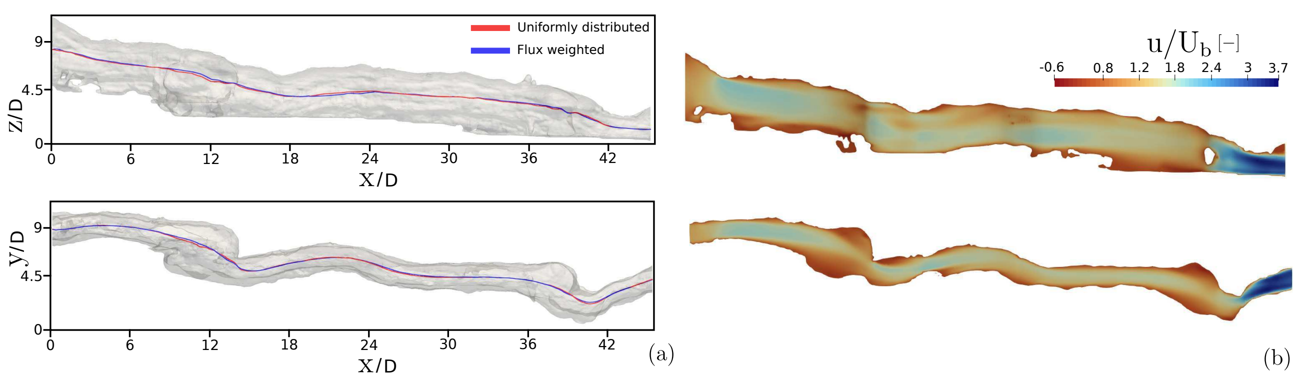

Figure 2: *a) Side and top views of the Archamps cave (Switzerland). The images presents also the flow-based centreline of the cave evaluated using a particle tracking simulation. b) Contours of the average velocity of the main component* (u/U_b) *extracted along the centrelines in the* $x-z$ *and* $x-y$ *planes starting from top to bottom, for* $\mathrm{Re} = 1000$.

The effect of porosity on the drag of a sphere

N. Conlin[1], K. Steiros[2] and M. Hultmark[1]

[1] Mechanical and Aerospace Engineering Department, Princeton University, Princeton, USA
[2] Aeronautics Department, Imperial College London, London, UK

key-words: Turbulent wake, porous bluff bodies

Abstract:
The motivation of this work stems from the recent introduction of 3D-printed, porous sports balls to the market, whose advantage is that they are ‘airless’, i.e., they do not need to be inflated [1]. Given that porosity is known to drastically alter the aerodynamic properties of bluff bodies, it would be of interest to characterize the flow-properties of porous spheres. Our initial expectation was that the introduction of porosity would drastically decrease aerodynamic resistance (thus affecting long range passes/shots). However, a preliminary experiment where we released two spheres from the 13th floor of a tall building (see figure 1a) revealed the opposite result: the lower-porosity sphere reached the ground first, suggesting a higher aerodynamic resistance when porosity increases, contrary to what is observed and predicted by theory for porous flat plates [2].

To investigate the cause of the above counter-intuitive phenomenon, we performed drag and particle image velocimetry measurements of D=150 mm diameter spheres with porosity ratio (defined as the ratio of the total open area introduced by the holes to the surface area of a non-porous sphere) equal to β = [0.025 0.1 0.2 0.3 0.4 0.5 0.95] in a 1.2 m × 1.2 m cross section wind tunnel (see figure 1b). The tunnel wind-speed was varied from 5 to 30 m/s to investigate Reynolds number effects. Drag measurements were also conducted for spheres with a solid ring attached at the $\theta = 90°$ position of their periphery. The effect of the ring was to fix the separation point for all spheres at the same location. In that manner we could test whether the increase of drag with porosity seen in the preliminary building experiment was due to a movement of the separation point (i.e., cancelling of the supercritical regime with porosity) or not.

The drag results for the porous spheres can be seen in figure 2a. In agreement with the building experiment, we found that porosity drastically increases the aerodynamic drag of spheres, to the point that a porosity of 95% nearly doubles the value of the very low porosity case. Figure 2b shows that this increase is not (in general) caused by a movement of the separation point (supercritical effect), as the ring had a significant effect only on the drag of the very low porosity cases. The average velocity results obtained via PIV are shown in figure 3 and indicate significant differences in the wake of the various tested cases. Using the PIV data we performed an approximate calculation of the losses due to the hole expansion (not presented here), which provide an explanation for the increased drag, i.e., the flow that enters and exits the porous sphere experiences high expansion losses from the presence of multiple holes and increases disproportionately the drag of the sphere.

References

[1] https://www.dezeen.com/2023/03/08/wilsons-airless-3d-printed-basketball/
[2] Steiros K. and Hultmark M. (2018). Drag on flat plates of arbitrary porosity. JFM Rapids, 853:R3

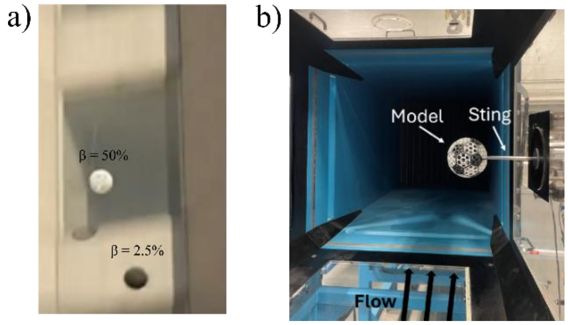

Figure 1: *(a) Photograph of two porous spheres in mid-air, after being dropped from a tall building (the weight and diameter was kept the same). (b) Wind tunnel experiment of porous spheres.*

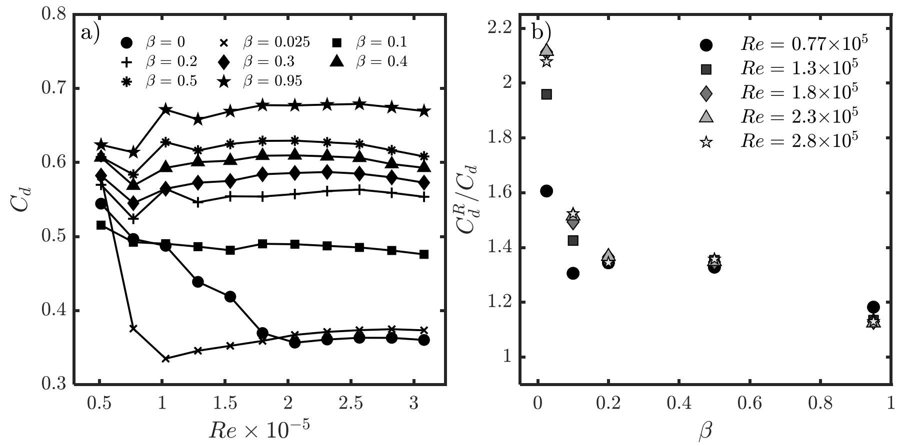

Figure 2: *(a) Drag coefficient versus Reynolds number for various porous spheres. (b) Drag coefficient of spheres with separation ring divided by the drag coefficient of the same sphere without the ring, plotted against the porosity ratio.*

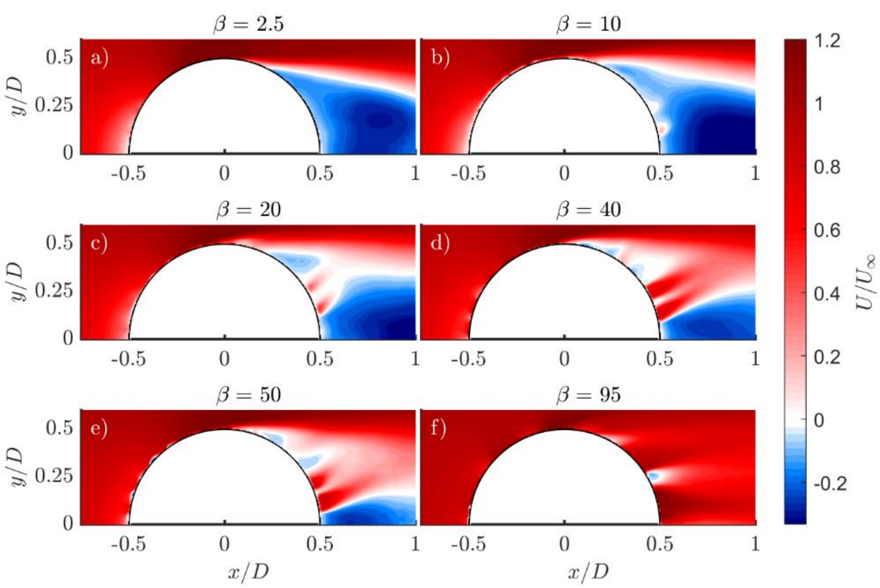

Figure 3: *Normalized average streamwise velocity, measured via PIV, for the various tested cases.*

Influence of wall temperature on separation-induced transition in boundary layers of real gas flows

D. Bulgarini [1], M. Dellacasagrande [2], A. Ghidoni [1], E. Mantecca [1] and G. Noventa [1]

[1] Department of Mechanical and Industrial Engineering, University of Brescia, 25123 Brescia, Italy
[2] Department of Mechanical, Energy, Management and Transport Engineering, University of Genova, 16145 Genova, Italy

key-words: Wall temperature, Transition, Real gas

Abstract:
At present days, many different techniques are used to perform flow control in a variety of both industrial and research application. One of the most craved benefits from the use of such techniques is the possibility to manage laminar to turbulent transition in boundary layers. However, despite many studies are present for ideal gas flows, the behaviour of transition within real gas flows, where thermophysical and transport properties may experience large variations, is much less investigated.
In this context, the aim of this work is to study a particular active flow control, i.e., the modification of wall temperature, to spotlight differences in the laminar to turbulent transition process of boundary layers within ideal and real gas flows. A high-order discontinuous Galerkin finite element solver is employed to perform implicit large eddy simulations of the T3L test case from the ERCOFTAC suite [1], using (i) two different wall to freestream temperature ratios $T_w/T_\infty < 1$ and $T_w/T_\infty > 1$, and (ii) two different freestream to critical temperature ratios $T_\infty/T_{cr} < 1$ and $T_\infty/T_{cr} > 1$. All simulations are conducted at a fixed freestream Reynolds number Re_∞, Mach number Ma_∞ and turbulence intensity Tu_∞, using a freestream supercritical pressure $p_\infty > p_{cr}$ and CO_2 (i.e., carbon dioxide) as working fluid. To capture real gas behaviour in the flows, the Peng-Robinson cubic equation of state [2] is used to compute thermodynamic properties, and the multiparameter model of Chung et al. [3] is used to calculate transport properties. A reference simulation is performed using the same Re_∞, Ma_∞ and Tu_∞ for the wall to freestream temperature ratio $T_w/T_\infty = 1$, but with a rarefied freestream having low p_∞ and high T_∞, to resemble ideal gas behaviour.
The differences between the reference and the real gas simulations are examined both qualitatively and quantitatively. In particular, the λ_2 criterion is used to visualize instantaneous fields, while dynamic mode decomposition is applied to characterize unstable modes in the flows. Turbulent kinetic energy spectra and boundary layer integrals are calculated, near wall behaviour is represented and friction coefficients are compared to correlate the influence that wall temperature has in the active control of real gas flows.

References

[1] Coupland J. and Brierley D., (1996): Transition in Turbomachinery Flows - Final Report, *BRITE/EURAM Project AERO-CT92-0050*

[2] Peng D.-Y. and Robinson D. B., (1976): A New Two-Constant Equation of State, *Industrial & Engineering Chemistry Fundamentals, vol. 15, pp. 59-64*

[3] Chung T. H., Ajlan M., Lee L. L. and Starling, K. E., (1988): Generalized multiparameter correlation for nonpolar and polar fluid transport properties, *Industrial & Engineering Chemistry Research, vol. 27, pp. 671-679*

Oscillating grid turbulence: the influence of Reynolds number and forcing

M. Iovieno[1], H. Foysi[2] and G. Khujadze[2]

[1] Dipartimento di Ingegneria Meccanica e Aerospaziale, Politecnico di Torino, Torino, Italy
[2] Chair of Fluid Dynamics, University of Siegen, Siegen, Germany

key-words: shear-free turbulence, oscillating grids, turbulent/non-turbulent interface, direct numerical simulations

Abstract:

Oscillating grid turbulence is generated by a grid made up of a series of bars or rods arranged in a regular pattern, which moves back and forth in an oscillatory manner, stirring up the fluid, and generates turbulence in the region around the grid. In a statistical sense, turbulence is generated in a plane and diffuses outward in the normal direction, while simultaneously being damped by dissipation until a balance between transport and dissipation is achieved. Due to the absence of mean shear, there is no turbulence production beyond the energy injection region around the grid. As such, this setup serves as a valuable tool for investigating the fundamental properties of turbulence in a controlled, reproducible environment [1]. Despite the simplicity of the flow, many aspects have not yet been fully investigated. Oscillating grids have been used to produce turbulent shearless turbulent flows close to homogeneity [2, 3].

This work aims to investigate the role of the Reynolds number and the forcing mechanism on the development of turbulence by using Direct Numerical Simulations in which the energy injection through the grid is replaced by a localized body force varying in space and time. Following [4], we consider the forcing localized around the mean position of the grid and composed by a deterministic part, which depends on the mesh geometry, and a random part, i.e.

$$f_i(t, \mathbf{x}) = \frac{n^2 S}{2} \left\{ f_i^D(nt, x_1/M, x_2/M) + \frac{\beta_i}{4} \right\} g(x_3/S)$$

where S is the amplitude of the stroke, M is the spatial period of grid, n the frequency, $f_i^D(nt, x_1/M, x_2/M)$ is the deterministic part of the forcing, periodic with respect to its arguments, β_i are independent random numbers and $g(x_3/S)$ is a Gaussian smoothing function which localizes the forcing within a layer with a width equal to the stroke around the mean grid position. An example is shown in figure 1. Three distinct flow regions can be identified: the region directly stirred by the grid, an almost steady region behind the turbulent front, where kinetic energy decays algebraically with distance from the grid; and a boundary region, where the entrainment process occurs, and kinetic energy decays exponentially with distance from the grid. As the turbulence propagates, there is a gradual reduction in intensity, which reduces the ability to entrain more fluid until the transport process becomes saturated. We determine the evolution of the transient state and the scaling laws for the statistically steady state, showing how they are influenced by the Reynolds number and by the shape of the deterministic grid forcing (see, e.g., figure 2, for an example of the second-order moments and figure 3, for an example of the spectra at different Reynolds numbers).

References

[1] Poulain-Zarcos, M., Mercier M., Halle, A. (2022) Global characterization of oscillating grid turbulence in homogeneous and two-layer fluids, and its implication for mixing at high Peclet number. *Phys. Rev. Fluids 7, 054606.*

[2] De Silva, I. & Fernando, H., (1994) Oscillating grids as a source of nearly isotrpoic turbulence, *Phys. Fluids, 6(7), 2455–2464.*

[3] Li, W., Zhang, P., Yang, S., Fu, X. & Xiao, Y., (2020), An experimental method for generating shear-free turbulence using horizontal oscillating grids, *Water, 12, 591.*

[4] Godeferd, F. S. & Lollini, L., (1999) Direct numerical simulations of turbulence with confinement and rotation, *J. Fluid Mech., 393, 257–308.*

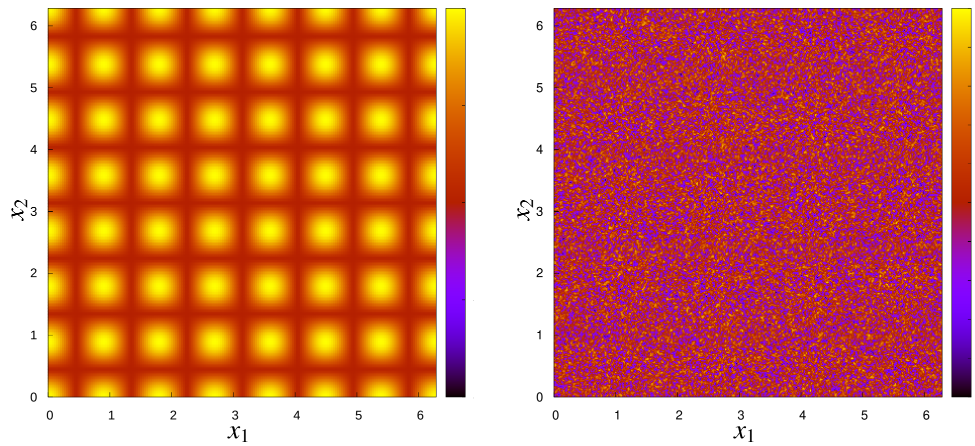

Figure 1: Example of forcing component $f_3/(n^2 S)$ in the grid normal direction x_3: on the left the amplitude f_3^D of the deterministic part of the forcing, on the right the random part.

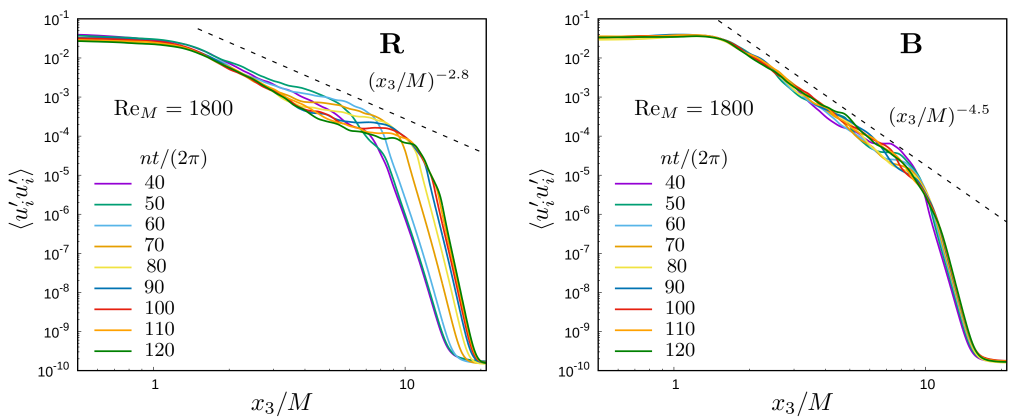

Figure 2: Second order moments $\langle u_u' u_i' \rangle$ for two different forcings, the rod-like forcing (left) and the bar-like forcing (right) at $\mathrm{Re}_M = nM^2/\nu = 1800$.

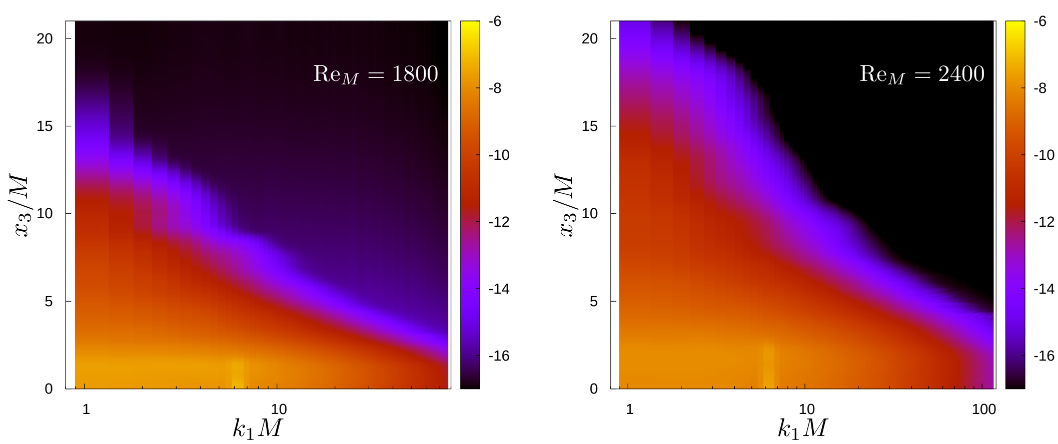

Figure 3: Spatial modulation of the spectra with distance x_3 from the grid at two Reynolds numbers, bar-like forcing.

Multi-point probability density hierarchy for homogeneous isotropic turbulence

S. Görtz [1,2], J. Conrad [1,2], N. Benedikt[1] and M. Oberlack [1,2]

[1] Chair of Fluid Dynamics, Technische Universität Darmstadt, Germany
[2] Graduate School of Computational Engineering, Technische Universität Darmstadt, Germany

key-words: Fundamentals, HIT, statistical description, probability density functions

Abstract:
Modern approaches to turbulence are from a statistical point of view. We aim to extend the theoretical knowledge of the statistics in homogeneous isotropic turbulence (HIT). A common approach to statistics from an engineering perspective is the consideration of multi-point moments. However, especially the tensor properties of velocity moments make it difficult to formulate a functional form for an isotropic moment beyond the famous treatment of the two point case by Von Kármán and Howarth [1]. We therefore consider probability density functions (PDFs), including all statistical properties. An n point PDF $f_{(n)}$ defines the average of a function Q depending on the physical velocities $u_{(1)}, \ldots, u_{(n)}$ at n points $x_{(1)}, \ldots, x_{(n)}$ by

$$\left\langle Q(\vec{u}_{(1)}, \ldots, \vec{u}_{(n)}) \right\rangle = \int_{\mathbb{R}^{3n}} Q(\vec{v}_{(1)}, \ldots, \vec{v}_{(n)})\, f_{(n)} \left(t, \vec{x}_{(1)}, \vec{v}_{(1)}, \ldots \vec{x}_{(n)}, \vec{v}_{(n)}\right) \mathrm{d}\vec{v}_{(1)} \ldots \mathrm{d}\vec{v}_{(n)}, \tag{1}$$

where $v_{(1)}, \ldots, v_{(n)}$ is the set of sample space coordinates. Lundgren [2] derived an infinite but linear multi-point hierarchy for the PDFs (the so called LMN hierarchy). Our aim is to link HIT with the LMN hierarchy, why the present work consists of three core elements. First, we introduce spherical coordinates as a natural way to assess HIT and express the PDF in a new set of coordinates, given by the scalar invariants under translation and the SO(3) group of rotations as described in [3], yielding a dimensional reduction of the problem to a minimal set of coordinates. Second, we transform the LMN hierarchy and its side conditions to the aforementioned new set of scalar invariants. As the LMN hierarchy includes all multi-point velocity moments by (1), the new reduced PDF equation represents a higher level equation for the moment hierarchy in HIT. The third step is the validation of the chosen PDF formulation by means of simulation data [4]. From this data, we construct homogeneous isotropic PDFs in the new set of coordinates, proving that the chosen approach is valid. We aim to use the resulting PDFs to explore further symmetry and similarity properties as well as the validity of the solution approaches to the reduced hierarchy, which were suggested in [3]. Beyond any solution of the LMN hierarchy, also the exploration of similarity properties would allow insight into scaling laws describing the physics of HIT.

References

[1] Von Karman, T., Howarth, L. (1938): On the statistical theory of isotropic turbulence, *Proceedings of the Royal Society of London. Series A, Mathematical and Physical Sciences, 164(917), 192-–215.*

[2] Lundgren T. S., (1967): Distribution Functions in the Statistical Theory of Turbulence, *Phys. Fluids, vol. 10, pp. 969-975.*

[3] Görtz, S., Plümacher, D., Conrad, J.H., Oberlack, M. (2024): Infinite Lundgren Hierarchy of Turbulence: Isotropy, Super-isotropy and a Finite Dimensional Eigenvalue Problem., *In:* Örlü, R., Talamelli, A., Peinke, J., Oberlack, M. (eds) *Progress in Turbulence X. iTi 2023. Springer Proceedings in Physics, vol 404. Springer, Cham.*

[4] Y.Li, E.Perlman, M.Wan, Y.Yang, C.Meneveau, R.Burns, S.Chen, A.Szalay, G.Eyink (2008): A public turbulence database cluster and applications to study Lagrangian evolution of velocity increments in turbulence., *Journal of Turbulence 9, No. 31, 2008.*

Convective organization and their influence on wind stress in a Large-Eddy Simulation ensemble

E. Foschi [1], L. Nuijens [1] and P. Lopez-Dekker [1]

[1] Civil Engineering and Geosciences, Delft University of Technology, Delft, The Netherlands

key-words: Atmospheric Flows, LES

Abstract:
Air-sea interaction plays a crucial role in the Earth system, but how the atmosphere and ocean are coupled at sub-mesoscales ranging from 100 m to 100 km is not well understood. At these scales, the atmosphere and ocean are both filled with rich spatial structure, which may influence air-sea fluxes, including wind stress, in ways that are not fully characterized. This study focuses on the significant variability observed in atmospheric shallow convection, as exemplified in figure 1, and how it influences patterns of wind and stability near the surface with impacts on surface wind stress. Shallow cumulus clouds over the subtropical oceans are organized in various ways: from cloud streets to convective cells, to patterns of precipitating cumuli organized in lines or arcs surrounding cold pools, to aggregated clusters with frequent precipitation to overturning circulations. These patterns introduce variability in wind through the circulations they introduce, and variability in precipitation and near-surface temperature (cold pools) [1]. This heterogeneity is clearly seen in SAR imagery of ocean surface roughness [2] and motivates a closer look at how surface wind stress is modeled and retrieved from space-borne observations and models. Wind stress is typically modeled and retrieved using bulk formulae that rely on Monin-Obukhov Similarity Theory (MOST) to describe the behavior of the near-surface, and which assumes flows are homogeneous, which may no longer hold true at sub-mesoscales. To study patterns wind stress in relation to atmospheric instability (convection), a large ensemble of subtropical shallow cloud fields is used, Cloud Botany [3]. These fields have been simulated using the Dutch Atmospheric Large-Eddy Simulation (DALES) [4] in a horizontal domain of 150 km x 150 km with a resolution of 100 m based on environmental conditions typical for the winter time subtropical Atlantic Ocean. This ensemble is used to explain how highly convective conditions, where turbulence is driven by buoyancy, modify surface heat and momentum fluxes compared to a weakly convective, shear-driven turbulent regime, as a function of Richardson number, as exemplified in figure 2. Turbulent transport and spectra are used to quantify the scales at which the modulation of near-surface wind patterns and shear stress changes behavior due to developing moist, precipitating convection. The insights gained into the mechanisms by which the atmosphere leaves an imprint on the ocean surface will provide near-wall statistics for scale-aware bulk flux models.

References

[1] Savazzi A., Nuijens L., Rooy W., Janssens M. and Siebesma A.P. Momentum Transport in Organized Shallow Cumulus Convection *Journal of the Atmospheric Sciences, 81*

[2] O'Driscoll O., Mouche, A., Chapron B., Kleinherenbrink M. and López-Dekker P. (2023) Obukhov Length Estimation From Spaceborne Radars *Geophysical Research Letters, 50*

[3] Jansson F., Janssens M., Grönqvist J., Siebesma A.P., Glassmeier F., Attema J., Azizi V., Satoh M., Sato Y., Schulz H. and Kölling T. (2023) Cloud Botany: Shallow Cumulus Clouds in an Ensemble of Idealized Large-Domain Large-Eddy Simulations of the Trades *Journal of Advances in Modeling Earth Systems, 15*

[4] Heus T., van Heerwaarden C., Jonker, H., Siebesma A.P., Axelsen S., Dries K., Geoffroy, O., Moene A.F., Pino Gonzalez D., Roode S.R. and Arellano J. (2010) Formulation of the Dutch Atmospheric Large-Eddy Simulation (DALES) and overview of its applications *Geoscientific Model Development, 3*

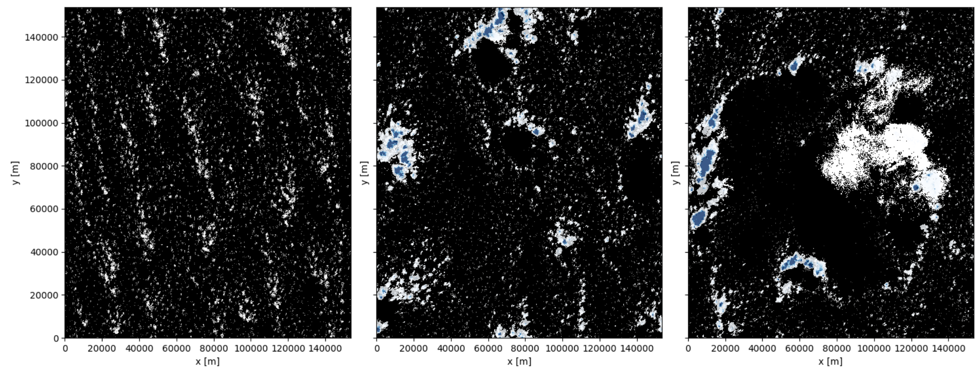

Figure 1: *Different types of cloud organizations seen in a member of the Cloud Botany ensemble time = 25h, 35h and 59h. Cloud albedo is shown in white and rain water path in blue.*

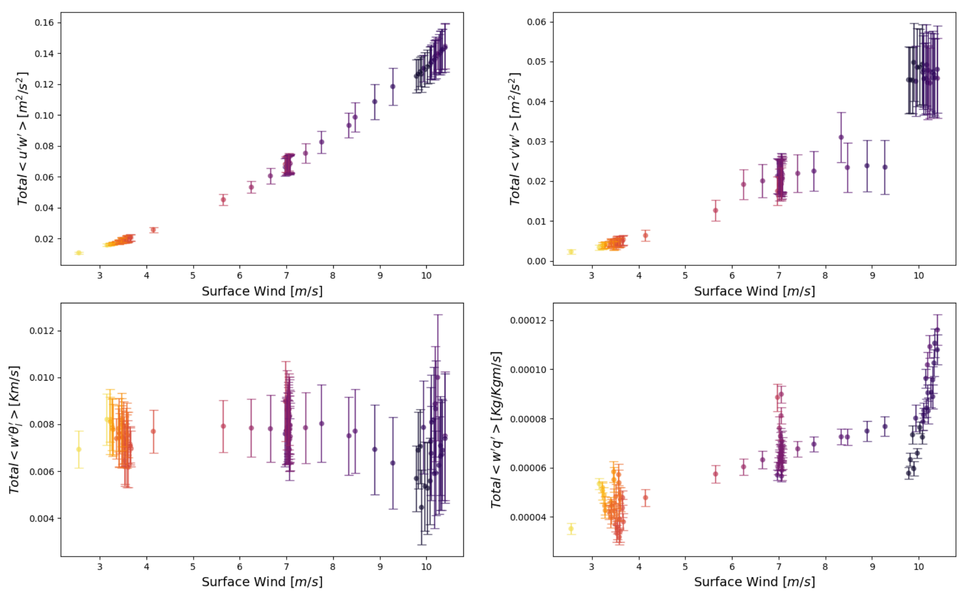

Figure 2: *Total surface fluxes (zonal momentum, meridional momentum, latent heat and sensible heat) plotted against surface wind speed and colored by stability parameter defined as $-z_i/L$, where z_i is the inversion height and L is the Obukhov length, with a color gradient from dark purple (weakly convective) to light yellow (highly convective). Error bars are derived from the standard deviation of the time series.*

Image Processing Analysis of Large-Scale Structures in Two-Dimensional Turbulent Channel Flow

Ryo Takai[1], Kosuke Takahara[1], Kai Sato [1], Sattaya Yimprasert[2], Kentaro Kato[1] and Masaharu Matsubara[1]

[1] Mechanical Systems Engineering, Shinshu University, 4-17-1, Wakasato, Nagano, 380-8553, Japan
[2] Department, Naresuan University, Chang Wat Phitsanulok, Thailand

key-words: Turbulence, Transition, Visualisation, Moving average, Streak

Abstract:
Wall-bounded turbulent shear flows have large-scale structures that are much longer than their shear width. Hot-wire rake measurements at very high Reynolds numbers ($Re = U_b d/\nu = 144,000$) by Monty et al.[1] showed the existence of large-scale structures of low-velocity streaks with lengths of about $10d$, where d and U_b are the channel width and the mean (bulk) velocity U_b, respectively. On the other hand, Seki et al.[2] confirmed that in transitional and low Reynolds number turbulent channel flows a low frequency peak is present in the spectra of the streamwise velocity measured by hot-wire anemometry. In addition, flow visualisation experiments by Yimprasert et al.[3] dense regions of wavy streaks of $10d$ length and $5d$ width at $Re = 2700$, whose streamwise scale corresponds to the low-frequency peak of the peak corresponding to Seki et al.[2]. Although the large-scale structures, which are about an order of magnitude larger than the channel width, clearly differ in width between high and low Reynolds number turbulent channel flows, the relationship between them is not well understood. It is also interesting to consider the presence of large-scale structures at intermediate Reynolds numbers. In this study, we visualised the flow by gradually increasing the Reynolds number just after the transition and then attempted to analyse the resulting images to extract the large-scale structures.

A two-dimensional water channel flow apparatus with a channel width of $d = 7.2$ mm and a glass test section 580 mm wide and 4650 mm long was used. A camera and two halogen lamps were installed perpendicular to both streamwise and spanwise directions, and pearl pigments were added to the water for the visualisation. Figure 1 shows the visualisation images and their moving average images. The imaging area is 162×122 mm^2 ($23d \times 17d$) and the left side of each image is the upstream. The visualisation images are normalised by the standard deviation of brightness after subtracting the time-averaged images, and the contrast of the moving average images is adjusted with a constant factor for ease of viewing. The streamwise and spanwise sizes of the moving average filter are $10d \times 3d$ respectively. In the visualisation image at $Re = 1800$, small vortices and large streak structures are observed. According to experiments by Seki et al. [2] and Yimprasert et al. [3], the turbulence fraction (intermittency) at this Re is about 0.5, which means that the flow state is halfway through the transition. The small eddy regions are considered turbulent, while the large streak regions are non-turbulent with no fine eddy structure, and these regions are distributed like a patchwork. The patch structure becomes clearer in the moving average image, where the non-turbulent areas are generally bright and therefore white in the moving average image, while the turbulent areas are black. At $Re = 2700$ the whole flow becomes turbulent, with irregular streaks and eddies. However, the moving average image still shows a patch structure, and even at $Re = 3000$ a patch structure is observed. The essential difference is that the streaks at $Re = 1800$ have a regular structure, whereas those at $Re = 2700$ are irregularly wavy. These results suggest that the streaks for $Re \geq 2700$ are irregular enough to be considered turbulent, although the dense regions of long streaks remain after the transition. The contrast in the moving average image at $Re = 4000$ is weakened, suggesting that this patch structure is more difficult to maintain as Re increases.

By processing the visualised image of the flow with gradually increasing Re from the transition state, it was clearly shown that the patch structure observed during the transition is maintained even after the transition. Whether this structure is maintained at higher Re is an important topic for future research.

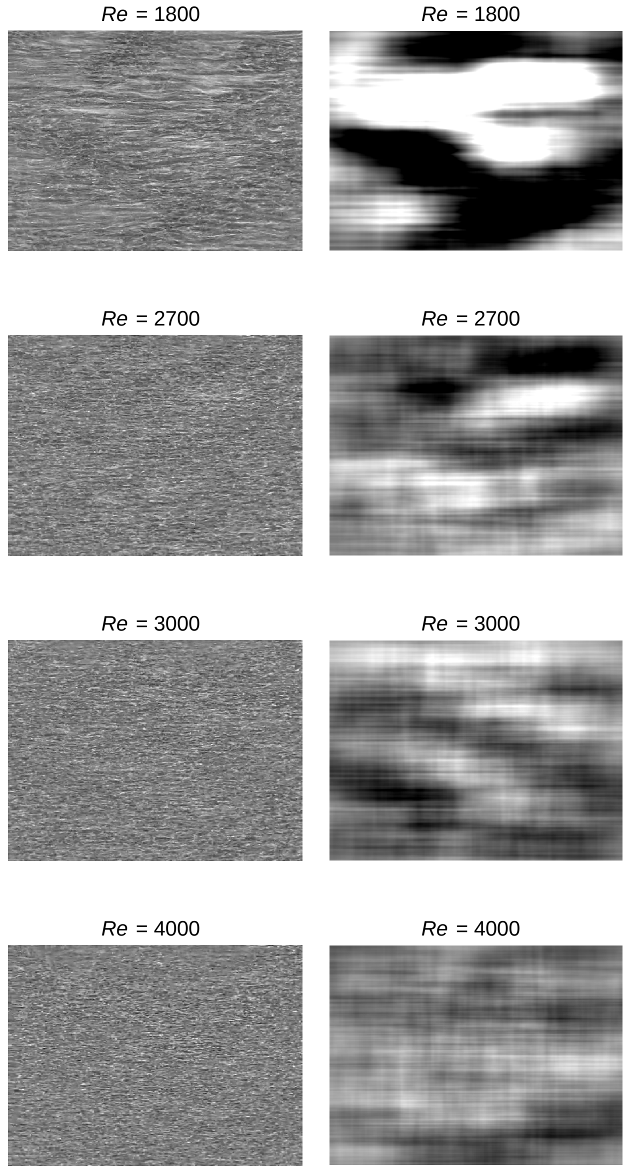

Figure 1: Original images(left) and moving average images(right). The contrast of moving average images is adjusted by the same constant factor.

References

[1] Monty, J.P., Stewart, J.A., Williams, R.C. and Chong M.S., (2007), Large-scale features in turbulent pipe and channel flows, *Journal of Fluid Mechanics*, vol. 889, pp. 147-156.

[2] Seki, D. and Matsubara, M., (2012), Experimental investigation of relaminarizing and transitional channel flows, *Physics of Fluids*, vol. 24 (12), 24102.

[3] Yimprasert, S., Kvick, M., Alfredsson, P.H., and Matsubara, M. (2021), Flow visualization and skin friction determination in transitional channel flow, *Experiments in Fluids*, vol.62, 31.

Physical significance of artificial numerical noise of DNS for turburlence

Shijun Liao [1] and Shijie Qin [1]

[1] School of Ocean and Civil Engineering, Shanghai Jiao Tong University, Shanghai, China

key-words: Clean Numerical Simulation (CNS), thermal fluctuation, DNS

Abstract:
It is a well-known phenomenon that numerical simulations of turbulent flow given by different groups and/or different methods often have large deviations, say, disagree with each other, before results of physical experiments are reported. Most of these numerical simulations are certainly wrong? Can we give any physical explanations for it?

It has been reported that turbulent flows are chaotic. Besides, all numerical algorithms have artificial numerical noises. So, due to the butterfly-effect of chaos, numerical simulations of NS equations given by the direct numerical simulations (DNS) become badly polluted by artificial numerical noises quickly, as currently illustrated in [1] and [2]. To overcome this restriction, Liao proposed the so-called "Clean Numerical Simulation" (CNS) [3]. Unlike DNS, numerical noise of CNS is rigorously negligible in a finite but long enough interval of time [4] so that we can do "clean" numerical experiment for turbulence by CNS [5].

Using clean numerical simulation (CNS), we provide evidence, for the first time, that artificial numerical noise in direct numerical simulation (DNS) of turbulence is approximately equivalent to thermal fluctuation and/or stochastic environmental noise. This confers physical significance on the artificial numerical noise of DNS of the Navier-Stokes equations. As a result, DNS on a fine mesh should correspond to turbulence under small internal/external physical disturbance, whereas DNS on a sparse mesh corresponds to turbulent flow under large physical disturbance, respectively. The key point is that: all of them have physical meanings and so are correct in terms of their deterministic physics, even if their statistics are quite different. This provides a positive viewpoint regarding the presence of artificial numerical noise in DNS.

For details, please refer to Liao and Qin [6].

References

[1] Qin, S. and Liao, S., (2022): Large-scale influence of numerical noises as artificial stochastic disturbances on a sustained turbulence, ,*J. Fluid Mech., vol. 948, pp. A7* (`doi:10.1017/jfm.2022.710`)

[2] Qin, S., Yang Y., Huang Y., Mei X., Wang L. and Liao, S., (2024): Is a direct numerical simulation (DNS) of Navier-Stokes equations with small enough grid spacing and time-step definitely reliable/correct?, *Journal of Ocean Engineering and Science, 9:293-310.*

[3] Liao, S., (2009): On the reliability of computed chaotic solutions of non-linear differential equations, *Tellus - A, vol. 61, pp. 550-564* .

[4] Liao, S., (2024): *Clean Numerical Simulation*, Taylor & Francis Groups, Boca Raton.

[5] Liao, S. and Qin, S. (2025): Noise-expansion cascade: an origin of randomness of turbulence, *J. Fluid Mech.* (accepted, `doi:10.1017/jfm.2025.140`)

[6] Liao, S. and Qin, S., (2025): Physical significance of artificial numerical noise of DNS for turburlence, *J. Fluid Mech.* (accepted, `doi:10.1017/jfm.2025.200`)

The Stability of The Frozen Top Bubble Model: Two-Dimensional Rayleigh-Bénard Convection on the Spherical Surface

Xiaoqiu HE [1], Patrick FISCHER [1], Khodor KHADRA[1] and Yongliang XIONG [2]

[1] Institut de Mathématiques de Bordeaux, Université de Bordeaux, Bordeaux, France
[2] School of Aerospace Engineering, Huazhong University of Science and Technology, Wuhan, China

key-words: Thermal Convection, Two-Dimensional Turbulence, Direct Numerical Simulation, Stability, Asymmetry

Abstract:

Symmetry-breaking is a fundamental phenomenon in fluid dynamics, significantly affecting the stability and dynamics of thermal convection systems [1]. This study proposes the frozen top bubble model, a novel two-dimensional Rayleigh-Bénard convection (RBC) configuration that incorporates vertical asymmetry between the hot and cold boundaries. The model is derived from the classical soap bubble model [2], which has been widely used to investigate two-dimensional turbulence. However, the frozen top bubble model introduces a frozen top boundary through the penalization method, creating a non-slip, immobile region at the top with a constant lower temperature, which serves as the heat outlet for the fluid.

Direct numerical simulations (DNS) are conducted to explore the model's stability and convection dynamics. The results reveal the existence of two distinct regimes governed by the vertical asymmetry parameter: the Conditionally Stable Regime (CSR) and the Unconditionally Stable Regime (USR). In CSR, pronounced asymmetry suppresses thermal convection, leading to stability loss as the Rayleigh number increases. This regime is characterized by inefficient heat transport and heat accumulation inside the convection zone, causing the global temperature to rise monotonically with increasing Rayleigh number. Conversely, in USR, where the asymmetry is weaker, the system remains stable regardless of the Rayleigh number, with active convection and efficient heat transfer. In this regime, the rise of Rayleigh number influences the temperature field in a more non-monotonic manner.

The study further demonstrates that the instability observed in CSR originates from the inverse energy cascade, which strengthens large-scale vortices. The non-dimensional asymmetry parameter, defined as the ratio of the cold boundary length to the hot boundary length, serves as a critical indicator for predicting the system's stability. As the parameter approaches unity, the model transitions from CSR to USR, where the effects of asymmetry are diminished, convection is sustained, and heat transport is enhanced.

This work highlights the pivotal role of vertical asymmetry in thermal convection systems and offers a novel framework for studying asymmetric convection dynamics. The frozen top bubble model provides new insights into geophysical and astrophysical flows, where boundary asymmetry is frequently encountered. Future extensions of the model could incorporate rotation, tilt effects, and variable boundary conditions to further explore the complex interplay between asymmetry and turbulent convection.

References

[1] Cheng B.-Y.-C., Zhang L., Xia K.-Q., and Xie Y.-C.,(2024), Effects of asymmetric rough boundaries on turbulent Rayleigh–Bénard convection, *J. Fluid Mech., vol. 997, pp. A72*

[2] He X. Q., Bragg A. D., Xiong Y. L., and Fischer P., (2021), Turbulence and heat transfer on a rotating, heated half soap bubble, *J. Fluid Mech., vol. 924, pp. A19*

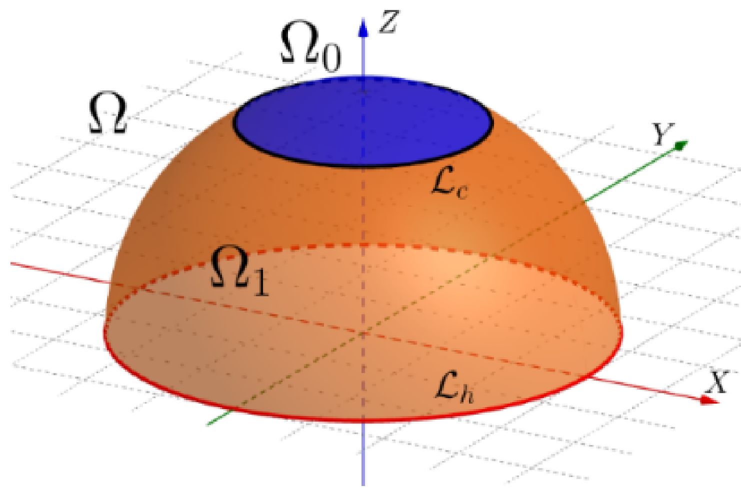

Figure 1: *Geometry of the frozen top bubble.The blue part is the frozen zone (Ω_0) and the orange part is the convection zone (Ω_1).The black circle is the cold boundary (L_c) and the red circle is the hot boundary (L_h).*

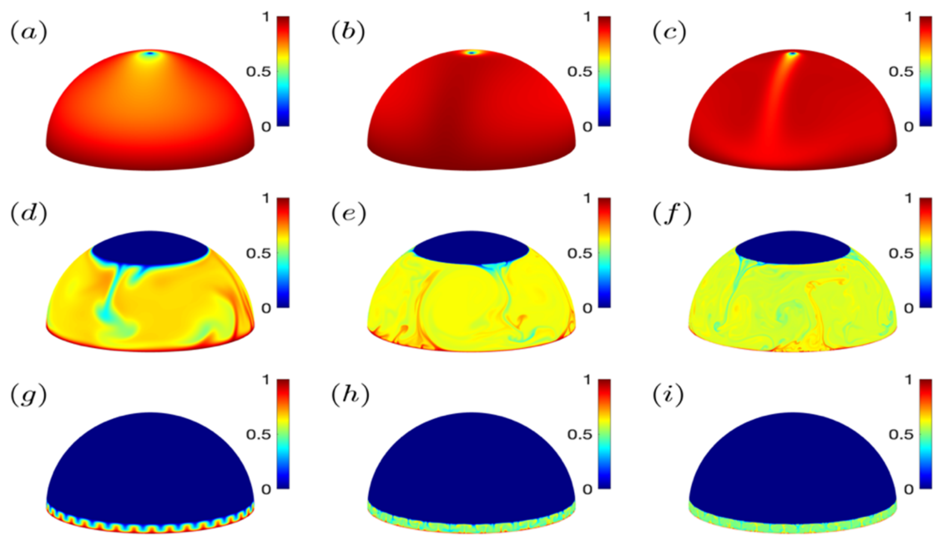

Figure 2: *Snapshots of the temperature field in stationary state of the frozen top bubble model. The top line illustrates the system with the small-scale frozen zone and in the CSR:* (a) $Ra = 1.12 \times 10^4$, (b) $Ra = 1.12 \times 10^5$ *and* (c) $Ra = 1.12 \times 10^6$. *The middle line illustrates the system with the moderate-scale frozen zone and in the USR:* (d) $Ra = 2.89 \times 10^6$, (e) $Ra = 2.89 \times 10^8$ *and* (f) $Ra = 2.89 \times 10^9$. *The bottom line illustrates the large-scale frozen zone and in the USR:* (g) $Ra = 3.49 \times 10^3$, (h) $Ra = 3.49 \times 10^5$ *and* (i) $Ra = 3.49 \times 10^6$.

Active heat-transfer control by pulsed jet in a turbulent pipe flow at high Reynolds numbers

L. Magnani [1], S. Discetti [3], A. Ianiro [3], GL. Morini [1], A. Talamelli [1,2], M. Rossi [1,2] and G. Bellani[1,2]

[1] Dipartimento di Ingegneria Industriale, University of Bologna, Bologna, Italy
[2] Centro Interdipartimentale di Ricerca Industriale aerospaziale, University of Bologna, Forlì, Italy
[3] Department of Aerospace Engineering, Universidad Carlos III de Madrid, Madrid, Spain

key-words: WORKSHOP, Active flow control, JICF, Convective heat-transfer enhancement

Abstract:

Control and enhancement of convective heat-transfer in wall-bounded turbulent flows, particularly in pipe flows, are crucial for many industrial applications [1, 2].

A common strategy to enhance heat-transfer is introducing controlled perturbations, such as cross-flow jets, which generate vortical structures that increase Reynolds stresses, enhancing momentum and thermal diffusivity. Studies have shown that pulsed jets, actuated at specific frequencies and duty cycles, outperform steady jets [3, 4, 5]. However, these findings are limited to a narrow Reynolds number range, and studies at higher, industrially relevant values are missing.

This work extends the one of Castellanos et al. [6] to higher Reynolds numbers, investigating the scaling of the optimal frequency. Experiments are conducted in the Long Pipe at the CICLoPE laboratory [7], a facility with a 0.9 m inner diameter (D) and 111.5 m length, capable of reaching Re_τ up to 50,000 ($Re_D = 3 \times 10^6$).

The setup (Fig. 1) consists of a rectangular slot ($\lambda \times d = 25 \times 1mm$) jet flush-mounted to the test section wall, pulsated via a solenoid valve triggered by a square wave. A thermally-thin Printed Circuit Board (PCB) downstream of the jet acts as a heat-flux sensor. The heat-transfer coefficient h and the Nusselt number Nu are computed assuming a steady-state energy balance:

$$h = \frac{q''_{joule} - q''_{rad} - q''_{cond}}{T_w - T_{aw}}, \qquad Nu = \frac{h \times D}{K_{air}} \tag{1}$$

where q''_{joule}, q''_{rad}, and q''_{cond} are the heat fluxes from Joule heating, radiation, and conduction, while T_w and T_{aw} are the PCB and air temperatures, respectively. Heat-transfer enhancement is quantified as $\overline{Nu}/\overline{Nu_0}$, where the pedix ”0” corresponds to the unactuated case. The local Nusselt number is spatially averaged by integrating the values over the test surface:

$$\overline{Nu} = \frac{1}{\lambda \times d} \int_{-0.6\lambda}^{0.6\lambda} \int_{-0}^{40d} Nu(x, z)\, dxdz \tag{2}$$

Tests are performed at a centerline velocity of 32.5 m/s (Re_τ = 31,000) and a jet velocity ratio of 1, with pulsation frequencies between 25 and 300 Hz and duty cycles of 25%, 50%, and 75%. Results (Fig. 2) show a peak heat-transfer enhancement at 150 Hz, which corresponds to a Strouhal number $St = 6.3$. This value is normalized with the radius of the Long Pipe and with an advection velocity equal to $10u_\tau$. At 75% duty cycle and 150 Hz, the pulsed jet outperforms steady jet actuation (Nu/Nu_0 = 1.25), demonstrating enhanced heat transfer with reduced mass-flow input. Further investigations will assess whether this optimal frequency scales with turbulence parameters as a function of Reynolds number.

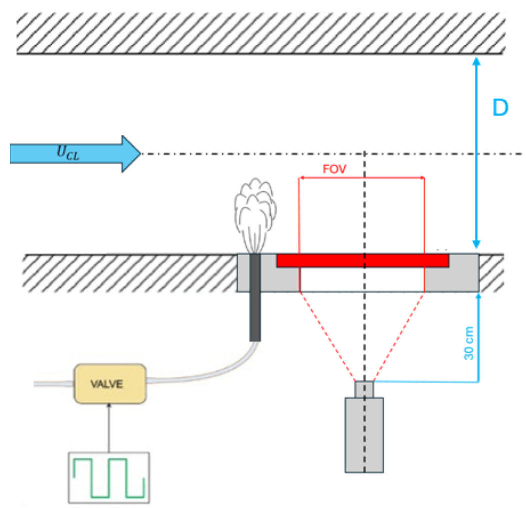

Figure 1: *Schematics of the experimental setup.*

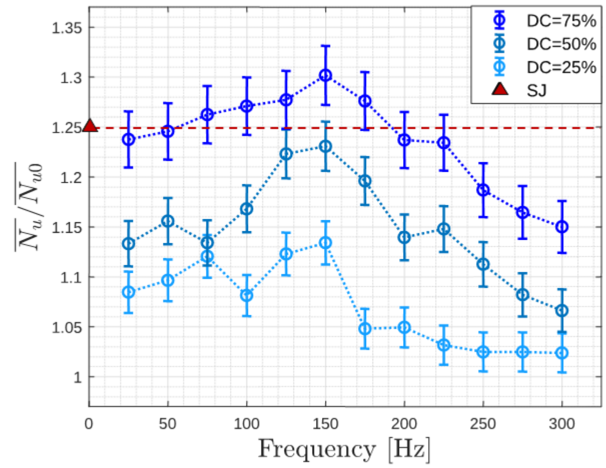

Figure 2: *Normalized average Nusselt number versus pulsation frequency for different Duty Cycle values.*

References

[1] A.E.Bergles, (2001), The Implications and Challenges of Enhanced Heat Transfer for the Chemical Process Industries, *Elsevier, vol.79, pp. 437-444*

[2] W. Li, S. Kadam, Z. Yu, (2023), Heat transfer enhancement of tubes in various shapes potentially applied to CO2 heat exchangers in refrigeration systems: review and assessment, *International Journal of Thermofluids, vol.20*

[3] J. Broadwell, R.E. Breidenthal, (1984), Structure and mixing of a transverse jet in incompressible flow, *Journal of Fluid Mechanics, vol.148, pp. 405-412*

[4] T. Liu, J.P. Sullivan, (1996), Heat transfer and flow structures in an excited circular impinging jet, *International Journal of Heat and Mass Transfer, vol.39, pp. 3695-3706*

[5] A. Eroglu, R.E. Breidenthal, (2001), Structure, penetration, and mixing of pulsed jets in crossflow, *AIAA J, vol.39, pp. 417-423*

[6] R. Castellanos, G. Salih, M. Raiola, A. Ianiro, S. Discetti, (2023), Heat transfer enhancement in turbulent boundary layers with a pulsed slot jet in crossflow, *Applied Thermal Engineering, vol.219*

[7] A. Talamelli, F. Persiani, J. Fransson, P.H. Alfredsson, A. Johansson, N. Hassan, J.D. Rueedi, K. Sreenivasan, P. Monkewitz (2009), CICLoPE - A response to the need for high Reynolds number experiments, *Fluid Dynamics Research, vol.41*

Scaling and Filtering of Sparse Wall-Pressure Measurements at the CICLoPE Long Pipe

L. Lazzarini [1], G. Dacome [2], W. J. Baars [2], G. Bellani [1] and A. Talamelli [1]

[1] Department of industrial Engineering, University of Bologna, Forlì, Italy
[2] Faculty of Aerospace engineering, Delft University of Technology, 2629 HS Delft, The Netherlands

key-words: Wall-pressure, High Reynolds Numbers, POD, hPOD, Spectral analysis

Wall-pressure measurements, Due to the relative ease of implementation compared to other sensing strategies, offers a viable solution to flow control strategies considering also their robust correlation to the velocity field [1]. However, measurements of turbulence pressure fluctuation are often contaminated by acoustic noise. It is therefore important to rely on robust algorithms to isolate turbulent pressure fluctuations from turbulence-induced fluctuations. For this purpose, several algorithms have been proposed [4]. These algorithms have been tested with a large number of closely spaced sensors. However, in practical applications, we often rely on sparse sensor configurations. In this paper, we apply three different noise removal strategies based on: Proper Orthogonal Decomposition (POD)[2], harmonic POD (hPOD)[3], and conditional spectral analysis (CSA)[4] respectively and applied in a sparse sensor configuration. The reported techniques are presented with decreasing degree of required user-input. The aim of applying these techniques is to isolate hydrodynamic wall-pressure fluctuations, which co-exist with acoustic pressure fluctuations within the raw pressure time series measured by different microphones integrated in the wall of the CICLoPE Long Pipe [5] and depicted in Fig.1. The effectiveness of the filtering approach is presented first by considering a set of synthetic signal designed considering a sparse array of five different microphones capturing wall-pressure fluctuations of a turbulent pipe flow. The techniques are then applied to a real pressure signal acquired in the CICLoPE Long Pipe facility in a Reynolds number range of $Re_\tau \approx 5\,000$ to $Re_\tau \approx 50\,000$ and an example of filtering data is shown in Fig.2. Resulting spectra of the reconstructed wall-pressure signals and wall-pressure intensities are presented to illustrate the efficacy of the filtering methods. Results highlight a proper scaling of both inner and outer scaled pre-multiplied power spectral densities [6], while pressure intensities shows a slight deviation with respect to a known trend that can be found in literature [7] and shown in Fig.3.

References

[1] Dacome, G., Lazzarini, L., Talamelli, A., Bellani, G., & Baars, W. J. (2025). Scaling of wall-pressure–velocity correlations in high Reynolds number turbulent pipe flow. *arXiv preprint arXiv:2501.08018.*

[2] Tinney C. E., Shipman, J. & Panickar, P., (2019), Proper-Orthogonal-Decomposition-Based-Reduced-Order Models for Characterizing Ship Airwake Interactions., *AIAA Journal , vol. 58, pp. 622-646*

[3] Towne A., Schmidt O. T. & Colonius T., (2018) , Spectral proper orthogonal decomposition and its relationship to dynamic mode decomposition and resolvent analysis. *Journal of Fluid Mechanics , vol. 847, pp. 821-867*

[4] Richardson R., Zhang Y., & Cattafesta L. N., (2023), Sensor decontamination via conditional spectral analysis, *Experiments in Fluids, vol. 64, pp. 163*

[5] Bellani, G., & Talamelli, A. (2016). The final design of the Long Pipe in CICLOPE., *Springer International Publishing. Progress in Turbulence VI*, Bertinoro, pp. 205-209

[6] Baars W. J., Dacome G., & Lee M. (2024). Reynolds-number scaling of wall-pressure–velocity correlations in wall-bounded turbulence, *Journal of Fluid Mechanics, vol. 981, pp. A15*

[7] Klewicki J. C., Priyadarshana P. J. A., & Metzger M. M. (2007). Statistical structure of the fluctuating wall pressure and its in-plane gradients at high Reynolds number, *Journal of Fluid Mechanics, vol. 609, pp. 195-220*

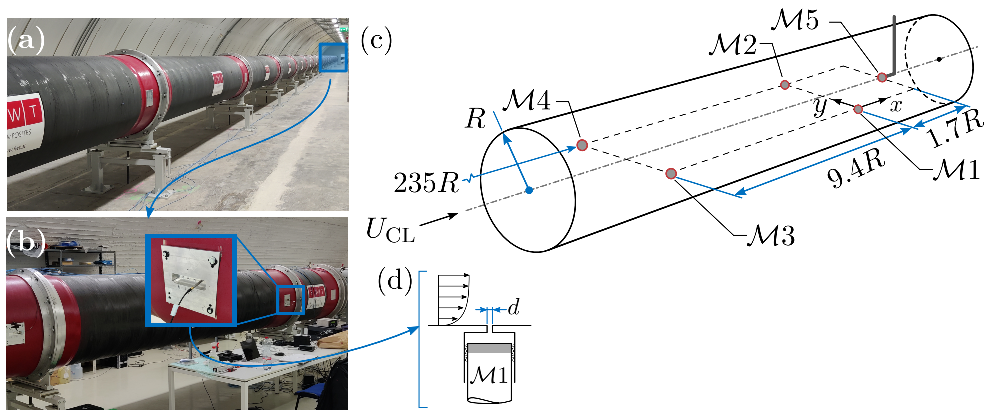

Figure 1: (a) Photograph of the Long Pipe facility in the CICLoPE laboratory. (b) Photograph of the test section at the downstream end of the Long Pipe facility. (c) Diagram illustrating the placement of sensors ($\mathcal{M}1$ to $\mathcal{M}5$) on the wall and on the centreline of the pipe. (d) Schematic displaying the design of the pinhole employed to integrate the pressure microphones.

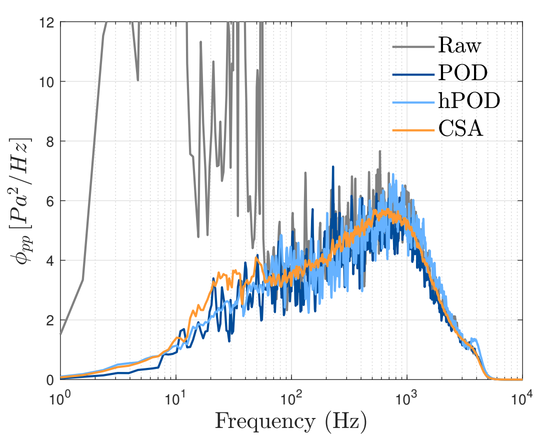

Figure 2: Power spectral densities of the hydrodynamic pressure fluctuation from microphone $\mathcal{M}1$ at $Re_\tau = 13853$: raw signal (grey), filtered using POD (blue), filtered with harmonic POD (light blue) and filtered using CSA (orange).

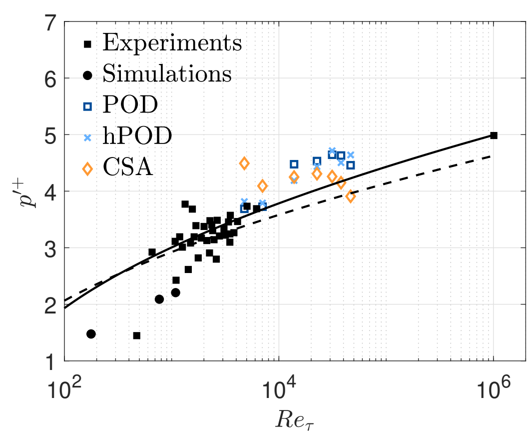

Figure 3: inner scaled wall pressure intensity taken as an integral of the spectra. filled black dots, solid black line and dashed black line refers to empirical results from [7]. Blue empty squares represents data obtained from POD filtering, light blue crosses represents data filtered using harmonic POD and orange diamonds shows data obtained from CSA filtering approach.

An experimental platform to investigate the propagation of turbulent fluctuations in a lung model

A. Ravaioli [1], G. Santi [2], B. Bortolani[3], E. Marcelli [4,5], A. Benassi [6] and G. Bellani [1]

[1] Department of Industrial Engineering, University of Bologna, Forlì, Italy
[2] Aerospace - Interdepartmental Center for Industrial Research (CIRI-Aerospace), University of Bologna, Bologna, Italy
[3] eDIMES Lab – Laboratory of Bioengineering, Department of Medical and Surgical Sciences (DIMEC), University of Bologna, Bologna, Italy
[4] Health Sciences and Technologies – Interdepartmental Center for Industrial Research (CIRI-SDV), University of Bologna, Bologna, Italy
[5] IRCCS Azienda Ospedaliero-Universitaria di Bologna, Italy
[6] Chiesi Farmaceutici S.p.A., Parma, Italy

key-words: Lung, Bifurcations, Transitional flow, Hot-wire Anemometry, 3D printing

Abstract:
Understanding airflow dynamics and aerosol deposition in lung airways is crucial for advancing respiratory therapies. However, the complex hierarchical structure of the lung—characterized by up to 23 generations of asymmetrically branching airways—poses significant challenges for both numerical simulations and experimental investigations, particularly in capturing turbulent fluctuations deep within the respiratory tract [1].

In this study, we introduce an experimental platform designed to investigate the propagation of turbulent fluctuations in a simplified lung model. Our approach employs a planar, 3D-printed airway geometry (inspired by Möller et al. [2]) that represents generations 5 to 7. Hot-wire anemometry, with three probes strategically placed along the centerlines of the branches, is used to measure the flow regimes and fluctuation characteristics simultaneously at multiple locations, under various inlet conditions. These inlet conditions are controlled by using different ducts, which also feature additional measurement stations. The manufacturing process using 3D printing (Formlabs and Stratasys 3D printers) also includes the fabrication of custom seals for each measurement station. To maintain Reynolds number similarity, the model is scaled 3:1 relative to anatomical dimensions—a compromise that balances the need for accurate generation diameters and achievable flow velocities. Careful calibration of the hot-wire probes is required, given the need to account for low-velocity effects in the deepest branches.

Preliminary results indicate that, for a quasi-laminar inlet flow (an equivalent flow rate of 30 L/min at the throat), turbulence is generated after the first bifurcation (G5), while a fully turbulent inlet flow (an equivalent flow rate of 60 L/min at the throat) induces an observable energy decay through subsequent generations (G6, G7). Notably, these findings diverge from recent CFD predictions (LES and RANS) [3] [4], underscoring the necessity for further investigation into the mechanisms of turbulent propagation in the lung.

This experimental platform lays the groundwork for comprehensive studies that will eventually extend the analysis from the upper airways to deeper generations, offering valuable insights for optimizing aerosol drug delivery, and improving treatments for respiratory diseases. Additionally, the data obtained will support the tuning and validation of CFD models, ensuring more reliable numerical predictions of airflow dynamics in lung airways.

References

[1] C Kleinstreuer and Z Zhang. Airflow and particle transport in the human respiratory system. *Annual review of fluid mechanics*, 42(1):301–334, 2010.

[2] Georg Möller, Malte Bieber, Stefanie Gürzing, Anja Lena Thiebes, Sarah Klein, Christian Gabriel Cornelissen, and Manuel Armin Reddemann. Transparent 23-generation airway model for experimental investigation of aerosol flow and deposition within the human respiratory tract. *Journal of Aerosol Science*, 156:105782, 2021.

[3] GH Spasov, R Rossi, A Vanossi, C Cottini, and A Benassi. A critical analysis of the cfd-dem simulation of pharmaceutical aerosols deposition in extra-thoracic airways. *International Journal of Pharmaceutics*, 629:122331, 2022.

[4] GH Spasov, R Rossi, A Vanossi, C Cottini, and A Benassi. A critical analysis of the cfd-dem simulation of pharmaceutical aerosols deposition in upper intra-thoracic airways: Considerations on air flow. *Computers in Biology and Medicine*, 170:107948, 2024.

Representation of turbulent structures in stable atmospheric boundary-layer regimes using large eddy simulations

L. Bührend [1] and A. Englberger [1]

[1] Institute of Atmospheric Physics, German Aerospace Center (DLR), Oberpfaffenhofen, Germany

key-words: stable boundary layer regime, large eddy simulation, subgrid-scale model

Abstract:

The atmospheric boundary layer is defined as the lower part of the atmosphere which interacts with the forcings of earths surface [1]. At daytime, the warming of the lower boundary leads to rapid mixing of the air and the evolution of the so-called convective boundary layer (CBL). With the sunset and the transition to night time, cooling of the surface reduces vertical mixing. This results in the so-called stable boundary layer (SBL). A typical characteristic of the SBL is weak, small-scale and intermittent turbulence [2].

Further aspects of the SBL are: an increase in temperature with altitude, known as a temperature inversion; a change in wind direction with altitude known as wind veer due to the predominance of Coriolis force (Ekman spiral) and supergeostrophic wind speeds in the upper part of the boundary layer due to decoupling from the surface, called low-level jet (LLJ) [1, 3]. In addition, the SBL can be described by two regimes, the weakly (wSBL) and the very stable boundary layer (vSBL) [2]. The wSBL occurs usually at higher mean wind speeds, includes weak stratification and continuous spatio-temporal turbulence [2]. In addition, coherent turbulent structures called hairpin or horseshoe vortices linked with temperature microfronts may occur in the wSBL [4]. In opposition, the vSBL is characterized by small wind speeds, a strongly-stratified flow and intermittent turbulence [2].

Atmospheric measurements, e.g. by LiDARs and microwave radiometers, are spatially limited. To gain a more complete understanding of the turbulent dynamics across the entire three-dimensional domain, our goal is to conduct numerical 3D simulations that capture the evolving turbulent flow and temperature fields over time. While still representing small scale turbulent structures like above mentioned hairpin vortices and temperature microfronts, the results should be obtained using a minimum of computational resources and time. These requirements are satisfied by large-eddy simulations (LESs), which solve the filtered Navier-Stokes equations for wind speeds and may solve in addition equations for temperature, pressure and other scalar quantities. Eddies in the turbulent flow that exceed the filter size Δ are explicitly resolved. Turbulence with a characteristic length scale smaller than Δ is parameterized by the so called subgrid-scale (SGS) model. In general, LESs play a major role in analyzing turbulence and transport processes in the atmospheric boundary layer (ABL) [5].

Due to the small size and weak nature of SBL turbulence, the results of SBL simulations are very sensitive to the applied SGS model. If the model is purely dissipative (i.e. energy is transported solely from larger to smaller scales to viscous dissipation), LES might result in an unrealistic fully laminar flow, neglecting shear-induced turbulence completely.

Our simulation setup is the numerical flow solver EULAG (Eulerian/semi-lagrangian solver, further information can be found in [6]). We have implemented a so-called Nonlinear Backscatter SGS model developed by B. Kosovic (details can be found in [7]). Briefly summarized, the inclusion of higher order moments of the strain-rate and rotation-rate tensor leads to energy transport from smaller to larger scales ("energy backscattering").

With EULAG and the Nonlinear Backscatter SGS model we are able to investigate the vSBL and the wSBL and to which extend coherent vortical structures and temperature microfronts are observable in these regimes. The results of these investigations will be presented in our talk. A first view of the simulated wind speed and temperature fields of the wSBL is visible in Figure 1.

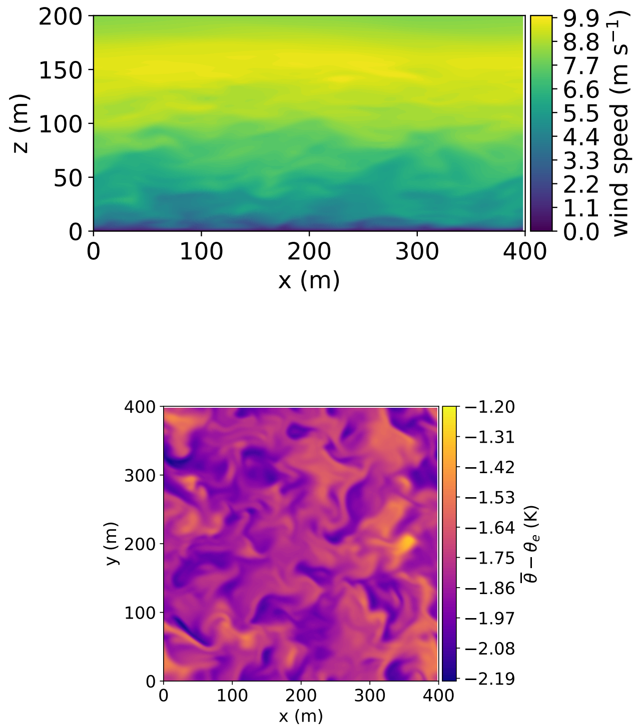

Figure 1: *Results of an LES of a weakly stable boundary layer simulations with a grid size of 2 m after 9 hours of simulation time. Boundary and initial conditions are similar to the GABLS1 benchmark case (see [8]). Top: xz-slice of the total wind speed with a visible LLJ. Bottom: xy-slice of the potential temperature deviation from the ambient temperature field with visible microfronts.*

References

[1] Roland B. Stull, ed. (1988). *An Introduction to Boundary Layer Meteorology*. Springer Netherlands.

[2] L. Mahrt (2014). "Stably Stratified Atmospheric Boundary Layers". In: *Annual Review of Fluid Mechanics* 46.1, pp. 23–45. ISSN: 1545-4479.

[3] Alan Shapiro and Evgeni Fedorovich (2010). "Analytical description of a nocturnal low-level jet". In: *Quarterly Journal of the Royal Meteorological Society* 136.650, pp. 1255–1262.

[4] Thomas Gerz, Jim Howell, and Larry Mahrt (1994). "Vortex structures and microfronts". In: *Physics of Fluids* 6.3, pp. 1242–1251. ISSN: 1089-7666.

[5] Rob Stoll et al. (2020). "Large-Eddy Simulation of the Atmospheric Boundary Layer". In: *Boundary-Layer Meteorology* 177.2-3, pp. 541–581.

[6] Joseph M. Prusa, Piotr K. Smolarkiewicz, and Andrzej A. Wyszogrodzki (2008). "EULAG, a computational model for multiscale flows". In: *Computers and Fluids* 37.9, pp. 1193–1207.

[7] Branko Kosovic (1997). "Subgrid-scale modelling for the large-eddy simulation of high-Reynolds-number boundary layers". In: *Journal of Fluid Mechanics* 336, pp. 151–182. ISSN: 1469-7645.

[8] Beare et al. (2006). "An Intercomparison of Large-Eddy Simulations of the Stable Boundary Layer". In: *Boundary-Layer Meteorology* 118.2, pp. 247–272.

Differential lag equations to predict the effects of pressure gradient histories on turbulent boundary-layers

M. Virgilio [1], T. Preskett [1], P. Jaiswal [2] and B. Ganapathisubramani[1]

[1] Aeronautical and Astronautical Department, University of Southampton, Southampton, UK
[2] Department of Mechanical Engineering, University of Wisconsin-Madison, Madison, USA

key-words: Turbulence, Pressure gradients

Abstract:
Turbulent boundary layers (TBLs) subjected to pressure gradients (PGs) are highly influenced by flow history and local boundary conditions, leading to complex dynamics that deviate from classical equilibrium assumptions. Research has shown that the development of TBLs is not solely determined by local parameters such as the Clauser pressure gradient parameter (β) [3], but also by the cumulative effects of upstream flow conditions. Non-equilibrium TBLs exhibit distinct inner and outer layer responses to PG variations, with rapid changes in β creating history effects that alter shear stress levels and turbulence statistics, even when mean velocity profiles appear self-similar.

Studies using large-eddy simulations (LES) and experimental investigations have demonstrated that non-uniform pressure gradient distributions weaken the wake region and alter the outer peak in streamwise velocity fluctuations. This indicates that local β alone is insufficient to characterize turbulence in non-equilibrium flows. Instead, additional parameters are needed to capture the influence of flow history accurately. Moreover, pressure gradient histories influence integral quantities such as momentum and displacement thickness, leading to lagged responses in the boundary layer evolution, which must be incorporated into predictive models.

To address these challenges, models such as those developed by **(author?)** [4] have attempted to define a universal parameter space for predicting TBL evolution under PGs. These models rely on similarity laws and momentum integral equations to capture the streamwise development of the boundary layer. However, experimental and numerical studies have shown that strong pressure gradients disrupt classical log-law formulations and alter the wake structure of the mean velocity profile. Recent work by **(author?)** [1] has sought to simplify these models by reducing their complexity into a single first-order equation, making them more practical for applications in engineering and experimental setups.

Building on these advancements, the present study proposes a data-driven approach to improve the predictive capabilities of TBL evolution under pressure gradients. Experiments are carried out in a smooth-wall turbulent boundary layer ($Re_\tau \geq 3500$) subjected to different pressure gradient (PG) histories. Oil-film interferometry (OFI) is used to measure the skin friction evolution over the entire history while wide-field particle image velocimetry (PIV) captures the mean flowfield. This data is used to demonstrate the influence of PG history on skin-friction as well as other integral quantities such as displacement (δ^*) and momentum thickness (θ). Based on observations from the data, a new set of ordinary differential equations (ODEs) are proposed to model the streamwise evolution of a turbulent boundary layer (TBL) subjected to different pressure gradient histories. The model is calibrated using limited number of experimental cases and its utility is demonstrated on other cases. Moreover, the model is applied to data from large-eddy simulations (LES) of flows in adverse pressure gradient (APG) conditions [2]. The model is subsequently used to identify the impact of pressure gradient history length on the boundary layer. This can also be interpreted as determining the spatial frequency response of the boundary layer to pressure gradient disturbances. Results suggest that short spatial variations in pressure gradients primarily affect a small portion of the TBL evolution, whereas longer-lasting ones have a more extensive impact.

References

[1] Rahul Agrawal, Sanjeeb T Bose, Kevin P Griffin, and Parviz Moin. An extension of thwaites' method for turbulent boundary layers. *Flow*, 4:E25, 2024.

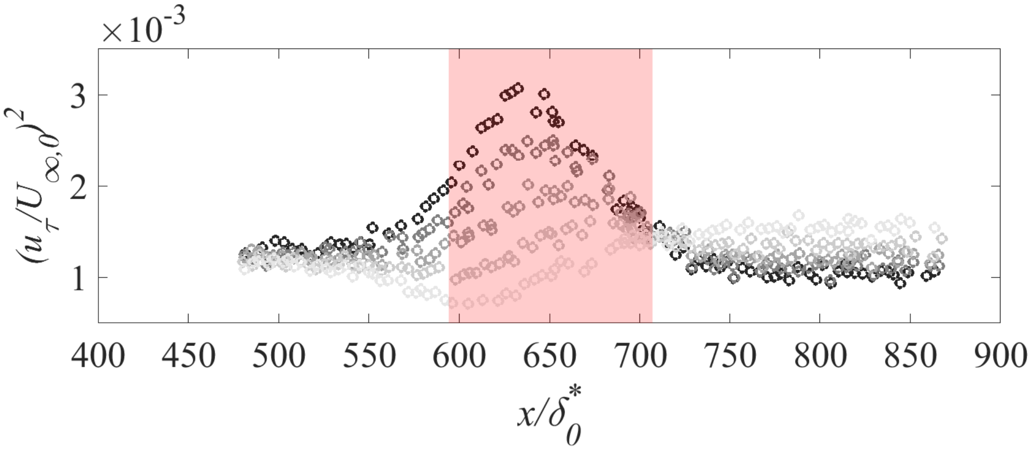

Figure 1: Wall shear stress measurements: gradients of gray from light to dark, AOA = 8°, 4°, 0°, −4°, −8°; light-red box, region below the airfoil at AOA=0°; $U_{\infty,0}$, free-stream velocity as x_0; u_τ, friction velocity.

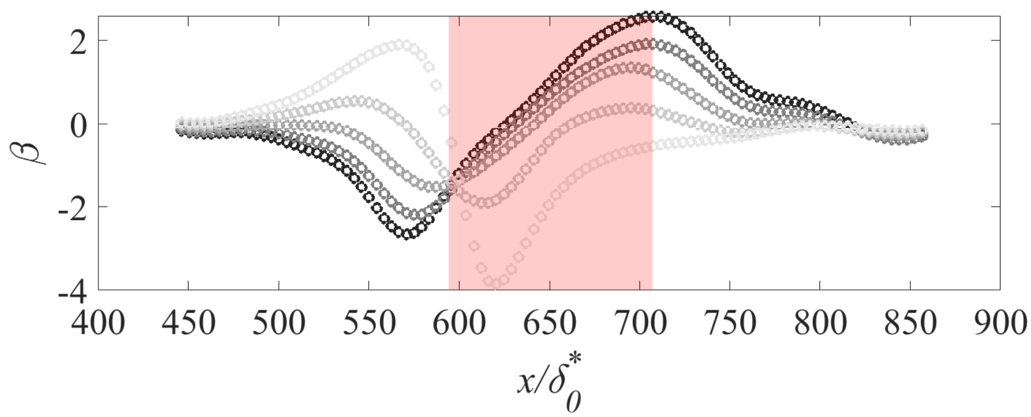

Figure 2: Measured Clauser parameter of the TBLs developing underneath the wing: β vs x/δ_0^*; light-red box, region below the airfoil at AOA=0°; gradients of gray from light to dark, AOA = 8°, 4°, 0°, −4°, −8°.

[2] Alexandra Bobke, Ricardo Vinuesa, Ramis Örlü, and Philipp Schlatter. History effects and near equilibrium in adverse-pressure-gradient turbulent boundary layers. *Journal of Fluid Mechanics*, 820:667–692, 2017.

[3] Francis H Clauser. Turbulent boundary layers in adverse pressure gradients. *Journal of the Aeronautical Sciences*, 21(2):91–108, 1954.

[4] AE Perry, Ivan Marusic, and MB Jones. On the streamwise evolution of turbulent boundary layers in arbitrary pressure gradients. *Journal of Fluid Mechanics*, 461:61–91, 2002.